Variational approaches in inverse problems for image-based characterisation of cellular dynamics

Aleix Boquet Pujadas

To cite this version:

Aleix Boquet Pujadas. Variational approaches in inverse problems for image-based characterisation of cellular dynamics. Fluid mechanics [physics.class-ph]. Sorbonne Université, 2019. English. NNT : 2019SORUS558 . tel-03384700

HAL Id: tel-03384700
https://theses.hal.science/tel-03384700

Submitted on 19 Oct 2021

THÈSE DE DOCTORAT
DE SORBONNE UNIVERSITÉ

Spécialité : Mathématiques appliquées

EDITE ED 130

présentée par

Aleix BOQUET PUJADAS

pour obtenir le grade de

DOCTEUR DE SORBONNE UNIVERSITÉ

Variational approaches in inverse problems for image-based characterisation of cellular dynamics

---

soutenue le 26 novembre 2019
devant le jury composé de :

Laure BLANC-FÉRAUD	Rapporteuse
Michael LIEBLING	Rapporteur
Dominique BÉRÉZIAT	Examinateur
Benoît LADOUX	Examinateur
Arrate MUÑOZ BARRUTIA	Examinatrice
Jean-Christophe OLIVO-MARIN	Directeur

Table des matières

Acknowledgements **9**

Outline and overview **13**

I Introduction **19**

I.1 PDEs and inverse problems in image analysis 19
  I.1.1 The modern quartet of image analysis 20
  I.1.2 Partial Differential Equations 20
  I.1.3 Inverse problems 22
I.2 Bioimaging for morphodynamics 23
  I.2.1 Overview 23
    I.2.1.1 The diversity of cell motility 24
  I.2.2 Detecting, characterising and following cells 27
    I.2.2.1 Cell segmentation 27
    I.2.2.2 Cell shape description 30
    I.2.2.3 Cell tracking and motion fields 32
  I.2.3 Biophysical measurements 34
    I.2.3.1 Active 34
    I.2.3.2 Passive 35
    I.2.3.3 Comparison 35
    I.2.3.4 FRET and photo-quenching 36
  I.2.4 Microenvironments 36
I.3 A research niche : image analysis for mechanobiology 37

II Measuring inside the cell **39**

II.1 BioFlow 39
  II.1.1 Optical Flow 41
    II.1.1.1 The aperture problem 44
  II.1.2 Theoretical framework 44
    II.1.2.1 Case study : modelling cytoplasmic streaming using fluid dynamics or *panta rhei* 45
  II.1.3 Numerical resolution 52

II.1.3.1 Evaluating the functional by solving the PDE : the Finite Element Method 52
II.1.3.2 Computing the gradient of the functional : the Adjoint method 54
II.1.3.3 Minimisation of the functional using L-BFGS-B 55
II.1.3.4 Multi-scale analysis for large displacements 56
II.1.3.5 Automatic estimation of functional weights 56
II.1.3.6 Cell segmentation : edge and region-based active contours 58
II.1.3.7 Delaunay meshing and surface/contour simplification via VSA 59
II.1.4 Implementation as open-source software in Icy 61
II.1.5 Advantages and limitations 64
II.2 Biophysical measurements inside the amoeboid cell 66
II.2.1 Preliminary analysis of the measurements 66
II.2.2 Study of single protrusions 71
II.2.3 Periodicity in amoeboid migration 73
II.2.4 Importance of actin dynamics on intracellular flow 75
II.2.5 Insight into amoeboid motility 75
II.3 Study of vector fields 79
II.3.1 Streamlines, pathlines and timelines 79
II.3.2 Volume measurements 83
II.3.3 Application to the study of bleb formation in primordial germ cells 83
II.4 Tracking of intracellular diffuse domains 87
II.4.1 Mesh advection and line integration 88
II.4.1.1 Advection of partitions 89
II.4.1.2 Integration over advected partitions 91
II.4.1.3 Implementation details 92
II.4.1.4 Preliminary experiments 94
II.4.2 The role of E-cadherin during amoeboid motility in the zebrafish embryo 95
II.5 Molecular forces in intracellular-mimicking nematic systems 98
II.5.1 Microtubule-kinesin mixtures 99
II.5.1.1 Nematohydrodynamics 100
II.5.2 A qualitative comparison between fluid and active nematic forces 101
II.5.2.1 Image analysis for the active nematic force 101
II.5.2.2 Image analysis for the fluid force 104
II.5.2.3 Calibration of nematic activity 104
II.5.3 Applications to the study of defect nucleation, spatio-tem-poral chaos and dynamical instabilites : wall stress, POD and Lyapunov exponents 105
II.6 The viscoelasticity of cytoplasm 108
II.6.1 Taylor-Couette inside the cell : viscoelasticity and shear-thinning 110

II.6.2 The Oldroyd B model for viscoelastic fluids 111
  II.6.2.1 Non-dimensionalisation 112
  II.6.2.2 Weak formulation : SU, DEVSS, and convergence problems 113
  II.6.2.3 Non-linearity : Picard's and Newton's methods, and benchmark simulations 115
  II.6.2.4 Inverting time-dependency : time adjoints and checkpointing 118
II.6.3 Advantages and limitations 119

III Measuring outside the cell **121**

III.1 Modified Optical Flow 121
  III.1.1 The local conservation differential form 122
  III.1.2 The energy integral form 124
  III.1.3 Regularisation via PDE constraints 125
III.2 Traction Force Microscopy 126
  III.2.1 Definition of the problem to extract cellular tractions 128
  III.2.2 Constitutive equations : a nearly-incompressible linearly elastic model 129
    III.2.2.1 The local conservation differential form 130
    III.2.2.2 The 2D case : plane stress 131
    III.2.2.3 The energy integral form 131
    III.2.2.4 Weak boundary condition via Nitsche's approach . . . 133
  III.2.3 Formulation of a PDE-constrained inverse problem for TFM . . 133
III.3 Deterministic PDE-constrained inverse problem 136
  III.3.1 First order variations to construct the gradient 136
  III.3.2 Second order variations to build the Hessian action 138
  III.3.3 Discretisation of the ∞-dimensional Newton's method 139
    III.3.3.1 Galerkin approximation : a finite formulation of the ∞ dimensional weak equations 139
    III.3.3.2 The right finite elements avoid locking in the elastic equations 140
    III.3.3.3 A discrete formulation transforms the problems into linear algebra 140
    III.3.3.4 Conjugate Gradient only requires matrix-free Hessian actions 142
    III.3.3.5 Riesz-inspired preconditioner achieves mesh-independent convergence 143
    III.3.3.6 Multi-frontal LDL^T factorises all saddle-point systems at once 145
    III.3.3.7 Regularisation depends on the biological motive 146
    III.3.3.8 An automatic implementation to promote usage 147
    III.3.3.9 Computational hardships are mostly mesh-related in 3D 149

III.3.4 Experiments and regularisation . . . 150
III.3.4.1 Non-optical-flow preliminary test . . . 151
III.3.4.2 Optical-flow test . . . 154
III.3.4.3 The regularisation parameter should concur with the noise . . . 159
III.3.4.4 The spectrum of the Hessian reflects the influence of the data . . . 160
III.4 Bayesian PDE-constrained inverse problem . . . 163
III.4.1 ∞-dimensional Bayesian inverse problem . . . 164
III.4.1.1 Prior analysis for well-posedness and scalability . . . 165
III.4.2 Discretisation of Bayes' formula yields a Gaussian posterior . . . 167
III.4.3 Marginalisation can account for imperfections in the elastic modulus . . . 169
III.4.4 Forward propagation of traction errors quantifies displacement uncertainty . . . 170
III.4.5 A null-hypothesis test to assign a significance to observed biological structures . . . 171
III.4.6 Implementation and experiments . . . 171

IV Conclusion and future perspectives **177**

A Some intuition on the Adjoint method **181**
A.1 Discrete intuition . . . 181
A.2 Continuous intuition . . . 183

B Oldroyd-B from a discrete damper/spring system **185**
B.1 Discrete system . . . 185
B.2 Tensorialisation into continuum fluid dynamics . . . 187

C Derivation of the modified optical flow functional **189**
C.1 Other situational conservation equations . . . 191
C.2 Leibniz's general rule extended to the divergence . . . 192

D Measuring elastic moduli **195**
D.1 Brownian microrheology . . . 195
D.2 Mechanical elastography . . . 196
D.2.1 Experimental set-up. . . . 196
D.2.2 Theoretical set-up . . . 197

E Regularisation weights : filters and diffusers **201**
E.1 L^2 regularisation behaves approximately as a low-pass filter . . . 201
E.2 Tikhonov regularisation is a smoothing isotropic diffusor . . . 201
E.3 Frobenius TV operator acts via anisotropic diffusion . . . 202
E.3.1 Expressions for the TV Hessian action . . . 203

F Low-rank approximation of the covariance **205**
F.1 Covariance of the Gaussian posterior as the inverse of the Hessian . . . 205
F.2 Prior-generalised eigenvalue problem to low-rank approximate the Hessian inverse . . . 206

G Additional Figures **209**

H French summary **215**

Bibliographie **231**

I acknowledge [1]

my parents and grandparents for all the love, support and independence I had while growing up ; and for always welcoming me back with a smile when I show up in my sunny beach-side hometown. Indeed, know that a good part of the path that brings us here is necessarily based on luck, but that I also tried.

Susana Cuervo, I would like to thank you for a thousand fruitful discussions and for your enthusiasm and support in all our projects ; you always see the bright side (and capitalise on it !) and bring us food, both are invaluable for me. Thank you also for teaching me all I know about nutrition, I will forever be counting macros.

I also want to thank Alexandre Dufour for helping me in getting my PhD grant and instilling in me an interest for cell movement and all the related quantitative problems in bioimage analysis. Thank you also for helping me find an interdisciplinary enough PhD topic that could satisfy so many of my interests, and for being my advisor during the first year of my thesis. Your commitment to reproducible research is still a relevant guide to this day.

I am grateful to my thesis director, Jean-Christophe Olivo-Marin, for putting a great deal of trust in me in all presentations, grant proposals and projects. I am very happy about all the liberties you have given me to pursue my curiosity and my intuition while making sure I was doing relevant science ; I think this made me grow a lot. I am fond of your engagement with unrushed research in this metric-driven craze, and owe you much insight into academia.

Thank you Karin Eiglmeier and Sophie Goyard for importing me to Pasteur in the first place and for all your support ; you are always there for everyone, and I'm sure your enthusiasm will keep helping students' careers for the longest time. In a similar direction, I would like to acknowledge Patrick Aloy, Josep Maria Mondelo González and Erik De Schutter not only for recommending me for the job, but also for hosting me in their labs back in the day ; they were all great experiences. On a recursive note, thank you Josep Maria for recommending me for these three internships.

I am thankful to my two rapporteurs, Laure Blanc-Féraud and Michael Liebling, for agreeing to peer-review this thesis. Their thorough comments not only improved this thesis aesthetically but also fundamentally, and are a reflection of their vast expertise. In addition, I want to highlight my appreciation for all the examinateurs for accepting

---

[1] Acknowledgement paragraphs appear (mostly) in no particular order ; and, when in a list, names are written in alphabetical order.

to consecrate their time to audit the thesis : Laure Blanc-Féraud, Michael Liebling, Dominique Béréziat, Benoît Ladoux and Arrate Muñoz Barrutia. I really hope they enjoyed it. Multiple anonymous reviewers were also involved during the review of my manuscripts and helped improve them greatly in the process ; thank you all.

I am thankful to my "comité de suivi de thèse", formed by Dominique Béréziat, Michael Liebling (thank you for all these early-morning trips from Switzerland !) and Jean-Yves Tinevez, for patiently attending the yearly meetings, and yet sill manage to be so responsive and to offer advise during the presentations.

Acknowledgement is also due to my collaborators for opening up new avenues of research with exciting projects, namely Jérôme Hardoüin, Mohammad Goudarzi, Cecilia Grimaldi and Erez Raz. I very much enjoyed learning about such diverse topics ! Micah Dembo was also so very kind to send me data on Traction Force Microscopy. You have all kept my curiosity awake.

Of course, I am also indebted to the Stack Exchange communities, the FEniCS forum and all the responsive GitHub/Bitbucket repositories (as well as search engines in general) for vastly improving my code ; and all the libraries (cited throughout the text) that have made implementing algorithms much easier. I would also like to credit many physics books that are cited throughout the text. The LaTeX template used in this thesis is by Jean Hare, which also offers active support.

Gracias Nancy Guillén for answering most of my biology-related questions, specially regarding *Entamoeba histolytica* , and giving me an overview of some of the fundamental questions still lurking in the life sciences. Thank you also for all the career advice, and for inspiring me to work hard. Also for going over the introduction of this thesis several times.

Merci Elisabeth Labruyère for always hearing me out and helping me put my work on layman's terms for the biological public. Your open-mindedness is a great asset in science. It has been a pleasure to work with you. Thank you also for going over the French summary of this thesis.

Gràcies Maria Manich for learning with me on Non-Newtonian fluids and teaching me how to do biological experiments (including pipetting), as well as passing on to me your love and knowledge of plants. Wherever I end up, I will be sure to remember you by starting off a new garden. Thank you also for sharing so much with me.

Also Daniel F. González Obando for helping me out with Java and compiling things in general, and Diana Mandache and Vannary Meas-Yedid (thank you for being my garant and helping me order electronics too !) for setting up and letting me use their server to store data. Thanks are also due to Fabrice de Chaumont for discussions on tracking and machine learning, and bien sûr to Stéphane Dallongeville for giving me sweet Icy support whenever necessary. Even if I never got to talk to you, thank you very much Timothée Lecomte for leaving behind an heritage of java to python code, it helped me greatly in building Icy plug-ins.

I credit Jean-Yves Tinevez for advice in microscopy and for being exemplary in his commitment to cured research and open source code. And Samy Gooba for advice on microfabrication and sailing in the Mediterranean sea, and for always staying scientifically critical (in the good sense!). I appreciate it a lot.

I would also like to thank Marie-Anne Lin for handling many of my administrative processes with diligence and kindness.

Wen Junhao, I have enjoyed very much all our trips to volcanic islands, and your great take on Chinese cuisine. Thank you a ton Candice for feeding me all these evenings, specially for the ramen! And Jackson for sharing all your scientific values.

Some particularly inspiring talks have also helped the direction of this thesis, in this regard I would like to thank Andrew G. Edwards, Omar Ghattas, Youssef Marzouk, Matthew Parno, Marcelo Pereyra, Georg Stadler and Umberto Villa.

For the good atmosphere in the lab I would like to thank all my colleagues and friends : Arturo Aguilar, Oscar Bauer, Pascal Bochet (thanks for helping me out with the French abstract), Alexandre Bouyssoux, Robin Chalumeau, Silvia Castellanos, Thibault Lagache, William Meiniel, Suvadip Mukherjee (thanks for helping me out with the title), Rituparna Sarkar, Piernicola Spinicelli (thanks for checking the French summary) and Thierry Rose. And the lab next door! Chak Hon Luk, Lisa Sánchez and Yuen Yan Chang.

The activities organised by the PPU steering committee were also very helpful. In this context, I thank Georges Azar and Mélanie Hamon for hosting a year-round journal club, Molly Ingersoll for giving us a course on oral presentations, Paulo Vieira for showing us how to organise a scientific conference, and Andrés Alcover for managing the EU grant, as well as Friederike Jönsson and Simonetta Gribaldo. I acknowledge Susanna Celli for directing the program, fighting for us with tireless enthusiasm and always fostering a rich discussion environment. I would also like to say it was great to share these years with my cohort.

My gratitude also goes to all the team at Pasteur's canteen for keeping us well fed in a daily basis. And the Institut Pasteur itself for putting this and all the rest together to create a fruitful and collaborative environment.

Funding. I am part of the Pasteur-Paris University (PPU) International PhD Program. This project received funding from the European Union's Horizon 2020 research and innovation programme under the Marie Skłodowska-Curie grant agreement No 665807, and from the Institut Carnot Pasteur Microbes & Santé (ANR 16 CARN 0023-01)[2]. I am thankful to them for taking care of my salary and offering very convenient travel grants. I would also like to thank the Amgen Foundation for some sporadic funding under their scholars program.

The Bioimage Analysis unit is supported by grants ANR-10-INBS-04-France BioImaging and ANR-10-LABX-62-IBEID and is part of the CNRS UMR 3691.

I would also like to thank several other funding sources, which I list chronologically.

- The "2017 Summer School in Computational Physiology" was a great chance to learn about the Finite Element Method an ODE integration schemes in modelling the mechanical and electric properties of the heart. It was held by Simula, the UC San Diego, and the University of Oslo; funded by (in order of contribution) : the

---

[2] https://www.pasteur.fr/fr/enseignement/ppu

Norwegian Ministry for Research and Education (under "SUURPh"), the Research Council of Norway (INTPART grant, number 249885/H30), and the Centre for Digital Life Norway via its Research School. I appreciate very much the scholarship I was granted to cover full board and flights to Oslo and San Diego for a full three week course[3]. Organisers : Andy G. Edwards, Rachel Thomas et al.

- The "2018 Gene Golub Summer School on Inverse Problems : Systematic Integration of Data with Models under Uncertainty". The school was sponsored by the Society of Industrial and Applied Mathematics through an endowment from the estate of Gene Golub. Additional funding was provided by the National Science Fundation (NSF), Division Of Mathematical Sciences (DMS), through grant DMS-1834756 ; and cloud computing resources (Jetstream) were allocated (TG-DMS180009) by the Extreme Science and Engineering Discovery Environment (XSEDE), which is in turn supported by National Science Foundation's grant number ACI-1548562. I am grateful for the two week full board in Colorado (and flights) that allowed me to learn a great deal in inverse problems and uncertainty quantification[4]. Organisers : Omar Ghattas, Youssef Marzouk, Matthew Parno, Noemi Petra, Georg Stadler, Umberto Villa.

- The trimester "The mathematics of imaging" and associated summer school held by the Institut Henri Poincaré. In this case, I would like to acknowledge the support of Institut Henri Poincaré (UMS 839 CNRS-Sorbonne Université), and LabEx CARMIN (ANR-10-LABX-59-01) for a one week full-board accomodation at the Centre International de Rencontres Mathématiques (CIRM), Marseille, to learn on cutting-edge mathematical formulations of imaging problems[5]. Organisers : Jean-François Aujol, Julie Delon, Agnès Desolneux, Jalal Fadili, Bruno Galerne, Gabriel Peyré.

- The trimester "The mathematics of climate and the environment" and associated summer school, also at the Institut Henri Poincaré. I would like to thank the Institut Henri Poincaré (UMS 839 CNRS-Sorbonne Université) and for a scholarship including full board during a week at Institut d'Études Scientifiques de Cargèse, in whicb I had the pleasure to learn about a variety of techniques in data assimilation[6]. Organisers : Michael Ghil, Hervé le Treut, Mickaël D. Chekroun, Anne-Laure Dalibard, Patrice Klein, Valerio Lucarini, Sabrina Speich.

I think all these lectures were key to guide this thesis in its most theoretical part.

---

[3] `https://www.simula.no/education/courses/summer-school-computational-physiology`

[4] `http://g2s3.com/`

[5] `https://imaging-in-paris.github.io/`

[6] `http://www.geosciences.ens.fr/CliMathParis2019/`

Outline and overview

In **Chapter I** we introduce the diversity of image analysis and propose a broad conceptual framework (**Section I.1**) from where to tackle several relevant problems in the bioimaging of cellular dynamics (**Section I.2**). To contextualise this outline, let us introduce the issue very briefly.

The ability of cells to define and alter their shape and initiate and regulate movement is central to numerous fundamental biological processes including development, microbial infection, immune response, and cancer metastasis. The mechanisms underlying cell shape and motility involve complex molecular machinery that actuates mechanical signals. For example, the contractile acto-myosin network is able to generate endogenous forces both inside and outside the cell. Even though the ensemble of molecular myosin motors contr-act locally and independently, by exploiting the biophysical properties of the cell, their proper coordination is able to exert traction forces on the extracellular matrix (ECM), as well as to push the cell's bulk forward. By undergoing these and other phases, the cell is able to translate local mechanical tension into whole-cell motion and eventually into global cell migration. Therefore, deciphering how cells deform and move requires a better understanding of the biophysical quantities that do not only drive but also reflect intracellular (IC) and extracellular (EC) dynamics, such as IC/EC forces and IC pressure.

Unfortunately, many of these quantities cannot be measured directly with current methodologies, especially at the IC level. Instead, they are typically estimated using either invasive experimental methods or indirect approaches. Direct methods are able to yield precise yet localised measurements at the expense of a more complex experimental set-up and at a loss of biological relevance. Indeed, at the present stage of miniaturisation, these techniques often hinder movement and risk cell damage. On the other hand, indirect methods offer measurements at a more global scale albeit with less accuracy and lower spatial resolution. Regardless of the method, many biophysical measurements remain elusive or scarce and are frequently limited by experimental constraints. In summary, there is a need for a method to measure biophysical quantities that is reproducible, non-invasive and is generalizable, notably within the cell.

In **Chapter II** we focus on the intracellular. We begin, **Section II.1**, by presenting a method that extracts IC measurements everywhere inside freely moving cells using live cell imaging. This is achieved by extracting the motion of intracellular material observed using fluorescence microscopy, while simultaneously inferring the variables of a physical description of the cell interior. Even though we devised the method to measure the IC as described, its framework is very general and extends easily to different models, including the EC. This framework is the result of integrating two techniques : optical flow, an image processing method that extracts motion information from image sequences ; and data assimilation. This is all formulated under a variational approach. Namely, we minimise a functional describing the movement of the pixel intensity within the images constrained by a system of PDEs that describe the relation between the movement of the observed material and its parameters of interest. In a first instance of the method, the theoretical description is chosen as a model in fluid dynamics. In particular, the cell interior is well described by a Stokes regime ($\mathrm{Re} \ll 1$) as inertia plays little role at the cell scale. In this case, the quantities of interest are IC velocity, IC pressure and IC forces (IC-vpf) ; while the motion of IC material captured by fluorescence microscopy constitutes the observations of the model. The problem is solved numerically with an algorithm that combines the finite element and adjoint methods into a multi-resolution scheme driven by Broyden–Fletcher–Goldfarb–Shanno gradient descent. The algorithm is automatised into a software module that segments the cell of interest from a given image sequence and computes the IC estimates.

In **Section II.2**, we illustrate and validate the efficacy of this approach in the context of amoeboid cell migration. In particular, we use our method to study the trophozoite stage of the unicellular parasite *Entamoeba histolytica*. These amoebas are characterised by the emission of bulges (blebs) at the cell surface that convert into protrusions and are filled via cytoplasmic streaming driven by acto-myosin contraction forces. Their high motility and the predominantly viscous nature of their cytoplasm constitute an appealing model from a biophysical standpoint. We show that, by using only a cytoplasmic label and confocal microscopy, our method yields IC-vpf spatiotemporal measures everywhere inside *Entamoeba histolytica* cells migrating on a conventional substrate *in vitro*. These measurements corroborate and extend both theoretical and experimental studies. Our contribution is notable in two aspects. One, we report for the first time a full quantitative description of the movement phases of the parasite, confirming several predictions such as the pressure-driven cytoplasmic streaming or the force-driven retraction of the cell rear. And two, we unveil a concealed double periodicity driving *Entamoeba histolytica* : $7.9 \pm 0.4s$ in-between consecutive protrusions and $4.6 \pm 1.1s$ characterising the cytoplasmic streaming.

Section II.3. The detail in which the cytoplasmic streaming is captured by our method has motivated the development of visualisation tools that are offered as add-ons to the software. These include overlayed vector fields, as well as streamlines and pathlines in 2D and 3D. In collaboration with Mohammad Goudarzi and Erez Raz, we use these tools to visualize and quantify the precise role of cytoplasmic streaming during bleb formation *in vivo*. The accepted model is that a redistribution of the internal cytoplasm is not enough to inflate the blebs and that an influx of water from the outside through the aquaporin proteins is necessary. Using zebrafish primordial germ cells (PGCs) and microscopy at cutting-edge spatiotemporal resolution, we show that : (i) morpholino knockdown of certain aquaporins does not seem to affect blebbing ability ;

(ii) cell volume changes are not related to blebs ; (iii) blebs are predominantly filled by a redistribution of cytoplasm from the back of the cells ; and (iv) previous models overestimated the elastic energy required by the cytoplasmic streaming to stretch the membrane because they did not take in account membrane folds and invaginations.

In **Section II.4**, we show how to use the velocity fields extracted by our method (or any other PIV approach) to build an advection-based tracking scheme that is able to follow diffuse molecular regions. This is done by solving the ODE posed by the field on an initially delimited region, and by correcting possible errors with Laplace's equation. The advected region is represented by a mesh that can be further divided into subregions of interest. Finite elements can then be cast onto the mesh and used to calculate line integrals seamlessly, which allows to define multiple integral measures. In collaboration with Cecilia Grimaldi and Erez Raz, we use this tracking scheme to study the role of E-cadherin in *in vivo* cell migration. This protein is involved in cell-cell adhesion. The main observation is that a reduction of E-cadherin decreases the directionality or persistence of cells that move within a zebrafish embryo, but does not decrease their speed. It seems that E-cadherin stabilizes the actin-rich structures at the front (called actin brushes) by reducing the "natural" flow of actin towards the cell rear. As a consequence, the brushes recruit more myosin, weaken the cortex and therefore bias the formation of blebs to the front. To test this hypothesis we wanted to quantify the stabilization of actin under different expressions of E-cadherin. Our new tracking method does not only allow us to follow the actim brushes accurately despite being very diffuse, but also to define an appropriate quantification measure. In this case, we quantify the depolarisation of the actin brushes along the front-rear axis of the cell in the presence and absence of E-cadherin to confirm the hypothesis.

Section II.5. Because of their novelty and of their theoretical nature, the forces estimated by the proposed method are hard to validate experimentally. In collaboration with Jérôme Hardoüin, we study a cytoskeleton-like nematic system consisting of a mixture of microtubules and kinesin in suspension at a water-oil interface. The active nature of the kinesin molecules (fuelled by ATP hydrolisis) induces forces in the system that can be deduced from the orientation of the filaments. Since these forces are in turn reflected on the underlying water at the interface, they can be compared to those extracted by our framework. In addition, computing the pressure and deviatoric stresses is showing good promise for studying the nucleation of so-called topological defects in active matter, and calculating the Lyapunov exponents of the flow field might help analyse the system's instabilities.

Section II.6. The intracellular Stokes model is only valid at certain time scales, which depend on the cell type and its motion. To substitute the viscous Newtonian model of the cytoplasm with a more accurate representation, we take advantage of several rheological experiments reported in the literature. In particular, the cytoplasm of amoeboid cells has been repeatedly reported as a viscoelastic fluid well described by Jeffreys' model. While this is a discrete spring-damper mechanical system, its extension to continuum mechanics is known as the Oldroyd B model. By explicitly deriving the latter from the former, we reproduce the exact link between the spring-damper constants documented in the articles and the viscoelastic parameters that govern the motion of an Oldroyd fluid. However, not unlike other viscoelastic models, Oldroyd B fluids suffer from several convergence problems. To stabilise the weak formulation of the problem, we resort to a combination of the streamline upwind method, which adds a diffusive term, and the discrete elastic viscous split stress approach. Time-stepping is then implemented as a backwards scheme and the non-linearity of the model is attacked with Newton's method. Once the forward problem has converged, we adapt the data functional and regularisation introduced in Section II.1 to this time-dependent problem. While the adjoint approach to minimise the resulting PDE-constrained is outlined, we have not employed it due to a lack of meaningful biological data.

In **Chapter III** we turn to the extracellular. However, we first reassess the optical flow functional in **Section III.1**. The 2D movement reflected on the image intensity is not always linked to the 3D movement of the material in a straightforward manner. We develop a reformulation of optical flow that clarifies this relationship and is able to take into account first-order out-of-plane movement in a confocal setting.

Section III.2. As exemplified in Section II.4 with E-cadherin-mediated adhesions, extracellular forces are essential to many biological functions. Traction Force Microscopy (TFM) measures the forces exerted by cells on the extracellular substrate by observing its deformation. The aim of this section is to refomulate TFM in our framework. In this case, the biophysical quantities of interest are EC displacement and EC traction forces ; while the motion of the EC substrate captured by microscopy constitutes the observations of the model. This remake of TFM promises several advantages : reduced uncertainty propagation, consideration of out-of-plane flow (by virtue of the modified optical flow), easier extension to 3D, flexibility of the elastic model and a reduced need for point-wise measurements (i.e. fluorescent beads within the substrate), as well as the possibility to consider force-unbalanced systems and non-zero boundary conditions.

Section III.3. We take the opportunity of reformulating TFM to reinvent the framework proposed in Section II.1. In particular, our original method has some occasional stability and convergence issues that we tackle by posing the problem on more solid mathematical grounds. In this direction, we study the importance of the Hessian to our inverse problem and subsequently introduce Newton's method. In addition, we analyse all the linear systems and propose appropriate preconditioners to make the problem scalable, which is particularly interesting for our multi-resolution scheme. We also find that optimising with respect to the boundary conditions is better approached through the so-called Nitsche's method. Finally, we present different regularisations and their corresponding interpretations. In the particular case of L^2 regularisation, instead of resorting to iterative descent methods, we show that the inversion can be solved directly by addressing a coupled system of linear equations.

Section III.4. The last part of the thesis extends the framework into a Bayesian setting. Inverting the deterministic PDE-constrained problem yields but single estimates of the quantities of interest. However, it is necessary to assess how reliable the reconstructions are because the images are noisy. Indeed, a crucial duty of experimental science is to report measurement errors, yet (to our knowledge) a systematic method to quantify uncertainty has not been developed neither in PIV nor TFM. Under the Bayesian framework that we propose, the result is a posterior density that expresses the probability distribution of the traction force that was exerted by the cells on the substrate given the observation of an image sequence. To make such a large problem tractable we rely on a Laplacian approximation that yields a Gaussian posterior whose covariance is related to the Hessian of the problem, which we address using a low-rank approximation. We also model the experimental errors of the measured elastic modulus of the substrate by pre-marginalising the optical flow functional. Lastly, we propose to use the resulting error estimates to determine whether structures that appear on the recovered force field are actually significant or artifacts.

Chapter IV wraps up the thesis with some concluding remarks and offers perspective on possible applications of this work.

I – Introduction

I.1 PDEs and inverse problems in image analysis

Stochastic models, wavelet analysis, variational methods and partial differential equations have overtaken traditional spectral analysis to drive the latest generation of image processing techniques. Each approach has its *forte*.

In order to tackle the statistical nature of images, probabilistic methods rely on Markov random fields or Bayesian networks to weigh multiple hypotheses according to their likelihood and some prior knowledge. For instance, probabilistic considerations are used to reconstruct lost portions of images from their surroundings in a process known as *inpainting*. Contrary to the rest of approaches, stochastic models typically address digital images directly in the discrete pixel domain.

Alternatively, variational methods tailor cost-functions to problems. That is they formulate an energy that is to be minimised, for example to fit the image data into an underlying model. More specifically, a *blurry* image can be deconvoluted by looking for the "clean" image that, after going through the point spread function of the optical system, best matches the former image. Similarly, an image pair is *registered* by finding a map that minimises the difference between the reference and the mapped images. However, the cost-function is often not specific enough. To guarantee a unique solution, the functional space is typically reduced to only include functions of certain regularity.

Also in a continuous setting, partial differential equations (PDEs) describe the evolution of phenomena as a function of the ratios of small changes in space and time, i.e. as local differences. A classic example is image *denoising*. Think of averaging nearby intensities to get rid of spurious oscillations ; this is precisely the action of the Lapacian operator ! In this regard, PDEs are used as non-linear filters whose anisotropy can be calibrated to preserve particular image features.

On the other hand, wavelets excel at tackling multi-scale and localisation problems. Behind this success is localised basis decomposition, which can be regarded as a natural answer to the inefficiency of traditional Fourier harmonics at representing local information. Image *segmentation* is a possible application. In particular, spatial-frequency localisation makes wavelets useful for texture-based partitioning of images.

I.1.1 The modern quartet of image analysis

The four approaches offer complementary frameworks from where to address the main problems in image analysis. Indeed, they all have their own answer to the classical quintet : denoising, deblurring, segmentation, inpaitining, and registration. At a more conceptual level, each framework is related to a way of representing images [1] : be it discrete or continuous, in one basis or another. Most importantly, they are all interconnected to varying degrees [2]. Exploring the common grounds supporting all these perspectives will provide further insight and might help us leverage their qualities into a more complete framework. Here is a map :

$$\text{Probabilistic} \leftrightarrow \text{Variational} \leftrightarrow \text{PDEs} \leftrightarrow \text{Wavelets.}$$

Take stochastic models and variational methods for example. The prior probability distribution that models our expectations of the solution in a Bayesian setting is equivalent to the choice of functional space in the variational context, whose norm enters the minimisation process as a so-called regularisation term. In addition, partition functions in statisical mechanics suggest a natural way to relate probabilities and energies whereby products such as Bayes' rule are converted into sums à la Tikhonov, and probability maxima correspond to energy minima.

Or PDEs and wavelets. For instance, consider the reaction-diffusion equation that is sometimes used for denoising. This PDE can be interpreted as a decomposition into smooth (Identity) and oscillatory (Laplacian) components, which respectively behave as coarse-scale and finely-detailed wavelet projections in the context of wavelet analysis. It is precisely this equivalence that inspired the Laplacian pyramid algorithm [3]. Other connections have been established with wavelet shrinkage [4, 5] and scale-space theory [6, 7].

Surely many analogies can be drawn between the disciplines, but it is the relation between variational methods and PDEs that stands strongest ; perhaps because of their long-lasting romance in the physical sciences, notably in continuum and Lagrangian mechanics. In the calculus of variations, the stationary points of a given cost-functional can be formulated as solutions to a set of second order PDEs known as the Euler-Lagrange equations. For example, minimising the total variation semi-norm leads to the equations of anisotropic diffusion, whereas the isotropic heat equation corresponds to the H_0^1 norm. Conversely, PDEs are often solved by rewriting them into their weak forms, which can typically be traced back to the minimisation of some physical energy functional. This quasi-bijection promises a good basis from where to articulate a strategy that encompasses the best of each four perspectives. And a solid one at that : PDEs are supported by extensive mathematical literature [8].

I.1.2 Partial Differential Equations

PDEs also have the gift of intuition. The very PDE-variational equivalence is but an example : integral-energy conservation principles (mass) can be reworded as locally-conserving PDEs (continuity) by using infinitesimal operators (divergence) and arguing about arbitrary domains. In this sense, so-called "weak" solutions to PDEs are not as much so. More generally, PDEs constitute a powerful and flexible framework to describe and model a myriad of phenomena such as diffusion, reaction or advection. It is local differences that describe the world so naturally. Indeed, it is easier to conceive that events behave locally, i.e. according to their most immediate neighbours, than globally. The same logic applies to image analysis ; after all, we are still trying to catch up with the discriminatory power of our visual system, and retinal neurons fire in response to local changes in space or time [9]. Nevertheless, let us note that locality can also be a flaw, some patterns are only discernible from afar ; but one that can be addressed by a change of scale.

While all these arguments were laid on a continuous setting, where intuition is most fluent, they still hold after discretisation. In this context, PDEs are often expressed in terms of finite element bases. Alternative efforts have focused on formulating the discrete schemes into wavelets, but non-periodic boundary conditions and non-regular domains remain problematic. In both theory and computation, PDEs can often be translated into problems of (linear) algebra. Computationally speaking, PDE research is remarkably active due to their importance in engineering, and of course has benefited extensively from any hardware revolution.

It is for all these reasons that PDEs are our starting point. However, it is not all a matter of convenience. In this thesis, we use PDEs to directly model the physical world, which only later is reflected on an image sequence. A first PDE is used to describe the scalar transport equation seen through the microscope lens. This is essentially a registration problem. Since the system is underdetermined, we rewrite it in variational language. Under these terms, we can try to make the problem more specific by controlling the space of solutions. Cue the second system of PDEs. These equations model the real physical movement that the camera captures, for example using continuum mechanics to describe the cytoplasm inside a cell. Now let us rewind : the only candidates to solve the first variational problem are functions that (also) satisfy the second physical model. Moreover, instead of restricting the space of registration maps directly, we can now reduce the space of any unknown physical variable in the second PDE set. The advantages are twofold. First, regularisation can happen in a physically relevant way. And second, physical quantities can be estimated from the images ; as will be presented in the next Section, this is the major topic of the thesis : progress in image analysis is welcome, but our real interest is taking measurements. Next, we exploit the connections that we took so much time to lay down. Not local enough ? We restrict the space through the variational perspective, for example by considering only physical functions of bounded variation. Not global enough ? We take a multiresolution approach à la wavelet. Are we certain about our measurements ? Enter stochasticity through Bayesian inference. We can interpret the physical regularisation as a prior, the variational functional as an energy, and quantify the uncertainties of our measurements using Bayes' rules.

I.1.3 Inverse problems

In short, we are fitting a continuum mechanics model to image data using a registration-like functional. To solve such a problem we draw from the theory of inverse problems. Whereas the forward problem can typically be formulated to be well-posed (uniqueness), local (spatial correlation decays fast) and causal, e.g. solve the PDEs given some physical parameters and use the results to warp an image ; inverting the problem, i.e. finding the original physical parameters from a given image pair, normally results in ill-posedness (many solutions are consistent with the data), globality (the parameters depend on the values of the images everywhere) and non-causality. Variational Tikhonov regularisation, as proposed by [10], has long been the go-to approach to make image processing tasks well-posed. This is equivalent to adding *a priori* information that matches our expectations of the result, or restricting the functional space. The five traditional problems of image analysis that we have introduced can be approached as inverse problems in this way.

Inverse problems are specially prevalent in the geosciences. Where on earth did that earthquake come from ? Given an epicenter it is much easier to compute the consequences of the trembling on the surface (forward) than it is to find out the epicenter from the readings of a couple seismographs (inverse). In this example, the forward model consists in "observing" (integrating) the results of a PDE on the boundary domain and thus is well-posed. What the hell is the earth's core made of ? Again, simulating wave propagation given the properties of the mantle is much better posed than figuring out the composition of the crust by studying how seismic waves propagate. Indeed, many combinations of material layers are possible given a limited set of data : the data might come from earthquakes themselves, which fortunately do not occur all that often.

The common theme is taking measurements indirectly because the object of interest is largely inaccessible. For obvious reasons this is usual in medical imaging : tomographies, magnetic resonances, elastographies... all are based in the theory of inverse problems. Other important disciplines that fit models into data, such as meteorology or shape optimisation (e.g. plane wings), also require such machinery. In a similar way, if we want to estimate any physical parameter in or outside a cell without being invasive, it is no surprise that we end up with an inverse problem.

Luckily, these are problems of financial (oil, weather, fuel efficiency) or medical impact and therefore the theory is rich. A collection of methods has been cured over time that has kept up with advances in computational power. This not only includes the adjoint or dual approach that we so fondly use throughout the thesis, but other techniques that can reveal how much we are informing the problem with the data (e.g. through the Hessian of the functional), or how sensitive it is to any change in the variables.

I.2 Bioimaging for morphodynamics

The next dozen of pages are meant as an introduction to cell motility (as the background question) and bioimaging techniques (as the means) with an special emphasis on biophysical measurements. The intention is to introduce several techniques that are used throughout this work and, at the same time, identify the needs (and problems) that we will be tackling in the thesis.

(Directed) movement is a decisive advantage in sustaining life at any scale. At the single-cell level, a myriad of migration modes [11] have evolved [12] because they enhance the ability of cells to thrive in natural selection : a longer range of action boosts their potential to colonize resources, evade predators and cooperate. Indeed, many biological processes, whether physiological or pathological, rely on changes in cell position or location. Physiological examples are that developing embryos require precise rearrangements of differentiating cells to shape the growing organism [13], and that mounting an immune response depends on the ability of lymphocytes to circulate through the blood and tissue to the target antigen [14]. On the pathological hand, tumor cell migration is a hallmark of cancer metastasis [15], and infectious agents have to navigate within the host to reach their niche [16]. Precisely for these reasons, many potential treatments aim to specifically impair the motility of pathological cells while preserving the normal behavior of the host [17]. However, it is generally difficult to develop pharmacological compounds that are specific enough as the molecular machinery underlying cell movement is highly conserved across different organisms [12]. Therefore, studies on cell motility do not only constitute fundamental research but are also at the leading edge of therapeutic investigation. We argue that research on cell migration profits from the combination of (at least) three approaches : imaging, biophysical measurements and the fabrication of microenvironments ; and that all of them can benefit from bioimage analysis (BIA). BIA promises to tackle the ever-growing quantity of data resulting from gene regulation assays and the inherent stochasticity of cell migration, and to increase the quality of their analysis by bringing reproducibility and objectivity onto biological grounds. It is in this context that we will be proposing our method : a BIA approach to take biophysical measurements in any microenvironment.

I.2.1 Overview

Since the late 17th century, shortly after microscopes became available, the study of cell behavior and migration has been inseparable from imaging : advances in optical magnification have allowed resolving increasingly smaller features, the combination of fluorescence microscopy and tags has permitted identifying some of the prime proteins that regulate motion, and other technical improvements have facilitated long-term observations both in vitro and in vivo. A quantitative analysis of these images is essential to ensure the objectivity and reproducibility of the findings, but also to pick up on subtle or complex differences invisible to the naked eye.

To study the physical mechanisms driving cell movement, it is not enough to solely watch the proteins involved [18]. Rather, their action has to be measured to determine whether they are able to generate the necessary forces and pressures. In this regard, physical measurements were introduced to biology experimentally : the first myosin forces were probed using an enhanced laser trap [19], overall cell strength was tested against a cantilever [20] and wrinkles on deformable substrates were used as indicators of traction forces [21] ; but quickly moved into more theoretical and non-invasive grounds by integrating imaging-data, either by way of simulations [22, 23] or inverse problems [24]. Finally, recent developments in tissue microfabrication have helped mimicking the real environment of the cell and demonstrated its profound impact on cell behavior (including differentiation) and motility [25]. For instance, patterned substrates, 3D extracellular matrices (ECM) and organotypic cultures, all can be tuned to try and reproduce a setting with the different key characteristics of in vivo conditions, where the cell-system interaction is more biologically relevant than on a glass slide [26]. In this case, an investment in image analysis is again crucial to keep up with the new acquisition systems required to analyze these more and more complex sceneries.

Fortunately, BIA techniques (such as segmentation, tracking, feature extraction and mechano-imaging methods) have evolved in parallel to tackle this ever-growing amount of data by exploiting equally fast breakthroughs in computing [27]. In this introduction, we narrate the evolution of the three approaches to studying cell movement from the perspective of the underlying BIA field. We illustrate the progressive repercussions of the developments in this field with a case study : the parasite Entamoeba histolytica. The reasons are twofold. Relevance : Eh is the causative agent of human amoebiasis, an enteropathic disease with an annual death toll of over a hundred thousand whose virulence results from the parasite's motility [28] ; and quintessence : this ancient protozoan is an elementary example of amoeboid migration as it only mobilizes basic cytoskeletal elements where actin is central.

I.2.1.1 The diversity of cell motility

Keeping in movement is a relentless task for a cell. While a single stroke of a whale's fluke is enough to coast it for meters ahead [29, 30, 31], inertia plays a drastically different role at the cell scale. In fact, inertia is irrelevant : relatively small size and speed and high kinematic viscosity (low Reynolds number), all add up to favor viscous forces over inertia [32]. This means that past forces matter little, or that a cell needs to exert forces constantly in order to make its way through the surrounding media. To this end, nearly all nucleated animal cells rely on the forces generated by their actomyosin cytoskeletons. This power can be harnessed in diverse ways, but we expect them all to induce cell shape changes in a (1) polarized and (2) cyclic way. Indeed. 1) Most moving cells present a marked directional arrangement with two poles : the cell front, characterized by intense actin polymerization and adhesion ; and the cell rear, where actin is more stable, adhesions disassemble and myosin gathers to generate contraction. 2) Most moving cells also have three iterant phases in common : the cell makes a protrusion, it interacts with its surroundings (most likely through adhesions) and then it further translocates its center of mass while retracting its rear [11].

Regardless of the cell type or migration mode, these processes are often regulated by the same proteins [33]. For example, actin de- and polymerization are almost invariably controlled by the cofilin and formin effectors. Likewise, Paxilin, a signal transduction adaptor, is highly conserved throughout focal adhesions. Also ubiquitous is the Rho family of small GTPAses (e.g. RhoA, Rac), which locally fine-tunes the contractility and spreading of the actomyosin complex in most cells [34]. The activity of all these proteins is correlated through different layers of feedback that integrate sensory information and range up to gene transcription. However, the precise molecular repertoire of a cell, either as present constitutively or activated as a response to environmental cues, does determine its mode of migration [35, 36]. In the literature, individual cell migration is loosely classified in a range between two diametric modes : mesenchymal and amoeboid [11, 37].

Mesenchymal cells exert constant forces by directly pushing on the leading edge of the membrane with the growing barbed end of actin polymers. The Arp2/3 protein complex promotes this process by nucleating new actin filaments as branches of the existing scaffold, which, braced by microtubules, give rise to very recognizable fan-like (lamellipodia) and spike-like structures (filopodia). This way of crawling requires strong focal adhesions (mediated via integrin receptors) that provide traction with the ECM and can also propel the cell forward under retrograde flows [38]. As the accumulation of all these structures reduces the deform-ability of the cell, pericellular proteolysis becomes necessary to cleave obstructing fibers. This "bulldozer-like" behavior is convenient to tread on with care, but long-term migration and exploration through complex environments can benefit from better agility and speed.

In amoeboid migration actin delivers in a different way than in mesenchymals : actomyosin contractility is enhanced through ROCK, especially in the actin cortex [39]. Myosin II makes pairs of these actin filaments slide past each other at the expense of ATP hydrolysis, creating localized contractile tensions and, when properly synchronized, whole-cell hydrostatic pressure gradients. In this way, cells become more plastic and the need of actively lysing the ECM is practically eliminated [40] in favor of squeezing their way through the interstices of the matrix. Here adhesions are weaker and turn over much faster, but they are frequently assisted by intercalations with small gaps in the ECM. Although polymerization-driven gliding and dendrites are possible propulsion mechanisms, so-called blebs are most emblematic in amoeboid cells. A bleb is a hemispheroidal protrusion that results from an expansion of the plasma membrane as a cellular hernia is filled by pressure-driven fluid [41]. The initial breach is nucleated when the cortical cytoskeleton breaks or detaches from the membrane as a result of weakened adhesion energies, regulated respectively by α-actinin and ezrin, or stronger pressures or tensions [42]. Once the bleb is full of cytoplasm (or filtered cytosol) because the pressure has stabilized, the actin cortex repolymerizes and binds back with the membrane [43], then retracts (non-motile) or becomes a pseudopod that will guide the cell onward. The last step of the cycle is to move the rear of the cell forward.

The amoeboid and mesenchymal migration modes are neither mutually exclusive nor necessarily discrete. Some cells can switch behavior in response to diverse factors such as the ECM architecture (density, stiffness, dimension, etc.). The transition between modes has been described as a quasi-continuum of states laying in-between these two apical modes [11], almost like attractors of a molecular dynamical system [44], or (alternatively) as a phase transition [45]. In fact, the ability of cancer cells to alternate between migration strategies during metastasis has been big publicity for motility studies, especially on the amebic mode because it had been less investigated. Conveniently, E. histolytica is understood to stay entirely within this amoeboid range. To invade the intestine and liver, the trophozoites need to traverse mucus, epithelia, connective tissue and, eventually, blood. Myosin contractility and transient adhesions (here anchored via integrin-like receptors and loaded to the cytoskeleton through vinculin [46]) are tuned according to the stage of infection. An initial exploratory stage is characterized by pseudorandom blebbing ; but, triggered by chemoattractant molecules such as ECM-derived proteins, the amoeba soon polarizes into pseudopod (front) and uropod (rear). These two distinctive actin-based formations are respectively enriched in stabilizing proteins like PAK and ABP-120 [47], and contraction-inducing proteins as myosin II [48]. Together, they direct the penetration of the parasite into the colonic tissue using the inflammatory response of the host as positive feedback and hijacking human matrix-degrading metalloproteinases to ease their way in [49]. This eagerness for secreted immune factors such as tumor necrosis factor (TNF) [50] is well backed up by an effective phagocytic system and a solid evasion mechanism whereby the immunoglobulins that identify the amoeba as a pathogen are packed into the uropod and ejected [48] to (presumably) misdirect the immune response.

In the forthcoming sections we will show how BIA not only helps the community understand how cells move but also why they move. As E. histolytica, most cells can move randomly or in a specific direction, normally following physical or chemical cues, such as stiffness or molecular (chemotaxis) gradients. However, the distinction is sometimes not straightforward, partly due to the small Reynolds number. Another consequence of this regime is that cells drag good part of their surrounding media with them ; therefore, short displacements, even when random, are little use to feed : cells have to move a certain distance before they can outrun (nutrient) diffusion [32].

Disclaimer : even though we have introduced movement at the single-cell scale, let us point out that a good part of cells are gregarious. Collective cell migration and rearrangement are at the heart of fundamental biological processes [51], including morphogenesis [52], wound repair [53], and tumor metastasis [54]. However, the emerging mesoscale properties of collective cell organization, as seen for example in epithelial sheets, cannot be predicted efficiently from the behavior of individual cells [55]. For instance, the fluid-to-solid-like phase transitions that have been characterised in cell monolayers [56] can be inferred from a small set of physical properties such as cell shape and alignment. In the likes of schools or flocks, it is the local interaction between neighboring cells (which are often coupled through cadherin-mediated cell-cell adhesion) that creates this global cell behavior. In short, choosing the appropriate time and length scales is paramount to studying the biological system at hand. It is for this reason that we include references to multicellular analysis in this introduction.

I.2.2 Detecting, characterising and following cells

I.2.2.1 Cell segmentation

Segmentation is a cornerstone of BIA ; it is the initial step of many other image analysis techniques, such as cell shape description or tracking (Figure I.1). The aim is to partition an image, typically into individual cells and background, using the distribution of its intensity. The result is disjoint groups of pixels that share some common characteristic, are delimited by a contour, and together add up to the whole field of view (see [57] for a thorough review).

Noise permitting, the most naïve approach to cell segmentation is thresholding the brightness, i.e. creating a binary domain where dark and bright pixels respectively belong to the background and the cells. Of course the threshold is chosen diligently, by bisecting the histogram that reflects the probability distribution of the intensity. Otherwise, the intensity may be clustered into multiple classes to capture cells with different shades, which ideally show up as peaks of this histogram ; or supported with additional information that can define alternative quantitative measures (e.g. texture, color, location) that further evidence the distance between the groups. As a last step, post-processing the resulting segments helps fight noise ; examples are merging potentially connected subsets and eliminating relatively small regions (compared to the expected cell size).

If no quantity seems homogeneous within a given cell, it is advisable to focus instead on the cell contours. Accordingly, edge detection techniques exploit the spatial derivatives of the image to look for significant changes in intensity, which are expected to correlate with a change of medium. The same conceptual basis presented above for thresholding is then readily applied to the resulting edge-image because the contours also need to be distinguished from the background before they are filled. In low contrast, conceptually more involved methods, such as wavelets and neural networks, are recommended ; in other cases, leveraging the motion of the cell with respect to the background (e.g. low-rank + sparse matrix decomposition) or imposing a pre-determined elliptical shape (model-based) is better suited.

Cell-cell interaction is another challenge. It is hard to assign a pixel to either of two cells in contact because of their similar physiognomy, especially when the acquisition-derived halos shine strongly. Watershed methods look for the boundaries between adjacent cells in the ridgelines of the brightness-mountains that cells feature over the darker background [58]. At a tissue scale, where cells are crowded, vertex/graph-based approaches seek to discriminate membrane-labeled tissue cells by building a network

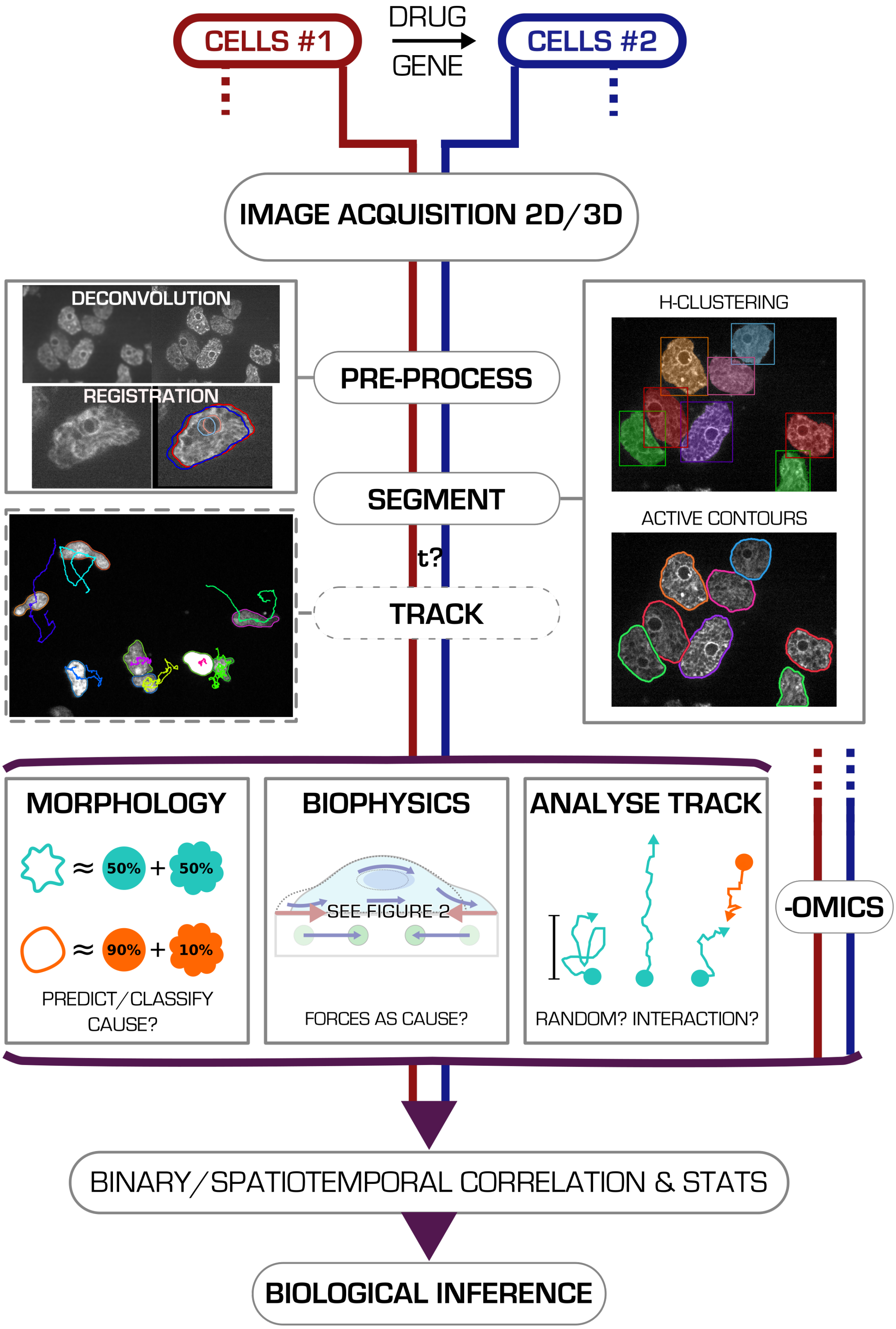
CELLS #1
DRUG
GENE
CELLS #2
IMAGE ACQUISITION 2D/3D
DECONVOLUTION
REGISTRATION
PRE-PROCESS
H-CLUSTERING
SEGMENT
ACTIVE CONTOURS
t?
TRACK
MORPHOLOGY
≈ 50% + 50%
≈ 90% + 10%
PREDICT/CLASSIFY
CAUSE?
BIOPHYSICS
SEE FIGURE 2
FORCES AS CAUSE?
ANALYSE TRACK
RANDOM? INTERACTION?
-OMICS
BINARY/SPATIOTEMPORAL CORRELATION & STATS
BIOLOGICAL INFERENCE

Figure I.1 – **Classic schematic of a bioimaging workflow.** One or more cell conditions (or strains) are to be compared. Once the image data has been acquired, the first step is pre-processing. For example, deconvolution and/or registration. Next, the cells can be segmented out via a myriad of methods, e.g. pixel-based (here H-clustering) or contour-based (here active contours). If time information is available, the cells can be tracked from the segmentation results. Examples of techniques are nearest-neighbours and multiple-hypothesis tracking. With this information the morphology can be analysed using descriptors or a combination of basis decomposition and machine learning. The resulting shape description is used to differentiate cell populations (classify) and thus to identify and predict conditions, or sometimes can be revealed as a causal agent. Additionally, the time-tracks can explain the reason a cell is moving based on statistical measures (such as mean squared displacement) : randomly, with a clear direction or in interaction with other cells. Biophysical measurements such as force estimates also constitute a great source of information, reporting directly on the effect and manner of the cells actions and bringing us closer to causality. in the form of forces. -Omics data can also be included. All this input can be combined to uncover any correlation and (hopefully) any causality, resulting in a biological discovery.

that connects the walls alike a honeycomb [59]. At both scales, including movement into the picture, as extracted from velocimetry techniques, might also help in distinguishing contiguous cells.

The methods presented are global in the sense that they incorporate information from the whole image to decide. To standardize this concept, variational methods write an energy functional that integrates several measures consisting of data-fitting expressions and regularizing terms. Lose of uniqueness is the trade-off for flexibility : convexification aside [60], there are multiple "solutions" (local minima). To find one possible solution, the image is searched locally by progressively resizing an initial region according to its surroundings. The most typical of these methods are contour-based (as opposed to pixel-based), where the image is divided by lines rather than by grouping pixels. For example, Active Contours gradually deforms a parameterized curve (or a level-set) by exerting localized forces according to energy-derived criteria such as intensity, edge information, geometrical constraints and other nearby curves. The evolution finishes when the forces equilibrate and the curve is (ideally) fitted around the cell. Most energy/force terms are based on Chan-Vese [61] ; this model splits the image into constant intensities and hence is bound to overlook heterogeneities around the cell border. There is some hope that the semi-local probing of the image might amend this issue, but it is certainly a double-edged sword. A more elegant way to enforce locality without losing the big picture is to model the cell intensity with extra degrees of freedom [62]. Anyhow, the convexity of the functionals has to be addressed complementarily, either by calibrations [60] or multi-scaling. In short, variational methods are very flexible, can combine several measures, and are more readily scalable to 3D problems. However, they need a seed (an initial contour for each cell) and they rarely consider the big picture, falling into local minima.

We have found active contours [63] the most convenient when describing the rapidly varying shape of amoeboid cells during migration, but their work is only optimal in fluorescence microscopy. Opportunely, texture filters like standard deviation translate texture into intensity and make phase-contrast or brightfield acquisitions more amenable to this fluoro-friendly technique. On another scale, subcellular localization is resolved likewise and can be complemented with statistical tools to examine a protein's place relative to the also-segmented cell (e.g. myosin is found at the back of uroid-capping trophozoites [64]), or to other proteic structures [65, 66] (e.g. Arp2/3 colocalizes with phagocytic macropinosomes [67]). Conversely, when the aim is to address the interactions within a sparse population of amoebas, the parasites are imaged small enough to apply spot-detecting techniques such as multi-scale wavelets [68].

In conclusion, cell segmentation is addressed on an ad hoc basis. Each acquisition technique and each tag has its exemplar image, but no characteristic that sets apart cell from backdrop seems to be general : there is a semantic gap between human heuristics and the algorithms. A common solution is to combine approaches. A seed can be obtained by a global method and the segmentation can later be smoothed and refined by a contour-based method. This strategy is especially fruitful if multiple channels with different labels are available, for example the cell nucleus can serve as a seed while the membrane signal drives the deforming contour. Artificial neural networks are booming in image segmentation ; they are promising because they can be extrapolated almost exhaustively to the different imaging modalities, but they still need to be trained case by case in a (progressively less) laborious process. Other possible directions of research are to include physical information that is not captured in standard images (e.g. refraction index, optical path, motion, etc.), knowledge regarding the image formation process, or biologically inspired cell shape priors. In any case, general image segmentation remains an open problem and yet is critical for any posterior analysis.

I.2.2.2 Cell shape description

Morphology has historically been regarded as a purely predictive marker of biological response (think of cell fate or differentiation), but has been more recently revisited as part of a complex feedback loop that integrates mechanical and chemical signals [69]. On the one hand, changes in cell shape overlie the constant reorganization of the actin cytoskeleton that adapts to specific whole-cell functions in response to intra- or extracellular cues. Movement, division, and interaction, all require morphological adjustments. On the other, it has been shown that cells can sense their own shape [70] via the self-organizing properties of the cytoskeleton and of reaction-diffusion systems [71]. Cell shape repercusses in the dynamics of molecular transport, and has other consequences stemming purely from geometric considerations. For instance, regions of higher membrane curvature will inherently have a higher spatial concentration of receptors when considered in 3D.

A segmented cell is represented as either a mask (a subgroup of pixels) or a contour (an ordered array of vertices in 2D or a mesh in 3D). While these data structures are friendly to the eye, their size and complexity make it hard to establish quantitative comparisons between populations of cells. Defining descriptors, which quantify potentially determinant traits, such as cell size or roundness, can reduce the dimensionality of the data. The choice of descriptors can be purely heuristic, by observing the cells, or educated with the help of artificial intelligence. Ideally, they should be resistant to noise and class-specific because the goal is to compare two non-necessarily-homogeneous cell populations. An extensive list of descriptors can be found in [72, 73], starting from very simple features (e.g. area, eccentricity) and covering a broad range of applications, e.g. the ramification factor and branching points are adapted to count filopodia and dendrites. Independent geometry-based examples are the use of skeletons to study the effect of myosin II on cellular branching morphogenesis [74] and the pipeline presented in [75] to analyse neurite growth cones.

Other approaches depend on a change of basis. Just like a color can be described via a bijection (one-to-one correspondence) to the Red-Green-Blue components, shapes can be mathematically decomposed as deviations from the circle (2D) or the sphere (3D). Respective example basis are the Fourier series and Spherical Harmonics (SH) [76]. In both cases, the original shape is decomposed as a sum of periodic functions of different frequencies. Alternatively, a color is also uniquely defined by a combination of Hue-Saturation-Brightness ; similarly, another base for 3D cell shape can be constructed with Spherical Wavelets (SW) [77]. Different bases ease different interpretations of the data. For example, SH are better descriptors of general shape as they are rotationally invariant ; however, this also makes them blind to location, which is a strong point of SW.

In the study of E. histolytica, we have used SW to automatically detect the position and number of blebs [78], a strong physiological indicator and a key driver of amoeboid migration (data not published). Conversely, SH have been used to inspect differences between populations. For example : when the adhesive properties of the parasite are reduced by signaling blockage of the Gal/GalNac lectin [79], the cells shrink and their surface coarsens/wrinkles significantly (the SH coefficients associated to higher frequencies become more dominant), which is consistent with membrane tension considerations (data not published). This strain can still navigate the ECM, but it can no longer cross the hepatic barrier [80], delaying the inflammatory response. Other studies based on SH concern medical imaging and general cell shape analysis, for example [81] studies the importance of the membrane-associated cytoskeleton in red blood cells.

Unfortunately, even when the dimensionality is reduced, it is common that results still lack human-ready interpretability [82]. Machine learning techniques (e.g. supervised : Support Vector Machine, decision trees ; or unsupervised : Principal Component Analysis) can exploit the now-smaller data to answer questions reflecting on the biological relevance of the descriptors and experimental conditions [83], as well as to discriminate populations ; but can rarely give a biologist-friendly picture of the combination of features (say SH coefficients) that make the difference. Therefore, we expect future work to be based on differential geometry because it is a natural and more illustrative way of dealing with manifolds such as the (2D) surface of a cell bending in (3D) space

[84, 85]. Indeed, more powerful descriptors can be obtained by eigen-decomposing the Laplace-Beltrami operator to assess the similarity between two shapes [86]. In this case, it is necessary to map both boundary surfaces (no sphere here), which can come at the expense of solving a non-convex optimization problem.

I.2.2.3 Cell tracking and motion fields

Diffusive, confined, intermittent and directed motions are four of many patterns of cell movement that can be inferred from the stochastic properties of cell trajectories. For example, mean squared displacement (MSD) is a good statistical measure to classify trajectories according to their directionality [87] or diffusivity [88]. Purely-Brownian motions are hardly expected at the scale of the cell [32] : the Reynolds number is low, cells are self-propelled, and molecular polarization carries some "inertia". Instead, cells display different degrees of persistence [89] that might reflect why or how they are moving.

Correlative studies have shown that E. histolytica alternates between low-persistence exploration and a highly polarized and invasive mode induced by signals from the intestinal environment that include TNF, erythrocyte factors, bacterial lysates, fibronectin residues [90, 91] and, perhaps most interestingly, self-secreted proteins [92]. Motility switches involve the activation of different molecular pathways that regulate the cytoskeleton in response to external stimuli (PI3K in the case of TNF [93]), and have been hypothesized to emerge from bifurcations of dynamical systems that model competing proteins [44]. During non-chemotactic migration, the fact that cells are still considerably persistent might reflect optimal environment-searching strategies [94]. In this context, cell persistence has been shown to exponentially correlate with cell speed. This general law results from a positive feedback loop between the asymmetric distribution of certain polarity cues such as myosin, which sustain cell directionality, and their advection by retrograde actin flows, which is often linearly coupled with cell speed [95].

Computationally, the problem of cell tracking is one of optimal mapping : two sets of already-segmented cells in consecutive frames (i.e. a bipartite graph corresponding to a pair of consecutive time frames) are to be matched almost-perfectly by minimizing a weighting function. Nearest-neighbors - a function assigning a cell's center of mass to the closest center in the next frame - is a simple and effective choice when the temporal resolution is high relative to the number of cells in the field of view. This is the case of most essays in morphodynamics. At a lower spatiotemporal resolution, where cell and particle tracking are practically equivalent, there is a need for more educated criteria that do not only privilege short distances but rather consider multiple hypothesis given the "historical" evolution of the particles and some statistical priors [96]. A collection of methods designed to deal with cluttered environments in which particles (here cells) "jump" across each other can be found in [96, 97]. The "social" behavior of cells is written down on their tracks too, and could be classified as done in mice [98, 99, 100]. In particular, cell-cell contact is a means of information exchange in multiple biological processes including the immune response wherein T-cells need to recognize surface antigens. Engineered molecular labels that are enzymatically transferred upon contact have been used to monitor the dynamics of these so-called kiss-and-run interactions [101], but cell tracking could help unveil any underlying interaction network. A last (and remarkable) instance of multicellular tracking concerns following cell lineages, for example to study morphogenesis [102, 103].

Yet another byproduct of tracking is cell speed, which frequently doubles as a measure of motility, for example to quantify the invasiveness of E. histolytica in biological environments such as (enterocytic-like) Caco-2 cell monolayers, enterocyte 3D models or hamster livers [104]. Intracellular velocity fields are also interesting in circumstances where there is nothing to segment. Active molecular transport administers the spatiotemporal distribution of intracellular proteins when diffusion alone is not sufficient [105] ; related myosin-dependent mechanisms are cytoplasmic streaming and cargo conveyance along the cytoskeleton. However, the fluorescence of bulk-advected molecules is too diffuse to be segmented consistently. The classic answers in biology are two : kymographs, which concentrate on the time evolution of a cross-section of the original image ; and projections, where the maximum intensity values across a temporal stack are casted onto a single image [106]. To avoid losing one dimension, bioimage analysts resort instead to speckle microscopy. In this case, multiple-particle tracking can be extrapolated into dense velocity fields [107]. Alternatively, correlation- velocimetry (PIV) techniques make do with standard fluorescence images by picking up on the movement of pixel intensity. This is achieved by maximizing the time correlation of local pixel-groups [108] or assuming that intensity is globally conserved, a technique known as optical flow (OF) [109]. However, there seem to be no clear results on how to use the resulting velocity maps to track the diffuse protein regions in the cell.

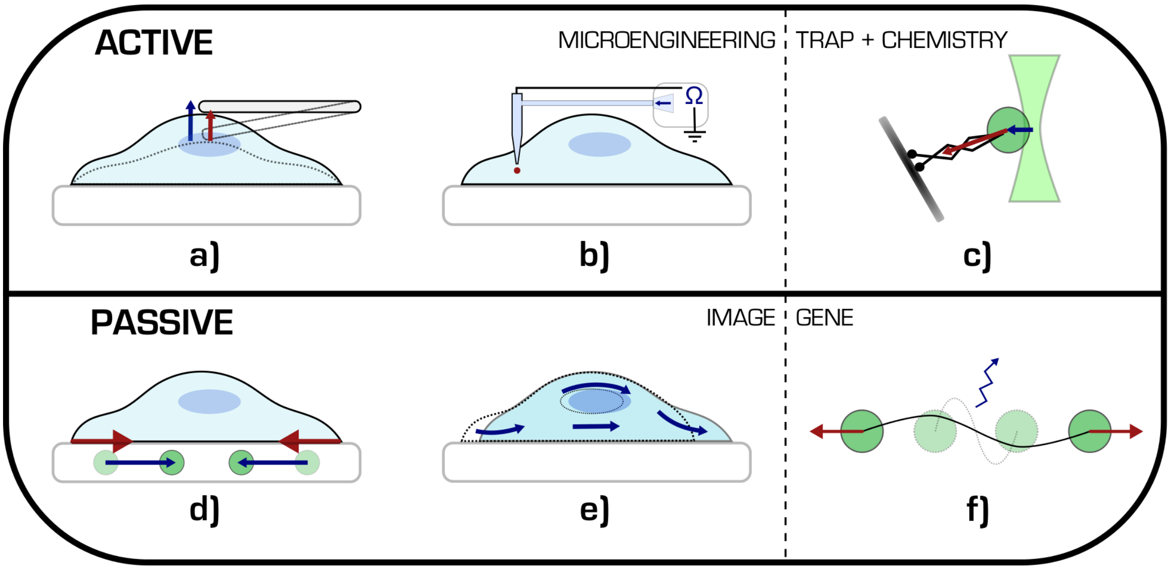

FIGURE I.2 – **Classification of methods to measure biophysical quantities. a)** Atomic force microscopy to measure force or elasticity. **b)** Servo-null micropipette to measure pressure. **c)** Optical trap to measure forces or probe properties (e.g. rheology). **d)** Traction force microscopy to measure forces on the substrate. **e)** Measurements of cytoplasmic streaming. **e)** FRET or photo-quenching to measure forces. While the first three methods require interacting actively with the cell (and possibly disturbing it), the last three use passive reporters that are captured by non-invasive imaging techniques.

I.2.3 Biophysical measurements

The mechanisms underlying cell shape and motility involve complex molecular machinery that senses and actuates both mechanical and chemical signals (external and internal) [110]. At the mechanical level, cells can detect peripheral stimuli through transducting sensors [111] such as the conformation-changing integrins at focal adhesions [112] and mechano-gated ion channels at the membrane [113], or propagate them within through the cytoskeletal scaffold. Together with the chemical input, these cues regulate the cells' response, including the generation of endogenous forces by the contractile acto-myosin network. Even though this ensemble of myosin motors contr-act locally and independently, by exploiting the biophysical properties of the cell, their proper coordination is able to (i) exert traction forces on the extracellular matrix (ECM), as well as to (ii) push the cell's bulk forward. By undergoing these and other phases, the cell is able to translate local mechanical tension into whole-cell motion and eventually into global cell migration. Therefore, deciphering how cells deform and move requires a better understanding of the biophysical quantities that do not only drive but also reflect intra/extra-cellular (IC/EC) dynamics, such as IC/EC forces and IC pressure.

Whereas molecular biology and fluorescence assays might allow correlating the different processes underlying motility with their protein actors, only measuring the actual quantities can establish causal protein-force relations and unveil the physical mechanisms behind. Unfortunately, many such measurements cannot be taken directly, especially at the IC level. Instead, current experimental methodology (review in [114]) is either I.2.3.1 invasive or I.2.3.2 indirect.

I.2.3.1 Active

These are active because they apply exogenous forces. For example, using micropipette aspiration [115] or Atomic Force Microscopy [113] to probe cortex tension or elasticity (Figure I.2a), microchip injection [116] or servo-null micropipette penetration to measure local IC pressure [117, 118] (Figure I.2b), or magnetic and optical tweezers to estimate molecular-level IC forces. Optical traps have been used to explore the stall forces exerted by the motor proteins dynein and kinesin during cargo transport in vivo [119]. This is done by tethering the molecules to phagocyted micron-sized beads (or endogenous vesicles) that are big enough to not be affected by the cellular activity, as well as to be manipulated by the radiation pressure of a near-infrared laser [120, 121] (Figure I.2c).

I.2.3.2 Passive

Or passive. This includes any combination of image-based data extraction, such as PIV [122], with posterior simulations of theoretical models [123, 124, 125] (Figure I.2e) ; or with inverse problems, e.g. using Traction Force Microscopy (TFM), where EC forces are estimated by watching cells (or tissue) freely interact with deformable substrates of known properties formed either of micro-pillars [126] or filled with fluorescent beads [127, 128] (Figure I.2d). If the constitutive relation of the substrate material is known, the traction forces can then be deduced from the deformation observed under the microscope (see [129, 130] for a review). A similar approach will be taken in this thesis, but studying cytoplasmic flows instead. In both cases, only “macroscopic” forces can be resolved because the implicit assumption of a substrate continuum does not hold at molecular length scales. An alternative technique on the same conceptual basis of passive approaches, but slightly invasive, is the embedding of micro-droplets to infer intercellular (anisotropic) stresses [131]. In more restrictive settings, notably in vivo where human intervention is limited, the experimenter relies instead on assuming several material properties and/or making use of force balance principles, giving rise to methods such as monolayer stress microscopy (reviewed in [130]).

I.2.3.3 Comparison

Active methods are able to yield precise yet localised measurements at the expense of a more complex experimental set-up and at a loss of biological relevance. Indeed, at the present stage of miniaturisation, these techniques often hinder movement and risk cell damage. On the other hand, passive methods offer measurements at a more global scale albeit with less accuracy and lower spatial resolution. These approaches constitute an area of active investigation but are still in their infancy and pose several computational challenges. First, the physical models are more complex and often lack generality because they are tailored to a specific context of cellular dynamics. Second, they suffer from error propagation. And third, they are hard to validate because equivalent measurements are typically unavailable. However, they are non-invasive and thus ideally suited for long-term monitoring of living cells ; and they are easier to extend to 3D because the experimental constraints are much weaker.

We remark that physical models underlie practically all techniques discussed so far because forces have to be assessed indirectly (Newton’s second law) by measuring other related quantities ; most commonly, the response of well-described materials. Ideally, all these models shy away from including any biological assumption in order to remain most general and impartial. In this context, in silico experiments are useful to test differing modeling hypotheses by comparing the simulated behavior of a cell or system with experimental data. This creates a positive feedback loop that accommodates progressively perfecting complex whole-cell models [132]. The combination of both approaches has been fruitful because they can be complementary [133].

As regards E. histolytica, micropipette aspiration has been used to study the role of the membrane-cortex pair [115] during bleb-based motility [134]. Magnetic tweezers have also been quite versatile. They have been used to study the response of the parasite to mechanical stimuli, whereby forces exerted on the cell rear are transduced and amplified into a biochemical signal that enhances the polarization of the cell by way of the phosphatidylinositol 3-kinase [135] ; and also to determine the rheological properties of the cytoplasm [136]. In this thesis, we will combine these measurements with estimates extracted by a new method that relates cytoplasmic streaming with several biophysical quantities within the cytoplasm.

I.2.3.4 FRET and photo-quenching

Other than invasive or indirect, a third set of gages is based on genetic engineering (Figure I.2f). Genetically-encoded biosensors based on the Förster resonance energy transfer (FRET) or photo-quenching are conceived to shine in response to tension across an intracellular protein of interest or at the cell surface, but cannot report forces between subcellular structures [137]. The results seem sensitive enough to resolve (non-directional) magnitudes down to the pN, but the exact range of measurement and application is still controversial [138]. In addition, the calibration process is very delicate : it requires, first, controls for protein function and environmental independence (e.g. pH) ; and, later, extensive image analysis [139] because of their low signal-to noise ratio. These techniques are somewhat reminiscent of the cell own sensors [140] whereby molecular conformational changes that lead to variations in affinity or activity (such as unfolding, extension or reorientation) are used as force probes.

I.2.4 Microenvironments

Historically, the lack of technological solutions at the micro scale has found good rationale in reductionism to justify 2D(/glass) experiments. However conducive this bottom-up avenue has been to singling out the key players in morphodynamics, it has also demonstrated that cell behavior in vivo should not be (carelessly) extrapolated from studies performed outside the native context of the cell. Indeed, cells consider the most variate environmental stimuli [141]. They take into account (i) multicellular factors : in the colon, Entamoeba histolytica interacts with the polarized epithelial barrier (enterocytes, goblet cells, etc.) by lysing integrin-ECM focal adhesions [49], with the immune system (macrophages, T cells. . .) by triggering a pro-inflammatory response, and (importantly to the virulence of the disease [142]) with the commensal microbiota through phagocytosis [143] ; (ii) biochemical cues such as cytokines, chemoattractants, ionic and nutrient gradients, and a lot of signaling molecules resulting from the cross-talk of all integrants ; and (iii) physical forces : e.g. shear flow can reprogram Salmonella gene expression [144] or regulate differentiation in the host [145], and peristaltic compression-stretch cycles have been shown to influence the outcome of infection in *Shigella* [146].

Notice that the ECM has a prominent role in tissue homeostasis : it creates a stable 3D architecture, regulates the dissemination of signaling molecules, and provides ligands for cell receptors. Regarding the latter, the dynamic composition and stiffness of the ECM exert a physical influence that is transduced into the cells and ultimately influences a lot of processes, including differentiation, proliferation and migration [147]. For example, E. histolytica regulates its mode of migration according to the ECM's density, and only uses proteolysis against high-density matrices [148].

In vivo experiments in animal models, fresh explants or grafts are closer to real conditions but are much more costly, difficult to handle (especially at long term) and invariably raise ethical concerns. To facilitate experimental design while retaining physiological relevance, great effort has been invested in recreating 3D microenvironments that integrate a select (e.g. in balance with the cost) subset of relevant variables. The implementation of these cell culture systems is diverse and ranges from co-cultures in suspension where cells can self-organize (known as bioreactors) [149], to reproductions of 3D structures that combine an ECM scaffold with the appropriate mix of cell lines or stem cells (organoids) [150], and to microfabricated models that include microfluidics and elastic compressions to mimic active processes of organ function (organ-on-chip) [151]. Examples of the relevance that these solutions can achieve are engineered cultures where cells differentiate and self-assemble into tissue-like structures.

The quest for increasingly relevant set-ups has put optical microscopy to a test [152]. For instance, the resulting multi-cellular 3D structures require higher penetration depth and multiple wavelength acquisition, and, if the system is to be imaged live, faster acquisition and reduced phototoxicity (e.g. lattice light sheet microscopy [153]). Under these circumstances, manual quantification is too far-fetched (think tracking, for example) and automatic image analysis is nigh imperative. In the latter context, the 3D nature of the acquisition (as compared to 2D) is more a question of increased computational complexity, stemming from the size of the data, than a conceptual jump (safe exceptions such as geometry or spatial analysis). Anyhow, the speed of many algorithms does not scale well with increasing dimensions and thus a lot of techniques have to be reformulated. An additional obstacle is the lagging acquisition speed in 3D imaging, which currently has to be circumvented via image analysis and further burdens algorithm design [154, 155].

I.3 Identifying a research niche : image analysis for non-invasive probing in mechanobiology

In light of the high interest of mechanobiology, we envisage that this area will be particularly profitable in the context of BIA. While century-old studies had anticipated the importance of physical forces in shaping and modeling the organism [156], only the relatively recent development of force-probing techniques has evidenced their far-reaching implications in morphogenesis, differentiation and migration. It is now established that physical forces can propagate information within (and between) cells and elicit mechanical and biochemical signals down to the metabolic [157, 158] and transcriptional [159] pathways. The different mechanisms of mechano- transduction and sensation span several scales ; and accordingly, the measuring range of the techniques discussed in Section I.2.3 stretches from the protein to the tissue levels. However, the final choice comes down to a combination of multiple factors : 2D/3D, in vivo/in vitro, relative/absolute values, resolution, sensitivity, time length, cost, difficulty, etc.

Regardless of the method, many biophysical measurements remain elusive (e.g. IC pressure gradients) or scarce (e.g. IC forces) and are frequently limited by experimental constraints. Indeed, the growing complexity of experimental set-ups in search for biological relevance (Section I.2.4) prevents direct access to the cells and thus favors methods that rely on least-intrusive measurements such as imaging or genetic engineering. Of course, non-invasiveness is also a requirement to study the natural behavior of cells. In summary, there is a newfound interest for methods to measure biophysical quantities that are reproducible, non-invasive and generalizable, especially within the cell ; and therefore an open opportunity for the bioimaging community. Additionally, BIA offers objectivity and reproducibility, as well as the promise of automatisation. This is especially relevant to the increasingly higher data throughput of modern imaging techniques, which often precludes manual analysis. For this reason as well, new methods have the opportunity to build on top of the current automatic workflow : i.e. pre-processing (denoising, deconvolution, registration, etc.), segmentation and tracking ; which travels all the way from pixel information to biological quantification.

In this thesis, we propose image-based methods to quantify multiple intra- and extra-cellular quantities such as pressure gradients, internal forces and external traction forces. We do it from the perspective outlined in Section I.1. The resulting approaches only require standard confocal fluorescence imaging and thus experiments are non-invasive and very easy to set-up. In particular, the methods only need to observe the movement of labelled cytoplasm and/or substrate. In short, the core of our approach is to solve an inverse problem where the temporal variation of image intensity (describing the underlying movement) is assumed to behave like a continuum model of the corresponding material that includes the biophysical quantities of interest. The resulting algorithms are automatic (safe parameter adjustments) and fit well at the end of a typical BIA workflow. In fact, our software automatises all the steps from raw data to biophysical measurements, including cell segmentation, into a module that is open-source and compatible with the ICY software. The intention is to provide a ready-to-use tool for biologists to quantify cellular mechanics, and at the same time encourage the wider bioimaging community to reproduce and extend our efforts.

II – Measuring inside the cell

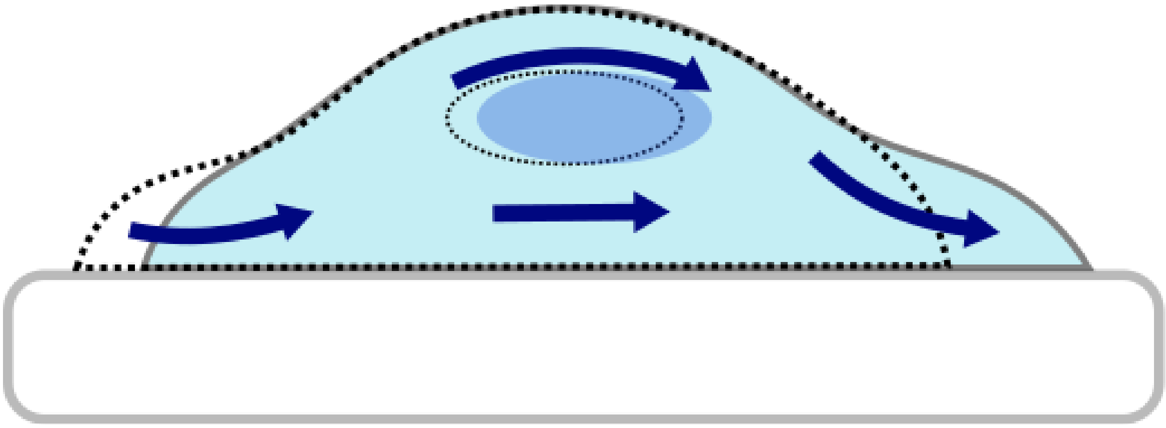

II.1 BioFlow

This section of the work was developed in collaboration with Timothée Lecomte, Maria Manich, Roman Thibeaux, Elisabeth Labruyère and Nancy Guillén ; and supervised by Alexandre Dufour. All at Institut Pasteur. This work is published in [160].

Given the lack of non-invasive measurements to measure intracellular quantities (Section I.2), we present a framework [1] that combines optical flow and a PDE constraint (here fluid) to estimate intracellular forces, pressure gradients, velocity and out-of-plane flow. Related software is open-source and freely available as a module in Icy. In the next section II.2 we illustrate the method by studying amoeboid motility.

In the same context that was set up during the introduction, recent complementary approaches that exploit image analysis and computational modelling have shown

---

[1] Disclaimer : the mathematical treatment in this initial part of the thesis is mostly expositional as is superseded by the more general framework discussed in Chapter III. However, we respect the historical development to be most accurate ; while remarking that this approach is still perfectly (though not optimally) functional and a good testimony of the potential of the method.

promising potential in the inference (or validation) of biophysical models from video-microscopy data. For instance, single-cell segmentation and tracking has been used to fit and validate theoretical models of cortical F-actin distribution during cell reorientation [124]. Likewise, cytoplasmic streams estimated using PIV techniques [133] have been further exploited to estimate the spatial distribution of intracellular shear stress and pressure using Monte-Carlo based computer simulations [125]. An inherent restriction to these approaches lies in the dependence of the modelling quality on the preliminary image analysis step. In addition, these implementations are tailored specifically to the theoretical model being validated, and cannot easily be applied to other theoretical models, dimensions or cell types.

In this section, we present a mechano-imaging method that can estimate biophysical quantities within living cells in a non-invasive manner, in two or three dimensions, by inferring the parameters of a given theoretical model of the cell interior from the motion information that is observable via video-microscopy. This is achieved by combining two concepts in an integrated framework : (i) optical flow and (ii) variational data assimilation, a highly-scalable framework designed to infer the parameters of a given theoretical model based on a limited set of observations (known as realisations) [161]. In the present case, the theoretical model is derived from a physical model of the cell interior comprising several parameters of interest, whereas the realisations of the model are given by the motion information observed through live microscopy and described by optical flow. More specifically, we use fluid dynamics to model cytoplasmic streaming, which defines a constitutive relation between the velocity and pressure of the cytoplasm and the forces therein. As a result, the proposed method is able to extract intracellular velocity, while simultaneously producing an estimation of these biophysical quantities everywhere inside the cell up to pixel resolution. In short, this computational strategy offers a number of advantages over existing methods : 1) it is non-invasive and relies exclusively on live microscopy data ; 2) it produces high-resolution measurements "everywhere" inside the cell in two or three dimensions ; 3) it is independent of the experimental context and thus easily adapts to other theoretical models, biological specimens and imaging techniques ; 4) it is open-source and available as a ready-to-use module for the Icy software [162].

In Section II.2, we illustrate this approach by studying amoeboid motility in *Entamoeba histolytica* , corroborating and extending both theoretical and experimental reports. This original framework is virtually independent of the chosen theoretical model, and is therefore adaptable to the biological specimen at hand. This allows testing and validating numerous experimental and theoretical hypotheses in a straightforward manner.

Outline - We start by introducing optical flow, justifying its use in biological images and presenting related literature. Second, we introduce the combined framework, constraining the optical flow functional to a physical model. Next, we apply this framework to a fluid model of the cell interior. We then dive into the numerical resolution : the Finite Element Method to solve the PDEs, the Adjoint method to compute the gradient of the constrained functional, and L-BFGS-B to minimise the functional ;

specific details regarding multi-scaling, segmentation and parameter estimation are also discussed. Finally, we explain how the algorithm is automatised and implemented in Icy.

II.1.1 Optical Flow

To take non-invasive measurements we would like to rely on classical fluorescence microscopy : it is almost harmless, it is wide-spread, and you are most probably going to be using it anyway. However, unless they are arduously engineered to (e.g. FRET, see I), most biophysical quantities are not a function of emitted light. Instead, light usually indicates position, for example of labelled proteins or fluorescent beads and dies. Could we infer the underlying forces at stake solely from the distribution of any such markers ? Precisely ; rheological studies gather experimental data regarding the response of a substance (position) to stimuli (forces) in order to build a constitutive set of equations. Most such constitutive relations are not concerned by position alone, but rather by its change, either in time (e.g. viscous fluids) or with respect to a resting state (e.g. elastic solids). Therefore, if we could automatically extract motion from sequences of fluorescence images we could then use a suitable constitutive equation to deduce the biophysical quantities of interest. Of course, we can only capture so much of the real movement, specially when working on 2D images[2]. To reflect this fact, the apparent motion as observed from the variations of intensity in a video sequence is called optical flow. Still, that is not to say we cannot extract a rich characterization of the underlying movement. In fact, microscopy images do not have it bad : in 2D they are usually orthogonal projections of the sample plane on which most motion occurs, and 3D z-stacks are only time lagged. Nevertheless, in this work we will try to account for some of these apparent-to-real differences by considering the thickness of a confocal slice as well as out-of-plane motion (respectively in chapters III, II).

As presented in the Introduction (I), there are three main approaches to follow the apparent movement in an image sequence[3] : tracking multiple particles and extrapolating the motion (feature-based) ; statistically correlating small windows between consecutive images (correlation-based) ; and exploiting partial derivatives to pose conservation laws (differential), for example assuming that the intensity of whatever is moving is preserved (optical flow constraint enforcing methods or OFs hereafter). Respective pros and cons of these techniques are as follows. Feature-based methods can extract high-frequency movement, but break down when the density increases or there are no persistent features. Correlation-based techniques adapt well to intensity

---

[2] Think of a faraway plane flying much faster than it would appear in you camera.

[3] There is a big conflict regarding the naming of techniques. Indeed, many authors will use the name "PIV" to refer to correlation-based techniques by opposition to techniques that exploit the so-called optical flow constraint (defined below), which are then referred as "optical flow". Originally, PIV stands for "particle image velocimetry" and refers broadly to the study of flows by seeding markers, whereas optical flow was meant as defined above. Thus, technically, both correlation-based and optical-flow-constrain techniques are PIV and measure optical flow.

variations, but are strongly dependent on the window size : each correlated window has a uniform displacement associated which is decided independently of the rest. OFs are able to consider the motion globally and thus can deal with higher noise and a wide range of densities ; they can also fill missing information by combining this globality with some prescribed prior knowledge. However, they are not the best at picking up high frequencies, they are not well-posed, and they often result in non-convex problems (see [8] for example). In the context of biological images, OFs have been repeatedly shown to outperform its competitor techniques not only in accuracy, but also in speed [163, 164]. Accordingly, we will be using OFs along this thesis.

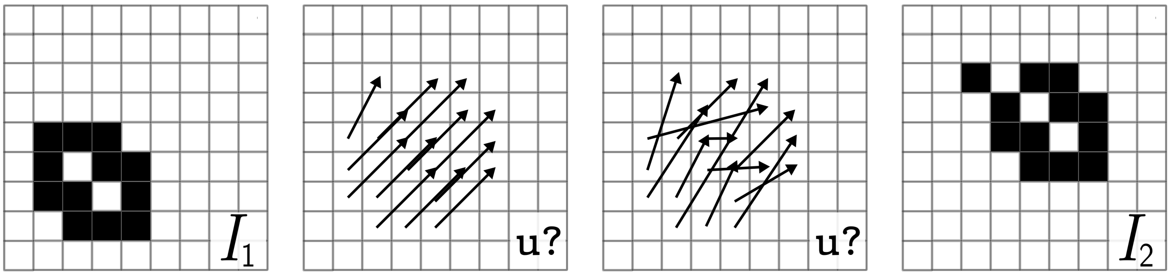

FIGURE II.1 – **Schematic of the optical flow constraint.** The velocity or displacement between two consecutive images (left-most and right-most) is extracted by assuming that intensity is conserved, here that is black pixels are to be mapped to black pixels and white to white. The central left drawing corresponds to the real mapping, but the other possible map (on the right) also preserves particle intensity even if the arrows are all scrambled. In a way this illustrates the need for a regularisation.

To be concrete, OFs aim at estimating a displacement (or velocity) field representing the transport of information (here pixel values) between consecutive image pairs. To this end, the method assumes that the pixel intensities are simply advected from one frame to the next without loss (Figure II.1). In other words, any moving particle in the image sequence has a constant intensity along its trajectory. More formally :

$$D_t I = 0, \tag{II.1}$$

where $D_t \bullet := \partial t \bullet + \mathbf{u} \cdot \nabla \bullet$ with $\mathbf{u} := d\mathbf{x}/dt$ is the material derivative usually present in the Lagrangian (as opposed to the Eulerian) specification of a flow field ; with $I : \mathrm{O} \times \mathrm{T} \longrightarrow \mathbb{R}$ where $\mathrm{T} \subset \mathbb{R}$ stands for the time and $\mathrm{O} \subset \mathbb{R}^{d_{\mathrm{O}}}$, typically $d_{\mathrm{O}} \in \{2, 3\}$, for the image domain. This is known as the optical flow constrain. Since all the particles present on the image must abide by this rule, we can write the problem in a variational form : minimise the functional[4] $\|D_t I\|^2_{\mathrm{O}}$. However, we only have images at discrete time points and are thus interested in discrete displacements. We integrate II.1 accordingly :

$$I(\mathbf{x} + \mathbf{u}\Delta t, t_1 + \Delta t) - I(\mathbf{x}, t_1) = 0, \tag{II.2}$$

---

[4] **NOTATION** : we use $\langle \bullet, \bullet \rangle_*$ to notate the L^2 inner product of the appropriate dimension over a domain $*$, and $\| \bullet \|_*$ the induced norm. For example, $\langle \nabla \mathbf{u}, \nabla \mathbf{v} \rangle_{\mathrm{O}} = \int_{\mathrm{O}} \nabla \mathbf{u} : \nabla \mathbf{v}$ with the Frobenius tensor product $\nabla \mathbf{u}_{i,j} \nabla \mathbf{v}_{i,j}$ or $\langle \mathbf{u}, \mathbf{v} \rangle_{\mathrm{O}} = \int_{\mathrm{O}} \mathbf{u} \cdot \mathbf{v}$ with the dot product. Occasionally, a $\star$ in $\langle \bullet, \bullet \rangle_{*,\star}$ is used to indicate an inner product other than the default L^2.

where the images at both time points are precisely our discrete images $I_1(\mathbf{x}) = I(\mathbf{x}, t_1)$, $I_2(\mathbf{x}) = I(\mathbf{x}, t_1 + \Delta t)$ because Δt is the acquisition lag. That is, if we warp image I_2 with the displacement map, we should recover image I_1. However, the resulting problem is highly non-linear and leads to a non-convex minimisation : $\|I_2(\mathbf{x} + \mathbf{u}\Delta t) - I(\mathbf{x})\|_{\mathrm{O}}^2$. To convexify the problem, we can linearise it by truncating its Taylor expansion :

$$\mathbf{u} \cdot \nabla I_2 + \frac{I_2 - I_1}{\Delta t} = 0. \tag{II.3}$$

While the derivation might feel loopy because it brings us back to the differential conservation we started with, it gives a good feel for what is going on. Just as in a physically-derived PDE, we have passed by both the local conservation differential form and its associated integral form. Finally, we can pose the associated minimisation problem, this time around with the term

$$J_{\mathrm{data}} := \left\| \mathbf{u} \cdot \nabla I_2 + \frac{I_2 - I_1}{\Delta t} \right\|_{\mathrm{O}}^2, \tag{II.4}$$

which is convex. However, notice that we are shuffling around a single equation, but we have as many velocity components as image dimensions : the system is underdetermined. In fact, we can only deduce the component of the motion that is normal to the isophotes[5]. Consequently, the minimisation problem is ill-posed. This is known as the aperture problem. To tackle this issue, we must specify the problem further so that the solution becomes unique. However, let us first discuss two extra problems that afflict OFs.

Linearisation - The linear approximation in (II.3) is only valid for small displacements. One approach (used in this thesis) is to consider a multi-resolution pyramid and solve the problem at increasingly bigger resolution, i.e. making a lot of small steps. A possible alternative, albeit daunting, would be to solve the non-convex minimisation, for example using convexification techniques.

Brightness constancy - Even though (II.1) is based on intensity conservation, there are many reasons this might not hold and thus one might want to relax the constraint. For instance, one could allow affine variations of the intensity in time to try and accommodate changes in light/shade conditions [165, 166]. On a similar note, the equation can be modified to reflect any information we might have regarding the origin of the sequence. For example, conservation of mass can be used to derive a slightly different constraint in meteorological imaging [167]. In a conceptually similar way, in Chapter III we derive a model-based conservation equation for confocal microscopy.

---

[5] Think of an image with an intensity gradient that is perfectly parallel to one of the axis, we can only hope to know how fast things are moving in that direction. If particles were to move in the perpendicular direction we would not notice : we could not tell them apart because they all have the same intensity.

II.1.1.1 The aperture problem

We now discuss one of many options to tackle the aperture problem. However, let us brush over another alternative for the sake of comparison ; for example, one option is to impose that the gradient of the intensity is simultaneously conserved, which yields additional equations but prevents rigid transformations and decreases the tolerance of the method to noise. The approach we focus on is to regularise the velocity field (Figure II.1). This is by far the most popular approach, perhaps because of its generality. In this case, the idea is to solve

$$\underset{\mathbf{u}}{\operatorname{argmin}}\, J_{\text{data}} + J_{\text{reg}}, \tag{II.5}$$

where we can determine how much weight we give to being true to the data in J_{data} with respect to the prior regularising knowledge imposed in J_{reg} by making the latter proportional to a tunnable constant $\alpha \in \mathbb{R}_{\geq 0}$. The seminal regularisation approach [109] was to impose first-order spatial smoothness [6],

$$J_{\text{reg}} = \alpha \|\nabla \mathbf{u}\|_{\text{O}}^2, \tag{II.6}$$

but many other less-arbitrary regularisations have been proposed since then. Some authors have penalised either the curl or divergence of the flow [7], or their higher-order derivatives [168, 169]. Other literature has attempted to preserve discontinuities on the flow (i.e. removing noise while conserving edges) [170, 171] by using the L^1 norm and working on the space of bounded variations [172]. A more recent approach is to help the regularisation using physically-inspired constraints [173], this is specially fruitful when considering several images at once as it is easier to achieve some form of spatiotemporal consistency. This is the case of several efforts, for example to exploit the shallow water equation for meteorology [174] or the vorticity transport equation [175], which are then constrained with an additional data fidelity term and an accompanying regularisation term. In line with our quest to extract biophysical quantities, in this thesis we take a similar approach, but with an aim that is completely opposed : we are interested in the physics, and optical flow is just a tool. This also tackles a classic limitation of OFs, namely that most methods do not take the underlying transport mechanism into consideration.

II.1.2 Theoretical framework

Here, we adapt and extend the standard optical flow constraint framework to bioimaging data using the theory of Optimal Control [176]. The general idea is to constrain the estimated displacement by a theoretical model of the observable motion defined

---

[6] If the intensity is well-behaved, this yields a strictly convex and quadratic functional, and a well-posed problem.

[7] Perhaps this could be formalised from the perspective of Helmholtz's decompositions.

by a number of so-called “control” variables c, which are estimated concomitantly. Formally, the minimisation problem becomes the following :

$$\underset{c}{\operatorname{argmin}} \left(J_{\text{data}}(\mathbf{u}(c)) + J_{\text{reg}}(c) \right), \quad \text{subject to } A(\mathbf{u}, c) = 0. \tag{II.7}$$

In other words, the goal is to match a dynamical observation (the temporally-varying image signal) with a given theoretical model of the intracellular material, whilst jointly estimating its parameters (the biophysical quantities of interest). This strategy offers two major improvements over existing image-based approaches. Firstly, the regularisation term J_{reg} can be specifically tailored to the problem at hand, while eliminating arbitrary smoothness constraints that may not always hold experimentally. This includes the possibility of regularising on the control variables, which might be more physically sensible. Secondly, solving this problem readily provides estimates for the biophysical quantities that minimize the cost function, without the need for additional simulations or model-fitting steps. This data assimilation strategy is particularly appealing since it is independent of the control parameters or theoretical model chosen, and can therefore be applied to a wide range of analogous problems in biology. It also eliminates the two-step approach of many algorithms whereby data assimilation and modelling are de-coupled and thus the information is regularised twice (see for example TFM in I).

The proposed framework is able to extract biophysical parameters integrating optical flow and data assimilation, we name it **BioFlow**. This method is straightforward to implement experimentally as it requires only two inputs : 1) time-lapse imaging data of intracellular dynamics (typically obtained by labelling the intracellular material with fluorescence), and 2) a theoretical model of the observable motion. In the remainder of this work we illustrate the use of BioFlow to study amoeboid motility using a fluid dynamics approach to model cytoplasmic streaming, while we stress that this framework is sufficiently generic and flexible to adapt to virtually any experimental context, given these two inputs.

II.1.2.1 Case study : modelling cytoplasmic streaming using fluid dynamics or *panta rhei*[8]

In the context of fluorescent microscopy sequences, the fluorescence emitted by cellular structures is considered as the information that is transported (or advected) by the cell material, which is reflected on the optical flow. In a first application of the method, we model cytoplasmic streaming, i.e. the flow of cytoplasm within a cell. To this end, we consider any fluorescent protein that is in suspension within the cytoplasm.We suppose that the resulting observable motion of this protein bulk describes that of the cytoplasm "everywhere" inside the cell during its movement, and

---

[8] Fluid/solid behavior sometimes depends on the time scale. Even rocks can behave as fluids at a very large time scale. In fact, salt tectonics are sometimes modeled with incompressible Stokes models in the context of seismic imaging.

thus constitutes a good input for the algorithm. Having covered the first "input", we now tackle the second "input", the theoretical model. In this case, we ask whether our method could extract the intracellular velocity, pressure gradients and forces driving cytoplasmic flow.

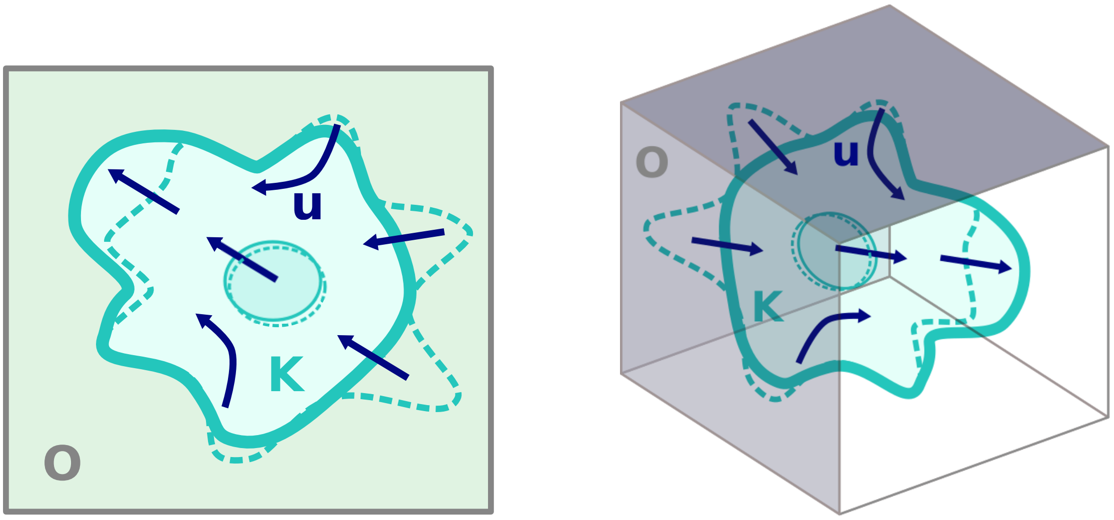

2D 3D

Figure II.2 – **Schema of BioFlow.**

a) Theoretical model of the cytoplasm. We model the observable intracellular material as a single-phase homogeneous fluid, neglecting for now the influence of organelles such as the nucleus and intracellular vesicles, following previous work [136]. The dynamics of a single-phase fluid are governed by the Navier-Stokes equations. Two important figures define the regime of solutions for these equations : the Reynolds number $Re = \rho V L/\mu$ (ρ : density ; V : velocity ; L : characteristic distance ; μ : viscosity) and the Mach number $M = c/c_0$ (c : characteristic speed ; c_0 : speed of sound). The Reynolds number is very small in cells (of the order of 10^{-5}, see Chapter I), implying that the flow is laminar and that the material derivative (including both time-variation and convection terms) in the Navier-Stokes equations can be neglected. In other words, inertia plays no role at the cell scale [32]. The Mach number is small enough such that the fluid can be considered incompressible. Finally, while the cytoplasm is generally considered visco-elastic rather than purely viscous, the elasticity component essentially affects deformations at short time-scales, and therefore has a negligible impact on whole-cell movements at longer (decisecond to second) time-scales [177]. Of course, the time scale depends on many factors, notably the cell type, but can be somewhat regulated by the acquistion set-up. Given these assumptions, the cell medium can be considered as a Newtonian fluid governed by the Stokes equations :

$$\begin{cases} \nabla p - \mu \Delta \mathbf{u} = \mathbf{f} & \text{in } K \\ \nabla \cdot \mathbf{u} = 0 & \text{in } K \\ \mathbf{u} = \mathbf{g} & \text{on } \partial K \end{cases} \tag{II.8}$$

where **f** are the local forces (per unit volume) acting on the cell medium, **g** is the boundary velocity, and K is the domain corresponding to the cell interior. The first equation expresses the balance of all the forces acting on the fluid : the first term corresponds to viscous drag (the laplacian acts as a neighbourhood averaging operator on the velocity, i.e. the fluid elements drag each other), the second term is the pressure gradient, and the third term accounts for the sum of all other forces, be they internal (e.g. contractility due to myosin activity) or external (e.g. gravity). The second equation indicates that the flow is not divergent, or equivalently that the fluid is incompressible and the mass is conserved. The third equation corresponds to the boundary condition (Dirichlet conditions in the present case). This set of partial differential equations (PDEs) defines the candidate model A in Equation II.7. It is worth stressing that the model presented here simplifies the numerical complexity of the problem (with respect to non-linear models for example), yet the proposed methodology is highly generic, and is easily adaptable to any fluid dynamics model of the intracellular material.

b) 3D : the general case. Given 3D imaging data and the aforementioned fluid dynamics model, we are able to recover the intracellular velocity, pressure gradient and forces from the observable motion of intracellular material by solving the following problem :

$$\underset{\mathbf{f},\mathbf{g}}{\operatorname{argmin}} \left(J_{\text{data}}(\mathbf{u}(\mathbf{f},\mathbf{g})) + J_{\text{reg}}(\mathbf{f},\mathbf{g}) \right), \text{ subject to } A(\mathbf{u}, p, \mathbf{f}, \mathbf{g}) = 0 \tag{II.9}$$

where

$$A(\mathbf{u}, p, \mathbf{f}, \mathbf{g}) = \begin{cases} \nabla p - \mu \Delta \mathbf{u} - \mathbf{f} & \text{in } K \\ \nabla \cdot \mathbf{u} & \text{in } K \\ \mathbf{u} - \mathbf{g} & \text{on } \partial K, \end{cases} \tag{II.10}$$

and with the image domain of J_{data} restricted[9] to $K \subset \mathrm{O}$. The regularisation term reads

$$J_{\text{reg}}(\mathbf{f},\mathbf{g}) = \alpha \|\mathbf{f}\|_K^2 + \gamma \|\mathbf{g}\|_{\partial K}^2, \tag{II.11}$$

where α and γ are non-negative empirical weights that regulate the balance between the fidelity to the data J_{data} and the prior (or imposed) knowledge J_{reg}. In this case, we use the L^2 norm to regularise both the force[10] and the boundary velocity. Alternatively, we have also regularised the gradient of the velocity along the boundary $\|\nabla_{\parallel}\mathbf{g}\|_{\partial K}^2$,

---

[9] The image gradient is computed on the whole image and only restricted after.

[10] See Chapter III for an interpretation of the action of a similar regulariser as a filter.

where $\nabla_{\parallel}\mathbf{g} := \nabla\mathbf{g} - (\nabla\mathbf{g}\cdot\mathbf{n})\mathbf{n}$ with $\mathbf{n}$ the normal of ∂K. In optimal control terms, the velocity $\mathbf{u}$ and pressure p describe the state of the system, and are controlled by the force $\mathbf{f}$ and boundary condition $\mathbf{g}$ via $A = 0$. Solving this problem numerically (see II.1.3) produces estimates for these quantities simultaneously in the entire (labelled) intracellular domain (Figure II.3). Again, we stress that this theoretical formulation can accommodate virtually any model for the cellular material, by adjusting the constraint model A and the regularisation $J_{\text{reg}}(\mathbf{f},\mathbf{g})$.

c) 2D : handling out-of-plane flow[11]

While we designed the method for the general case of 3D imaging data, we recognise that live cell imaging in 3D may raise technical limitations, either by compromising cell viability due to photo-toxicity, or by being too slow. Acquisition speed is specially relevant in z-stacks because it increases the time lag between consecutive z-images that "theoretically" belong to the same time point. In case 2D imaging is preferred, conservation of mass between consecutive images is no longer a valid assumption, due to the appearance and disappearance of intracellular material in and out of the imaging plane of focus. We therefore amended our model in 2D to compensate for this artefact. This is achieved by introducing an additional term r that estimates the divergence of the observed flow from the image data and relaxes the incompressibility assumption. Under this condition, the general problem to solve is

$$\operatorname*{argmin}_{\mathbf{f},\mathbf{g},r}\left(J_{\text{data}}(\mathbf{u}(\mathbf{f},\mathbf{g},r)) + J_{\text{reg}}(\mathbf{f},\mathbf{g},r)\right), \text{ subject to } A(\mathbf{u},p,\mathbf{f},\mathbf{g},r) = 0 \tag{II.12}$$

where the candidate model A becomes

$$A(\mathbf{u},p,\mathbf{f},\mathbf{g},r) = \begin{cases} \nabla p - \mu\Delta\mathbf{u} - \mathbf{f} & \text{in } K \\ \nabla\cdot\mathbf{u} - r & \text{in } K \\ \mathbf{u} - \mathbf{g} & \text{on } \partial K, \end{cases} \tag{II.13}$$

and the functional needs to be regularised accordingly, i.e. :

$$J_{\text{reg}}(\mathbf{f},\mathbf{g},r) \quad = \quad \alpha\|\mathbf{f}\|_K^2 + \gamma\|\mathbf{g}\|_{\partial K}^2 + \eta\|\nabla r\|_K^2, \tag{II.14}$$

where η is a new non-negative weight. Note that $\|\nabla r\|_K^2$ could also be replaced by $\|r\|_K^2$, should r be assumed small. This new 2D problem is then numerically solved in the same way as the general 3D case, but with one additional control variable (and thus derivative direction). It is worth noticing that r is a measure of out-of-plane motion. Given that the fluid is considered incompressible, and assuming that fluorescence does not degrade between consecutive images, the actual 2D fluid motion cannot diverge ($\partial u_x/\partial x + \partial u_y/\partial y = 0$) and thus $r = -\partial u_z/\partial z$ reflects the flow in the z-direction. In fact, the volume of fluid leaving the imaging plane between two images is $\Delta t \int_K u_z \, dK$,

---

[11] In Chapter III we present a way to compensate for the thickness of the laser slicing, which induces mixing of on-plane and out-of-plane information. These two methods are not mutually exclusive, but rather complementary because they deal with two different error sources.

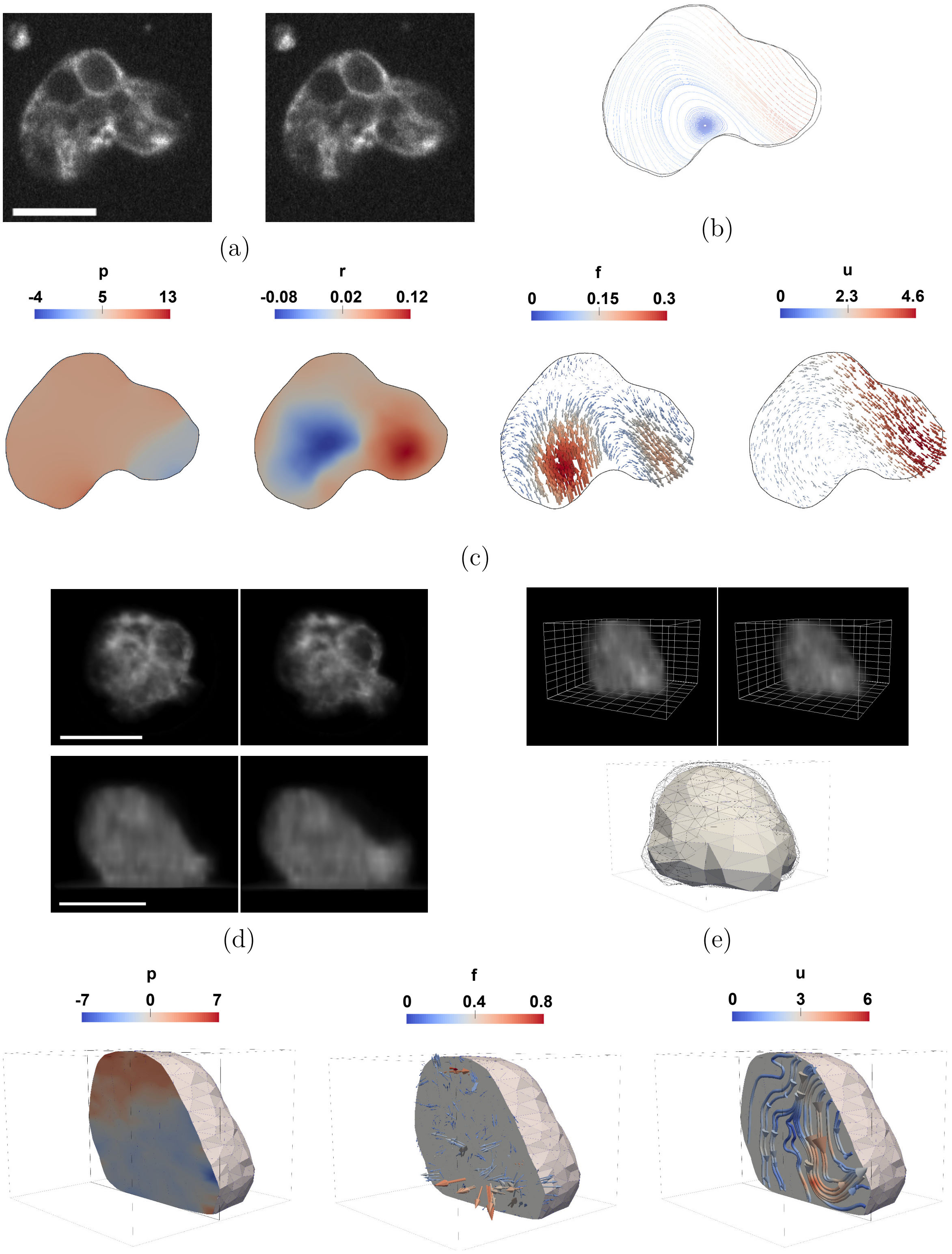

(a) (b)

(c)

(d) (e)

(f)

FIGURE II.3 – **Overview of BioFlow** (a-c) BioFlow in 2D. (a) Two consecutive frames of a 2D time-lapse microscopy sequence ; scale bar : $10\mu m$. (b) Cell contours extracted from the first (black) and second (grey) frames, and streamlines of the extracted velocity field (integrated using a Runge-Kutta 4 algorithm, see Section II.3). (c) From left to right, estimated 2D intracellular pressure p (Pa), out-of-plane flow r (s^{-1}), forces $\mathbf{f}$ ($nN/\mu m^2$) and velocity $\mathbf{u}$ ($\mu m/s$). (d-f) BioFlow in 3D. (d) Axio-lateral slices of two consecutive frames of a 3D time-lapse microscopy sequence. (e) Top row : 3D volume rendering of (d) ; grid spacing $2\mu m$) ; Bottom row : Cell contours extracted from the first (black wireframe) and second (solid mesh) frames. (f) From left to right, sliced view of the estimated 3D intracellular pressure, forces and velocity (the velocity field is displayed as streamlines for better visualisation). Taken from [160].

while the change in cell area is $\Delta t \int_K r \, dK$. From a Dynamical Systems perspective, the fact that this model does not heavily enforce the conservation of mass permits the creation of velocity sinks and sources, instead of relying exclusively on saddle points. The effects of the out-of-plane reformulation of the problem is illustrated in Figure II.4. We note that we have considered $K \subset \mathrm{O}$. This is certainly more justified in the 3D case than it is in a 2D projection, which comes back to the issue of apparent motion as defined by optical flow [12].

d) Fluid stress. The stresses within the cytoplasm and at the boundaries, where some contraction occurs, are also of biological relevance. The stresses can be computed from the resulting state variables $\mathbf{u}$, p [178, 179]. In particular, the Cauchy stress tensor in the isotropic incompressible Newtonian case,

$$\sigma = -p\mathrm{I} + \tau_{\mathrm{v}}, \tag{II.15}$$

can be divided into the hydrostatic stress tensor $-p\mathrm{I}$ that tends to "change the volume" of a body as in a expansion or compression, and the deviatoric stress tensor $\tau_{\mathrm{v}} := 2\mu\epsilon(\mathbf{u})$, which here is traceless and describes a distortion of the body by means of the strain rate tensor $\epsilon(\mathbf{u}) := (1/2)(\nabla \mathbf{u} + (\nabla \mathbf{u})^T)$. In addition, $\sigma_{i,j}$ are called normal stresses when $i = j$ (the mechanical pressure is the mean normal stress $p = -\overline{\sigma_{i,i}}$), and shear stresses when $i \neq j$. Notice that since the fluid is incompressible, the viscous stress does not have any compressional contribution ($\propto \nabla \cdot \mathbf{u}\ \mathrm{I}$). Therefore, only the pure shear tensor, which is proportional to the shear strain rate tensor in Newtonian fluids, is left.

While these are the general stress tensors, stress on the boundary might be particularly interesting in some biological settings. The stress vector $\mathbf{T}^{(\mathbf{n})}$ across an imaginary surface defined by the unitary normal $\mathbf{n}$ can be computed as $\mathbf{T}^{(\mathbf{n})} := \mathbf{n} \cdot \tau_{\mathrm{v}}$, and decomposed into the normal $\mathbf{T}^{(\mathbf{n})}_{\mathrm{v,n}} := (\mathbf{T}^{(\mathbf{n})} \cdot \mathbf{n})\mathbf{n}$ and tangential $\mathbf{T}^{(\mathbf{n})}_{\mathrm{v,s}} := \mathbf{T}^{(\mathbf{n})} - \mathbf{T}^{(\mathbf{n})}_{\mathrm{v,n}}$ component. Their magnitudes are respectively : $\tau_{\mathrm{v,n}} := \mathbf{T}^{(\mathbf{n})} \cdot \mathbf{n}$ and $\tau_{\mathrm{v,s}} := \sqrt{(\mathbf{T}^{(\mathbf{n})})^2 - \tau_{\mathrm{v,n}}}$.

---

[12] We address this topic in Chapter III. See footnote 11 for further details.

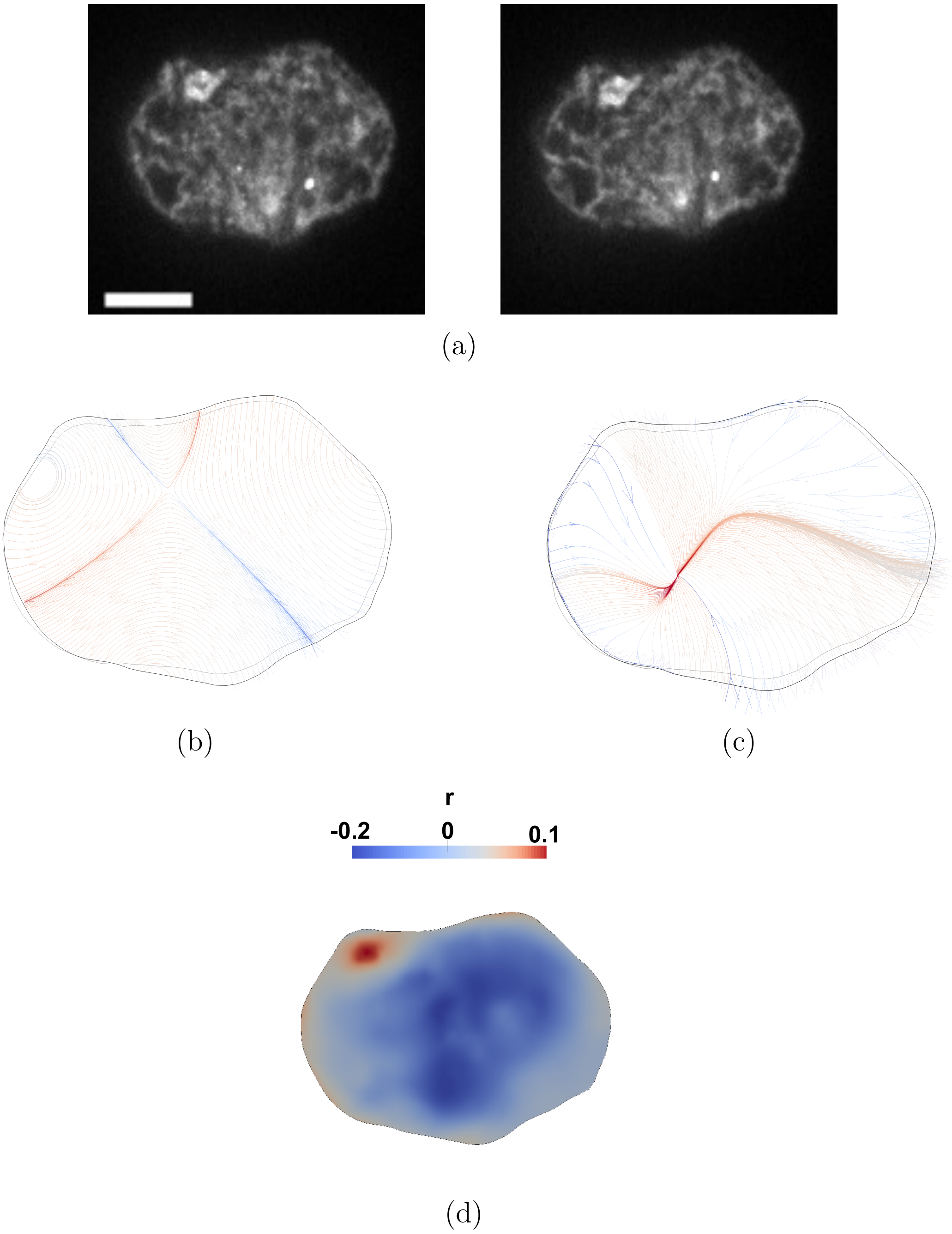

(a)

(b)

(c)

(d)

FIGURE II.4 – **Estimation of out-of-plane flow in 2D. a)** Two consecutive frames of a 2D time-lapse microscopy sequence displaying out-of-plane motion ; Scale bar : $10\mu m$. **b-c)** Cell contours extracted from the first (black) and second (grey) frames, and streamlines of the extracted velocity field without (a) and with (b) estimation of out-of-plane flow. **d)** Estimated out-of-plane flow r (s^{-1}) ; negative (resp. positive) values correspond to material leaving (resp. entering) the plane. Taken from [160].

As a reference, we take the example of a standard horizontal infinite pipe with a flow along the x-axis and the cross-section on the $y - axis$. The components of the stress on the walls (with normal $\mathbf{n} = (0,1)$) are then $\tau_{\mathrm{v,n}} = 2\mu \partial u_y / \partial y$ and $\tau_{\mathrm{v,s}} = \mu(\partial u_y/\partial x + \partial u_x/\partial y) = \mu \partial u_x/\partial y$.

II.1.3 Numerical resolution

Solving the problem defined in II.7 entails minimising a functional (II.11 or II.14) constrained by a system of partial differential equations (PDE) with non-zero boundary conditions (II.11 or II.13 as $A = 0$). The minimisation process provides an estimate for three quantities, namely the force field $\mathbf{f}$, the boundary velocity $\mathbf{g}$ and the divergence r in 2D (hereafter we refer to this set as $m := (\mathbf{f}, \mathbf{g}, r)$), while the velocity $\mathbf{u}$ and pressure p are obtained by solving the PDE for a given m (hereafter $\theta(m) := (\mathbf{u}, p)$). A classical solution to the constrained minimisation is to transform the problem into an unconstrained optimisation framework by introducing Lagrange multipliers [176] and deriving the associated optimality system. Unfortunately, attacking the resulting system directly does not scale well when the number of unknowns is large. In particular, m contains two vector fields and a scalar, all defined on a grid with a size depending on the spatial resolution of the acquired images, which is potentially large. In such situations, many approaches are computationally untractable.

Here we adopt gradient descent, which is numerically simpler and theoretically robust because the functional is convex and well-posed in principle (m is regularised and the PDE is linear). Implementing gradient descent comprises two main steps, which are repeated sequentially until convergence : 1) computing the functional J (which requires solving the PDE system for a given m), and 2) computing the gradient of J, which provides a direction in the parameter space m where a better solution can be found.

II.1.3.1 Evaluating the functional by solving the PDE : the Finite Element Method

Computing J requires solving the so-called *forward problem* defined by expression II.13 as $A = 0$: calculate $\theta = (\mathbf{u}, p)$ given $m = (\mathbf{f}, \mathbf{g}, r)$.

To avoid potential numerical round-off errors due to working with both small and large numbers, and to assess the importance of each term in the equations, we rewrite the system into a dimensionless form by posing the following change of variables : $x = x^* l$, $y = y^* l$, $z = z^* l$, $t = t^* \Delta t$ $p = p^* \frac{\mu}{\Delta t}$, $\mathbf{f} = \mathbf{f}^* \frac{\mu}{\Delta t l}$, $\mathbf{u} = \mathbf{u}^* \frac{l}{\Delta t}$, $r = r^* \frac{1}{\Delta t}$, $g = g^* \frac{l}{\Delta t}$, where l is the length scale defined by the size of the image (arbitrarily taken as the y length) and Δt the acquisition lag. Furthermore, to simplify the resolution, we modify the problem such that it has zero-boundary conditions, by posing $\mathbf{u}^* = \mathbf{u} + \mathbf{u}_0$ (while we write it $\mathbf{u}$ as before, this one is dimensionless, and so is $\mathbf{u}_0$). With these new variables, equation II.13 becomes :

$$\begin{cases} \nabla p - \Delta \mathbf{u} & = & \mathbf{f} + \Delta \mathbf{u}_0 & \text{in } K \\ \nabla \cdot \mathbf{u} & = & r - \nabla \cdot \mathbf{u}_0 & \text{in } K \\ \mathbf{u} & = & 0 & \text{on } \partial K \\ \mathbf{u}_0 & = & \mathbf{g} & \text{on } \partial K \end{cases} \tag{II.16}$$

Another possibility to deal with the boundary condition would be to apply Nitsche's method [13]. In any case, equation II.16 cannot be solved analytically. We therefore relax the problem by deriving its so-called *weak variational form*. The idea is to integrate the first (force balance) equation and the second (conservation) equation over the domain of interest, weighted by some test functions $\mathbf{v}$, q :

$$\begin{aligned} w &:= a(\mathbf{u}, \mathbf{v}) + b(\mathbf{v}, p) + b(\mathbf{u}, q) \\ &= \int_K \nabla \mathbf{u} : \nabla \mathbf{v} + \int_K p \nabla \cdot \mathbf{v} + \int_K q \nabla \cdot \mathbf{u}, \\ L &:= -\int_K \nabla \mathbf{u}_0 : \nabla \mathbf{v} + \int_K \mathbf{f} \cdot \mathbf{v} - \int_K q \nabla \cdot \mathbf{u}_0 + \int_K qr, \end{aligned} \tag{II.17}$$

where the pressure sign is switched for stability. Our goal is now to find a pair of trial functions velocity and pressure $(\mathbf{u}, p)$ belonging to some mixed space $V \times M = {H_0}^1(K)^n \times L^2(K)$ such that $w = L$ for all test functions $\mathbf{v}$ and q belonging to $V \times M$. While this reformulation is valid, solutions may exist without necessarily satisfying the original system of equations. This is however a reasonable simplification, given that many laws of physics expressed in terms of differential equations are often derived from their original integral form. For example, the incompressibility equation $\nabla \cdot \mathbf{u} = 0$ is derived from the continuity equation $\int_K \nabla \cdot \mathbf{u} = 0$ originally expressing the conservation of mass (and recovered in equation II.17). In fact, given that a is a continuous coercive bilinear form and b is a continuous bilinear form satisfying the LBB condition, the Brezzi splitting theorem [180] states that, given a reasonable triad $\mathbf{f}$, $\mathbf{u}_0$ and r, a unique solution to this problem exists.

To solve this new problem numerically, we take advantage of the fact that the weak mathematical formulation is compatible with the Finite Element Method (FEM) [181]. Applying the FEM consists in dividing the domain K in smaller subdomains that are modelled by simpler equations. These can then be reassembled into a larger system that models the weak formulation of the full problem. This is achieved here by discretising the function space, representing our trial and test functions using a basis of piecewise polynomials. Piecewise functions guarantee that each subdomain depends only on its neighbors, while polynomials provide a good local approximation. In our case, the stability of the solutions of the Stokes equations is ensured using a specific combination of these finite elements [182]. That is Taylor-Hood elements [183], where the velocity and the pressure are respectively described as piecewise quadratic and linear polynomials, ensuring that the discretisation of the weak form is stable and well-posed. Finally,

---

[13] A more flexible approach that is implemented in Chapter III.

by substituting the discretised functions in the weak formulation (equation II.17), the problem reduces to solving a very sparse linear system of equations. In particular, To solve the weak problem for θ we use a very flexible and high-level FEM library called FEniCS [184, 185]. The linear system resulting from the FEM method is symmetric indefinite and we solve it using the minimum residual (MINRES) iterative method with $\int_K \nabla \mathbf{u} : \nabla \mathbf{v} + \int_K pq$ as preconditioner. Once θ is known, computing J from θ and m is straightforward. Finally, the PDE constraint $A = 0$ must be now understood as $w - L = 0$.

II.1.3.2 Computing the gradient of the functional : the Adjoint method

The second step involves computing the gradient of J with respect to the control functions (dJ/dm, i.e. $dJ/d\mathbf{g}$, $dJ/d\mathbf{f}$ and dJ/dr), which is specially expensive for high-dimensional problems. A classical finite difference approach would be computationally intractable, since it involves computing J (and thus solving a PDE) several times for each of the many degrees of freedom in m. Instead, we use the adjoint method [161], which can compute the derivative of the functional with a fixed cost with respect to the size of m. The adjoint method can be approached from two different angles : derive the adjoint equations from the infinite problem written in the weak formulation, and then discretise them ; or discretise the weak formulation first and directly derive the adjoint system in its discrete form [186]. In theory, these two approaches should be consistent in the limit of infinite mesh resolution, but the underlying conceptual differences become relevant in the finite case. Discretise-first computes the exact gradient with respect to the (discrete) functional, and is conceptually straightforward (i.e. mechanic) to implement, which has led to heavily automatised libraries. Conversely, discretise-last highlights the underlying physical meaning of the adjoint system, and is simpler to program, all while requiring less memory. In this first part of the thesis, we chose to take a discrete-first approach. Very simply put, the adjoint method consists in using the chain rule and the dual space on $A := w - L$ and J :

$$\frac{dJ(\theta(m), m)}{dm} = \frac{\partial J}{\partial \theta}\frac{d\theta}{dm} + \frac{\partial J}{\partial m} = -\lambda^* \frac{\partial A(\theta, m)}{\partial m} + \frac{\partial J}{\partial m}, \tag{II.18}$$

$$\left(\frac{\partial A(\theta, m)}{\partial \theta}\right)^* \lambda = \frac{\partial J}{\partial \theta}^*, \tag{II.19}$$

to avoid computing the total derivative $d\theta/dm$, which has the size of the state space times that of the control space, and instead compute the adjoint variable λ of size the state space. This can be achieved by first solving equation II.19 for λ, and only then computing the gradient via equation II.18. Notice here that the adjoint operator $(\partial A/\partial \theta)^*$ corresponds to the linearisation of the PDE A about the solution θ and therefore equation II.19 is very similar to the linearised forward PDE system. In Annex A we offer some informal intuition on the adjoint approach. In summary, computing the gradient of J at m consists in 1) solving the forward PDE (II.17) for θ given m ; 2) solving the adjoint system (II.19) for λ given θ and m ; and 3) assembling the gradient with (II.18).

The discrete approach taken here is automatised by the dolfin-adjoint library [187, 188]. Similarly to how automatic differentiation uses the chain rule to compose the derivative of a model from the individual derivatives of each of its sequential elementary operations, the dolfin-adjoint library is able to differentiate sequences of equation solves by exploiting the high-level abstraction of the FEniCS FEM library. The reason behind choosing such an automatised process was to fully exploit the flexibility of the method proposed in section II.1.2 : any model could be plugged in in its weak form and be automatically constrained to the optical flow equations ; the problem would then be minimised by deriving the corresponding adjoint equations (also) automatically. This strategy was indeed very convenient to try out different formulations, and we have later checked it to be reliable and accurate by comparison to a few implementations of the full continuous model. Of course, successful tests were performed previously by comparing the resulting gradient of the discrete adjoint system to finite differences of the original functional J. Yet, however much is gained in flexibility by automatising the derivation of the adjoint of any model, is lost in flexibility as regards tailoring the optimisation. This difficulty includes (but is not limited to) the discretisation of the adjoint, taking any approximations that might help convergence, and computing higher derivatives. For instance, in Chapter III we capitalize on the continuous approach to examine the Hessian of the associated optimal control problem. In this way, we accelerate convergence by formulating Newton's method, which requires approximating the resulting expression so that it is positive definite (e.g. in total variation regularisation) and choosing an appropriate preconditioner. The influence of the data and the regularisation weights can be studied from the eigenvalues of the Hessian. In addition, the same Hessian opens the door to some Bayesian analysis. In other words, we switched to a functional analysis (and more manual) approach in order to refine our framework.

II.1.3.3 Minimisation of the functional using L-BFGS-B

To drive the gradient descent through control space, we use the Broyden–Fletcher–Goldfarb–Shanno (BFGS) algorithm, a quasi-Newton method ; that is a method that iteratively approximates the Hessian from gradient evaluations (here provided by the adjoint method). However, the secant equation

$$\mathrm{B}\Delta m = \frac{dJ(\theta(m_k+\Delta m), m_k+\Delta m)}{dm} - \frac{dJ(\theta(m_k), m_k)}{dm} \tag{II.20}$$

(where k indexes the optimisation step) is under-determined in multiple dimensions so the solution has to be further constrained. In particular, BFGS looks for an approximation B_k that not only fulfills the secant condition (i.e. the approximation coincides with the finite difference of gradients at this step size, see (II.20)), but also is symmetric, positive definite, and minimises the change w.r.t. to the previous Hessian approximation under the Frobenius norm : $\mathrm{B}_{k+1} = \mathrm{argmin}_{\mathrm{B}} \|\mathrm{B} - \mathrm{B}_k\|$. The resulting analytic matrix can be inverted using the Woodbury formula, yielding a clear update rule that can be consulted in the literature. More precisely, we use the limited-memory (L) version of BFGS that also handles box (B) constraints, L-BGFS-B. Since the functional is convex and the PDE constrained by $\mathbf{f}$ is linear, the Hessian should be positive definite and the Hessian approximations computed by BFGS should converge to the actual Hessian.

II.1.3.4 Multi-scale analysis for large displacements

When displacements between consecutive images I_1, I_2 are too large (e.g. typically when the imaging frame rate is insufficiently high compared to intracellular movements), the assumption that displacements are small and local (II.3) is no longer valid. To handle these situations, a multi-scale strategy is used [189] : a coarse-to-fine pyramid of sequences is obtained via iterative Gaussian filtering coupled with downsampling until a sufficiently coarse scale is reached (i.e. where the largest observable displacement is no more than one pixel). The displacements are first evaluated at a coarser scale ($\mathbf{u}_w$) and then propagated to the next scale by : 1) warping the image to a new grid ($I_w := I_2(\mathbf{x} + \mathbf{u}_w \Delta t)$) and 2) adjusting the data attachment term J_{data} accordingly :

$$\left\| (\mathbf{u} - \mathbf{u}_w) \cdot \nabla I_w + \frac{I_w - I_1}{\Delta t} \right\|_K^2 . \tag{II.21}$$

This two-step process is then iterated from the coarsest scale until the finest scale is processed (see Figures II.6 and G.2). The resulting method is capable of handling arbitrarily large displacements. In practice, we use the dimensionless variables and splitting scheme (as written in (II.16)) and thus (II.21) becomes

$$\|(\mathbf{u} + \mathbf{g} - (\mathbf{u}_w + \mathbf{g}_w)) \cdot \nabla I_w + I_w - I_1\|_K^2 , \tag{II.22}$$

where I can be normalised at will because the constant would affect all the functional equally.

II.1.3.5 Automatic estimation of functional weights

The result and quality of the estimated variables depend on the choice of the empirical weighting factors in equations II.11 and II.14. Small values of α, γ, and η will tend to over-fit the difference between image pairs, including the experimental noise, and may favour the estimation of large forces. Conversely, large values of α or η (e.g. compared to γ) will either constrain the estimated forces or disregard the out of plane motion, which might no longer describe the observed movements correctly. In order to adjust these parameters in a less biased manner, we employ an automated strategy that selects, for a given image pair, the parameter set that best predicts the previous and following images[14]. In practice, this defines an error measure to be

---

[14] In Chapter III, we introduce two different criteria that are based only on the current time point and that are better motivated.

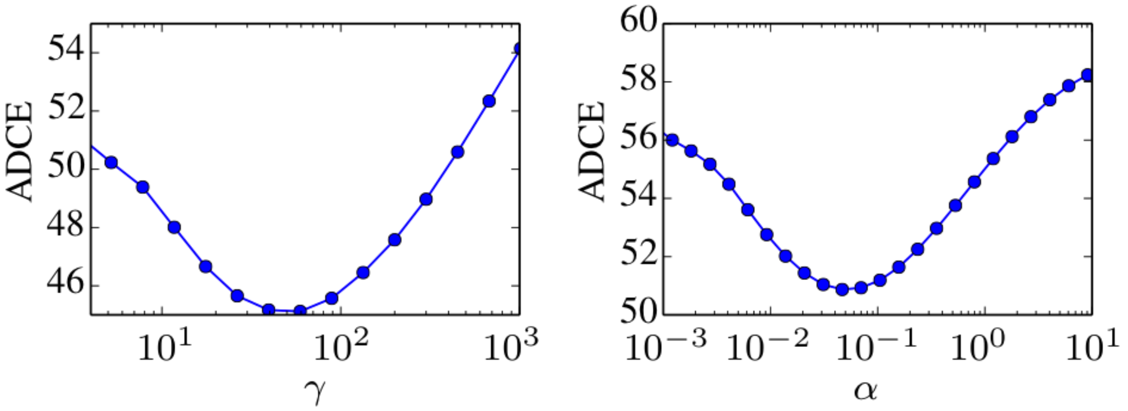

FIGURE II.5 – **Automatic parameter estimation.** Illustration of the dependency of the ADCE error measure on the empirical model parameters α and γ (see equations II.11 and II.14). The optimal parameter values are the minimum of each curve. Taken from [160].

minimised, which is known as the Average Data Constancy Error (ADCE) [190] :

$$ADCE = \sum_i \left(I_{i-1} - \hat{I}_{i-1}\right)^2 + \sum_i \left(I_{i+2} - \hat{I}_{i+2}\right)^2, \tag{II.23}$$

where $\hat{I}_{i-1}$ is estimated by propagating I_i backwards using $-\mathbf{u}\Delta t$, while I_{i+2} is obtained likewise by propagating I_{i+1} forward with $\mathbf{u}\Delta t$.

The minimum ADCE can be found using a fast derivative-free minimisation algorithm such as the Brent method [191]. Given that multiple parameters must be estimated simultaneously, we apply a two-step process, which we illustrate here for γ and α, regularising the force field. We first estimate γ and $\mathbf{g}$ using the unconstrained optical flow. Secondly, we run a second estimation for α and $\mathbf{f}$ with the constrained optical flow, keeping $\mathbf{g}$ constant. Thirdly, we fix the estimated α and γ and conduct a final joint estimation of $\mathbf{f}$ and $\mathbf{g}$ to refine the results.

Although the ADCE criterion is not guaranteed to be convex neither in α nor γ, we have found in practice that this criterion behaves well (its shape is close to parabolic) when either parameter varies on a logarithmic scale between reasonable bounds (see Figure II.5). In our experiments, we noted a range for α where the ADCE reaches a local plateau, indicating that any value within this range is equally satisfying. This behaviour is directly linked to the definition of the Stokes system (equation II.8). Indeed, the images are linked by $\mathbf{u}$, which is the first term of the first Stokes equation. There are however two possible ways to compensate $\mu\Delta\mathbf{u}$ for equality (either via ∇p or via $\mathbf{f}$), and α defines the balance between the two. We assume here that the cell favours small interior forces to minimise energy consumption (letting the pressure gradient become comparatively large [134]), and therefore select the largest value of α on that plateau to favour a large pressure gradient and small internal forces.

II.1.3.6 Cell segmentation : edge and region-based active contours

To segment the cell domain K on each image O of the time sequence we use yet another variational method. In particular, we use the piece-wise constant "Chan-Vese" [61] version (here the constants are I_K and I_{K^C}) of the more general Mumford-Shah [192] partitioning problem, but modified to include edge information. That is we combine region-based and edge-based terms. The functional and associated minimisation problem can be expressed as a weighted ($\lambda, \nu \in \mathbb{R}_{\geq 0}$) combination of energies

$$\underset{K, I_K, I_{K^C}}{\operatorname{argmin}} \left\| I - I_{K^C} \right\|_{K^C}^2 + \lambda \left\| I - I_K \right\|_K^2 + \nu \int_{\partial K} g_I, \tag{II.24}$$

where the complementary is taken with respect to the image superset. Notice that if K is fixed, $I_K(K)$ and $I_{K^C}(K)$ correspond to the mean intensities of their respective domains, and thus we can use an alternating scheme. g_I is an edge detection function based on intensity variations, for example as given by the gradient magnitude ∇I : $g_I := 1/\left(1 + \rho |G * \nabla I|\right)$ [193], where $\rho \in \mathbb{R}_{\geq 0}$, the gradient is convoluted with a progressively-finer Gaussian filter G to blur away local minima, and the function is set up so that it is minimised when the gradient blows up at an edge. Even though the same edge-detector can act as a regulariser, e.g. the surface area [61] (or curve length) $\int_{\partial K} 1$ is minimised for $\rho = 0$, some extra regularisation of ∂K is sometimes desirable. In such cases, we can impose an extra smoothness constraint, for example on the curvature : $\int_{\partial K} \kappa^2$. An extra volume (or area) constraint $\left(\int_K 1 - V\right)^2$ can also be added to enforce some temporal regularity by comparison to a reference volume V that is extracted as an averaging function of previous volumes. Finally, extending the problem to multiple cells (known as multi-phase) is the result of summing the individual functionals and avoiding collisions by adding additional terms that frown upon any overlap of the regions : $\int_{K_i \cap K_j} 1$. To be a bit more intuitive, problem (II.24) is, in some sense, looking for the best approximation of the image that can take only two values (the data-fitting terms express the distance to the original image), but with some edge information that aims at regularising the problem into uniqueness or to reduce the influence of noise.

In this work, we implement active contours (Figure II.6) as presented in (II.24) with some small regularisation of the surface via curvature, and extended to the multi-phase case to handle touching cells [63]. There are also a lot of choices as regards representing the surface or contour ∂K. Instead of using the more classic level set approach, which represents the surface implicitly as the 0-isosurface of a higher-dimensional function [15], here we use an explicit discrete representation that defines a contour as a set of ordered points and a surface as a triangulated mesh. While level set methods are easier to implement and more topologically flexible, discrete models are computationally lighter and are more easily adapted to handle collisions.

---

[15] The function is generally taken to be of opposite signs on each side of the surface and with absolute value the distance to the 0 level set. It can be moved by solving the advection equation.

The energy can be minimised by deriving an evolution equation from the Euler-Lagrange equations corresponding to the energy functional. [194, 195] The derivatives of the energy can be interpreted as forces acting on the contour or surface vertices that progressively deform the initial boundary until it reaches a local minimum. Indeed, the resulting functionals are non-convex and therefore the final result depends on the initialisation [16].

II.1.3.7 Delaunay meshing and surface/contour simplification via VSA

To implement the FEM and the Adjoint method we need to derive a mesh from each of the segmented cell domains K. However, meshing is a delicate subject as the quality of interpolation (and thus of the results) depends directly on the quality of the mesh. To maintain a high quality we re-mesh the cell at each time point ; that is each mesh is constructed independently at every time point, instead of mapping the older mesh onto the newer domain. While this is much easier to implement, it has down-sides : having a time-consistent mesh would not only help in keeping track of all the variables, but also in formulating time-dependent problems.

We choose Delaunay triangulation (tetrahedrisation in 3D) as the meshing algorithm [198]. In this case, the algorithm is constrained or restricted by the polygon or surface mesh resulting from the discrete segmentation, which preserves any important feature in the shapes. The mesh is constructed by progressively adding points following a Delaunay refinement that ensures a nice spread of the vertices [199, 200]. Termination of the process is dictated by circumradii of the elements : when they fall below a user-specified size, which reflects the desired resolution, the algorithm stops. Later, a global criteria such as Optimal Delaunay Triangulation (ODT) smoother is used to optimally reposition the vertices [201, 202] according to a mesh energy that describes the error fit of the piece-wise linear interpolation of a quadratic function. Since the latter criteria is global, a second phase is required to fix the worst mesh elements ; this is achieved via perturbation [203] and exudation [204].

Another non-trivial endeavor is to downscale the initial contours or surfaces to a coarser resolution. This is necessary in order to implement the multi-resolution strategy outlined above. In a 2D setting, it works well to resample the polygonal contour on the Fourier domain (see the top rows in Figure II.6). However, the same strategy is not satisfactory when applied to a 3D surface mesh. Instead, we use a variational shape approximation (VSA) method [205] to try to preserve shape and salient features. Very broadly put, the aim is to partition $(\mathcal{S})$ the initial surface into a given number k of subsurfaces $\mathcal{S}_i$, $i \in \{1\,..\,k\}$, each of them to be well approximated by a so-called proxy P_i according to an error measure. Proxies are a planar fit of the subsurface defined only by a point x_i and a normal vector n_i. To find the set P of proxies the error measure is to be minimised across all subsurfaces :

$$\underset{P}{\operatorname{argmin}} \sum_i \|\mathbf{n} - \mathbf{n_i}\|^2_{\mathcal{S}_i} \,, \tag{II.25}$$

---

[16] Some convex relaxation efforts can be found in [196] and [197].

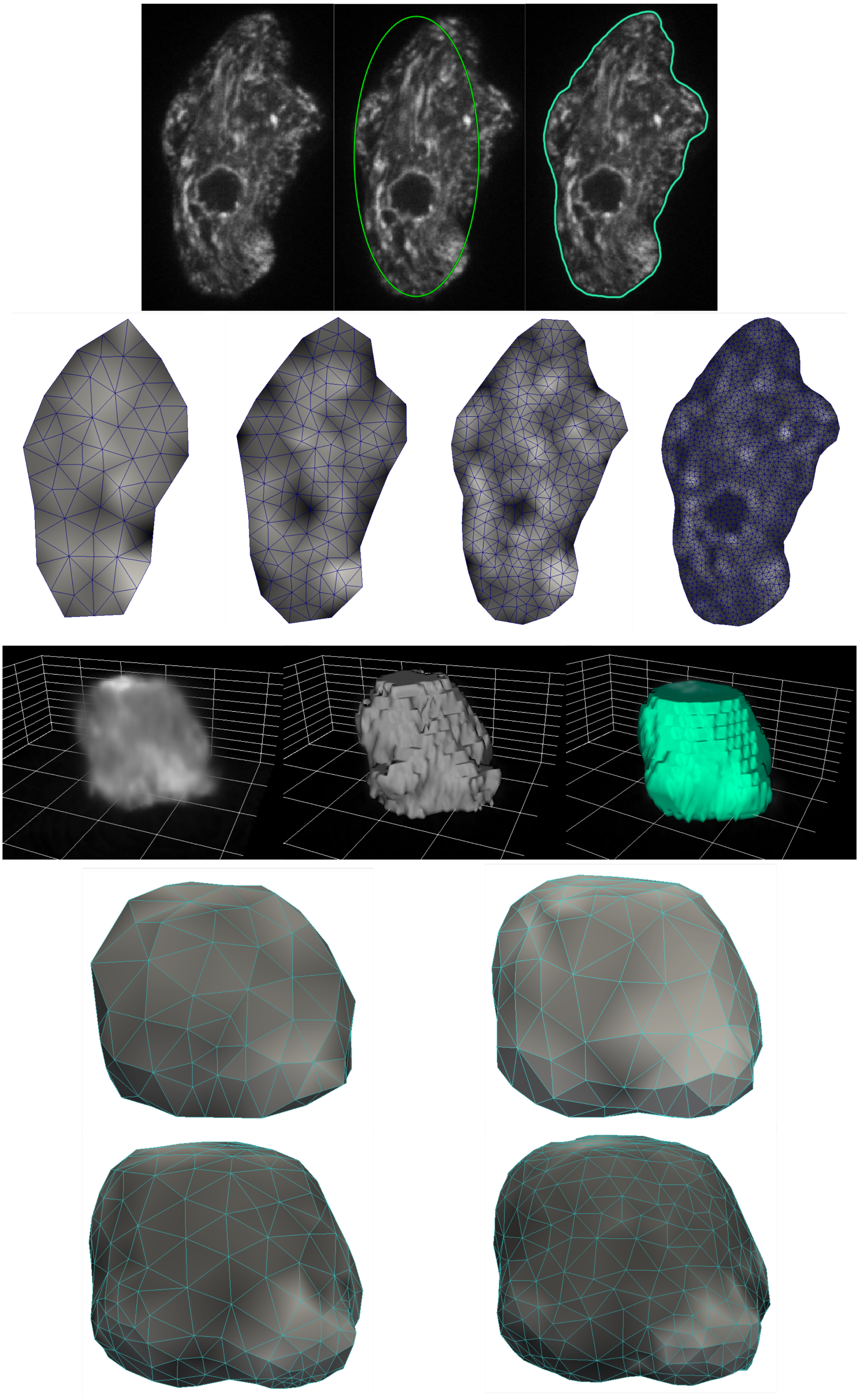

Figure II.6 – **Segmentation and multi-scaling in 2D and 3D. Row 1)** Raw 2D image, initialisation (green ellipse), and final segmentation with active contours (∼ turquoise contour). **Row 2)** Pyramid of meshes (blue triangles) that progressively refine the problem. Underlying each mesh is the warped image I_w at the corresponding scales. **Row 3)** Raw 3D image, initialisation (grey area with HK-means), and final segmentation with active contours (∼ turquoise surface). **Row 4)** Pyramid of meshes (∼ turquoise triangles) that progressively refine the problem. Underlying each mesh is the warped image I_w at the corresponding scales. See Figure G.2) for the velocity (and pressure) in 2D and 3D at scales 2 and 4.

where **n** is the spatially-varying surface normal. This "normal" metric captures very well the anisotropy of the surface [205]. In addition, it is intuition-friendly as not only approximating the normal field of surfaces is normally a better approach (akin to focusing on gradient interpolation errors), but also visual perception is very sensitive to changes in normal fields because they govern lighting effects. Minimisation is conducted via optimal discrete clustering using a fixed point iteration algorithm [206]. While this method gives very good results (bottom row, Figure II.6), it is not specially fast. Since accuracy is not that important until we reach the finest scales, in Chapter III we introduce a faster (but less accurate) "cost-driven" alternative. In our software, the multi-scaling is automatically created by setting a decreasing pyramid of k values. Theoretically, the same progression of the algorithm can be harnessed to extract each of the scales from a single minimisation to the coarsest scale. However, this is more straightforward to implement in the latter cost-driven method because it advances locally on the discrete mesh. This strategy was not implemented in the VSA version and thus the algorithm had to run once per scale. The CGAL library has a very good C++ implementation of the VSA approach by Pierre Alliez, David Cohen-Steiner, Mathieu Desbrun, Lingjie Zhu (in alphabetical order).

II.1.4 Implementation as open-source software in Icy

The workflow was implemented within the Icy [162] software and is available as an automatically downloadable module (or plug-in) called BioFlow (more details on the Icy website (`http://icy.bioimageanalysis.org/plugin/BioFlow`). Icy is free open-source software dedicated to bioimage analysis, offering a lot of different image analysis techniques and associated visualisation tools that can help process (shorten, re-size, register, deconvolute, etc.) a video sequence. By implementing BioFlow inside Icy, we facilitate pre- and post-processing of the image sequences, and at the same time benefit from exposition to its active community.

After loading a video-microscopy sequence into the software, an initial contour is defined around the cell on the first frame (this manual step can be automated using any available segmentation technique such as HK-means [207]), as shown in Figure II.7. The main BioFlow script (written in Jython) is launched from Icy's script editor and starts by segmenting (active contours, see Figure G.4) and tracking (nearest neighbours) the

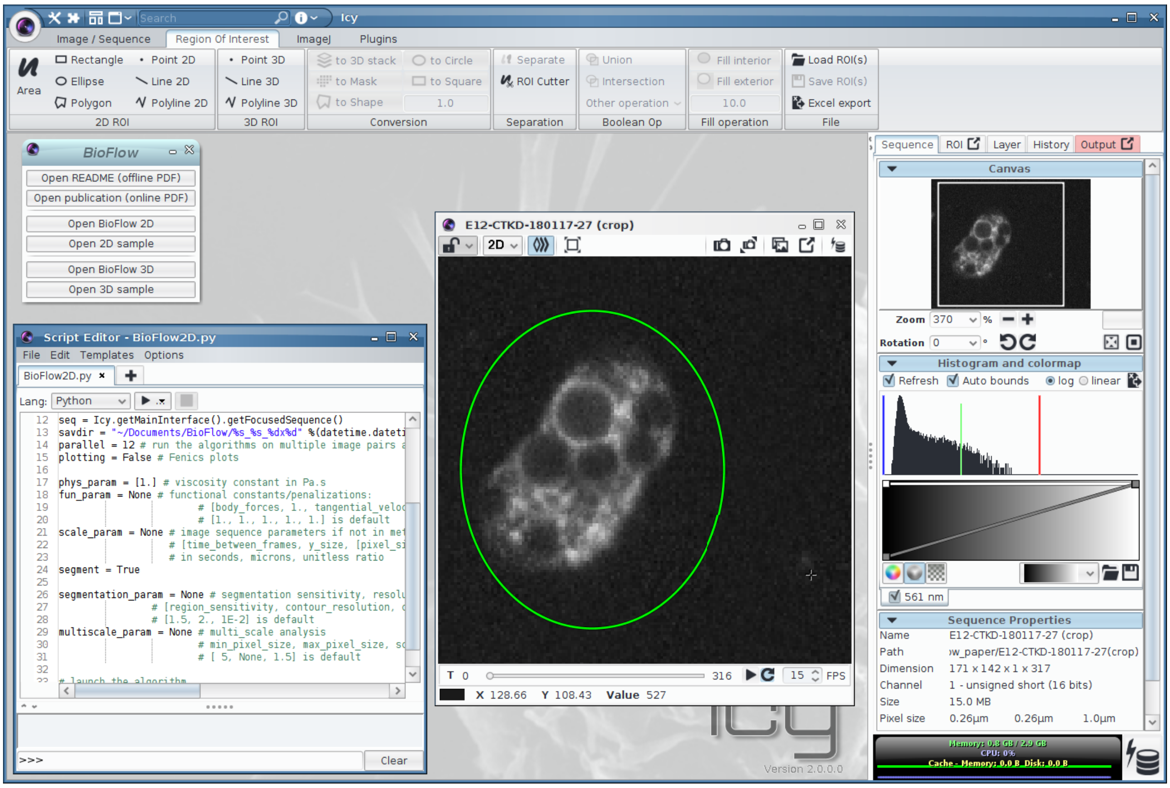

```
seq = Icy.getMainInterface().getFocusedSequence()
savdir = "~/Documents/BioFlow/%s_%s_%dx%d" %(datetime.dateti
parallel = 12 # run the algorithms on multiple image pairs a
plotting = False # Fenics plots

phys_param = [1.] # viscosity constant in Pa.s
fun_param = None # functional constants/penalizations:
                        # [body_forces, 1., tangential_veloc
                        # [1., 1., 1., 1., 1.] is default
scale_param = None # image sequence parameters if not in met
                   # [time_between_frames, y_size, [pixel_si
                   # in seconds, microns, unitless ratio
segment = True

segmentation_param = None # segmentation sensitivity, resolu
                # [region_sensitivity, contour_resolution, c
                # [1.5, 2., 1E-2] is default
multiscale_param = None # multi_scale analysis
                        # min_pixel_size, max_pixel_size, sc
                        # [ 5, None, 1.5] is default

# launch the algorithm
```

Name E12-CTKD-180117-27 (crop)
Path w_paper/E12-CTKD-180117-27(crop)
Dimension 171 x 142 x 1 x 317
Channel 1 - unsigned short (16 bits)
Size 15.0 MB
Pixel size 0.26µm 0.26µm 1.0µm

FIGURE II.7 – **BioFlow software and initialisation.** BioFlow plug-in running on the Icy software. Steps to run the software : 1) the video sequence can be opened or dragged into the window ; 2) a region of interest is drawn around the cell to initialise active contours ; 3) open BioFlow from the top search bar and select 2D/3D on the pop-up window ; 4) change any parameter ; 5) Press the black arrow to run.

cell boundary over time, then creates a multi-scale version of the image and contour for each frame. More specifically, the image scaling is performed via Gaussian filters and interpolation (NumPy [208], SciPy [209] and PIL libraries), whereas the contours are down-sampled in the Fourier domain in 2D (SciPy), or using the VSA method in 3D (CGAL). The contour-image pairs are subsequently transferred to a python script (using execnet) where the remainder of the computations take place : a) the image and contour are converted into a Finite Element mesh by Delaunay triangulation using the *mshr* library, which calls the CGAL library [210] via SWIG ; b) the PDE system in 3D (equation II.11) or 2D (II.13) is assembled into matrices by the FEniCS [185] library and then solved using a MINRES Krylov solver from the PETSc library [211, 212, 213] ; c) the gradient of the functional J is computed by deriving the adjoint equation (II.19) using the *dolfin-adjoint* library ; and d) the gradient is used to minimise J via an interface with the optimization module scipy.optimize that implements the L-BFGS-B algorithm. This process is iterated until convergence and repeated from coarse to fine image scales (Figure G.5) using appropriate warping : the interpolation is done via cubic splines (SciPy), and the image gradient is implemented as a five-point difference stencil (fourth-order accuracy). Lastly, the results are transformed from normalised to unitful (p also has to be re-inverted) using the metadata from the video sequence (default) or user-input values.

To reduce computation time, each pair of frames in the video sequence is processed in parallel according to the number of processors specified by the user. This is achieved by exploiting the execnet library in python. The results are output as a tree of folders corresponding to the estimated parameters ($\mathbf{u}$, p, $\mathbf{f}$, $\mathbf{g}$, r, mesh, I_1, I_2) each containing a list of time points in .xml and .pvd/.vtu (VTK format by Kitware, readable in C++, Java, and Python) format. The final results and figures were produced either within Icy or with the ParaView software (`http://www.paraview.org`). In the case of Icy, a second associated plug-in, BioFlow Display (see Figure II.8), reads the output folder and generates an overlay on each frame of the original video-sequence. The arrows used to display the fields (dots for scalar quantities) can be heavily customised : one can change the absolute scale of the field, scale by magnitude, color by magnitude, set a constant arrowhead, set some black contour around the arrow, etc.

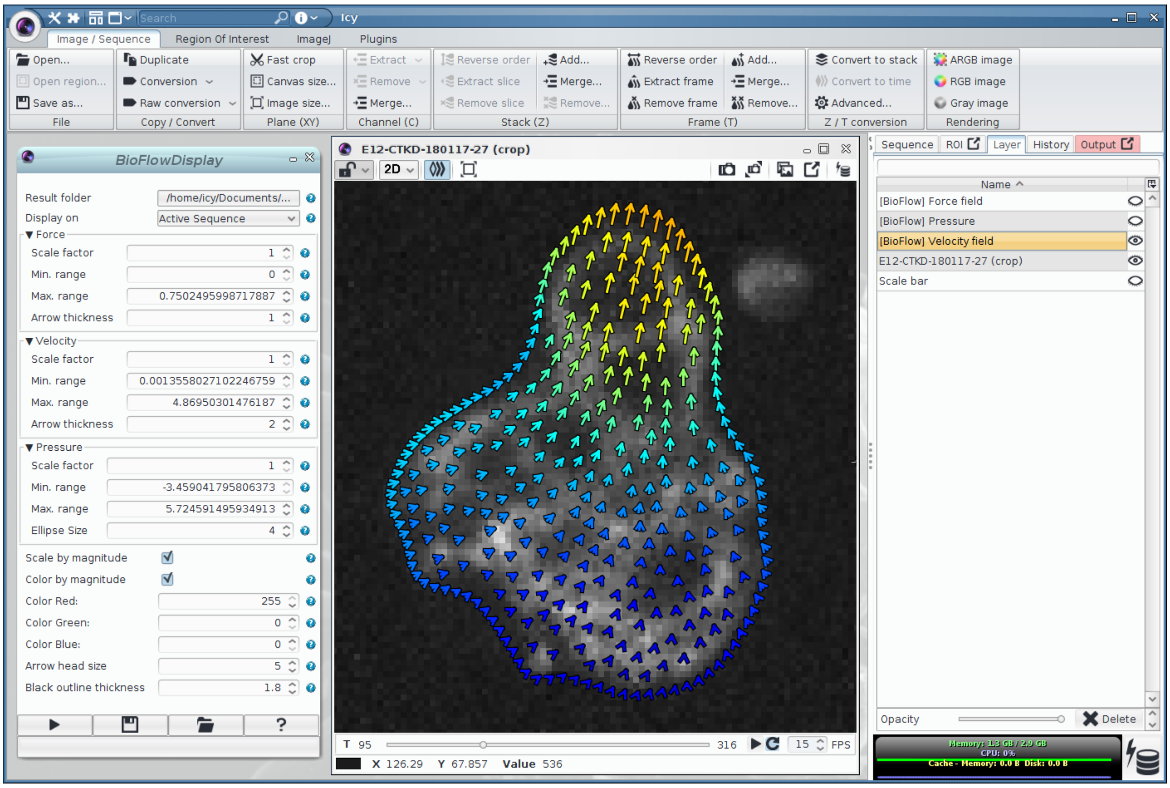

Result folder /home/icy/Documents/...
Display on Active Sequence

▼ Force
Scale factor 1
Min. range 0
Max. range 0.7502495998717887
Arrow thickness 1

▼ Velocity
Scale factor 1
Min. range 0.0013558027102246759
Max. range 4.86950301476187
Arrow thickness 2

▼ Pressure
Scale factor 1
Min. range -3.459041795806373
Max. range 5.724591495934913
Ellipse Size 4

Scale by magnitude ☑
Color by magnitude ☑
Color Red: 255
Color Green: 0
Color Blue: 0
Arrow head size 5
Black outline thickness 1.8

FIGURE II.8 – **BioFlow Display.** This plug-in is associated to the original BioFlow plug-in and allows to display vector and scalar fields on the original sequence. Steps : 1) open from the search bar ; 2) load output folder from BioFlow and choose the corresponding video sequences ; 3) adjust visualisation parameters ; 4) press play. The results are shown as layers of velocity, pressure and force that can be activated or deactivated at will.

Installation of the BioFlow plug-in in Icy is straightforward : type "BioFlow" on the search bar and it will download automatically. However, actually running the algorithm requires installing the FEniCS library on the default (or change paths) python of your workstation. Alternatively, we have created a plug-in that connects Icy to Docker and automatically runs an image that containts the appropriate library. Of course, this requires having Docker running on the computer along with Icy, and also slows down the algorithm because the data has to be packed and unpacked (pickle module in python) due to security issues. BioFlow will check by itself whether the libraries are installed and launch Docker otherwise. On the other hand, BioFlow Display is fully in Java and has no further requirements. While the plug-in is made to run now on a single cell, extension to multiple cells is conceptually unambiguous and perfectly parallelisable.

II.1.5 Advantages and limitations

Our method brings together image analysis, physical modelling and mathematical optimisation to perform direct and non-invasive intracellular measurements of invisible mechanical quantities from 2D and 3D fluorescence video-microscopy data. BioFlow is designed as a flexible mechano-imaging data assimilation framework, in which we adapted the standard optical flow algorithm such that the observed movement of intracellular material is extracted under the constraints of a biophysical model of the intracellular dynamics. This permits a simultaneous extraction of the intracellular velocity as well as the biophysical parameters of the chosen model, all with high spatial resolution. The flexibility and ease of use of BioFlow lies in three complementary aspects : 1) its theoretical foundation provides a method that is virtually independent of (and adaptable to) any theoretical model of the cell ; 2) it relies exclusively on conventional video-microscopy data of living cells, and thus permits non-invasive single cell studies in diverse experimental contexts ; 3) its open-source software implementation lets any component of the workflow be tailored to the specific problem at hand (for instance, implementing a new theoretical model solely requires deriving its weak formulation).

In this section we presented one possible implementation : a Newtonian fluid dynamics model of the cell material to study the amoeboid motility of *Entamoeba histolytica* trophozoites, which results in high-resolution maps of intracellular velocities, pressure gradients, forces and out-of-plane flow (in 2D). While validating some of these measurements is experimentally challenging, we believe that the study proposed in II.2 constitutes a good case study to both validate the method and enrich the landscape of experimental and theoretical reports on amoeboid motility with new quantitative insight.

We stress that our choice of theoretical model only assumes that the observable intracellular material behaves as a fluid, without making any assumption on the molecular mechanisms underlying the observed motion. This change of paradigm shifts the weight from whole-cell models, which assume the underlying biology, to purely physical models that stay neutral in this regard and thus are at an advantage towards drawing unbiased biological conclusions. However, the interpretation of the estimated quantities still depends on the validity of the chosen model. It can be argued, for instance, that the chosen Newtonian fluid model is incomplete and should account for a viscoelastic component [136]. More concretely, this would require replacing the homogeneous viscous stress of the incompressible Stokes system τ_{v} (that results in $\mu\Delta\mathbf{u}$, see (II.8)) by the non-homogeneous form of the full incompressible Navier-Stokes system, i.e. $2\mu\epsilon(\mathbf{u}) + \tau_{\mathrm{e}}$, where the elastic stress τ_{e} is modelled by an additional evolution equation. This extension is presented in Section II.6 using an Oldroyd-B viscoelastic model derived from experimental data in the literature. Treating μ as an additional unknown to the problem is also possible, but would substantially increase the complexity of the theoretical model and its numerical resolution. Given the size of the cell and the time-scale of the imaging (of order between the decisecond and the second), we believe that the uniformity of μ is a good preliminary approximation and that the estimated quantities are only minimally affected by the elasticity component. In addition, a detailed *a posteriori* sensitivity analysis (not shown here) of the related inverse problem (obtain $\mu(\mathbf{x})$ from $\mathbf{u}$) shows that the resolution with which the flow field is captured is not enough to distinguish the small variations in elastic moduli reported in the literature.[17] However, at other scales or in other cell types, the biophysical model should perhaps be extended to consider the fact that some cellular organelles (such as the nucleus) do not necessarily behave like a fluid. In addition to permitting a more faithful estimation of biophysical quantities, this would allow a better segregation of the various forces acting within the cell. The membrane forces (e.g. pulling, pushing or friction) are not directly accounted for by the chosen physical model, and are implicitly taken into account through the boundary displacements, which is reflected by the traction stresses.

While the method constitutes an original addition to the landscape of methods to study intracellular dynamics in evermore complex environments, we expect that the flexibility of the underlying framework will broaden the applicability of the method to other fields of life sciences. For instance, the current implementation offers an straightforward and appealing alternative to multi-cellular modelling in developmental biology, where an equivalent Newtonian assumption was used to infer physical quantities from tissue dynamics during drosophila gastrulation [214]. At an even higher scale, the ability to measure out-of-plane flow can be of great interest to decipher the mechanisms establishing and regulating blood-flow in the beating heart, where live imaging in 3D remains a technical challenge [215]. In chapter III, we present an application of a similar (but re-formulated) framework to quantify uncertainty in Traction Force Microscopy, a widely used method to extract forces exerted by cells on the substrate. However, as discussed in part II.1.3.2, the flexibility required to implement this (as well as to tailor the convergence of the model and explore it further) hampers the automatisation of the adjoint derivation.

---

[17] However, this idea opens an avenue for the method to tackle the segmentation of "invisible" bodies where the elastic moduli ratios are higher such as in microfluidics or elastography (see Annex D and Conclusion IV). This work is not included in the present thesis.

II.2 Biophysical measurements inside the amoeboid cell

This section of the work was developed in collaboration with Timothée Lecomte, Maria Manich, Roman Thibeaux, Elisabeth Labruyère and Nancy Guillén ; and supervised by Alexandre Dufour. All at Institut Pasteur. This work is published in [160].

What follows uses the method presented in Section II.1 to study amoeboid motility, unveling a hidden periodicity in *E. histolytica* and confirming several loosely-supported hypothesis in the literature that concern bleb-based motion.

We applied our BioFlow approach to study amoeboid motility, taking as a model organism the parasite *Entamoeba histolytica* , the causative agent of human amoebiasis, a disease still today characterised by substantial mortality and morbidity [216]. This unicellular parasite is an appealing model from a biophysical standpoint thanks to its relative simplicity, notably due to the lack of microtubules outside the nucleus [217] and apparent lack of intermediate filaments [218]. The cytoskeleton is therefore essentially formed of actin filaments. During its obligatory amoeboid migration, the cytoplasmic material flows in the direction of motion, a feature common to many primitive cell types [219, 220] as well as invasive cancer cells [221]. As a reminder from chapter I, this mode of migration differs from lamelipodium-based [222] in that amoeboid migration is thought to be driven by myosin-drive contractility that regulates intracellular pressure and causes the emission of blebs (protrusions) at the cell surface [42], which result in forward movement. Amoeboid movement has been studied both experimentally, for example using micro-pipette aspiration experiments [134], and with theoretical models [223, 224, 225]. Could our method complement these studies by quantitatively characterising the intracellular velocities, pressure gradients and forces driving the cytoplasmic flow into the protrusions ?

a) Imaging data. To observe the movement of the cytoplasm, we labelled actin with a very low dose of fluorescent Cytochalasin D and performed live 2D and 3D fluorescence microscopy experiments (see Figures II.3 and II.4). Cytochalasin D binds to the free barbed-end of actin filaments [226], and yields the appearance of short fluorescent filaments in suspension within the cytoplasm. The observable motion of this actin bulk well describes that of the cytoplasm everywhere inside the cell during its movement, and thus constitutes a good input for the algorithm.

II.2.1 Preliminary analysis of the measurements

Figure II.3 depicts the biophysical quantities (here velocities, pressure, forces, and out-of-plane flow in 2D) estimated from two consecutive images in 2D and 3D. All quantities are estimated in each node of the underlying Finite Element mesh, which

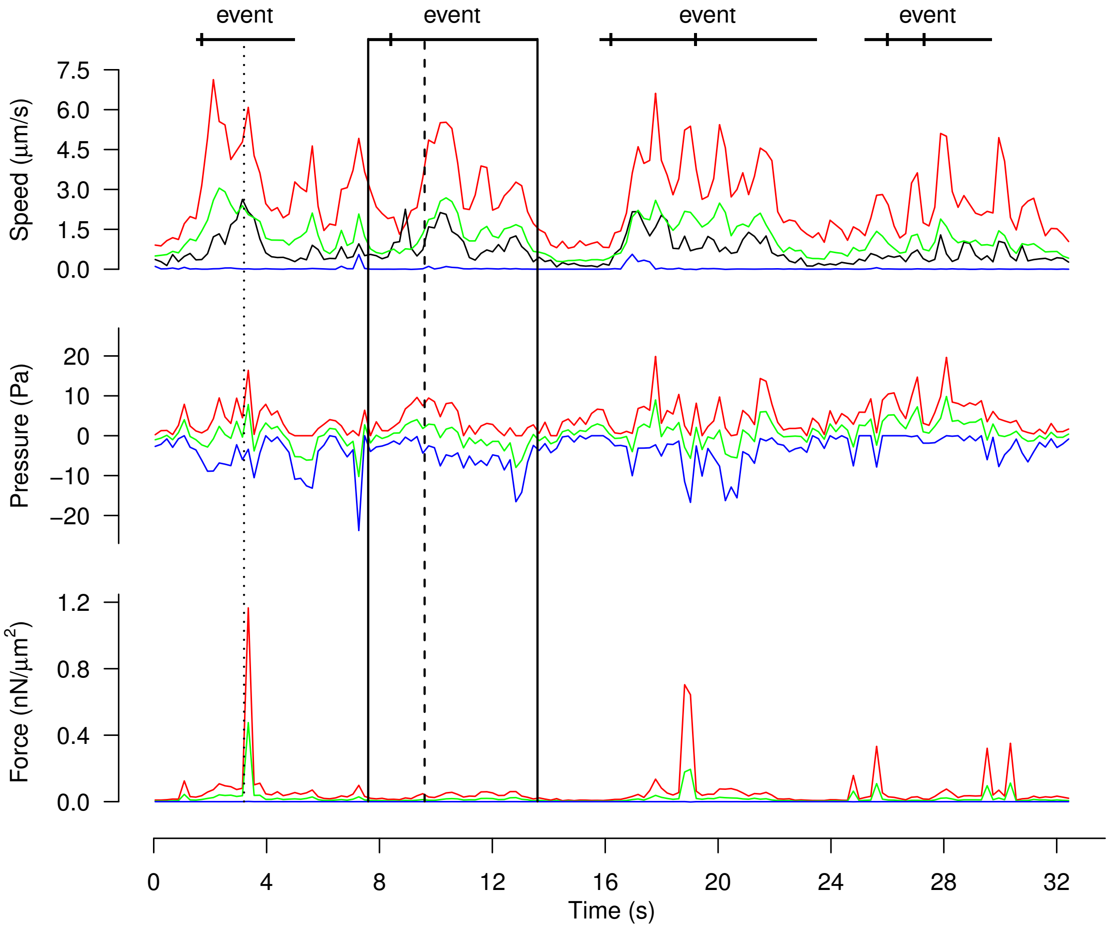

Figure II.9 – **Temporal profile of intracellular quantities during amoeboid migration** Maximum (red line), minimum (blue line) and average (green line) magnitude of the intracellular velocity, pressure and forces extracted from an image sequence. The black line represents the velocity of the cell centroid, calculated via automated cell tracking. The dotted line ($t = 3.2s$) corresponds to Figure II.3. The black rectangle isolates a portion of the sequence surrounding a protrusion event (dashed line at $t = 9.6s$), and is further analysed in Figure II.10. Taken from [160].

can be defined up to a single-pixel resolution (Figure G.1). By repeating this analysis over time (Figures II.9 and II.13b), BioFlow enables a quantitative analysis of the intracellular dynamics in both space and time. In the remainder of this sub-section we illustrate the results in 2D for easier visualisation, noting that measurements obtained on both 2D and 3D datasets were found in good agreement both qualitatively and quantitatively.

The **pressure** field p (Figure II.3c) exhibits a global gradient in the direction of migration, with higher pressure at the rear of the cell and lower pressure at the cell front. Assuming[18] a constant viscosity of 1 $Pa\ s$, the pressure values are of the order of 1 to 10 Pascals, which is consistent with both theoretical simulations [223] and in agreement with Darcy's law (see II.2.5). Since pressure is only present in Stoke's equation through its gradient, only the resulting pressure gradient is reliable. In other words, any analysis should be performed on the basis of pressure differences rather than single values.

It is worth pointing out that only the pressure gradient (and thus differences between pressure values) is reliable because

The **divergence** field r (Figure II.3c) represents out-of-plane flow. On the depicted image pair, r captures material leaving the plane of focus near the cell rear (blue area, $r_{\text{avg}} = -0.01s^{-1}$), as well as material entering the plane of focus towards the cell front (red area, $r_{\text{avg}} = 0.05s^{-1}$). A Fermi order estimation suggests that approximately $0.2\mu m^3$ of material leaves the focal plane at the cell rear, and $0.5\mu m^3$ flows into the focal plane at the cell front. It is worth noting that the integral of r over the entire cell is positive ($5\mu m^2 s^{-1}$), indicating that the visible cell area increases roughly $1\mu m^2$, although this does not imply a change in overall (3D) cell volume.

The **force** field $\mathbf{f}$ (Figure II.3c) is represented as an arrow-field indicating the magnitude and the direction of intracellular forces. The sum of all intracellular forces (with the exception of the viscous drag and the pressure gradient) has a magnitude in the order of the 0.1 to 1 $nN/\mu m^2$ and is therefore non-negligible when describing the flow (as a reference, the cell depicted here has an area of $240\mu m^2$). While such intracellular force measurements are unique and cannot be directly validated using experimental techniques, the estimated values fall well in range with that obtained using traction-based approaches [227, 228, 229].

The **velocity** field $\mathbf{u}$ is represented as streamlines (Figure II.3b) and as an arrow field (Figure II.3c) indicating the magnitude and direction of movement between the two consecutive frames. The streamline representation offers a good indication of the direction of the flow (Figure II.3c), and well depicts cytoplasmic streaming in the direction of migration, as expected for amoeboid migration. The flow also describes a global rotational movement stemming from the rear (where the cell displays a slightly concentric motion, indicating contraction) and ending at the front, where the fastest displacements take place. The instant velocity inside the cell has a magnitude ranging

---

[18] We decide on a defined value to make reading easier, but the results (e.g. $\mathbf{f}$ and p) can be obtained up to the viscosity constant because the method computes (first) the dimensionless quantities (see II.1.3).

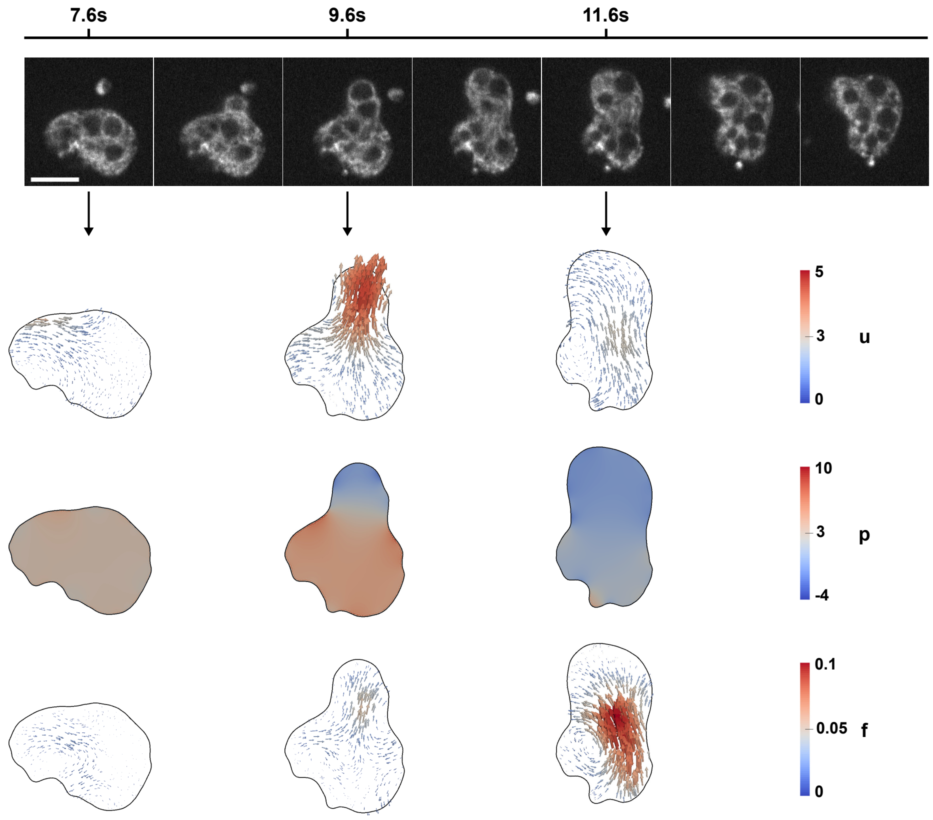
7.6s
9.6s
11.6s
5
3
0
u
10
3
-4
p
0.1
0.05
0
f

(a)

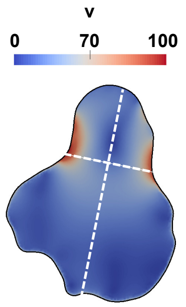
v
0
70
100

(b)

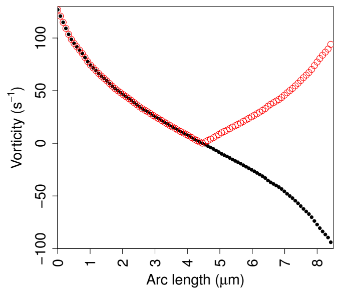
Vorticity (s^{-1})
−100
−50
0
50
100
Arc length (μm)
0
1
2
3
4
5
6
7
8

(c)

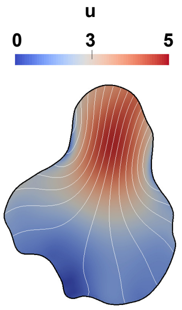
u
0
3
5

(d)

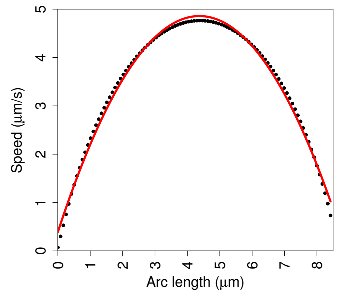
Speed (μm/s)
0
1
2
3
4
5
Arc length (μm)
0
1
2
3
4
5
6
7
8

(e)

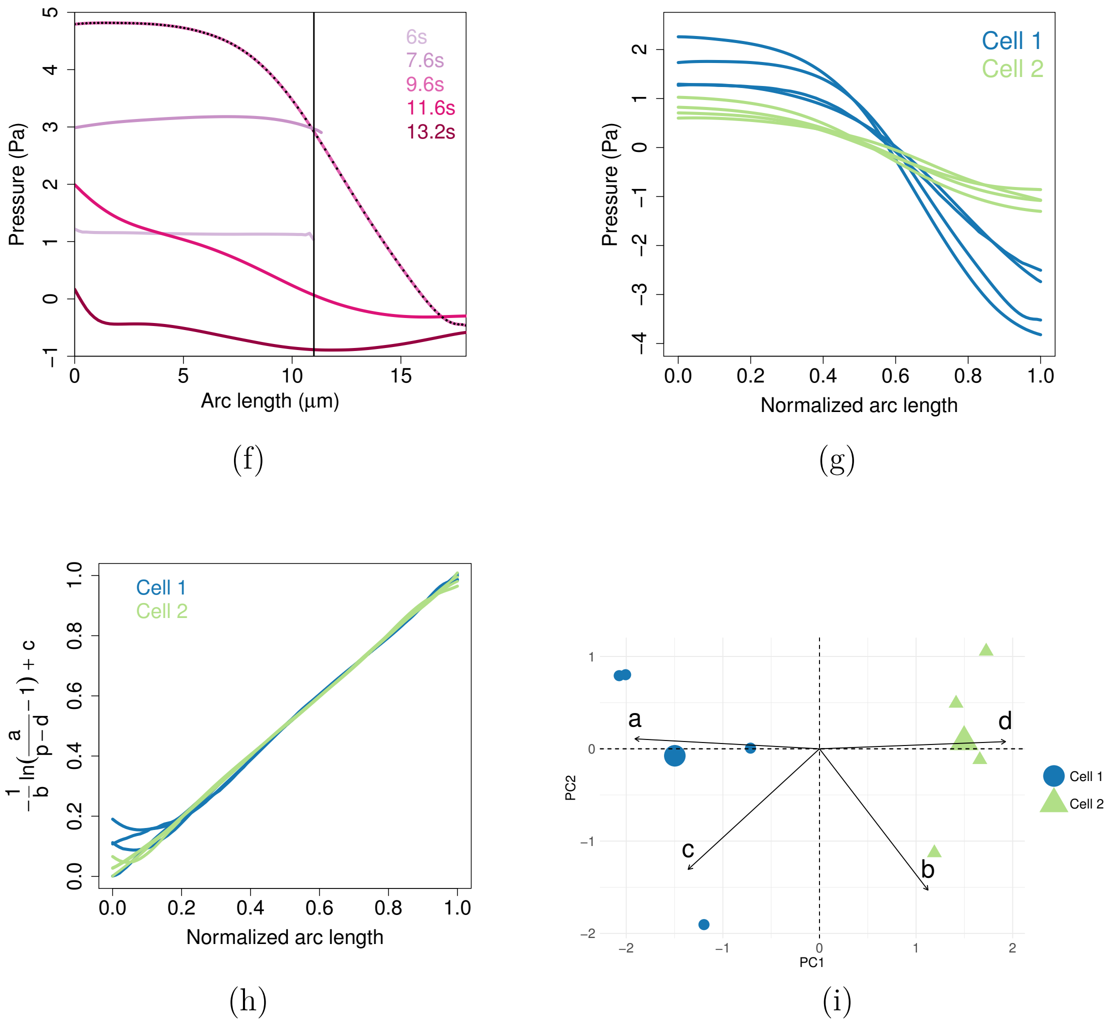

(f)

(g)

(h)

(i)

FIGURE II.10 – **Intracellular velocity, pressure and forces during cell protrusion.** **a)** Top row : snapshots of a 2D video-microscopy sequence ; Bottom : estimated intracellular velocity $\mathbf{u}$ ($\mu m/s$), pressure p (Pa) and force $\mathbf{f}$ ($nN/\mu m^2$) before ($t = 7.6s$), during ($t = 9.6s$) and after ($t = 11.6s$) protrusion, respectively. **(b-e)** Velocity analysis during protrusion ($t = 9.6s$). **b)** Magnitude of the vorticity v (s^{-1}). The long and short white dashed lines indicate cuts along the direction of protrusion and across the bleb, respectively. **c)** Vorticity profile (black : v ; red : $|v|$) across the bleb. **d)** Magnitude of the velocity u and its streamlines (white). **e)** Velocity profile across the bleb (black) and a second-degree polynomial fit (red). **f)** Pressure values (Y-axis) at several time points along the direction of protrusion (represented on the X-axis from cell rear to cell front) ; the black line indicates the cell front before blebbing. **g)** Pressure profiles along the direction of protrusion, obtained on 2 different cells (colour separated) for 4 different protrusion events. **h)** Sigmoid collapse of the curves in (g). **i)** PCA analysis and k-means clustering of the sigmoid parameters *(a,b,c,d)* (as defined in text) obtained from (h). $PC1$ (X-axis) is a linear combination of mainly a and d, whereas $PC2$ (Y-axis) is a linear combination of mainly b and c. Taken from [160].

from 1 to 10 $\mu m/s$, and faithfully captures the observed movement of intracellular material. This was confirmed by verifying that the average velocity over the cell ($\propto \int_\Omega |\mathbf{u}| d\Omega$) was similar to that of the cell centroid ($\propto |\int_\Omega \mathbf{u} d\Omega|$), as illustrated in Figure II.9.

Figure II.9 presents the temporal evolution of the minimum (blue), maximum (red) and average (green) values for each quantity within a cell over time. A statistical analysis on 20 cells yielded a maximum velocity, pressure range and force magnitude of 9.2 ± 3.8 $\mu m/s$ (mean, s.d.), 21.8 ± 6.3 $Pa\ s$, and 0.52 ± 0.70 $nN/\mu m^2$, respectively.

II.2.2 Study of single protrusions

During amoeboid motility, the process driving bleb nucleation and subsequent cell protrusion is thought to be powered by myosin, which is assumed to regulate hydrostatic pressure within the cell by exerting contractile forces on the actin cortex lying beneath the plasma membrane [42, 134]. Here we asked whether the extracted quantities can give more insight into the underlying mechanism, by studying their spatio-temporal profiles during natural (non-induced) protrusion events.

Figure II.10 depicts the biophysical quantities extracted inside the cell before, during, and after protrusion (Figure II.9-black box). Before bleb initiation (t=7.6s) the cell appears stable : the pressure builds up while the velocity and forces remain small. At t=9.6s, a pressure gradient across the cell drives the intracellular material inside the expanding bleb, which is reflected by the increase in velocity at the cell front. After stabilisation of the flow (t=11.6s), the pressure begins to equilibrate, while the cell body moves forward with the help of an increased force at the rear.

A detailed analysis of the velocity field during protrusion (Figure II.10d) reveals areas where the intracellular material flows from rear to front in a rotating fashion. A vorticity analysis of the velocity field (II.10b, c) highlights two vortices, one on each side of the bleb, where directions of rotation are opposite. The velocity profile across the bleb (Figure II.10e, short white line in II.10b) is smooth and well describes a Poiseuille flow (typical of a viscous fluid flowing through two static plates). This observation was validated by noticing that Poiseuille's planar equation was able to accurately recover the bleb width (data not shown). This evidence implies that the underlying cortex imposes a no-slip boundary condition to the flow, possibly hinting to the location of the rupture points.

Figure II.10f presents a time-diagram of the intracellular pressure profile measured along the direction of protrusion (Figure II.10b, long white line). It can be seen that the pressure first builds up from a steady-state, then suddenly drops (suggesting cortex breakage) and creates a decreasing gradient towards the cell front causing intracellular material to flow forward, and stabilises again as the flow stops. Figure II.10g depicts 4 consecutive pressure profiles extracted over time from 2 different cells. The curves resemble a sigmoid-like shape, which is a characteristic pattern of contraction [230]. Fitting a sigmoid to each curve yields an equation of the form $p = d + a / \left(1 + e^{-b(s-c)}\right)$, where s is the normalised arc length and (a,b,c,d) are the sigmoid parameters. By trans-

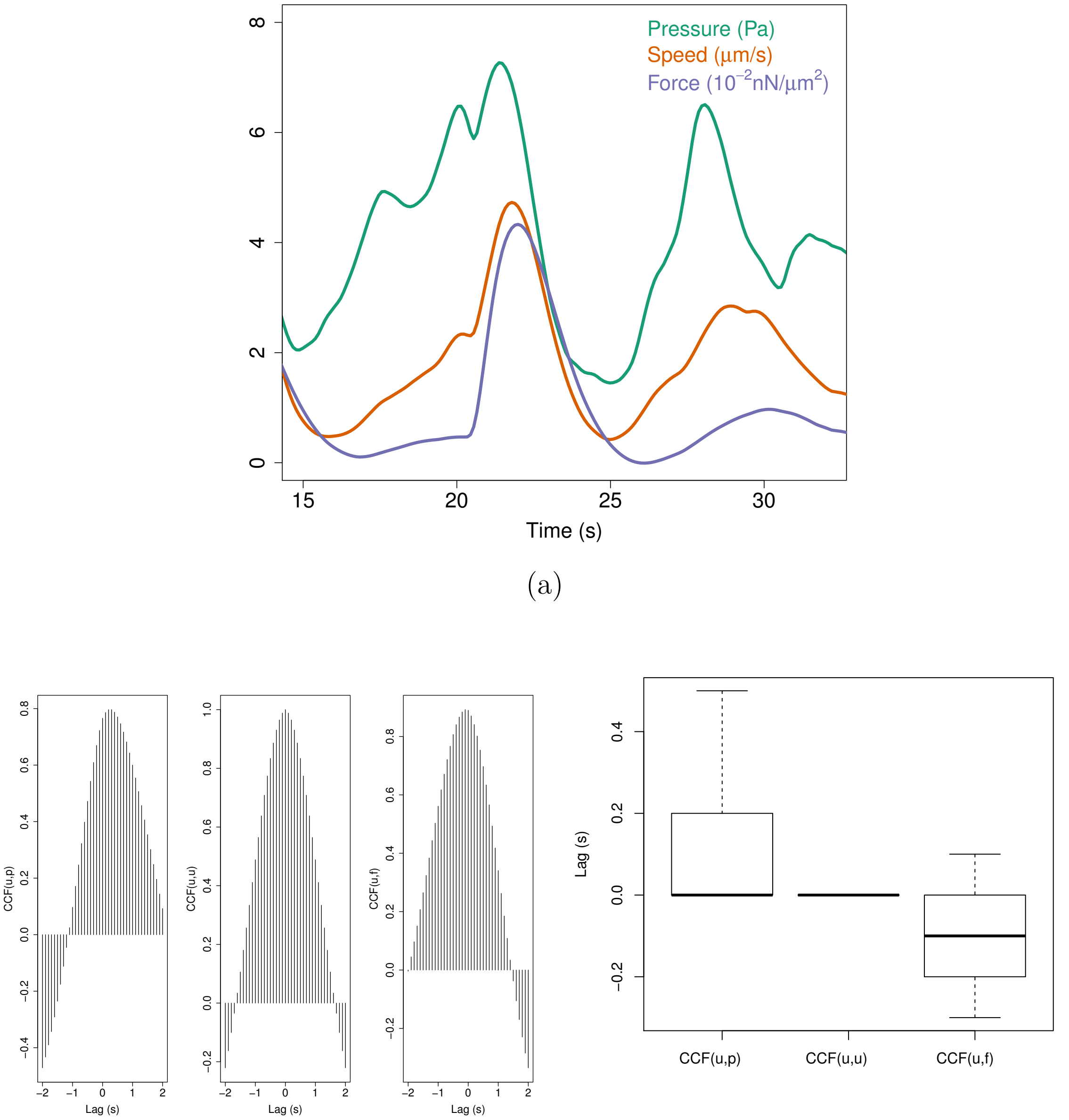

(a)

(b)

(c)

FIGURE II.11 – **Relative timing of intracellular force, pressure and velocity. a)** Estimated range (difference between maximum and minimum across the cell) of the intracellular velocity (red), pressure (green) and force magnitude (blue) for a single cell during a protrusion event. **b)** Temporal cross-correlation diagrams between $\mathbf{u}, p$ (left), $\mathbf{u}, \mathbf{u}$ (middle), and $\mathbf{u}, \mathbf{f}$ (right), representing the lag between quantities (given by the shift of the maximum peak away from 0). **c)** Cumulated analysis of the cross-correlation shift over $n = 10$ cells. Taken from [160].

forming the sigmoid into a linear model, i.e. $c - ln\left(a/(p-d)\ -1\right)/b$, all curves can be collapsed into the same unitary line (Figure II.10h), thereby verifying the sigmoid hypothesis. The parameter space (a, b, c, d) is able to capture both inter-cellular and intracellular variations (Figure II.10i). The 2 cells can be distinguished using (a, d). These parameters describe the amplitude range and the height of the sigmoid and thus reflect the ability of each cell to generate pressure. Conversely, (b, c) are able to distinguish different protrusion events of the same same cell. These parameters characterise the spatial geometry of the sigmoid (its slope and position) and therefore reflect the length and position of the protrusion.

The estimated force field $\mathbf{f}$ (Figure II.10a) seems to have a low overall magnitude during pressure build-up and cytoplasmic streaming, and only increases during the retraction phase, when it localises mostly at the rear of the cell. These observations suggest that the pressure gradient alone is sufficient to initiate cytoplasmic streaming, while cell retraction is not due to the pressure gradient, but rather hints at a myosin-based mechanism. We further investigated the timing and potential causality between pressure, velocity and forces during protrusions, by performing a correlative analysis over time (Figure II.11). We first plotted the difference between maximum and minimum values (i.e. *range*) for pressure, velocity and forces over the course of a video sequence, and applied a low-pass Butterworth filter [231] to eliminate spurious small scale fluctuations while preserving the magnitude of the original (Figure II.11a). We then calculated the pairwise cross-correlation function (CCF) between quantities (Figure II.11b) and measured the time lag where the correlation is highest. This analysis was repeated on $n = 10$ cells (Figure II.11c) and shows that pressure precedes velocity by $1.1 \pm 1.7s$ (mean ± s.d.) and that velocity precedes force by $0.9 \pm 1.2s$, thus further supporting the hypothesis that pressure drives cell expansion while myosin forces drive cell retraction.

II.2.3 Periodicity in amoeboid migration

An interesting feature of *Entamoeba histolytica* migration is the apparent periodicity of protrusions (see Figures II.9 and II.11a). Previous experiments using micropipette aspiration pointed to a periodicity of 8 seconds between protrusion events [134], but such a measure could not be confirmed in a non-invasive setting. We therefore asked whether BioFlow could allow recovering such a periodicity based on the temporal profiles (Figure II.12. To do so, we analysed the Fourier spectrum of the range of the velocity curve (Figure II.12a) using a Tukey window to reduce spectral leakage of the Discrete Fourier Transform. Note that a similar analysis could be obtained with the pressure or force profiles, given that all curves are coherent).

In this example, the two biggest coefficients (in black) that form the experimental measure (in red) correspond to periods of $8.1s$ and $3.6s$ respectively. The blue curve represents the sum of these functions (added to the mean of the original signal) and reproduces the general patterns of the original signal. We then calculated the density distribution of the two periods by repeating this analysis for $n = 10$ cells (Figure

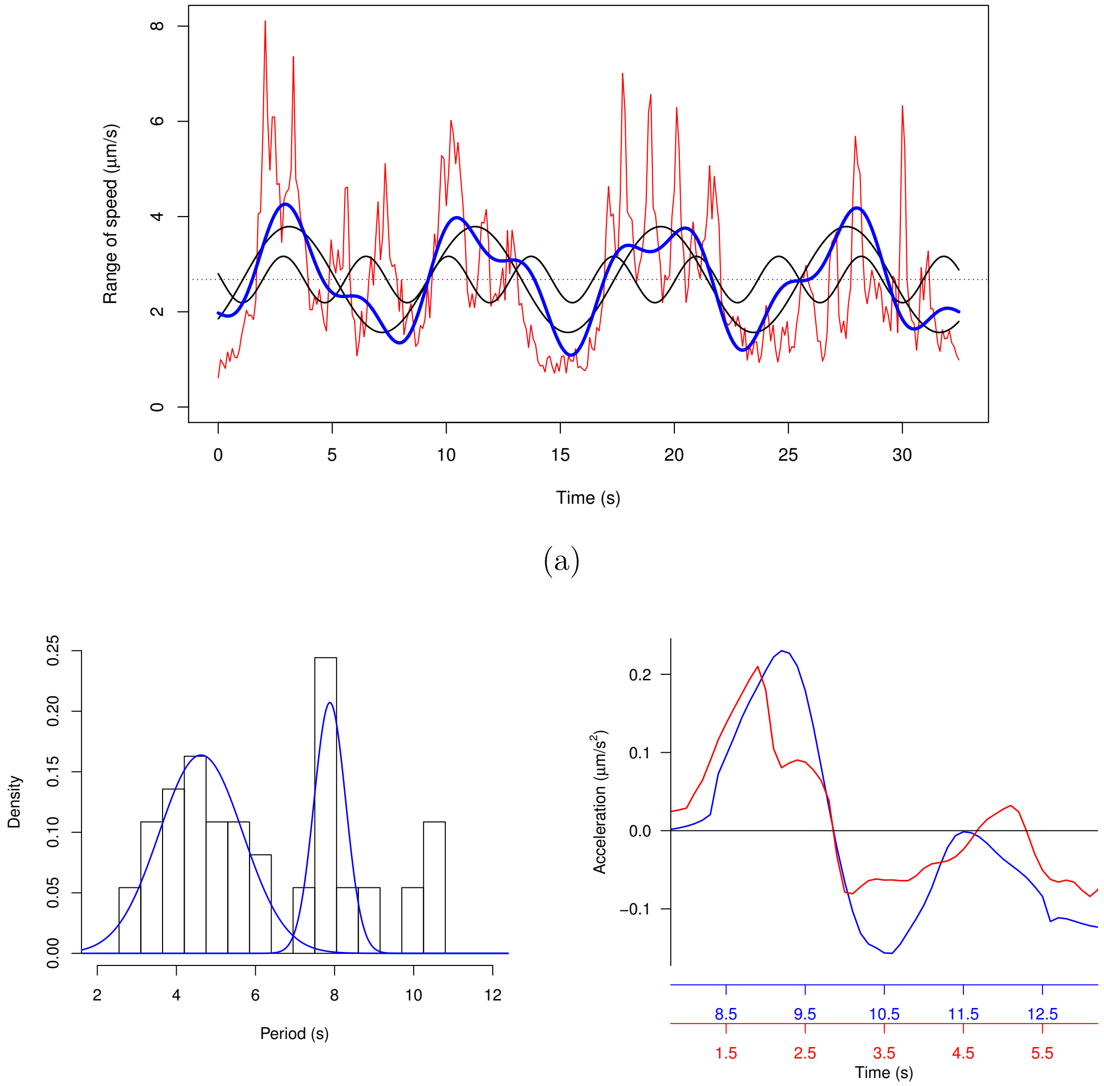

(a)

(b)

(c)

FIGURE II.12 – **Periodicity in amoeboid migration. a)** Velocity range extracted from a single cell over time (red line), and its partial Fourier decomposition (blue line), formed of the average speed (dashed line) and the two most relevant frequency components (black lines). **b)** Histogram of the associated periods extracted from 10 cells, and the associated sum of Gaussians fit (blue curves) obtained by nonlinear least-squares fitting. **c)** Time-aligned acceleration profiles along the direction of protrusion for two blebs of a same cell. Taken from [160].

II.12b), and obtained two distinct periods of $4.6 \pm 1.1s$ (mean±s.d.) and $7.9 \pm 0.4s$ (Non-linear least-squares fitting residual error : 0.03). Although it is only visually perceptible in few of the analysed videos, the longest time period matches the periodicity obtained using invasive techniques and thus demonstrates the robustness of the method.

Most interestingly, the shorter period of $4.6s$, which is not visually perceptible, describes a more subtle process underlying amoeboid migration. To highlight this period, we first calculated the average velocity over time across the bleb (i.e. along the line joining the two surrounding vortices, see Figure II.10b-short white line) and then calculated the corresponding acceleration (i.e. the difference in average velocity between frames). We repeated this analysis on two different protrusion events and superimposed the curves in Figure II.12c. It can be seen that the intracellular material first accelerates as the pressure gradient establishes, then decelerates as this gradient fades. This cycle takes 3 to 5 seconds, which is precisely captured by the periodicity analysis, and seems to describe the characteristic time of the cytoplasmic streaming. Together with the higher variance measured for the shorter period, this might indicate a dependence on protrusion size, which would take longer to fill with cytoplasmic material because the streaming velocity is roughly homogeneous across cells. In turn, this time scale might be reflective of the characteristic time of actin polymerisation.

II.2.4 Importance of actin dynamics on intracellular flow

We also challenged the experimental model by adding $100nM$ of Latranculin B in the medium to halt actin polymerisation, and measured the biophysical quantities immediately after the addition of the molecule. The behavior displayed in Figure II.13 is representative of the addition of the drug and contrasts with the demeanor of the wild-type cells. Shortly after addition of Latranculin B, the cell exhibits a final protrusion that is remarkably slower than in the control condition (2.5 $\mu m/s$ as opposed to 9.2 $\mu m/s$ in the control case), and progressively changes from the natural protrusive phenotype to a rounder and immobile configuration (Figure II.13a). This translates quantitatively into a stable decrease in the intracellular pressure gradient, as well as a stabilisation of the velocity and force fields (Figure II.13b).

II.2.5 Insight into amoeboid motility

A hallmark of amoeboid motility is the emission of protrusions at the cell surface, largely believed to be induced (directly or indirectly) by pressure-induced actomyosin contractility. Once a bleb is initiated, the membrane locally delaminates from the cortex and fills with cytosol. In some cases, the bleb retracts without generating movement, while in other cases the actomyosin cortex locally disrupts (either via depolymerisation or breakage), causing an influx of intracellular material into the protrusion, eventually leading to pseudopodia and initiating whole cell movement. While *Entamoeba histolytica* exhibits both types of blebs, the Cytochalasin-D labelling used in this work only captures the latter, as it highlights the intracellular actin bulk and

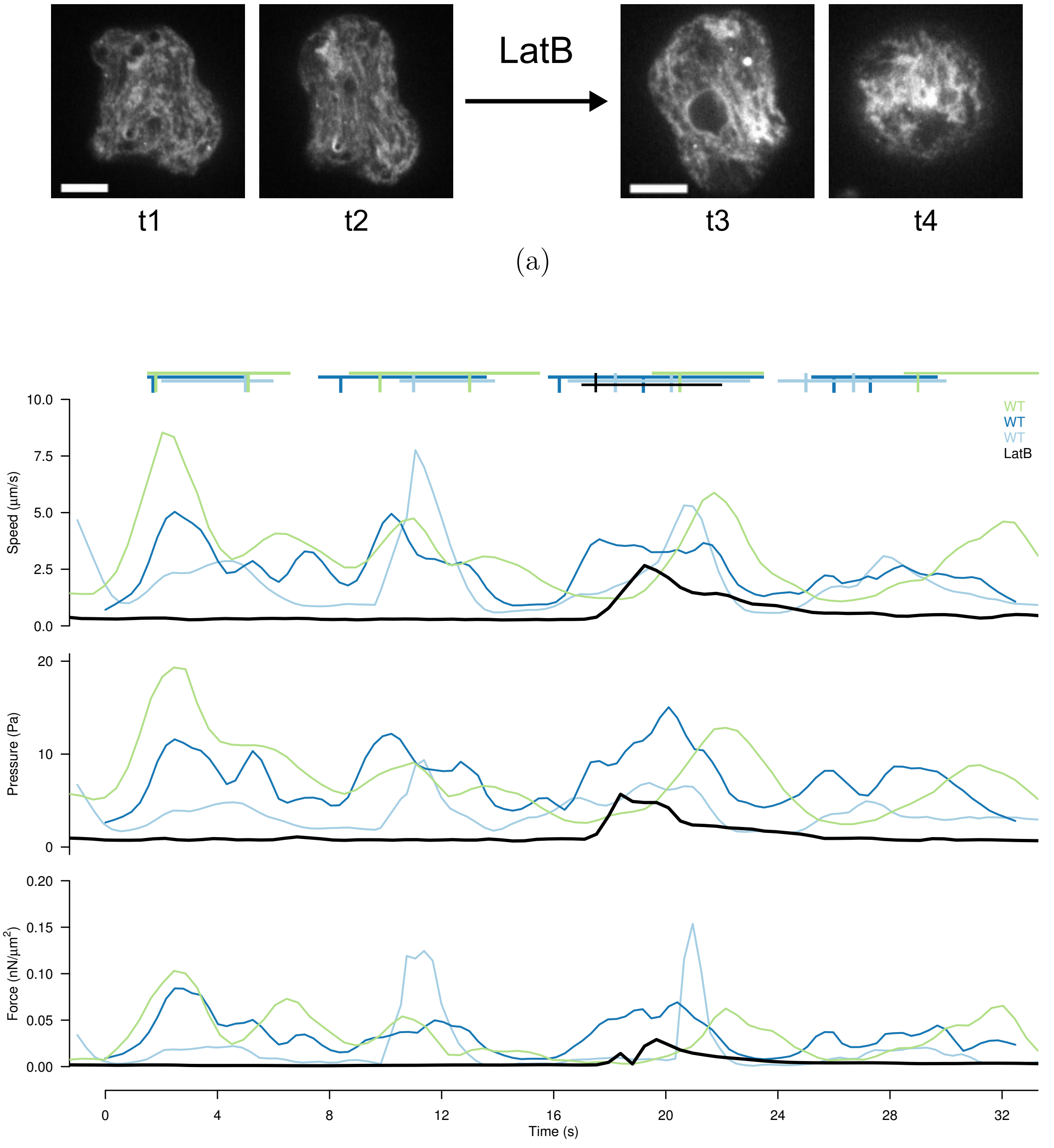

(a)

(b)

FIGURE II.13 – **Effect of Latranculin B on cell protrusion. a)** Two consecutive frames of a 2D time-lapse microscopy sequence before (left, t1 and t2) and after (right, t3 and t4) addition of Latranculin B. **b)** Estimated range (difference between maximum and minimum across the cell) of the intracellular velocity, pressure and force magnitude for the treated cell (LatB, black line) and 3 non-treated cells (WT, coloured lines). Protrusion events are marked by segments of the corresponding colour above the graph. Taken from [160].

not the outer cell membrane. If we consider the pressure drop Δp across the cortex (of thickness $h \sim 1\mu m$ [115]) necessary to drive the percolation of cytosolic fluid (of viscosity close to water, i.e. $\nu \sim 10^{-3} Pa\ s$) through the pores of the actin mesh (of characteristic size $l \sim 0.01 - 0.1\mu m$ [232]), dimensional analysis leads to a value of $\Delta p \propto u\nu h/l^2 \sim 1 - 10 Pa$. The same relation can also be reached by rearranging Darcy's law ($u/A \propto \nabla p/\nu$), governing the flow of slow fluids through porous media. Once the actin cortex disrupts, this same pressure gradient then drives the cytoplasm (with a viscosity of $\mu \sim 1 Pa\ s$ [136]) inside the bleb. Remarkably, the estimated spatiotemporal profile of the intracellular pressure during protrusion (Figure II.10) estimated by BioFlow is in good agreement with this picture both qualitatively and quantitatively, further supporting the reported role of myosin : 1) increase in intracellular pressure caused by contraction of the actomyosin cortex ; 2) sigmoid-shaped pressure curves during cytoplasmic streaming into the bleb (analogous to a contracting heart, also powered by myosin), with pressure values matching Darcy's law estimation ; 3) retraction of the cell rear after stabilisation of pressure and accompanied by an increased force. Interestingly, the sudden rise in pressure gradient at the onset of protrusion suggests breakage of the actin cortex in *Entamoeba histolytica* rather than depolymerisation. Finally, an analysis of multiple protrusion events revealed that different pressure gradients are able to generate blebs without disturbing periodicity (Figure II.12), suggesting that pressure alone might not suffice to regulate bleb initiation. This was confirmed by recent evidence that bleb formation and regulation involves additional mechanisms such as Rho-GTPase activity (e.g. Rho1 [233, 234] or Rac1 [235]) or localised contraction [236]. Verifying these hypotheses would however require the ability to measure myosin forces everywhere inside the cell, which remains a technical challenge.

The velocity field extracted by BioFlow corroborates existing reports of cytoplasmic streaming in other amoeboid cells (Figure II.3b). However, our high-resolution measurements, in conjunction with the other estimated quantities, provide further speculative insight into the underlying mechanisms. Indeed, our temporal analysis (Figure II.11) indicates that the pressure gradient precedes the velocity increase of the intracellular material, suggesting a cause-consequence relationship. As the pressure stabilises and the protrusion is filled, the initial acceleration vanishes (Figure II.12c). Interestingly, the intracellular material flows towards the protrusion in a rotating fashion, as shown by the two vortices on each side of the bleb (Figure II.10b), while the Poiseuille nature of the observed flow (Figure II.10e) implies a no-slip boundary condition. This evidence further supports a localised breakage of the cortex, while the remainder of the cortex holds in place. It is also worth pointing out that the cytoplasmic streaming is noticeably smooth (the intracellular material, including diverse vesicles and organelles such as the nucleus, seems to be dragged uniformly), although this was not imposed by the theoretical model. This behaviour might reflect the lack of microtubules in *Entamoeba histolytica* as opposed to other cell types such as *Physarum* amoebae, where the streaming appears more irregular [133].

Using BioFlow we have been able to provide for the first time (to our knowledge) a detailed map of intracellular forces. Regions of high force magnitude were found to generally appear in one of two cases : a) when the cell reorients, causing rotational movements (similarly to a Taylor-Couette flow [237]) that might stem from forces exerted by the cell on the substrate (Figure II.3c) ; b) more frequently, during protrusion events, yet with a slight delay after stabilisation of the pressure gradient and velocity field (Figures II.10a and II.11). This suggests that forces are highest during the retraction phase (i.e. when the bleb is practically filled and the flow stabilises) and might be a consequence of the actomyosin contractility at the cell rear. This hypothesis is further supported by the acceleration profile of the protrusion (Figure II.12c), where the first acceleration-deceleration cycle (linked to the pressure drop and stabilisation discussed above) is followed by a second more subtle acceleration phase concomitant with the force increase.

The robustness of the method is illustrated by the overall coherence of the quantities extracted from multiple cells, and successfully challenged by measuring the dramatic impact of Latranculin B (a known actin inhibitor) on the intracellular measurements (Figure II.13). This has led us to highlight a characteristic period of $7.9s$ between two consecutive protrusions of *Entamoeba histolytica* trophozoites with low variance (Figure II.12), which is in line with previous reports using micropipette aspiration in a confined environment [134], although it had never been measured in free moving cells. Furthermore, we were able to isolate a (second) novel characteristic period of $4.6s$, although with a higher variance. Interestingly, we found that this duration matches that of the acceleration-deceleration cycle observed during protrusion (Figure II.12c). Since this cycle characterises the cytoplasmic streaming towards the bleb, we speculate that this period could describe the characteristic time of actin cortex re-polymerisation at the edge of the protrusion.

Taken together, our results were found in excellent agreement with the currently accepted model of bleb-based amoeboid motility, and illustrate how our approach can be used to either validate or provide novel quantitative insight into the underlying mechanisms.

II.3 Study of vector fields

This section of the work was developed in collaboration with Mohammad Goudarzi[19]**, and supervised by Erez Raz, both at Universität Münster. This work is published in [238].**

The intracellular vector fields resulting from Section II.1 offer unprecedented detail in resolving cytoplasmic streams. We introduce several methods to visualise the flow, notably streamlines and pathlines ; and outline how to estimate 3D volume from Active-Contour segmentations. The resulting streamlines and volume measurements were used to analyse bleb formation in *in-vivo* amoeboid-like-moving cells at cutting-edge spatiotemporal resolution. The results of the study disagree with some of the latest literature (done at a similar scale) that affirms that a water influx from the outside media is necessary for bleb formation. In the same experimental context, our study shows that blebs result mainly from a redistribution of intracellular material, and that volume changes are negligible at this scale. This work thus questions the grounds that sustain part of the currently-accepted paradigm of bleb formation and, at the very least, calls for more experiments. This complements the analysis on amoeboid motility done in Section II.1.

II.3.1 Streamlines, pathlines and timelines

Let us first extend the velocity and cell domain fields to a continuous setting to homogenise the notation with upcoming Section II.4. Since the time-dependent data are originally discrete, we index the available measurements at times t_i by $i \in \{0, \dots, N_\mathrm{T}\}$. In the present case, the N_T points are evenly-spaced and thus the mapping is $t_i = t_0 + ih$ with $h = (t_f - t_0)/N_\mathrm{T}$. Conversely, the spatial dependency is already continuous by virtue of the finite element functions, which are piece-wise polynomia.

Cell. We notate $K(t)$ the moving cell at time $t \in \mathrm{T} := [t_0, t_f]$, where $K(t_i) = K_i$ results from the segmentation of the cell at each time frame.

Velocity field. We extend the velocity field $\mathbf{u_i}(\mathbf{x})$ defined at time t_i inside the cell domain ($\forall \mathbf{x} \in K_i$) to all $t \in \mathrm{T}$ by linear interpolation :

$$\mathbf{u}(t, \mathbf{x}) = \alpha \mathbf{u}_{\lfloor \mathbf{t/h} \rfloor}(\mathbf{x}) + (1 - \alpha)\mathbf{u}_{\lceil \mathbf{t/h} \rceil}(\bar{\mathbf{x}}), \tag{II.26}$$

where $\alpha = t/h - \lfloor t/h \rfloor$ and $\bar{\mathbf{x}} = \arg\min_{\mathbf{y} \in K_{i+1}} \|\mathbf{y} - \mathbf{x}\|_2$.

---

[19] First author of the study.

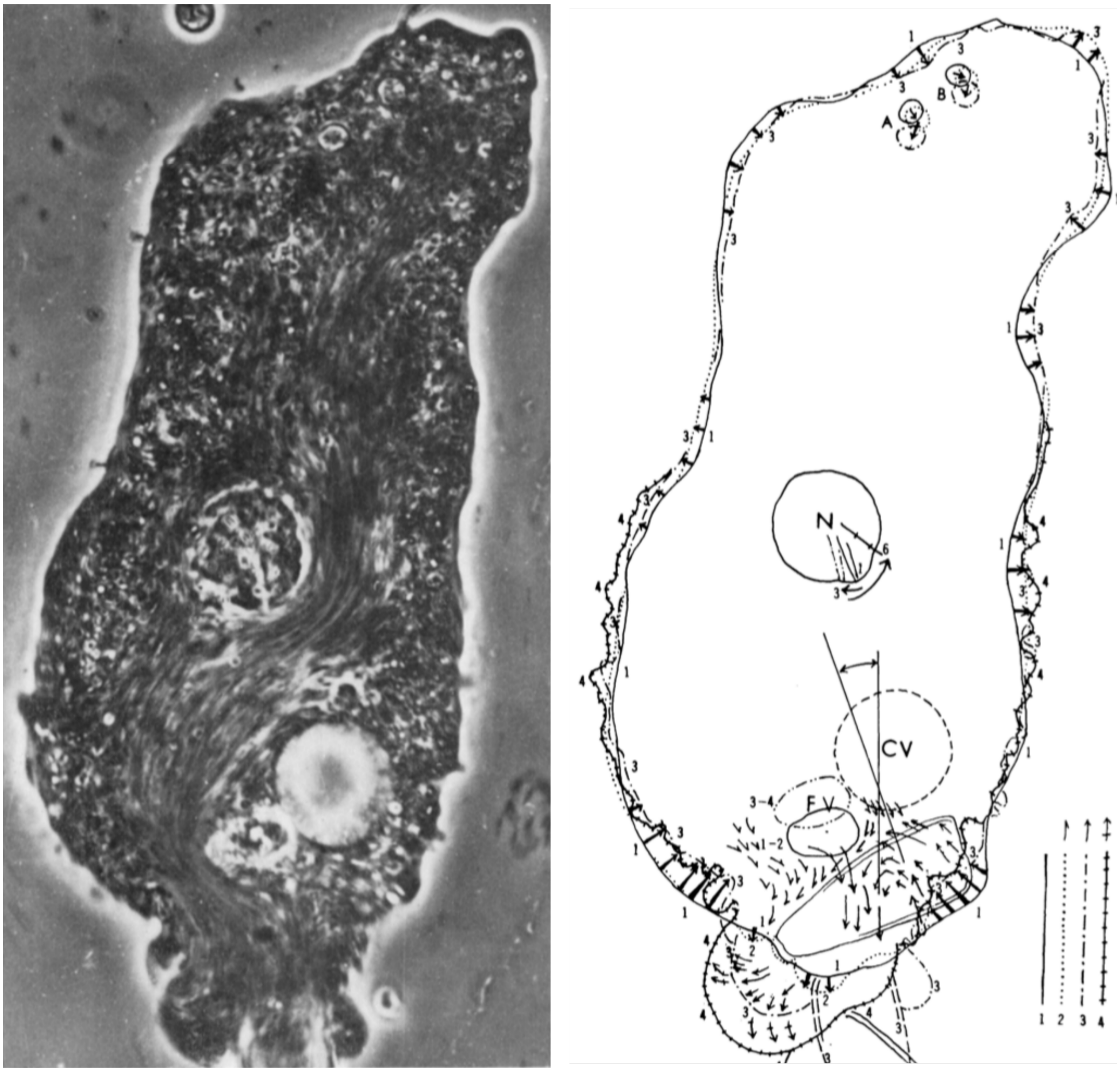

FIGURE II.14 – **Characterising cytoplasmic streaming has long been a relevant topic.** From *Proceedings of a Symposium on the Mechanism of Cytoplasmic Streaming, Cell Movement, and the Saltatory Motion of Subcellular Particles*. Held at Princeton University, April 2–5, 1963. Pages 228 and 230, Figures 3 and 5.

a) Streamlines. A **streamline** is defined as an s-parameterized curve $\mathbf{c_s}\colon S \subset \mathbb{R} \to K(t_i)$ that is tangent to the velocity at each spatial point at a fixed t_i. More formally :

$$\frac{d\mathbf{c_s}(s)}{ds} \times \mathbf{u}(\mathbf{c_s}) = 0, \tag{II.27}$$

where S is the biggest interval such that $\mathbf{c_s}(S) \subset K(t_i)$. As a consequence, streamlines constitute a good visual display of the speed and direction of the fluid flow. In particular, if the continuity equation holds, the speed flow is inversely proportional to the separation between contiguous streamlines, and no mass can cross the streamlines. At fixed time, given an initial point $\mathbf{c_s}(s = 0)$ (seed) we can construct a streamline by forward and backwards integration in space, for example using a Runge-Kutta (RK) scheme [239]. In practice, a collection of initial points is given (randomly or as an inital partitioned line) so that many streams are generated that span the entire cell domain K (see Figure II.15).

b) Pathlines. Conversely, **pathlines** are time-parameterized curves $\mathbf{c_t}\colon \mathrm{T} \to K(t)$ that follow the velocity at each time point

$$\begin{cases} \dot{\mathbf{c}}_\mathbf{t}(t) = \mathbf{u}(\mathbf{c_t}(t), t), \\ \mathbf{c_t}(t_0) = \mathbf{c_{t_0}}, \end{cases} \tag{II.28}$$

and thus constitute an ordinary differential equation (ODE) with initial condition $\mathbf{c_{t_0}} \in K(t_0)$, where $\dot{\bullet}$ notates the time derivative. RK is also a good choice. Notice how pathlines and streamlines are conceptually similar but on different dimensions. Therefore streamlines coincide with pathlines in steady flows. While Stokes flow is steady by definition, in our case both the domain and the boundary conditions change with time and both lines do not necessarily coincide (though perhaps between frames). While the pathline originates from a single point $\mathbf{c_{t_0}}$, a timeline is the equivalent temporal ODE integration of a line. In Section II.4 (see Figure, II.20 for example) we borrow this concept to advect sub-cellular regions instead of lines.

c) ODE integration. We have implemented RK4, i.e. of fourth order, with a local truncation error of order $\mathcal{O}(h^5)$ to integrate the ODEs discretely. Successive points $\mathbf{x_i}$ of a curve are computed as :

$$\mathbf{x_{i+1}} = \mathbf{x_i} + \frac{\mathbf{k_1} + 2\mathbf{k_2} + 2\mathbf{k_3} + \mathbf{k_4}}{6}, \tag{II.29}$$

where $\mathbf{k_1} = h\mathbf{u}(t_i, \mathbf{x_i})$, $\mathbf{k_2} = h\mathbf{u}(t_i + h/2, \mathbf{x_i} + \mathbf{k_1}/2)$, $\mathbf{k_3} = h\mathbf{u}(t_i + h/2, \mathbf{x_i} + \mathbf{k_2}/2)$, $\mathbf{k_4} = h\mathbf{u}(t_i + h, \mathbf{x_i} + \mathbf{k_3})$; h is the step (spatial or temporal) and $\mathbf{x_i}$ is the discrete solution corresponding to either $\mathbf{c_s}(t_i)$ or $\mathbf{c_t}(t_i)$. The integration was tested to be exact when using cubic functions.

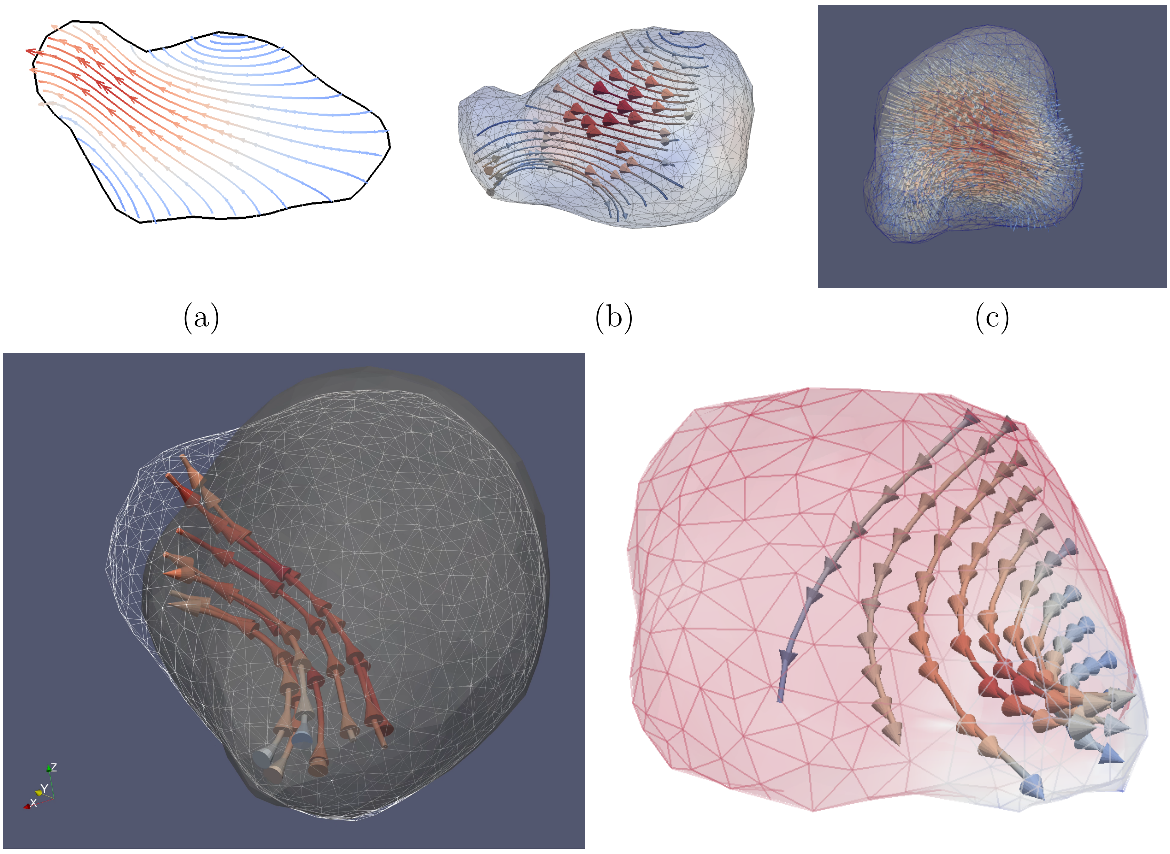

(a) (b) (c)

(d) (e)

FIGURE II.15 – **Streamlines in 2D and 3D show redistribution of material into a cell protrusion. a)** 2D streamlines in a PGC. **b)** 3D streamlines in a PGC extracted from (c). **c)** Dense vector field used to generate the streamlines in b). **d)** 3D streamlines in *E. histolytica*, solid cell volume shows the initial time point whereas white cell mesh indicates the following time point (see also Figure G.3). **e)** 3D streamlines in *E. histolytica* same frames as Figure II.3 ; notice how a good integration yields more consistent streamlines. Pressure is used to color the mesh (higher in red at the back, lower in white at the front). **all)** Arrows from the corresponding vectors are superimposed on streamlines and color-coded. All displayed in ParaView.

II.3.2 Volume measurements

The vector field and streamline analysis of the cells was complemented with a volume-change study. The volume of the cell at each time frame $|K_i|$ can be computed directly from the corresponding segmentation obtained by a 3D version of active contours. The segmentation is represented as a 3D mesh and the volume can be computed using the shoelace formula, also known as Gauss' volume formula because it is based on the divergence theorem. Figure II.16 shows a comparison between the segmentation in Icy and in Imaris (a propietary bioimage analysis software).

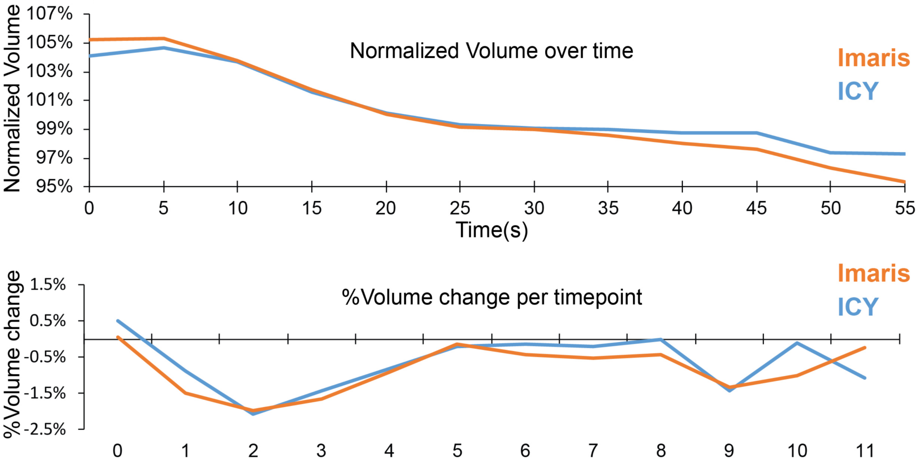

Figure II.16 – **Volume measurements.** Top plot shows $V_t/\bar{V}$, the constant decrease is due to bleaching. Bottom plot shows $\Delta V_t/V_t$. Icy and Imaris compared. Blebs occur around $5s$ ($\sim$ frame 1), $25s$ ($\sim$ frame 5), $45s$ ($\sim$ frame 9) and thus show no apparent correlation with volume increase. Modified from [238], by M. Goudarzi.

II.3.3 Application to the study of bleb formation in primordial germ cells

According to the latest literature [224], bleb formation in *in vivo* primordial zebrafish germ cells (PGCs) is correlated with an increase in cell volume. In this context, the relevant influx of water was announced to be regulated by aquaporins Aqp1 and Aqp3, a pair of isoform membrane proteins that act as adjustable water channels. More precisely, some studies highlight the strict need for such an inward flow to inflate the bleb, painting the process as a rather local event. These statements were also supported by *in silico* experiments conducted on a cell model considering the biomechanics of cortex-membrane deformations.

To investigate this matter, we analysed both cytoplasmic streaming and cell volume during bleb formation, as well as the role of the alleged aquaporins. Finally, we critically examined the computational model.

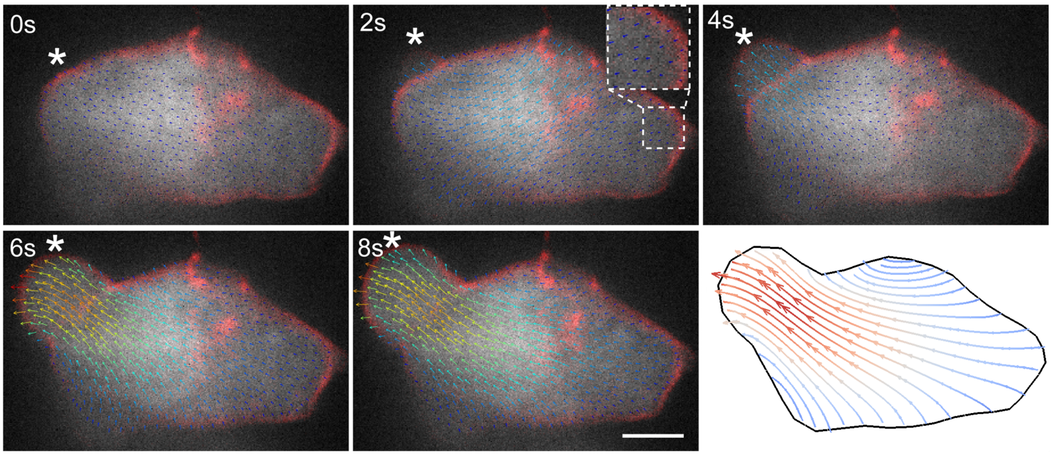

FIGURE II.17 – **Velocity field analysis of cytoplasmic streaming during bleb formation.** 5 snapshots show how the bleb is inflated by surrounding material. Inset zooms in on the rear of the cell, which retracts as the bleb expands. Streamlines corresponding to the last image. are also presented. High speed in red, low in blue, bleb marked with white asterisk. Modified from [238].

To study **intracellular flow**, PGCs were engineered to express green fluorescent protein (GFP) in the cytoplasm [240] ; and imaged inside the developing embryo with a spinning-disk confocal microscope at high spatiotemporal resolution. Since the expressed GFP is the source of image intensity, BioFlow acts as a flow tracker of the fluorophores. In particular, no model of the whole cell or of the membrane is imposed, and the boundary velocity of the GFP signal is directly derived from the data. In addition, the proposed assumptions are not divergence-free and thus are able to account for both out-of-plane flow and volume loss, which is critical in the study presented here. This is possible because divergence can also be inferred from the intensity data. Observing the fluorescence signal level yields velocity estimates of the underlying cytoplasmic flow up to the microscope's resolution, both in time and space. These data capture the progressive redistribution of the cytoplasm and thus allows conducting a non-invasive analysis of bleb formation. Indeed, as shown in Figures II.15a and II.17, cytoplasm flows within the cell as the bleb inflates. This is particularly well captured in the streamlines of the velocity field. More precisely, a flux of cytoplasm is directed straight into the forming bleb accompanied by a retraction of the cell rear. In addition, we did not observe any significant water influx at the leading edge of the cell, which would have mixed or stirred the cytoplasmic GFP (the membrane is impermeable to GFP).

To increase the precision of **volume measurements** PGCs were membrane-labelled with m-Cherry [241] and cytoplasm-labelled with GFP. Cells were imaged at high spatiotemporal resolution during bleb formation in the embryo. As shown in Figures II.16 and II.18, no significant temporal correlation between volume changes and bleb formation was observed after analysing 15 cells (60 seconds each). Overall, volume variations were small, and predominantly negative due to photo-bleaching. We attribute the conservation of cell volume to the retraction of other parts of the cell that compensate for the volume trans-located into the forming protrusion.

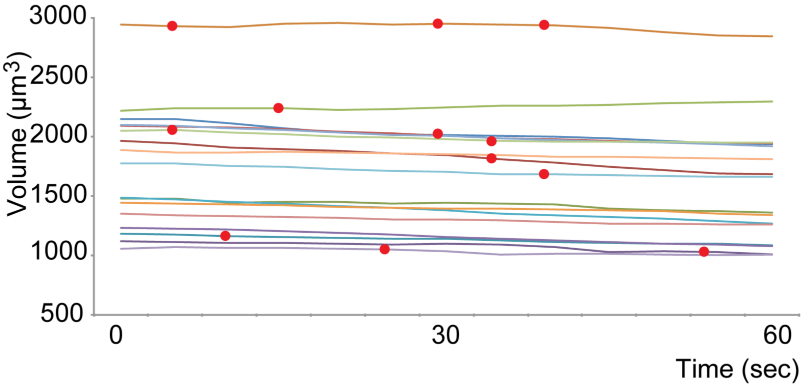

FIGURE II.18 – **Volume fluctuations during bleb formation.** Volume of 15 PGCs (morpholino control) over time, blebs are marked as red dots. No correlation between blebbing and volume change is observed. Taken from [238], by M. Goudarzi.

The role of the suspect **aquaporins** was first examined by investigating the expression in the cells of the mRNAs encoding for Aqp1 and Aqp3 using deep mRNA sequencing at the time of active PGC migration [242]. We found that aqp1a mRNA was not expressed in PGCs, whereas aqp3a mRNA was expressed only at very low levels. In addition, controlled morpholino knock-down of the aquaporins using the same species as in [224] had no visible effect on bleb formation and did not prevent PGCs from reaching the developing gonad, in spite of the negative effects of the experiment on the embryo. Together, these results show that Aq1 and 3 do not play a fundamental role in PGC migration at the time of interest. This is also in contrast with [224], where morpholino injection was not controlled.

Finally, we analysed the **model** presented in [224], while well formulated and solved with the appropriate techniques, we found that it is inherently biased to disable the main mechanisms of bleb formation. First and foremost, there are membrane invaginations in PCGs [243] that are not present in the model, this means that increasing membrane surface is incredibly expensive in those simulations because, instead of unfolding new surface, one has to fight against the increasing elastic energy. Put differently, the model does not assume volume conservation but it does impose a fix number of nodes in the cortex and the membrane. Second, bleb nucleation occurs (in the model) because an initial perturbation grows as a result of weakened bonds (that stem from the random stiffness distribution). In reality there are myosin motors, which exert active and continued contractions that are not entirely random. Third, the cortex is also permeable and likely more so than the plasma membrane. We think the first two reasons might explain why the time-scale of the simulated bleb is off by an order of magnitude and the blebs are not protuberant.

In summary, our analysis suggests that bleb formation results primarily from a redistribution of intracellular material.

II.4 Tracking of intracellular diffuse domains

This section of the work was developed in collaboration with Cecilia Grimaldi, and supervised by Erez Raz, both at Universität Münster. The first part of this work is published in [244], the second is under submission.

Active molecular transport ensures a purposeful spatiotemporal distribution of cellular proteins and is therefore key to a wide range of processes such as morphogenesis, homeostasis or migration. However, redistributions of intracellular molecules in bulk are seldom quantified because the regions involved are too diffuse to be segmented consistently. In this section, we use the dense velocity fields estimated in Section II.1 to advect a triangulated mesh over time using any ODE integration scheme and a Laplacian-based error correction. In this way, our framework can follow the movement and deformation of multiple parts of a diffuse region at once and offers a seamless combination with spatiotemporal line integration in Lagrangian coordinates. This allows the flexibility to taylor specific measures to the question at hand, e.g. mechanical work, bringing long-established physics concepts into biology grounds. We exemplify our approach by quantifying the effect of E-cadherin on the intracellular retrograde movement of the frontal actin rim during PGC migration. In particular, we show that E-cadherin regulates the directionality of the migration by stabilising the rim, which then recruits myosin and biases bleb formation. This further complements the analysis on amoeboid motility done in Sections II.1 and II.3.

A controlled redistribution of material within the cell is essential to biological function : molecules need timing and placing to fulfill their role in the context of whole-cell coordination. This spatiotemporal organisation is enforced by multiple chemical and physical processes. Diffusion can passively transport biomolecules along concentration gradients, but it is speed-limited and one-directional ; therefore, other complementary and more active mechanisms have had to take on at the expense of energy [105]. One such mechanism is cytoplasmic streaming, an advective flow that can relocate large regions of cytoplasm and is most typically driven by cortical actomyosin. Another is motor-driven conveyance along the cytoskeletal scaffold. The specificity and diversity of these solutions reflect the relevance of molecular transportation in a wide range of systems. Two examples are that (i) partitioning-defective proteins need to be at opposite poles of the zygot during morphogenesis in *Caenorhabditis elegans* [245], and (ii) directed translocations of the cytoplasm drive bleb-based migration [236, 238].

Despite its relevance, redistribution remains hard to study quantitatively. The standard approach in biology starts by video-imaging the fluorescently-labelled protein of interest and proceeds in either of two ways : maximum intensity projections, where time is projected onto a single image ; or intensity kymographs, which focus on the time evolution of a single spatial dimension [106]. While movement information can be extracted from these two visualizations, they are inherently biased because they disregard a dimension “arbitrarily”. The longstanding answer by the image analysis community has been tracking algorithms [246]. However, the region of interest of bulk-advected molecules is often too diffuse to be segmented consistently in practice (e.g. Fig. II.19). On some occasions, using speckle microscopy can bring the problem back to multiple-particle tracking [107]. On most other occasions, particle image velocimetry (PIV) is used to extract displacement fields, but these often span the whole image or, at best, are restricted to identifiable regions such as the cell border [107, 163].

II.4.1 Mesh advection and line integration

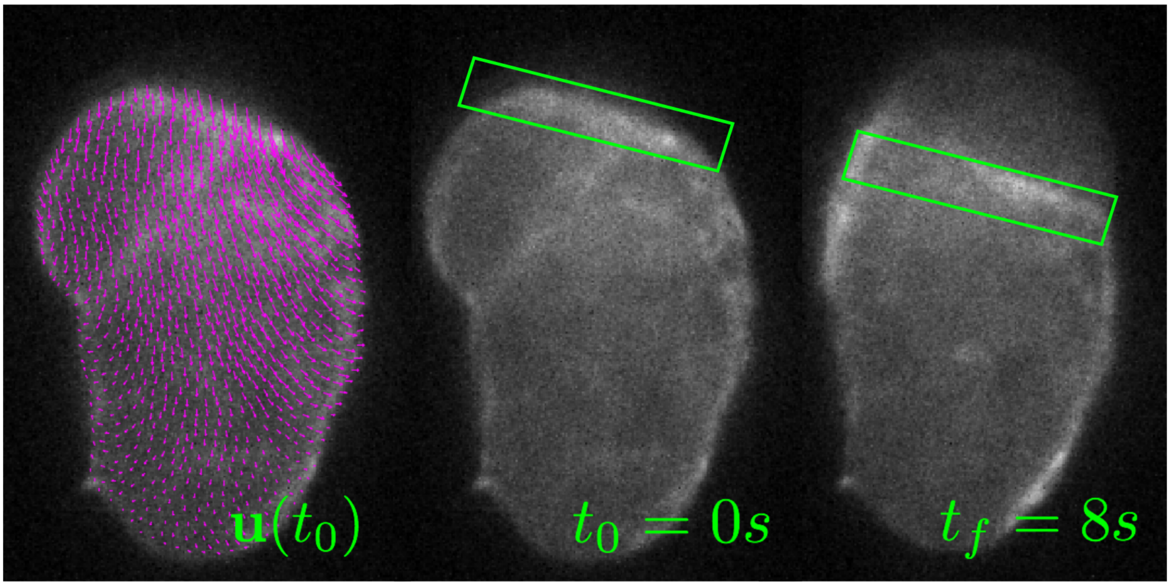

FIGURE II.19 – **Example of a diffuse molecular region.** The backwards-moving protein rim is approx. delineated by the green rectangle at $0s$ and $8s$. The velocity field at $0s$ is shown in magenta. Taken from [244].

a) Proposed approach In order to follow arbitrary diffuse regions during redistribution studies inside a moving cell $K(t)$, $t \in \mathrm{T}$, we propose a corrected advection of an initially delineated region $\Omega(t_0)$. The region is represented as a Finite Element mesh to facilitate the computation of integrals. The evolution of the subdomain $\Omega(t) \subset K(t)$ is driven by a velocity field $\mathbf{u}(t, \mathbf{x})$ that can be estimated via simulation or data assimilation, as presented in Section II.1. Advection is then the result of solving the ODE posed by the field

$$\begin{cases} \dot{\Omega} = \mathbf{u}(t, \Omega), \\ \Omega(t_0) = \Omega_0, \end{cases} \tag{II.30}$$

The advected region is repeatedly corrected by Laplace’s equation or a Kalman filter as segmentation data becomes available. These ideas are developed in Sec. II.4.1.1.

In addition to following diffuse regions, our approach offers further advantages. First, it is possible to partition the subdomain without loss : $\Omega = \bigcup_{j\in P} \Omega^j$ and $\mathring{\Omega}^j \cap \mathring{\Omega}^{j'} = \emptyset \ \ \forall \ \ j \neq j', \ \ j, j' \in P := \{1, \dots, N_P\}$. This allows to compare the behavior of multiple (N_P) zones within the diffuse region. Second and most important, this framework enriches quantification. Of particular interest is the possibility to calculate curve integrals from a Lagrangian perspective ; i.e. of forms similar to

$$I^j(\bullet) := \int_{\mathrm{T}} w^j(t) \int_{\Omega^j(t)} \bullet \ \ d\Omega^j \ dt, \tag{II.31}$$

where $w^j(t)$ is intended as a weighting function. These integrals bridge biological quantification with established concepts in physics. For example : they can compute the average of a given quantity within the region over space and time, determine the amount of material that is being advected, or calculate the energy spent on motored-transport using the force $\mathbf{f}$ (e.g. from Section II.1) and velocity fields : $I^j(\mathbf{f}\cdot\mathbf{u})$, $w^j = 1$. Moreover, the integrals are seamlessly integrated with the advection method because our underlying framework is based on a triangulation onto which finite elements are cast. We elaborate in Section II.4.1.2.

b) Example application An important concept in biological literature is the anisotropic (or polar) distribution of proteins within the cell. This directivity can be reduced or enhanced dynamically by molecular transport. For example, the protein rim in Fig. II.19 moves towards the "back", varying the cell's molecular distribution. To assess changes in directivity, we propose to estimate how much a given protein region is advected towards the back/front with respect to a reference unit axis $\mathbf{n}$. To this end, we define

$$I^j\left((\mathbf{u}(t,\mathbf{x}) - \mathbf{r}(t)) \cdot \mathbf{n}\right), \ c^j(t) = \frac{1}{|\Omega^j(t)|}, \tag{II.32}$$

where $\mathbf{r}(t)$ is a ref. velocity, e.g. the cell's center of mass ; and the dot product projects the movement onto the direction $\mathbf{n}$ of cell directivity or polarity. Notice that $c(t) \neq 1$ computes by how much (on average) a protein is being displaced (length). This is necessary to account for bias in size because the final aim is to compare the redistribution of diffuse regions between different physiological conditions and across multiple parts within a region. An experiment is shown in Section II.4.1.4 and the method is fully applied in Section II.4.2.

II.4.1.1 Advection of partitions

To follow the diffuse region through time we divide the subdomain into triangles and use (II.30) to advect them.

a) Triangulation The initial subdomain Ω_0 within the cell is selected and meshed by triangulating it into a set of elements $\mathcal{T}_0 = \{\triangle\}$ such that $\bigcup_{\mathcal{T}_0} \triangle = \Omega_0$ and any intersection between them is either a shared vertex or edge. The triangulation induces a subtriangulation $\mathcal{T}_0^i \subset \mathcal{T}_0$ of the partitions Ω_0^i[20]. To ease integration, each $\triangle$ is mapped to a common reference triangle $\hat{\triangle}$ by an affine transformation $\triangle = \mathcal{A}^{\triangle}(\hat{\triangle})$. $\hat{\triangle}$ is defined by its vertices at $(0,0)$, $(1,0)$ and $(0,1)$.

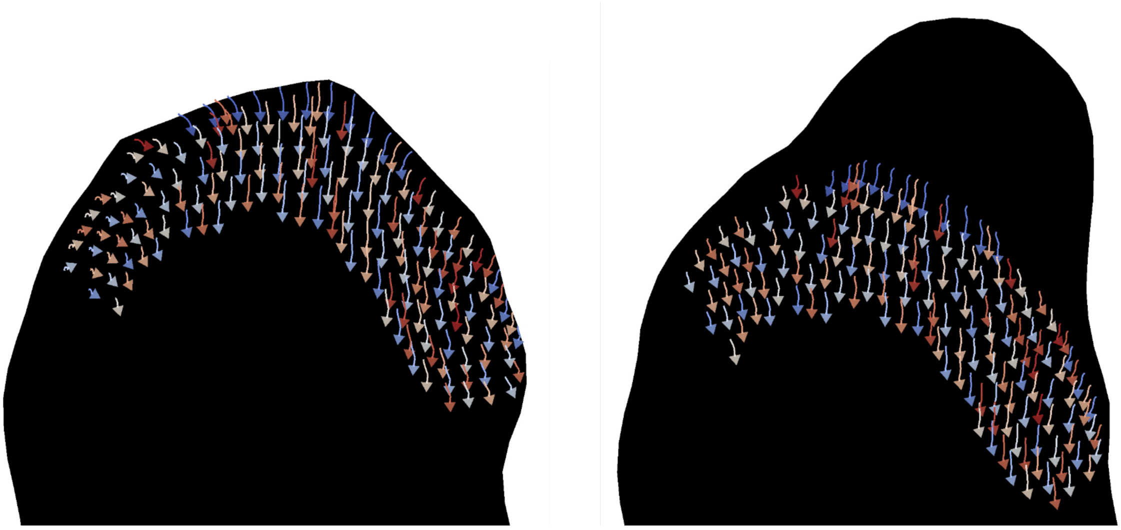

FIGURE II.20 – **Point-wise advection of each vertex in the meshed region.** Evolution of each vertex in the triangulated partition (different colors are only meant to identify each vertex).

b) Initial value problem The extended vector field (interpolated as described in (II.26)) drives the advection of the subdomain and its partitions via (II.30). To integrate the system we can use one of two options depending on the source of the velocity. RK4 is convenient in cases where $\mathbf{u}_i$ is the instantaneous velocity at point t_i, e.g. for fields resulting from simulations or continuous assimilation. Conversely, in Section II.1 the velocity is already computed as an optimal map between consecutive time points and therefore can be readily used to map the vertices of the subdomain, this integration can also be thought of as Euler's time-stepping method (RK1). Whichever the method, the result defines an operator $\mathcal{R}_i$ that advects the subdomain, each triangle or each point through time (see Figure II.20). For example, we would have $\mathbf{x_{i+1}} = \mathcal{R}_{i+1}(\mathbf{x_i})$ in (II.29). Precisely, the advected region in the next time point is $\Omega_{i+1} = \mathcal{R}_{i+1}(\Omega_i) \cap K_{i+1}$, and can be considered on each partition (or simplex) independently : $\Omega_{i+1} = \bigcup \Omega_{i+1}^j = \bigcup(\mathcal{R}_{i+1}(\Omega_i^j) \cap K_{i+1}) = \bigcup(\mathcal{R}_{i+1}(\Omega_i^j)) \cap K_{i+1} = \mathcal{R}_{i+1}(\bigcup \Omega_i^j) \cap K_{i+1}$. This defines an affine transformation $\mathcal{R}_i^{\triangle}$ from t_{i-1} to t_i on each triangle starting from $\mathcal{R}_0^{\triangle} := \mathcal{A}^{\triangle}$. We call $\mathcal{R}_{1|i}^{\triangle}$ the complete advection from the reference triangle through time until t_i, $\mathcal{R}_{1|i}^{\triangle} := \mathcal{R}_0^{\triangle} \circ \cdots \circ \mathcal{R}_i^{\triangle}$, and note that it is affine because it is a composition of affinities (Fig. II.21a). We are most interested in the linear map $R_i^{\triangle}$ within each affinity and hence the composition is a multiplication of matrices. In fact, we are only

---

[20] **NOTATION :** subindexes denote discrete time points, whereas superindexes refer to partitions.

concerned with determinants, $\det R^{\triangle}_{|k} = \prod_{i=0}^{k} \det R^{\triangle}_{i}$, because they keep track of the variable and area changes when calculating the line integrals. Notice that, instead of recording the cumulative advection, we could map all triangles directly to the reference. However, this provides no computational advantage at the cost of flexibility.

c) Leveraging segmentations In order to correct the approximation errors that might be introduced by advecting the subdomain, we incorporate segmentation data. When a segmentation of the subdomain is available at time t_i, it is used to replace Ω_i. However, the partitions Ω_i^j cannot be reproduced. Therefore, we adjust the partitions to the new subdomain by using Laplace's equation

$$\nabla^2 \mathbf{v} = 0, \quad \mathbf{v}({\mathbf{x_i}}^{\text{old}})|\partial\Omega_i^{\text{old}} = {\mathbf{x_i}}^{\text{new}} - {\mathbf{x_i}}^{\text{old}}. \tag{II.33}$$

By setting the boundary condition of the PDE to be the difference between a vertex ${\mathbf{x_i}}^{\text{old}}$ on the old border $\partial\Omega_i^{\text{old}}$ and its corresponding point ${\mathbf{x_i}}^{\text{new}}$ on the new border $\partial\Omega_i^{\text{new}}$, we bring the old partitions into the new subdomain smoothly. The correspondance between boundaries (bigraph) is established by the optimal mapping that minimises the sum of pairwise euclidean distances. This minimum-weight perfect matching problem is solved by the Hungarian method. The displacement solution $\mathbf{v}$ of (II.33) is then used to advect the triangles and is incorporated as an affinity composed with $\mathcal{R}_i^{\triangle}$ (Fig. II.21b). Alternatively, if only a rough approximation (e.g. HK-means) is available but its accuracy can be estimated, the problem is addressed similarly via a Kalman Filter. In this case, the combined transformation is also included as an affinity.

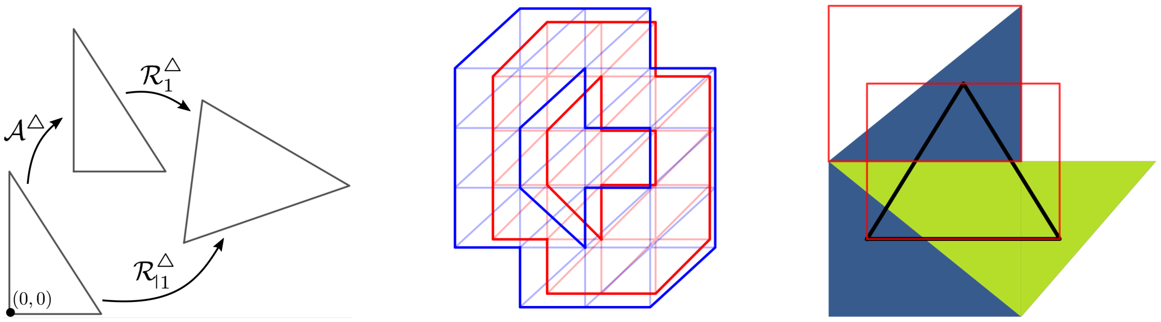

(a) (b) (c)

Figure II.21 – **Schematics of the discrete geometry. a)** Diagram of the Runge-Kutta advection on triangles. **b)** The red mesh and its two subdomains are brought to the new blue border by solving Laplace's equation. **c)** Triangles from two different domains (blue, green) of the old mesh are intersected with a triangle of the new mesh (bold black). Bounding boxes of two triangles are in red. Taken from [244].

II.4.1.2 Integration over advected partitions

To integrate a given quantity $\mathbf{f}$ on the moving subdomain, we cast finite elements on the triangle mesh and handle the integrals with the Finite Element Method [185].

This has two further advantages : (i) the velocity field estimated in Section II.1 is expressed in a finite element basis ; and (ii) it is convenient when solving (II.33) in its weak form. The function $\mathbf{f_i}$ at time t_i is originally obtained in a basis defined on the whole cell K_i, but can be projected onto finite elements defined on $\mathcal{T}_i$. Here we use Lagrange elements of second degree : we choose $\phi_{i,j}(\mathbf{x})$ piecewise polynomials such that $\phi_{i,j}(\mathbf{p_{i,k}}) = \delta_{j,k}$, where the nodes $\mathbf{p_{i,k}}$ are all the vertices and midpoints in $\mathcal{T}_i$. Since the values of a $\mathbb{P}_2$ function on a triangle edge are determined by the values on its three nodes, this family is a basis of $\{\phi \in \mathcal{C}\left(\bar{\Omega}_i\right) \mid \phi_{|\triangle} \in \mathbb{P}_2,\ \forall \triangle \in \mathcal{T}_i\}$ and we can write $\mathbf{f_i} = \sum_j \mathbf{f_{i,j}} \phi_{i,j}$ with coefficients $\mathbf{f_{i,j}} = \mathbf{f_i}(\mathbf{p_{i,j}})$. We then choose another set of polynomials $N_{i,j}^{\triangle}$ that coincide with $\phi_{i,j}$ only on a triangle $\triangle$ but are easier to integrate because they are non-piecewise. These functions depend on the nodes $p(\triangle)$ of their associated triangle, so it is easier to change variables and calculate the integrals on the reference triangle : $\hat{N}_{i,j} := N_{i,j}^{\triangle} \circ \mathcal{R}_{|i}^{\triangle}$.

a) Numerical integration The time integral (II.31) is evaluated using the composite trapezoidal rule,

$$I^k(\mathbf{f}) \approx h \left(\frac{F_0^k + F_{N_\mathrm{T}}^k}{2} + \sum_{i=1}^{N_\mathrm{T}-1} F_i^k \right), \tag{II.34}$$

and the advected partition integral $F_i^k := \int_{\Omega_i^k} \mathbf{f_i}$ is reduced to

$$F_i^k = \sum_{\triangle \in \mathcal{T}_i^k} \int_{\triangle} \sum_{j \in p(\triangle)} \mathbf{f_{i,j}} N_{i,j}^{\triangle} = \sum_{\triangle \in \mathcal{T}_i^k} \frac{|\det R_{|i}^{\triangle}|}{C} \mathbf{f_i}^{\triangle}, \tag{II.35}$$

where $\mathbf{f_i}^{\triangle} := \sum_{j \in p(\triangle)} \mathbf{f_{i,j}}$ and $C^{-1} = \int_{\hat{\triangle}} \hat{N}_{i,j} = 1/6$. The alternative midpoint quadrature rule would also be adequate in this degree-2 Lagrange example, but we do not use it because higher order rules are neither straightforward to implement nor general (e.g. other elements). Moreover, the N functions are anyway needed to solve Laplace's equation.

II.4.1.3 Implementation details

a) Triangulation The initial meshing of the subdomain is constructed from a given contour at t_0. The planar straight-line graph defined by the polygonal contour serves as the basis of a constrained Delaunay triangulation that is progressively refined by adding points and ends with Lloyd's relaxation algorithm. This is implemented using Mshr and its CGAL [210] SWIG. As the mesh is advected, it degenerates and gradually loses its Delaunay properties, which locally decreases the quality of the interpolation. To mitigate this effect, we run a quality check at each time step by assessing the ratio of every cell's inradius to circumradius [200].

b) Projection of partitions If the mesh is deemed inadequate we prescribe two alternatives depending on the degree of degeneration : smoothing by local averaging [247] or entirely remeshing from the current border. Regardless of the case, the partitions, which are sets of triangles $\mathcal{T}_i^j$, have to be projected on the new triangulation that does not necessarily match (rightmost Fig. II.22). In order to assign a partition to a new-mesh triangle, we compare its intersection area among all the old-mesh triangles it collides with and choose the partition that is most represented. The areas are calculated using the shoelace formula on the polygon resulting from the Sutherland-Hodgman algorithm [248], which is used here to clip pairs of triangles (Fig. II.21c). To avoid comparing non-colliding triangles, we use an axis-aligned bounding-box tree (AABB). The collision detection (Fig. II.21c) is further used to find and remove triangles (without remeshing) that venture out of the cell domain (remember $\Omega_{i+1} = \mathcal{R}(\Omega_i) \cap K_{i+1}$).

c) Advection and integration The implementation is largely based on the Fenics platform [184], which is used to manage the subdomains and the projection on finite elements, as well as to solve Laplace's equation in its weak form. Two python libraries, NumPy [208] and SciPy [209], are used to implement interpolation, solve the initial value problem and keep track of the affinity matrices. They also serve the integration together with a re-purpose of the assembly function within the Fenics framework [249].

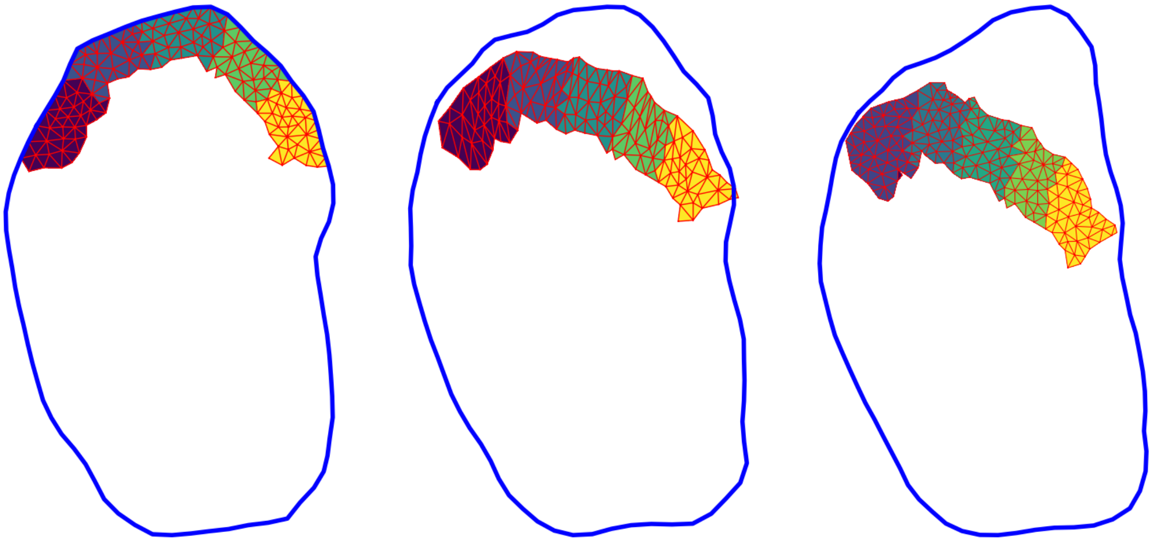

Figure II.22 – **Mesh advection and remeshing of a region**. Evolution of each triangulated (red mesh) partition (different colors) as a cell (blue contour) moves. On the right-most image, the partitions have been remeshed because the quality decreased. Taken from [244].

II.4.1.4 Preliminary experiments

We first assessed the numerical implementations. To test the integration scheme (II.34, II.35), we proved that quadratic-in-space and linear-in-time polynomials were integrated "exactly" up to machine precision.

In order to evaluate the ability of measure (II.32) to quantify changes in protein directivity we established a comparison between wildtype cells and a mutant expressing the constitutively active version of RhoA, which is qualitatively known to show bigger variations in polarity [250]. Namely, we measured by how much the protein rim was pulled backwards with respect to the “long” axis $\mathbf{n}$ of the moving cell (see Figs. II.19 & II.22).

We used the method presented in Section II.1 to segment the cell and estimate the velocity field throughout the image sequence, obtaining K_i and $\mathbf{u_i}(\mathbf{x})$. Next, we defined $\mathbf{n}$ via an intensity-weighted PCA and used it to set the initial zone Ω_0 at the leading edge of the cell, defined by two parameters : width and solid angle. We divided Ω_0 into $N_P = 5$ wedges Ω_0^j evenly spaced according to the arc length (leftmost Fig. II.22). This is the minimum number of partitions that separates sides from center. The triangulated partitions were advected as described above (Fig. II.22). With this information, we calculated the spatiotemporal integral with (II.34, II.35). Since all steps are automatic (segmentation needs sparse supervision), the pipeline can be readily iterated over all the cells.

As expected qualitatively, the results (10 cells) show that the change in directivity is significantly (t-test p-value=0.005) higher [21] in the mutant ($1.80 \pm 0.2 \mu m$) than in the wildtype ($0.54 \pm 0.1 \mu m$). Furthermore, we see that the difference between the central partition and side partitions [22] is significantly increased (binomial p-value=0.0001), indicating that the central part of the rim is specially affected. For comparison, we checked the maximum velocity of the advected protein rim on both strains, a measure resembling that of a manual kymograph (the standard method in biology), and found the differences less significant (t-test p-value=0.03). While in the *kymographic* case the differences were still significant, this method did not reflect the change in the isotropy of the cell's molecular distribution, as opposed to our integral approach.

In summary, we provide a framework that tracks diffuse cellular regions that are not amenable to the classical segmentation+tracking scheme, and also computes arbitrary line integrals. This allows defining measures to precisely quantify biological questions that are otherwise addressed qualitatively in the community. We exemplified the approach by assessing the notion of intracellular protein redistribution and proved that (II.32) was able to quantify the movement of the protein rim and boost the significance of the study.

---

[21] The sign depends on the definition of the reference axis $\mathbf{n}$.

[22] See a newer example of the effect of E-cadherin (not RhoA) on the acin cortex in Figure II.24.

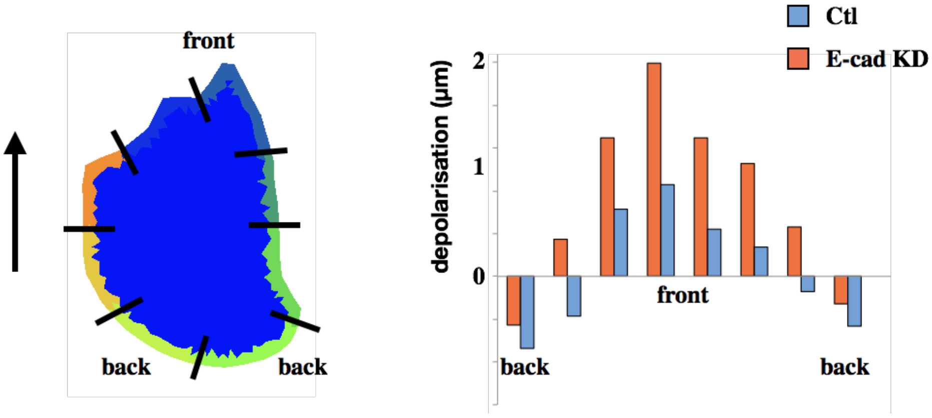

FIGURE II.23 – **Depolarisation of the actin cortex divided into eight regions**. The cell on the left-hand shows the eight divisions of the studied actin cortex. On the right hand side, we show the average ($n = 20$) depolarisation suffered by each region.

II.4.2 The role of E-cadherin during amoeboid motility in the zebrafish embryo

After fine-tuning the algorithm, we use it to study the role of E-cadherin in amoeboid motility. This will be explained thoroughly in Cecilia's thesis as the first author of the work. Therefore, the results presented here are only preliminary (albeit full results are available) and reflect only my naive interpretation of the data. In particular, we only describe the main findings for three reasons : they are important for the study of amoeboid motility conducted in this work, they partly motivate the next Chapter, and they are a good illustration of the framework presented so far in this section.

It is still debated whether cell adhesion is imperative for cell migration. While some studies have found that specific adhesions are not strictly necessary for single cell migration *in vitro*, it is not clear how these results translate into an *in vivo* setting. In this context, cells can not only interact with the ECM, but also with other cells. For example, newly specified zebrafish PGCs make their way to the gonads by navigating through the developing embryo with the help of a chemokine gradient [251, 252]. Similarly to *E. histolytica*, these cells rely on bleb-based amoeboid migration, which exploits myosin contraction to generate pressure driven protrusions. Perhaps more specific to PGCs is their polar form. During directed motion, Rac1 and RhoA are activated at the leading edge of the cell [250]. Rac1 is a regulator of the actin cytoskeleton and in this case acts by assembling an actin-rich structure (actin brush) at the front, whereas RhoA (used in Section II.4.1.4) has been shown to enhance actomyosin contractility and here induces a mild retrograde flow of the actin brush (Figure II.23).

Another protein involved in the migration of PGCs is E-cadherin, a cell adhesion molecule that forms cell-cell junctions. This protein is expressed during early embriogenesis, but its presence on the membrane is slightly reduced shortly before migration starts, presumably to loosen adhesion and initiate movement. In fact, E-cadherin has been regarded as necessary for the displacement of PGCs [250]. However, Cecilia et al. realised that interfering with the protein does not affect a cell's propulsion nor migration speed per se, but instead reduces its ability to reach long-range targets. Indeed, a rigorous quantification of multiple cell tracks showed (Figure not shown) that under E-cadherin knock-down (KD) PGCs continued to migrate through the embryo at the same instantaneous speed, but lost their directionality as evidenced by a decrease in the computed persistance. Since retrograde actin flow plays a role in cell polarisation, the team asked whether E-cadherin might influence directionality by regulating the dynamics of the actin brushes.

In this study, we showed that E-cadherin stabilises the actin brushes at the leading edge by reducing the frontal flow of actin towards the cell rear (Figure II.23) ; stable brushes recruit more myosin, enhancing contractility and biasing bleb formation towards the front. Accordingly, when E-cadherin is knocked down, the speed, depolarisation and overall movement of the actin brush increases with respect to the direction of cell polarisation (see Figure II.24). The quantification was done using the protocol described in II.4.1.4 ; that is segment and track the cell, define a region at the leading edge, advect it around the cell over time, and compute the integrals using $c^j(t) = \frac{1}{|\mathrm{T}||\Omega^j(t)|}$ or $c^j(t) = \frac{1}{|\Omega^j(t)|}$.

The movement of the actin cortex surrounding the whole cell was studied in the same way, but by dividing the structure into eight regions. The results in Figure II.23 show that the leading edge undergoes a more severe depolarisation. All the results are shown in units of length, i.e. the average backwards displacement of the depolarising actin brush.

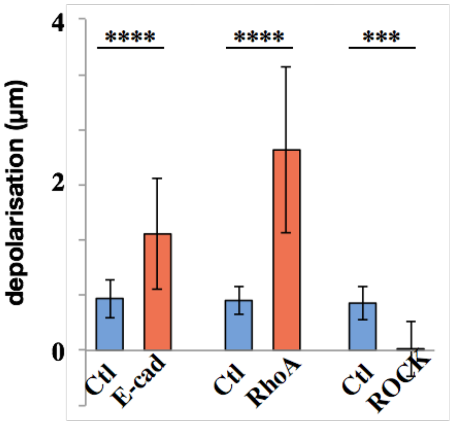

Figure II.24 – **Depolarisation of the actin brush in E-cad KD, RhoA overexpression, and ROCK KD**. Knocking-down E-cadherin results in a significantly higher depolarisation as compared to the control. As expected, RhoA over-expression increases retrograde flow significantly, and knocking-down ROCK inhibits actomyosin activity and therefore stabilizes the brush. A p-value of **** corresponds to < 0.0001, and *** to < 0.001 ; $n = 20$ cells.

In a nutshell, adhesion via E-cadherin is crucial to maintain the directionality of

PGCs in the zebrafish embryo, but seems dispensable for cell movement in itself.

II.5 Molecular forces in intracellular-mimicking nematic systems

This section of the work was developed in collaboration with Jérôme Hardoüin at Universitat de Barcelona. This work is still under development.

Because of their novelty and of their theoretical nature, the forces estimated by the method proposed in Section II.1 are hard to validate experimentally. In this section, we study a cytoskeleton-like nematic system consisting of a mixture of microtubules and kinesin in suspension at a water-oil interface. The active nature of the kinesin molecules (fuelled by ATP hydrolisis) induces forces in the system that can be deduced from the orientation of the filaments. Since these forces are in turn reflected on the underlying water, they can be compared to those extracted by our framework. In addition, computing the pressure and deviatoric stresses is showing good promise for studying the nucleation of so-called topological defects in active matter, and calculating the Lyapunov exponents of the flow field might help analyse the system's instabilities.

Nematics are concerned with long-range orientation order without much regard for positional structure, most notably in reference to elongated molecules with head-tail symmetry whose principal axes align into loosely parallel lines. This is namely the case of the well-studied nematic phase in liquid crystals (LC) [253], which is exploited in LC Displays. Active nematics study how the properties of these systems change when their constitutive elements are able to individually extract energy from their surroundings and turn it into mechanical work, maintaining the nematic system out of equilibrium and giving rise to emergent collective motion (see I). From this perspective, active nematics is the subset of active matter that displays nematic order [254]. Introducing 'activity' into a nematic system shortens the range of the orientational order and thus induces turbulent-looking flows, which manifest in the form of chaotic-like features such as jets and swirls. The active forces might orient two contiguous regions of the nematic system differently, creating a singularity in the orientation field known as a topological defect, which would otherwise only be present as a result of a structural inhomogeneity in the nematic material. 2D topological defects can be classified into comet-like (winding number $+1/2$) and trefoil-like ($-1/2$) according to the change in orientation. Active comet defects are motile and annihilate upon meeting their negative counterpart. On the other hand, both defects are actively nucleated in pairs of opposite signs. The dynamics created by the generation and destruction of defects is intimately tied with the active turbulence described before and can be regarded as impeding long-range order.

Multiple biological systems can be considered nematic active matter. At a multicellular scale, dense assemblies of bone-synthesising osteoblasts [255, 256], expanding bacterial colonies [257, 258], and epithelial tissue[23], all display nematic behavior. Examples at the intracellular level are mostly related to efforts in reproducing the collective dynamics of the cytoskeleton and involve mixing biopolymers, such as microtubules or actin, with ATP-fueled molecular motors, e.g. kinesin or myosin [260].

II.5.1 Microtubule-kinesin mixtures

We consider microtubule-kinesin mixtures at a 2D water-oil interface, a minimalist model frequently used to study cytoskeletal machinery (see rows 1 of Figures II.26 and II.27). More specifically [261], the system contains fluorescently labelled microtubules, polyethylene glycol as a depleting agent that helps in forming bundles of microtubules, streptavidin to join pairs of biotinylated kinesins into two-headed motors, and ATP as a tunable [262] energy source. The result are aligned bundles of microtubules that extend and fold continuously in a sort of dynamical steady state flow known as active turbulence. Underlying this higher scale dynamics is the polar action of the motors. Microtubule filaments have minus and plus ends, and kinesin motors walk only in this very direction : if the polarities of two contiguous filaments are opposed, the two-headed motors will make the two microtubules slide past each other ; whereas filaments of the same polarity will experience no relative motion. Therefore, microtubule bundles are locally sorted according to their polarity, which results in extensional motion [254]. The search for a globally polarised system drives the creation of the dynamical steady state as it competes with the occasional fracturing and disintegration of the bundles. While the resulting turbulent-looking flow is referred to as "active turbulence", this is but a visual analogy. In fact, these nematic systems do display some spatial coherence, which can be defined by a characteristic length scale [263] of order around the length of 10 microtubules. Despite their organisation at a local level, we recall that the systems do not seem to achieve long-time long-range orientational order and thus they might be well described by spatio-temporal chaos.

In summary, active stresses act along the microtubules, pulling the filaments apart but leaving the director field unchanged. However, the extensile system is coupled to the solvent. The hydrodynamic interactions suck the solvent in from the sides and expel it along the stretching direction [264]. Under these conditions, active stresses amplify any bending deformation of the director field leading to unstable behavior [265, 266], which is reminiscent of buckling instabilities and presumably derives into active turbulence [267]. The growing deformation is bound to self-fracture and generate a pair of oppositely signed defects. The positive defects are self-propelled because the high variations in orientation generate a force unbalance that points in the comet direction. Positive defects create the characteristic vortices of active turbulence as they interact, and are annihilated when they meet their negative counterparts, eventually reaching a steady state with a constant number of defects.

---

[23] The apoptotic sites of some epithelial tissues have been found to be highly correlated with positive topological defects [259], where compressive stresses are high. In fact, the stress peak triggers cell death and expulsion via mechanotransduction.

In the absence of boundaries, the unstable behavior is always present independently of the activity level. However, there exist multiple ways to stabilise the system, for example by controlling the viscosity of the underlying fluid to increase friction and slow down defects [268, 263]. Confining the system is perhaps the most fruitful of the alternatives. Physical geometric constraints, such as packing the system into a disk (as in Figures II.26 and II.27), help stabilise chaotic motion and prompt longer-ranged order (e.g. [269]) as the characteristic size of the confinement shrinks to around the order of the length scale of the activity. In our setting, the microtubule-kinesin mixture is confined to a disk and we observe quasi-steady flow and structural patterns.

II.5.1.1 Nematohydrodynamics

Nematohydrodynamic models aim at describing active nematics under a continuum theory, which summarises the microscopic detail of active molecules into coarse-grained or macroscopic quantities such as the nematic tensor Q or the fluid velocity $\mathbf{u}$ (Figure II.27) [258, 270]. The evolution of each of these two parameters is described by respective dynamic equations that are mostly coupled through a common velocity. More concretely, the behavior of the underlying fluid is described by the incompressible Navier-Stokes equations where the stress tensor not only includes the classical viscous contribution but also elastic and active terms. In particular, the momentum equation reads

$$\rho D_t \mathbf{u} = \nabla \cdot \left(-p\mathrm{I} + \tau_{\mathrm{v}} + \tau_{\mathrm{e}} + \tau_{\mathrm{a}} \right), \tag{II.36}$$

where ρ is a constant density. Elastic stresses are a function of Q itself and of a field H that describes the elastic relaxation of Q via a free energy. However, in a microtubule-kinesin mixture, the nematic orientation relaxes at low speeds compared to the rate of energy injection. Therefore, elastic stresses are typically neglected in favor of active stresses [254]. Active stresses are directly proportional to the nematic tensor :

$$\tau_{\mathrm{a}} := -\xi \mathrm{Q}, \tag{II.37}$$

where $\xi > 0$ reflects the extensile nature of microtubule-kinesin mixtures, whose molecules pull the fluid towards their sides and push it away along their axis. A precise understanding of active stresses requires a proper explanation of Q. The nematic tensor Q provides a macroscopic characterisation of the orientation field as a function of the unitary director field $\mathbf{o}$ (Figure II.26, row 2), which describes the local alignment of the microtubules. In 2D,

$$\mathrm{Q} = 2q(\mathbf{o} \times \mathbf{o} - \mathrm{I}/2). \tag{II.38}$$

Thus Q is an order parameter that adds magnitude (q) to $\mathbf{o}$ and tensorialises it, making explicit the head-tail symmetry ($\mathbf{o} = -\mathbf{o}$). In particular, q quantifies the "strength" of the local alignment in reference to a normalised scale ranging between 0 (isotropy) and 1 (perfect alignment). Notice that $\mathbf{o}$ is an eigenvector of Q with eigenvalue q, whereas the vector perpendicular to $\mathbf{o}$ is a second eigenvector but of eigenvalue $-q$. This is a consequence of the tensor being traceless, which reflects our indifference towards isotropic conditions [253]. The tensor is also symmetric and real. The second system of equations describes the dynamics of the nematic tensor as they are advected by the flow. The equations model how the elongated molecules align with the flow as a function of the flow derivatives (S), i.e. of its vorticity and rate of strain ; and how the system relaxes as described through the molecular field (H). In this case, the dynamics of the nematic tensor read

$$D_t \mathrm{Q} - \mathrm{S} = \Gamma \mathrm{H}, \tag{II.39}$$

where Γ is a diffusivity. While the free energy underlying H accounts for both bulk energy and the elastic cost of spatial homogeneities ($\propto (\nabla \mathrm{Q})^2$), it is worth mentioning that in extensile systems the former can be safely ignored.

II.5.2 A qualitative comparison between fluid and active nematic forces

Conveniently, the system also has little inertia. Indeed, the sizes at play are microscopic, and the speeds relatively low. Together with the simplifications introduced by the extensile nature of the mixture, the small Reynolds number further eases the PDEs. Specifically, we derive

$$\nabla \cdot (-p\mathrm{I} + \tau_{\mathrm{v}} + \tau_{\mathrm{a}}) = 0. \tag{II.40}$$

By comparison with the Stokes equation introduced in II.1, we identify the divergence of the active stress with the forcing term :

$$\mathbf{f} = -\xi \nabla \cdot \mathrm{Q}. \tag{II.41}$$

But, could we compare (in practice) these active nematic forces with the forces exerted on the fluid as extracted by our framework ?

II.5.2.1 Image analysis for the active nematic force

To compute the active force via (II.41), we need to extract the nematic tensor Q out of the image sequence. The videos of the flowing mixture are taken using fluorescence confocal microscopy. The director field is extracted from each of these images using a method based on anisotropic filtering [271], namely coherence-enhanced diffusion filtering [272]. In short, one looks for the directions along which intensity variations are weakest, that is the eigenvector corresponding to the smallest eigenvalue of the intensity gradient tensor. Obligedly, the image is pre-filtered to reduce the influence of noise, yielding an intensity I'. In addition, the gradient tensor is convoluted with a Gaussian filter G in order to increase the range of the measure because the intensity variations concerning microtubule bundles occur at a scale longer than a pixel. Finally, the eigenvalue $\mathbf{o}_i$ of $G * (\nabla I')(\nabla I')^T$, known as the coherence direction in image analysis, corresponds to the local orientation of our nematic system.

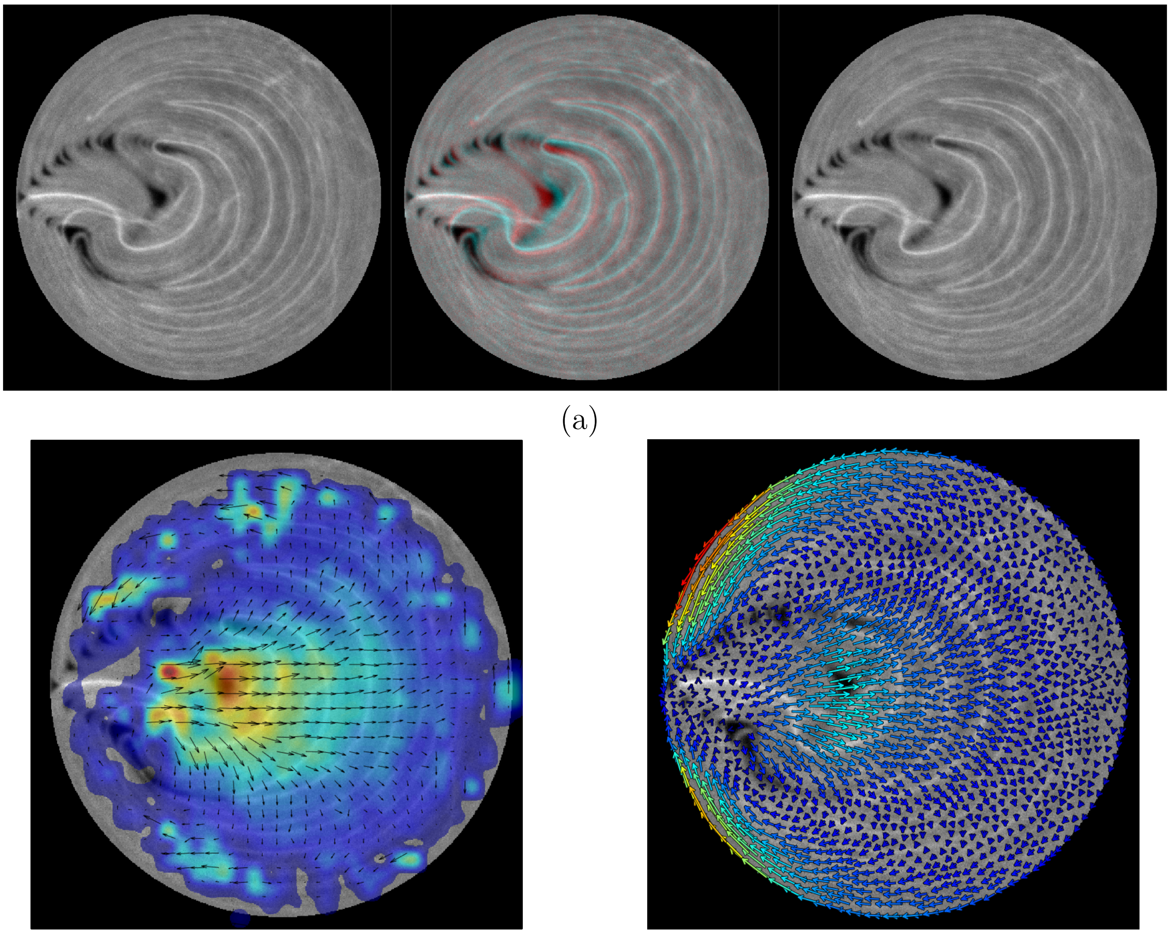

(a)

(b)

(c)

Figure II.25 – **Qualitative comparison of PIV techniques. a)** Two consecutive frames of a microtubule-kinesin mixture interluded by their superposition in cyan and red in an attempt to display motion (cyan+red = white). **b)** Velocity field extracted from state-of-the-art PIV techniques used in the field of active nematics. **c)** Velocity field extracted by our approach, outlined in Section II.5.2.2.

The nematic tensor is more reliably constructed by averaging over m neighbouring pixels : $\mathrm{Q} = \frac{1}{m}\sum_{i=1}^{m} \mathbf{o}_i \times \mathbf{o}_i - \mathrm{I}/2$. Notice that the "averaged" $\mathbf{o}$ (Figure II.26, row 2) and q can be obtained by diagonalising Q. The active force (up to a constant) can be finally computed as $\nabla \cdot \mathrm{Q}$ (see Figure II.26, row 3).

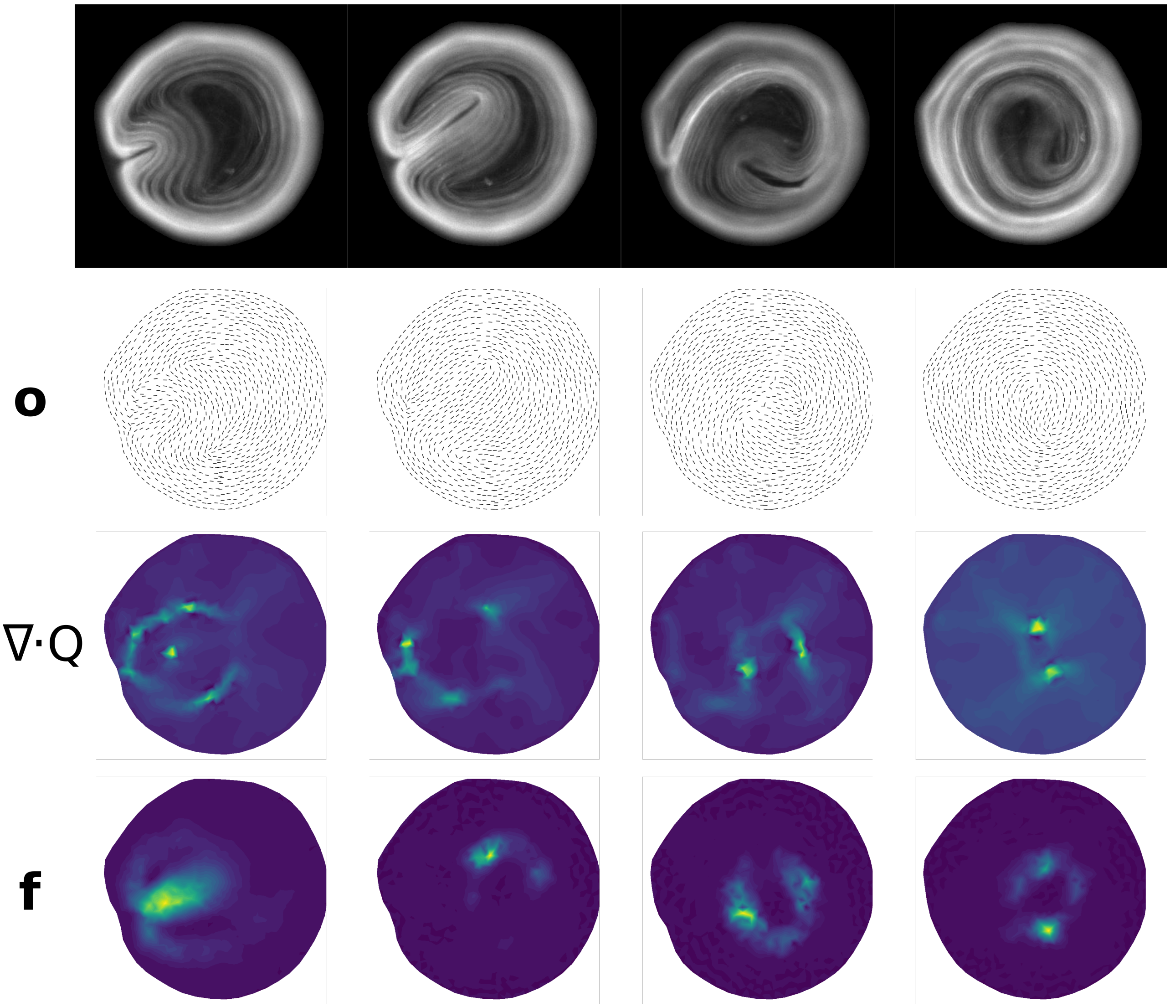

Figure II.26 – **Comparison between active nematic forces and fluid forces. Row 1)** 4 frames of a sequence showing a mixture of microtubules and kinesin. **Row 2)** Director field $\mathbf{o}$ extracted from the images in (Row 1) as detailed in Section II.5.2.1. **Row 3)** The divergence of the nematic tensor Q, which is a function of $\mathbf{o}$ in (Row 2), is proportional to the active force. **Row 4)**. Fluid force extracted from the image sequence as detailed in II.5.2.2 ; to be compared with (Row 3). The last forces are shown as the square of the magnitude. Together with Jérôme Hardoüin. The raw video is taken from [269].

II.5.2.2 Image analysis for the fluid force

On the other hand, we solve the minimisation problem (II.12) with

$$J_{\text{reg}} \quad = \quad \alpha\|\mathbf{f}\|_K^2 + \gamma\|\mathbf{g}\cdot\mathbf{n}\|_{\partial K}^2 + \eta\|r\|_K^2 \tag{II.42}$$

to obtain the external force **f** felt by the fluid from each image pair of the same sequence. Here K stands for the domain of the active nematic system, a disk in our case. In line with the experimental setting, we weakly enforce a free slip condition on the disk border ∂K, penalising only velocities that are perpendicular to the boundary normal **n**. In principle, the flow should be incompressible but we allow some leeway to accommodate anomalies, mainly related to occasional misrepresentations of the system by the image intensities. The assimilated velocity field **u** (Figure II.25, but see also Figure II.27) appears very accurate and seems to offer unprecedented detail within the active nematics community. Take the zones near the wall for example. Resolving the movement in these regions is particularly challenging because the velocity field aligns with the microtubules, a direction in which contrast is poor[24]. As opposed to correlation-based methods, which are too local, our approach is able to capture the movement near the wall. This is because the fluorescent microtubules are advected by the underlying fluid and therefore the motion reflected in the intensity is well described by our fluid dynamics assumption ; together with the optical flow functional, the globality of the method manages to fill in the regions without contrast.

II.5.2.3 Calibration of nematic activity

Comparing the active and fluid forces in magnitude is not possible because ξ, and possibly the viscosity μ too, are unknown ; rather we have to compare their spatio-temporal distribution. If the results are positive, we might be confident enough to try to calibrate the nematic parameter ξ with the much more easily accessible μ by equaling forces. This might be relevant to the active nematics community because there is no reliable way to measure ξ experimentally as of now. Moreover, if the relation is correct, this might also reassure us of the adequacy of our framework regarding the study of intracellular mechanics[25], specially concerning forces exerted by molecular motors.

While there are some discrepancies regarding forces close to the walls, the distribution of active and fluid forces appears qualitatively similar in respective rows 3 and 4 of Figure II.26. Of course, the latter are much smoother, i.e. less localised, because of their fluid nature[26]. However, it is noteworthy that the maxima of both forces match almost perfectly, especially considering that both approaches are very different. Indeed, active forces are computed by informing the nematic equations with the **o** field

---

[24] In addition the zone has little texture, decreasing the amount of information available, as seen in the cyan+red superposition of Figure II.25.

[25] By way of simulations, we already know that the forces are well recovered when the Stokes equations are strictly fulfilled.

[26] Perhaps this could be alleviated by using a vectorial TV regularisation as introduced in Chapter III.

extracted from the gradient eigenvalues of a single image, whereas fluid forces are computed from pairs of images and are based on the optimisation method presented in Section II.1. If we compare the spatial integrals of both force sources, it appears that the product μ/ξ is typically not far from order $10^2 s$. This result is preliminary and must not (yet) be taken at face value.

II.5.3 Applications to the study of defect nucleation, spatio-temporal chaos and dynamical instabilites : wall stress, POD and Lyapunov exponents

Further interesting problems in active nematics can be tackled with the extracted information. These ideas and their repercussions in the field will be presented in depth in Jérôme's thesis on active nematics, but we outline some in this text.

For example, one could explore the factors that trigger defect nucleation at walls, where it occurs preferentially due to elastic considerations. This can be approached by computing the deviatoric stress $\tau_{\mathrm{v}} = 2\mu\epsilon(\mathbf{u})$ of the fluid underlying the nematic system (see Section II.1.2.1d). Specially relevant is the stress across the surface defined by the boundary normal $\mathbf{n} \cdot \tau_{\mathrm{v}}$, which coincides with the radial direction of the disk (Figure II.27). While the normal $\tau_{\mathrm{v,n}} := \mathbf{n} \cdot \tau_{\mathrm{v}} \cdot \mathbf{n}$ component of this stress is highest at defects present on the wall (Figure II.27), the tangential component $\tau_{\mathrm{v,s}}$ is highest at the sides immediate to these defects (Figure II.27), possibly explaining why sometimes additional defects are nucleated there (e.g. think of stress-induced bending in plate theory [273]).

Another direction is to try to analyse the active flows in terms of classical spatio-temporal chaos, but active nematics appear too complex to be approached with standard methods. However, it might be possible to characterise the flows through the underlying fluid instead, where we can have estimates of classical quantities such as pressure. In this direction, a parallel could be drawn with Rayleigh-Bénard convection flows : the active forces in the nematic system would correspond to the temperature gradient that forces the convective system. In the convective case, temperature differences lead to pressure gradients, whereas nematic flows seem to follow pressure gradients (p in Figure II.27) that are generated by the active forces ($\mathbf{f}$ in Figure II.27). Therefore, it seems viable to apply standard methods to the fluid underlying the nematic system. An in depth analysis of this relation will be provided in Jérôme's thesis.

A third possibility is to analyse the system from a dynamical systems perspective. In this context, one could attempt to fit a dynamical system into the computed velocity fields by representing their fluctuations with respect to the mean via a finite set of modes that maximise kinetic energy, for example via Proper Orthogonal Decomposition (POD). Alternatively, another relevant approach is to study the advection of the fluid by considering Lagrangian Coherent Structures (LCSs) [274]. LCSs are the most (locally) attracting or repelling surfaces within the flow [275] (pages 66 and 67) and thus bring out the flow topology. These regions can be extracted by ana-

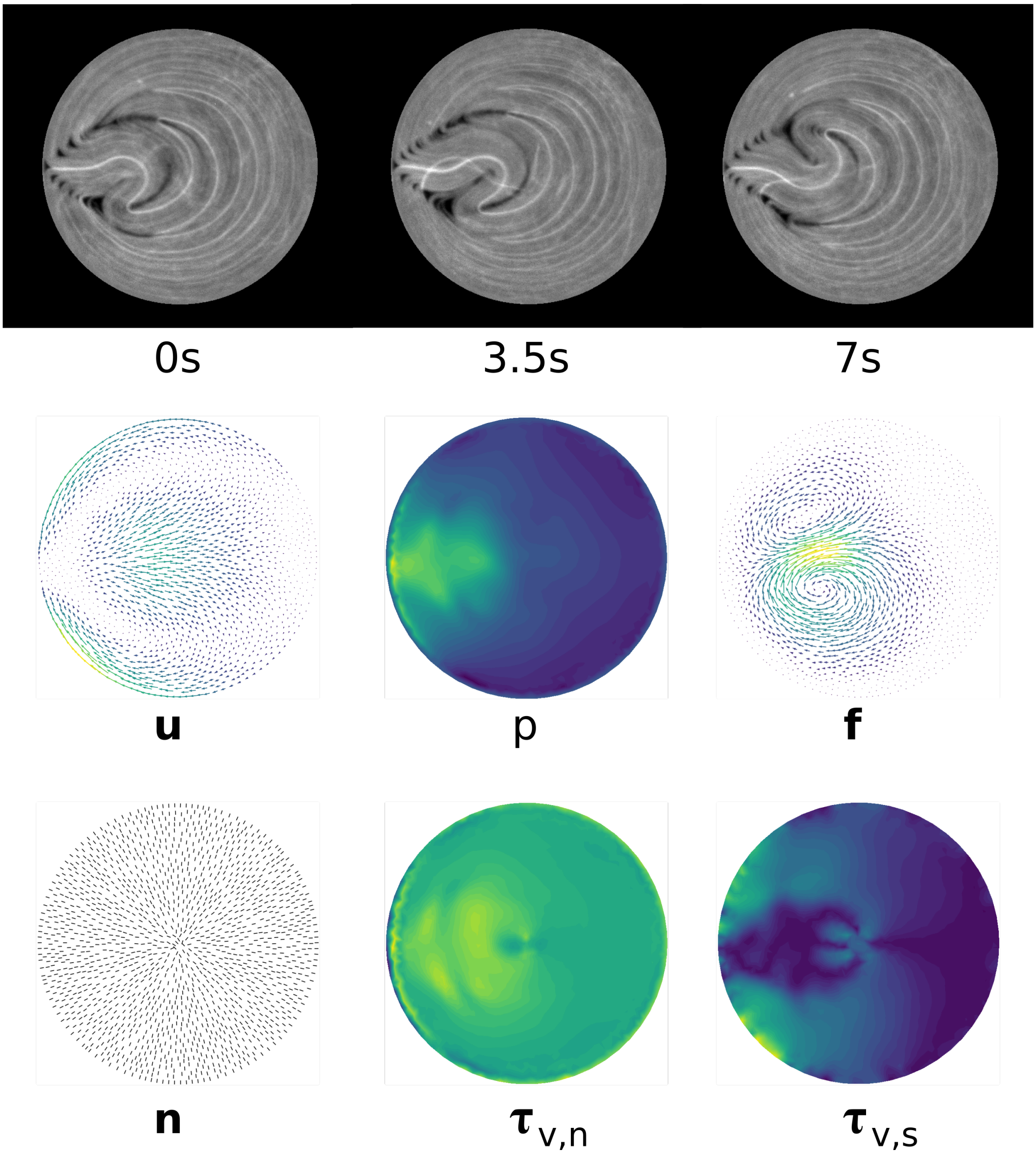

Figure II.27 – **Analysis of the quasi-steady-state regime of a nematic system. Row 1)** 3 frames of a sequence showing a mixture of microtubules and kinesin reaching a steady state. **Row 2)** Average velocity field $\mathbf{u}$, average pressure field p and average force field $\mathbf{f}$. **Row 3)** Field of normals $\mathbf{n}$, average normal stress $\tau_{\mathrm{v,n}}$ and average tangential stress $\tau_{\mathrm{v,s}}$. Together with Jérôme Hardoüin.

lysing the spatial distribution of finite time Lyapunov exponents (FTLEs) [276], as done for example in heart flows [277]. In turn, FTLEs are computed from the largest eigenvalues of the Cauchy-Green deformation tensor $\left(\nabla F_{t_0}^t\right)^T \nabla F_{t_0}^t$ as derived from integrating the velocity field forward (repelling) or backwards (attracting) into a flow map $F_{t_0}^t : \mathbf{x}_0 \to \mathbf{x}(\mathbf{x}_0, t_0, t)$ from a starting position $\mathbf{x}_0$ and time t_0 until t; and reflect the separation rate of "particle" trajectories at long time. Since the microtubule-kinesin mixture is extensile, the direction of maximum stretch should be that of the nematic orientation field $\mathbf{o}$ and therefore the FTLE (being the largest) can be computed from $|\mathbf{o}(t_0, \mathbf{x}_0) \cdot \nabla F_{t_0}^t \cdot \mathbf{o}(t, \mathbf{x})|$. Under ergodic conditions, a recent study points out that the Lyapunov exponents can be calculated directly as a spatiotemporal average of $\mathbf{o} \cdot \nabla \mathbf{u} \cdot \mathbf{o}$. Lyapunov exponents (and LCSs) should reflect the instabilities (and flow topology) of the nematic system and perhaps shine light on defect nucleation and the chaotic characteristics of the flow.

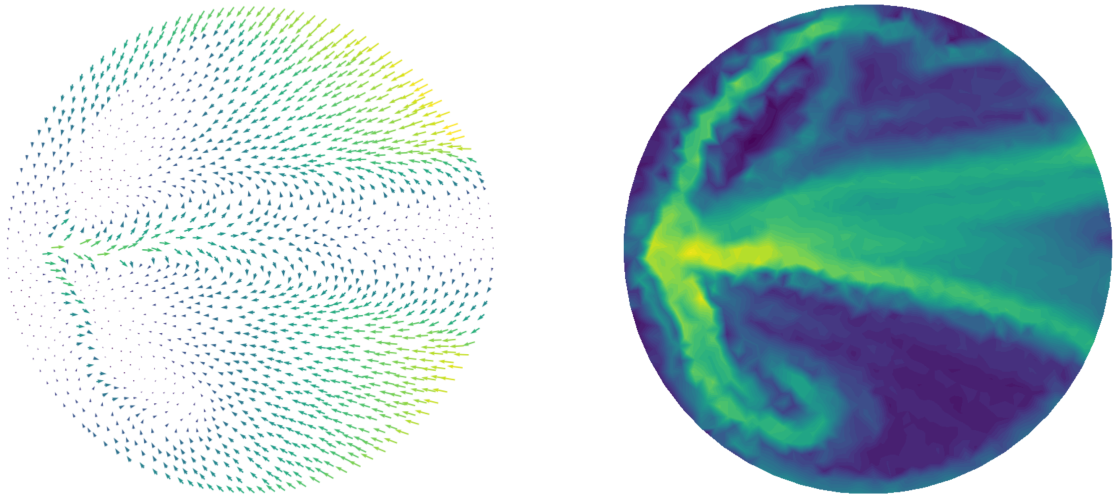
(a) (b)

Figure II.28 – **Finite time Lyapunov exponents of the mixture at quasi steady state. a)** Flow map $F_{t_0}^t$, see text. **b)** FTLEs. The maximal (real) eigenvalue $\lambda_{\max}$ of the (symmetric) $(\nabla F_{t_0}^t)^T \nabla F_{t_0}^t$ tensor are computed at each vertex of the mesh with NumPy, which interfaces with LAPACK routines. The FTLE is then formed as $\ln\left(\sqrt{\lambda_{\max}}\right)$. Since the integration was performed forward, the plot shows potential repelling LCSs. Together with Jérôme Hardoüin.

II.6 The viscoelasticity of cytoplasm

This section of the work is fully developed conceptually but was "abandoned" due to a lack of experimental support that could derive meaningful application problems.

The intracellular model implemented in Section II.1 is only valid at certain time scales, which depend on the cell type and its motion. To substitute the viscous Newtonian model of the cytoplasm for a more accurate representation, we base ourselves on several rheological experiments reported in the literature. In particular, the cytoplasm of amoeboid cells has been repeatedly reported as a viscoelastic fluid well described by Jeffreys' model. While this is a discrete spring-damper mechanical system, its extension to continuum mechanics is known as the Oldroyd B model. By explicitly deriving the latter from the former, we reproduce the exact link between the spring-damper constants documented in the articles and the viscoelastic parameters that govern the motion of an Oldroyd fluid. However, not unlike other viscoelastic models, Oldroyd B fluids suffer from several convergence problems. To stabilise the weak formulation of the problem, we resort to a combination of the streamline upwind method, which adds a diffusive term, and the discrete elastic viscous split stress approach. Time-stepping is then implemented as a backwards scheme and the non-linearity of the model is attacked with Newton's method. Once the forward problem has converged, we adapt the data functional and regularisation introduced in Section II.1 to this time-dependent problem. While the adjoint approach to minimise the resulting PDE-constrained is outlined, we have not implemented it due to a lack of meaningful data.

The polymeric nature of biological fluids and solids is better described by viscoelastic models [278, 279]. It is precisely the interaction between the constitutive proteins of biological materials that condition their response to stress, giving rise to a wide range of behaviors that combine both viscous and elastic responses. Take for example a protein solution. In this case, the chains first reorganise (e.g. untangle) in order to accompany the stress, aligning with the streamlines and eventually flowing. While most energy is dissipated as the solution flows, some of it is preserved in internal elastic stresses that act to return the polymers to their original spatial configuration. This is a very preliminary example of a viscoelastic fluid. At the opposite end, in viscoelastic solids, there is first some leeway wherein the proteins rearrange (creep) until the stress is compensated. Different combinations of these and other phenomena result in different viscoelastic regimes that can be further classified as either fluid, such as the cytoplasm where proteins interact more weakly, or solid, such as the extracellular matrix where proteins are often fully cross-linked.

Pure elasticity describes materials that respond immediately to stress, respectively storing or releasing all the energy as they are strained or relaxed. Conversely, viscous

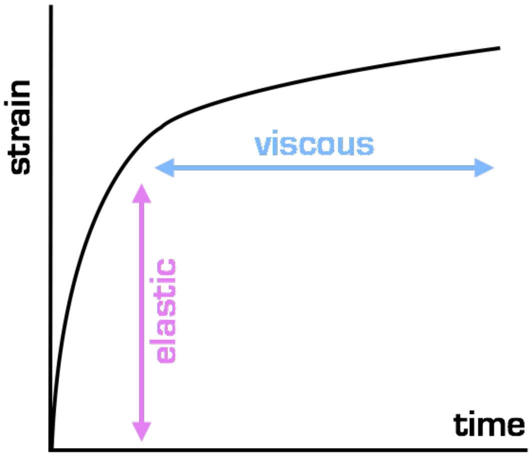

Figure II.29 – **Viscoelastic creep.** Very simple schematic of a viscoelastic fluid responding to a stress step. When the stress is applied there is an almost instantaneous elastic response that is retarded by viscous components. As more time passes, the contribution of the elastic component is saturated and the behavior becomes fundamentally viscous. For comparison, a purely viscous fluid would display a perfectly linear function, whereas the strain of a purely elastic material would respond instantly, mimicking the step function imposed on the stress. Depending on the fluid, any combination of these responses at multiple time scales (e.g. retardation or relaxation times) is possible, giving rise to many different behaviors ; these can be modeled for example by mechanical circuits (see Annex B).

.

behavior is entirely dissipative and strains depend on time. In the most simple elastic and viscous models, strain and strain rate are proportional to the stress. The combination of both models translates into mixed properties, for example viscoelastic fluids display anisotropic stresses and have memory, i.e. the internal stress depend on the fluid history (see review in [280] and computational considerations in [281, 282, 283]). From the perspective of internal rearrangements, viscosity and elasticity represent the limits of instantaneous and infinitely-long rearrangements. The balance between the two regimes is characterised by one or more timescales that result in the different viscoelastic responses (for example Figure II.29). As shown in Annex B, a good way to recapitulate these properties and their associated time scales is to build increasingly complex (but linear) circuits of mechanical springs and dampers. In practice, the great flexibility to model viscoelasticity, as opposed to the one standard Newtonian fluid and linearly elastic solid, results in models that are eminently phenomenological. Of course this is also the case in cells : different cell types can be described by different timescales ; and thus studying the fluid-like behavior of the cytoplasm requires great experimental support. In other words, rheology is necessary to assess whether it is worth to include an elasticity component on our Newtonian model of the cytoplasm given the cell type and spatiotemporal scale under study. While we do not have the appropriate set-up to approach this question, we can draw some inspiration from the literature.

II.6.1 Taylor-Couette inside the cell : viscoelasticity and shear-thinning

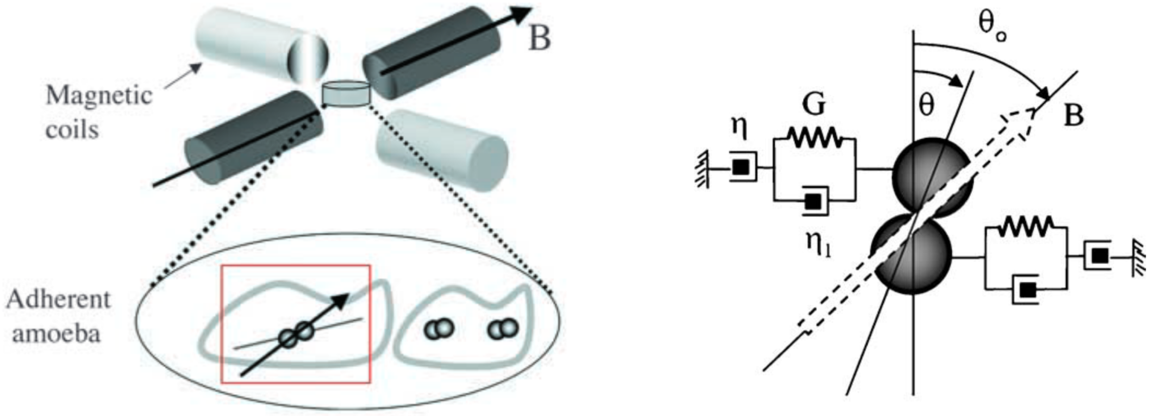

(a) (b)

FIGURE II.30 – **Taylor-Couette [237] inside a cell and the associated viscoelastic mechanical circuit. a)** Pairs of electromagnetic coils are used to create a magnetic field on the imaging plane that is used to orient pairs of phagocyted beads against the resisting torque induced by the fluid. In this way, the rheology of the material can be explored. **b)** Mechanical model of the viscoelastic cytoplasm of *Entamoeba histolytica* . The constants depicted in the figure as η_1, G and η are written as η_1, E_1 and η_2 in this text. Both images are taken from [136].

The rheology of cells has been probed extensively. In this case we focus on a report on the behavior of the *Entamoeba histolytica* cytoplasm [136], but similar studies have been performed in many other cell types such as Dictyostelium discoideum [284], fibroblasts, or HeLa cells [285] ; the majority of which coincide in that the cytoplasm is well approximated as a viscoelastic fluid. Most cell rheology is approached via magnetism, and the analysis presented in [136] is no exception. In this study, they induce the parasites to phagocyte magnetic beads that serve as microrheometers (Figure II.30a). Two pairs of electromagnetic coils are then used to create a static magnetic field B on the imaging plane. If the current is direct, the field orients according to the ratio of intensities. Alternatively, feeding alternating currents to the coil pairs that are $\pi/2$-out-of-phase results in a rotating magnetic field. In both cases, the dipole formed by the bead pair will be subjected to a magnetic torque that tends to align it with the magnetic field against the viscoelastic torque. The magnetic torque induced by B is a function of the angle between field and dipole, and of the magnetisation of the bead pair, which can be characterised with a Foner device ; whereas the viscoelastic torque depends on a geometric constant that can be calibrated using a known fluid.

a) Transient response : viscoelastic creep. By observing how the beads progressively align when a static field is suddenly applied, one can capture the viscoelastic response of the material (see Figure II.29). Both [136] and [284] found that the best fit to explain the observed behavior of the cytoplasm was a spring-damper discrete mechanical model known as a three parameter fluid model (Figure II.30b). In Annex B, we show how a classical fluid model from continuum mechanics known as the Oldroyd B model can be derived from this experimental discrete model, and give the equivalence between the constants of the spring-damper system and the constants governing the continuum model.

b) Permanent response : shear-thinning. If the beads are made to permanently follow a rotating magnetic field, both shear strain rate and magnetic torque are constant. Therefore, one can capture the effective viscosity of the fluid under different strain rates. In [136] they found that viscosity decreases with increasing shear rates ; i.e. the fluid is shear-thinning. At a molecular level, this can also be interpreted intuitively as the proteins gradually aligning themselves to produce less resistance, or by aggregates that break into smaller pieces.

In what follows, we focus on viscoelasticity and leave the modelling of the shear-thinning behavior for future work. Of course, this is not to say that one or the other are more important, for example shear thinning could facilitate cytoplasmic streaming, but rather that biological literature seems more concerned with the former [279].

II.6.2 The Oldroyd B model for viscoelastic fluids

The Oldroyd constitutive equations are perhaps the simplest among all continuum models that describe the viscoelastic behavior of dilute polymeric solutions and contain relaxation and retardation. They were first derived [286] by extrapolating experimental observations while trying to satisfy certain requirements, namely : causality, locality and frame indifference. To preserve frame invariance, the material derivative is not enough in the context of second-rank tensors such as the stress ; instead, a set of so-called objective derivatives can be deduced by considering the change of the base vectors (at each material point) that form the tensor. Perhaps the most used of these is the upper convected time derivative,

$$\overset{\nabla}{\bullet} := D_t \bullet - \left((\nabla \mathbf{u})^T \cdot \bullet + \bullet \cdot (\nabla \mathbf{u}) \right) . \tag{II.43}$$

This frame-invariant time derivative corresponds to the rate of change of a second-rank tensor expressed in a coordinate system that moves and deforms with the underlying fluid.

Interestingly, one of Oldroyds' most successful models, the Oldroyd B model, can also be derived by considering a suspension of linear spring dumbbells in a Newtonian fluid. In this case, one can define polymeric μ_p and solvent μ_s viscosities and dissociate the stresses within the fluid into viscous τ_v and elastic τ_e contributions :

$$\rho D_t \mathbf{u} = -\nabla p + \nabla \cdot (\tau_\mathrm{v} + \tau_\mathrm{e}) + f, \tag{II.44}$$

$$\tau_\mathrm{v} = 2\mu_\mathrm{s}\epsilon, \tag{II.45}$$

$$\lambda_2 \overset{\nabla}{\tau}_\mathrm{e} + \tau_\mathrm{e} = 2\mu_\mathrm{p}\epsilon, \tag{II.46}$$

$$\nabla \cdot \mathbf{u} = 0, \tag{II.47}$$

where the boundary conditions can be specified by fixing $\mathbf{u}$ or imposing zero traction as in the Stokes flow (Dirichlet/ Neumann/ Robin), as well as by fixing the stress tensor, and we require initial conditions because of the time dependency [283]. Indeed, a viscoelastic fluid has memory ; and its scale is dictated by the relaxation time λ_2, which in turn is a function of the elastic modulus. More precisely, in Annex B we show how the Oldroyd B model can also be derived by tensorialising the discrete experimental system presented in Figure II.30b into a fluid continuum. The resulting equivalence between the polymeric/viscous constants to the elastic/damper constants is as follows :

$$\mu_\mathrm{s} = \frac{\eta_1 \eta_2}{\eta_1 + \eta_2}, \tag{II.48}$$

$$\mu_\mathrm{p} = \frac{\eta_2^2}{\eta_1 + \eta_2}, \tag{II.49}$$

$$\lambda_2 = \frac{\eta_1 + \eta_2}{E_1}. \tag{II.50}$$

Therefore, a strong elastic modulus E_1 will reduce the relaxation time of the fluid, accelerating its return to an equilibrium state. Most importantly, we now have a fluid-like description of the rheological experiment ! However, the Oldroyd B model is known to be unstable (turning from mostly elliptic to mostly hyperbolic) in certain regimes, which can be defined in terms of some dimensionless constants.

II.6.2.1 Non-dimensionalisation

We scale the problem to recover the characteristic constants of the system. First, notice that $\eta_2 = \mu_\mathrm{s} + \mu_\mathrm{p}$ so we can define $\mu_\mathrm{s} = (1-\alpha)\eta_2$ and $\mu_\mathrm{p} = \alpha\eta_2$, where $\alpha := 1 - \lambda_1/\lambda_2$ and reflects how close the fluid is to following a standard Newtonian model (i.e. $\alpha = 0$) or a Maxwell model ($\alpha = 1$) (see Annex B). The appropriate change of variables reads : $\mathbf{x} = \mathbf{x}^* l$, $t = t^* \Delta t$, $\mathbf{u} = \mathbf{u}^* \frac{l}{\Delta t}$, $p = p^* \frac{\eta_2}{\Delta t}$, $\mathbf{f} = \mathbf{f}^* \frac{\eta_2}{\Delta t l}$, $\tau_\mathrm{e} = \tau_\mathrm{e}^* \frac{\eta_2}{\Delta t}$, where l, Δt are the length and time scales of the problem. Dropping the asterisk for readability we get :

$$\mathrm{Re} D_t \mathbf{u} = -\nabla p + (1-\alpha)\Delta \mathbf{u} + \nabla \cdot \tau_\mathrm{e} + f, \tag{II.51}$$

$$\mathrm{We}\overset{\nabla}{\tau}_{\mathrm{e}} + \tau_{\mathrm{e}} = 2\alpha\epsilon, \tag{II.52}$$

$$\nabla \cdot \mathbf{u} = 0. \tag{II.53}$$

The scale of the equations is characterised by the Reynolds number $\mathrm{Re} := \rho l^2/(\eta_2 \Delta t)$, where ρ is the density ; and the Weissenberg number $\mathrm{We} := \lambda_2/\Delta t$, which compares elastic and viscous forces by looking at the ratio between the relaxation time λ_2 and a related characteristic time of the experiment[27], for example the inverse of the shear rate. In a way, this reflects the anisotropy resulting from the deformation of the fluid. It is precisely because the fluid and its properties are rearranged during (in the same timescale as) the experiment, that strain and stress cannot have a constant relation and thus time-dependency arises.

In the cellular context, the inertial contributions are negligible and thus $\mathrm{Re} \ll 1$ (as in Section II.1). However, depending on the polymeric composition of a cell's cytoplasm, which can vary wildly by cell type, and the time scale of the shear rate, the Weissenberg number might not be negligible. In some applications, we have $\mathrm{We} \sim 1$. In the case study of *Entamoeba histolytica* , the literature reports $\eta_2 \approx 0.35\mathrm{Pa\ s}$ and $E_1 \approx 2.3\mathrm{Pa}$[28] ; while η_1 is not given, we can assume that it is of the same order and thus $\lambda_2 \sim 0.1$. Since the shear rates are applied at around $\dot{\xi} \sim 1$ (and we do not expect much higher from contraction-induced cytoplasm streaming), this drives us below the critical Weissenberg number of 1, from which convergence becomes specially hard as the flows become more strongly elastic. In fact, the We number drives up the hyperbolicity component[29] of the elliptic-hyperbolic (steady) Oldroyd B model.

II.6.2.2 Weak formulation : SU, DEVSS, and convergence problems

To solve the Oldroyd B equations we write their corresponding weak formulation. First, the conservation equations :

$$a_{\mathrm{S}} := 2(1-\alpha)\langle \epsilon(\mathbf{u}), \epsilon(\mathbf{v})\rangle_K + \langle \tau_{\mathrm{e}}, \epsilon(\mathbf{v})\rangle_K - \langle p, \nabla \cdot \mathbf{v}\rangle_K + \langle \nabla \cdot \mathbf{u}, q\rangle_K, \tag{II.54}$$

$$L_{\mathrm{S}} := \langle \mathbf{f}, \mathbf{v}\rangle_K, \tag{II.55}$$

which are eminently Stokesian. Second, the constitutive equations :

$$a_{\mathrm{c}} := \mathrm{We}\langle \overset{\nabla}{\tau}_{\mathrm{e,a}}, \phi\rangle_K + \langle \tau_{\mathrm{e}}, \phi\rangle_K - 2\alpha\langle \epsilon(\mathbf{u}), \phi\rangle_K, \tag{II.56}$$

$$L_{\mathrm{c}} := \langle \frac{\mathrm{We}}{dt}\tau_{\mathrm{e},\,0}, \phi\rangle_K, \tag{II.57}$$

$$\overset{\nabla}{\tau}_{\mathrm{e,a}} := \frac{1}{dt}\tau_{\mathrm{e}} + \mathbf{u}\cdot\nabla\tau_{\mathrm{e}} - \Big((\nabla\mathbf{u})^T \cdot \tau_{\mathrm{e}} + \tau_{\mathrm{e}} \cdot (\nabla\mathbf{u})\Big), \tag{II.58}$$

---

[27] See footnote 8.

[28] In fact, it is not clear what they are reporting as the notation for the damper system and the relaxation time do not match.

[29] I.e. the first-order hyperbolic equation that describes the evolution of the elastic stress.

where we have discretised the time derivative with a backward difference with time step dt and the elastic stress $\tau_{\mathrm{e},\,0}$ evaluated at the previous time point. Of course the simplest scheme, albeit highly unstable at large We, is the mixed method defined by the set of equations above : find τ_e (symmetric, i.e. three values in 2D), $\mathbf{u}$, p, such that (II.54)-(II.58) $\forall\ \phi$, $\mathbf{v}$, q.

a) SUPG-SU. To stabilise the enhanced hyperbolicity of the equation system at higher We numbers (see [280] for an overview), an approach known as SUPG (Streamline Upwind Petrov-Galerkin method) adds a consistent upwind diffusion term $\langle \mathrm{We}\overset{\nabla}{\tau}_\mathrm{e} + \tau_\mathrm{e} - 2\alpha\epsilon, \phi + \beta\mathbf{u}\cdot\nabla\phi\rangle_K$ to the stress [287], where $\beta \in \mathbb{R}_{\geq 0}$ weights the introduced diffusivity tensor. However, under the SUPG formulation, the convergence of the resulting method is still problematic near geometry-induced singularities [288]. Conversely, settling for a SU scheme [287], which only includes the diffusion term

$$a_{\mathrm{c},\ \mathrm{SU}} := \beta\langle \mathbf{u}\cdot\nabla\tau_\mathrm{e}, \mathbf{u}\cdot\nabla\phi\rangle_K \tag{II.59}$$

in addition to the original stress, maintains convergence up to high We at the price of losing consistency. Indeed, although the resulting predictions are good [289], we should not expect the SU to be more than first-order accurate [290, 291].

b) DEVSS-EVSS. Additional work accounts for the mixed nature of the coupled system (and compatibility conditions thereof) to propose complementary stabilising schemes. Indeed, whereas the Stokesian equations are stable for fairly simple discretisations fulfilling the LBB condition ; in the viscoelastic context, the mixed trio $(\mathbf{u}, p, \tau_\mathrm{e})$ is only stable for very costly elements that satisfy a generalised compatibility condition. An approach in this direction is to search for a change of variables that, at least, behaves well in the Stokesian limit [292, 293] ; for example by trying to retain the elliptic contribution of the force balance equations. An instance of this is the elastic viscous split stress (EVSS) formulation, which uses the change of variables $\sigma := \tau_\mathrm{e} - 2\alpha\epsilon$ to rewrite the equation system [294, 295, 296]. However, the proposed change of variables is not adaptable to the majority of constitutive equations and it includes the strain rate tensor into the convection-derivated terms, requiring second derivatives of $\mathbf{u}$. To amend this, the discrete alternative to EVSS (DEVSS) [297] introduces an additional unknown $\bar{\epsilon}$, which is the continuous L^2 projection of the discrete rate of strain tensor, in order to pose a similar change of variables $\sigma := \tau_\mathrm{e} - 2\omega\bar{\epsilon}$ for some $\omega \in \mathbb{R}_{\geq 0}$. As it turns out, the change of variables is not necessary ; instead, it is enough to add the terms

$$a_{\mathrm{S},\ \mathrm{DEVSS}} := 2\omega\langle\epsilon(\mathbf{u}), \epsilon(\mathbf{v})\rangle_K - 2\omega\langle\bar{\epsilon}, \epsilon(\mathbf{v})\rangle_K + \langle\epsilon(\mathbf{u}), \psi\rangle_K - \langle\bar{\epsilon}, \psi\rangle_K, \tag{II.60}$$

where the last two summands make up the projection, and the corresponding trial $\bar{\epsilon}$ and test ψ functions have been introduced (look below for the full problem). While these additions might look like a null operation, the key lies on the different discrete formulations of $\bar{\epsilon}$ and $\epsilon(\mathbf{u})$; in particular one ought to choose the finite approximation space of the projection such that it is not rich enough to fully represent $\epsilon(\mathbf{u})$. In practice, the iterative nature of non-linear solving methods allows to easily split the Oldroyd stabilised equation and the projection $\langle \epsilon(\mathbf{u}), \psi \rangle_K = \langle \bar{\epsilon}, \psi \rangle_K$ into a two-step computation.

The resulting $(\mathbf{u}, p, \tau_\mathrm{e}, \bar{\epsilon})$ quartet is remarkably stable, and it has been shown to require no extra compatibility condition (aside from LBB) in a linearised version of the Oldroyd B model [293]. As a result, DEVSS [298], and specially the combination SU-DEVSS, displays better convergence properties as compared to the other formulations presented and is our choice of implementation.

c) The underlying cause of convergence problems in viscoelastic fluids. Just like for the general Navier-Stokes equations, well-posedness of the Oldroyd B model is still open for debate, mainly due to the lack of scale-dependent stress dissipation[30] in the advection equation [299]. However, some solutions have so far helped numeric implementations assess their results ; for example, the norm of the elastic stress tensor is a good indicator of existence [300]. In addition, the equations can be proven to be globally well-posed under unrealistically small initial data and very favorable geometries [301].

Molecularly, one of the problems mining the theoretical and computational analysis of the Oldroyd B model can be traced back to the linear elasticity of the immersed spring model, which does not limit how long the dumbbells can be stretched and thus might break down during steady extensional flow [302]. However, this is certainly not the only problem since efforts that model finite extensibility (e.g. FENE-P, Giesekus, PTT) still suffer at high Weissenberg numbers. It appears that large stress gradients induced by the advection of the elastic stress around extensional points might be the common cause underlying the numerical difficulties involved in modelling viscoelastic fluids, specially in long-term simulations [303].

II.6.2.3 Non-linearity : Picard's and Newton's methods, and benchmark simulations

While the origins of the Oldroyd B are certainly linear (e.g. see Annex B), non-linearity sneaks in the final equation system via the objective upper-convected derivative. It is from this perspective that the Oldroyd B model is regarded as a quasi-linear model. The full set of non-linear weak equations, including the SU and DEVSS stabilisation terms, reads : find $\mathbf{U} := (\mathbf{u}, p, \tau_\mathrm{e}, \bar{\epsilon})$ such that

$$a_{\text{O-B}} := a_\mathrm{S} + a_{\mathrm{S,\ DEVSS}} + a_\mathrm{c} + a_{\mathrm{c,\ SU}} \tag{II.61}$$

$$L_{\text{O-B}} := L_\mathrm{S} + L_{\mathrm{S,\ DEVSS}} + L_\mathrm{c} \tag{II.62}$$

---

[30] Note how adding some unnaturally large dissipation stabilises the equations. There is some natural stress diffusion that stems from the molecular model but it is negligible.

$$a_{\text{O-B}} - L_{\text{O-B}} = 0 \tag{II.63}$$

$\forall\ \mathbf{V} := (\mathbf{v}, q, \phi, \psi)$. The problem can be posed in the standard spaces H_0^1 for the velocity, and L^2 for the pressure and the three components of the stress (in 2D ; not 4 because of the symmetry). To approach the problem numerically we use the Finite Element Method discretised via continuous biquadratic elements for the velocity $\mathbf{u}$, mixed with discontinuous linear elements for the pressure p and continuous linear elements for both the stress τ_{e} and the rate of deformation tensor $\bar{\epsilon}$ [298]. Even though hereafter the variables will be discrete functions belonging to discrete subspaces of the originals, we will be representing them with exactly the same symbols to ease notation. Notice that a non-linear problem has to be solved at each time step.

a) Picard's method. There are two main strategies to attack non-linear PDEs computationally, both of them iterative. The simplest is Picard's method and is fundamentally a fixed-point iteration. Concretely, one turns the problem linear at each iteration by substituting all the variables within non-linear terms by the solution resulting from the previous iteration. Writing k to index the iterations, at $k+1$ we solve

$$a_{\text{O-B}}(\mathbf{U}^{k+1}; \mathbf{V}) - L_{\text{O-B}} = 0 \tag{II.64}$$

$\forall\ \mathbf{V}$ with the convected derivative (the only non-linear term) adjusted to use the stress from the previous iteration, i.e. $\overset{\nabla}{\tau}_{\mathrm{e,a}}(\mathbf{u}^{k+1}, \tau_{\mathrm{e}}^{k})$. The result is a new solution indexed by $k+1$ that is (ideally) closer to the real solution. Termination is decided according to the norm of the difference between the last two successive solutions.

b) Newton's method. The second method is Newton's, which can be applied at the algebraic level, i.e. to the non-linear system of algebraic equations resulting from introducing the finite elment basis, or at the earlier PDE level. In the latter case, consider an approximation $\mathbf{U}^k$ of the vectorial solution field at iteration k, and a perturbation $\delta\mathbf{U}$ such that $\mathbf{U}^{k+1} = \mathbf{U}^k + \delta\mathbf{U}$ is the real solution. Of course, the problem is still non-linear if we substitute the change of variables into (II.63). However, if we are taking small enough steps we can linearise the resulting expression around the previous solution. Precisely, this is equivalent to applying Newton's method with the Gâteaux differential at $\mathbf{U}^k$ in direction $\delta\mathbf{U}$ w.r.t. $\mathbf{U}$, i.e. $d_{\mathbf{U}^k,\delta\mathbf{U}}a := \lim_{\xi\to 0} d_{\xi} a(\mathbf{U}^k + \xi\delta\mathbf{U})$. The resulting linear system, which gives a new update step $\delta\mathbf{U}$ at each iteration, is given by

$$d_{\mathbf{U}^k,\delta\mathbf{U}} a_{\text{O-B}} = -a_{\text{O-B}}(\mathbf{U}^k; \mathbf{V}) + L_{\text{O-B}} \tag{II.65}$$

$\forall\ \mathbf{V}$. Again, as the equations are quasi-linear, we only need to adjust the objective derivative. Concretely, we have $d_{\mathbf{U}^k,\delta\mathbf{U}} a_{\text{O-B}} = a_{\mathrm{S}}(\delta\mathbf{U}; \mathbf{V}) + a_{\mathrm{S,\ DEVSS}}(\delta\mathbf{U}; \mathbf{V}) + d_{\mathbf{U}^k,\delta\mathbf{U}} a_{\mathrm{c,\ SU}}(\mathbf{U}; \mathbf{V}) + \langle \delta\tau_{\mathrm{e}}, \phi\rangle_K - 2\alpha\langle \epsilon(\delta\mathbf{U}), \phi\rangle_K + \mathrm{We}\langle d_{\mathbf{U}^k,\delta\mathbf{U}} \overset{\nabla}{\tau}_{\mathrm{e,a}}, \phi\rangle_K$. That is all the terms were linear and thus $d_{\mathbf{U},\delta\mathbf{U}} a_{\bullet} = a_{\bullet}(\delta\mathbf{U}; \mathbf{V})$ except for i) the latter upper-convected derivative in a_c, which expands by the product rule :

$$d_{\mathbf{U}^k,\delta\mathbf{U}} \overset{\nabla}{\tau}_{\mathrm{e,a}} = \overset{\nabla}{\tau}_{\mathrm{e,a}}(\delta\mathbf{u}, \tau_{\mathrm{e}}^{k}) + \overset{\nabla}{\tau}_{\mathrm{e,a}}(\mathbf{u}^k, \delta\tau_{\mathrm{e}}) - \tau_{\mathrm{e}}/dt; \tag{II.66}$$

and ii) the SU diffusive term $a_{\mathrm{c,\,SU}}$, which expands similarly. In this Dirichlet-based context, notice that the step $\delta\mathbf{U}$ (and thus II.65 by extension) requires homogeneous boundary conditions.

c) Numerical simulations. To implement the Oldroyd B model we used a backwards difference scheme to approximate the time derivative and the Finite Element Method [184] to discretise the problem in space. Within this framework, we use Newton's method, i.e. we solve equation (II.65) iteratively until the stopping criterion is fulfilled. At each iteration, GMRES is used to solve the linearised system. In steady situations, the problem is first initialised by solving the corresponding Stokesian problem and then slowly stepped with increasingly higher values of We, a method known as continuation. This is sometimes not necessary in time dependent problems (think of having null initial elastic stress for example). To test the convergence of the software, we use one of two classic benchmarks for viscoelastic fluids [280, 304, 305, 306, 307, 308, 309, 310]. We focus on the flow past a cylinder in a channel, but contraction flows would be as good an option.

In particular, we use the measurements of a very idealised cell to construct the cylinder problem. We take a 16 long times $W = 8$ wide pipe with a cylinder C of diameter $R = 3.5$ (more or less the proportional size of a nucleus), an inflow average speed of about $\bar{U} = 5$, and a relaxation time as reported in the literature $\lambda_2 = 0.2$. When considered in μm and s, these numbers reflect the size and rheology of *Entamoeba histolytica* , as well as the characteristic speed of its cytoplasmic streaming. The corresponding Weissenberg number is $\mathrm{We} := \bar{U}\lambda_2/R \approx 0.3$. At this regime, the total drag $f_d = -\oint_C \mathbf{e}_x \cdot (-p\mathrm{I} + \tau_{\mathrm{v}} + \tau_{\mathrm{e}}) \cdot \mathbf{n}$ experimented by the cylinder is 138, of which 90 are due to the pressure gradient, 45 to the viscous stress, and 3 to the elastic stress ; where $\mathbf{n}$ stands for the normal and $\mathbf{e}_x$ for the unitary vector in the flow direction. The components of the computed elastic stress tensor can be consulted in Figure II.31. Further tests on convergence for increasingly higher We numbers show that the algorithm holds, at least, until $\mathrm{We} = 4$.

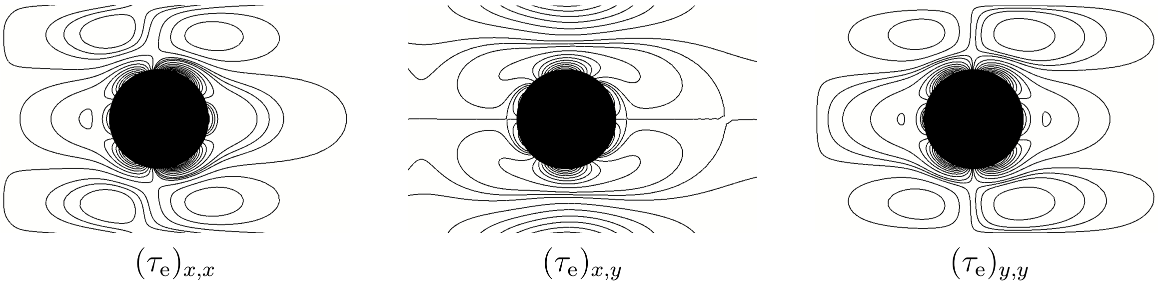
$(\tau_{\mathrm{e}})_{x,x}$ $(\tau_{\mathrm{e}})_{x,y}$ $(\tau_{\mathrm{e}})_{y,y}$

FIGURE II.31 – **Isolines showcasing the components of the simulated elastic stress tensor in the wake behind a cylinder.** Simulation at $\mathrm{We} = 0.3$, see text for the exact size of the channel and the cylinder.

II.6.2.4 Inverting time-dependency : time adjoints and checkpointing

In accordance with our aim of extracting biophysical quantities from imaging data, we adapt the data fidelity term posed by the optical flow constraint to account for the time evolution :

$$J_{\mathrm{data}} = \sum_i \left\| \mathcal{T}_i \mathbf{u} \cdot \nabla I_{i+1} + I_{i+1} - I_i \right\|_{\mathrm{K}}^2 . \tag{II.67}$$

The data are a video sequence of images I_i sampled at times t_i from the continuous time interval T. Since the movement between two consecutive images is the result of a continuous motion, the observation operator (see [311] for example) is defined here as the time integral of the velocity : $\mathcal{T}_i \mathbf{u} = \int_{t_i}^{t_{i+1}} \mathbf{u}$. Of course, our intention is to constrain this new functional to the Oldroyd equations and thus we can regularise the problem according to the physical quantities therein. In this new context, the control parameters are still **f** and **g**. In fact, there is a third candidate to control for, the possibly unknown initial elastic stress $\tau_{\mathrm{e},\,0}$, but we set it to zero because (fortunately) a lot of experiments can be started at a resting state. Under these circumstances, we propose the following regularisation :

$$J_{\mathrm{reg}} = w_1 \int_{\mathrm{T}} \|\mathbf{f} \cdot \mathbf{u}\|_K^2 + w_2 \int_{\mathrm{T}} \|\mathbf{f}\|_K^2 + w_3 \int_{\mathrm{T}} \left(\|\mathbf{g}\|_K^2 + \|\partial_t \mathbf{g}\|_K^2 \right) , \tag{II.68}$$

which encourages temporal smoothness of the boundary condition, controls the norm of both controls, and also tries to minimise the work done ; all through the three weights w_j. Intuitively, this should better pose the system, but a more formal analysis is required to analyse how well the functional and the regularisation will fare when constrained to the non-linear problem.

How do we minimise $J_{\mathrm{data}} + J_{\mathrm{reg}}$ constrained to the Oldroyd B model ? As explained in Section II.1, the adjoint equations can be derived before or after discretisation. From the discrete-first perspective, it is clearer that the adjoint equations reverse time. Indeed, consider a linear problem but know that the same intuition extrapolates to non-linear situations ; if one thinks of capturing the time structure of the problem as a block matrix, the resulting matrix will be lower triangular, representing the forward propagation of information as dictated by causality. Taking the adjoint of the system turns the matrix upper triangular, reversing the propagation of information and running back in time. Accordingly, a terminal (instead of initial) condition is required to fully specify the adjoint problem.

Most conveniently, the adjoint problem derived from a non-linear problem is linear because it only involves partial derivatives of the model and functional (see Annex A). Therefore, the computational cost of evaluating the functional derivative (one linear solve) is only a fraction of solving the original non-linear problem (a linear solve per Newton iteration). However, there is a downside : the linearisation happens about the solution of the problem. Storing the solution is not a problem if the equations are steady, but any time-dependent component of the solution will have to be stored all throughout its time trajectory. This might evolve into a massive storage problem. To tackle this issue, checkpointing algorithms only store part of the solution and recompute the rest when needed (see [312]). The optimal balance between storage and additional computational expense is generally determined in advance if the number of time steps is known *a priori*, otherwise the checkpoints can also be updated "online". Given the dolfin-adjoint library [187, 188] also provides automatic checkpointing, it might be a very good option to automatically derive the time adjoint. Alternatively, deriving the continuous time adjoint[31] is conceptually straightforward because most terms are linear and "self-adjoint" ; it will also allow for more freedom regarding the minimisation and discretisation schemes, but any implementation will have to involve a careful study on how to manage the storage of the time solutions. Neither option has been implemented in practice due to a lack of a meaningful biological questions, and of resources to set-up a system that can reproduce and expand the rheological measurements reported in the literature.

An additional difficulty lies on the domain : the cell K is constantly moving and reshaping. Handling the weak formulation can be achieved with a moving Lagrangian coordinate system (à la immersed boundary method for example) but it is not clear how to coordinate the segmented cell at each time point with the simulated movement of the fluid, specially in the adjoint context.

II.6.3 Advantages and limitations

While Oldroyd B fluids are known to be the simplest model that reproduces retardation and relaxation, as well as the simplest closed model with a molecular derivation, it is perhaps this simplicity that causes convergence issues. For example, linear elasticity is problematic in extensional flows because Hookean springs are unbounded. Even though mechanical circuits exclusively model linear responses, they set the background for non-linear behavior. The missing inspiration can be drawn from molecular considerations. In this way, one can build on a kinetic theory by considering microscopic interactions inside a flow to derive a set of constitutive equations on a macroscopic level that ideally obey the admissibility conditions set by Oldroyd. However, it is worth noting that most viscoelastic models continue to suffer at high We numbers, requiring similar stabilisation techniques to the ones already discussed.

The Phan-Thien-Tanner (PTT) model [278] is a good candidate in all these respects : it is non-linear, has a molecular explanation based on entangled polymers that can "break", and does better in extensional flow. Not only that, but it also includes shear-thinning. Although, to be completely fair, shear-thinning is usually reported in

---

[31] The weak equation needs to be integrated over time to form the Lagrangian together with the data and regularisation functionals. Integrating by parts prompts the appearance of an integral evaluated at the final time that can be eliminated by setting a terminal condition on the test function, and latter on the adjoint. The derivative with respect to $\mathbf{f}$ (for example) depends on time because $\mathbf{f}$ does and because the adjoint variables do, i.e. the full time history of the adjoint variables is required. For example, the term in the force derivative (in direction $\tilde{\mathbf{f}}$) that stems from the weak equation is $\int_T \langle \tilde{\mathbf{f}}, \mathbf{v} \rangle_K$ and thus requires the values of the adjoint variable $\mathbf{v}(t)$ over time. The two remaining terms that form the derivative (this time they originate from the functional) are $\int_T \left(2w_1 \langle \mathbf{f} \cdot \mathbf{u}, \tilde{\mathbf{f}} \cdot \mathbf{u} \rangle_K + 2w_2 \langle \mathbf{f}, \tilde{\mathbf{f}} \rangle_K \right)$ and also call for time storage.

experimental biological literature as a power law [136]. This specific behavior is modeled by generalised Newtonian models, where the viscosity is dependent on the strain rate, i.e. $\mu(\epsilon)$, but the tensorial structure remains Newtonian and strain still responds instantaneously to stress (time independence). In this context, $\partial_\epsilon \mu < 0$ and $\partial_\epsilon \mu > 0$ are respectively called shear-thinning (or pseudoplastic) and shear-thickenning (or dilatant). While perhaps shear-thinning is better apprehended, both materials can be explained from molecular interactions : for example by considering polymer alignment under shear in the former case, and hydroclustering or molecular repulsion in the latter. This phenomenon is not to be confused with viscoelasticity, which is modeled by altering the constitutive equation to include memory (stresses depend on the history of the fluid) and stress anisotropy.

Computational cost aside, an additional downside of all these models, is that they lack in automatisation. The sheer number of considerations that must be accounted for (e.g. We or geometry) to make the models converge prevents any implementation from working reliably without supervision. If the aim is to develop a framework that can be used by a wide audience without numerical training, there is still a lot of work to do. One possibility would be to explore surrogate models that can account for the deviations as uncertainties (see Chapter III for a similar approach).

To capture the properties of differently concentrated solutions involved in other cell types, other models that can capture more time scales might have to be considered. The biggest underlying problem is to decide how much is gained at a given spatiotemporal resolution and cell type by incorporating a non-Newtonian model. Answering these questions requires having access to rheometers, specially for shear-thinning and viscoelastic fluids as models are many and mostly phenomenological, and is precisely why we have abandoned this quest. With appropriate equipment, possible experiments would be : 1) magnetic beads spun under a controlled magnetic field as in [136] ; 2) micropipette experiments under controlled pressure conditions [115] ; or 3) optical tweezers to drag around a fluorescently labelled protein. In all three experiments, the fluid movement would be recorded, and the forces and pressure estimated by our method could be compared to the ground-truth. In this way, it would be possible to validate our framework and at the same time extend it to a broader audience.

III – Measuring outside the cell

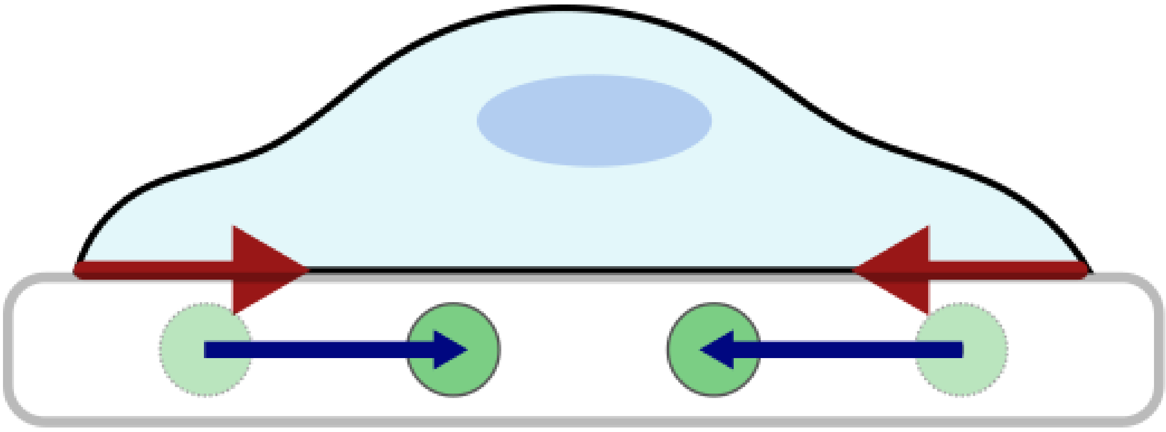

The aims of this chapter are twofold. The first is to better the framework introduced in II.1. To this end, we begin by deriving a modified optical flow functional that adapts the seminal assumption of intensity conservation to confocal microscopy. Next, we address numerical considerations ; most notably, we study the importance of the Hessian to our inverse problem and subsequently introduce Newton's method. Lastly, we extend the framework into a Bayesian setting to allow for uncertainty quantification. The second aim is to complement the internal insight from Chapter II with extracellular measurements. The importance of the extracellular matrix is extensely reported in the literature and is refound in the relevance of E-cadherin-mediated adhesions during zebrafish PGC migration (Section II.4). To serve both aims, we illustrate our new framework by reformulating the standard Traction Force Microscopy, reducing uncertainty propagation and providing error bounds of extracellular forces. Even though this chapter revolves around extracellular measurements, the results are general and thus hold both in and outside the cell.

III.1 Modified Optical Flow

The seminal optical flow constraint, as introduced in Section II.1, assumes that intensity is conserved. However, this does not necessarily reflect the underlying movement ; for example, think of projecting a 3D movement

onto a 2D image. In this section, we study the constancy assumption in the context of confocal microscopy and propose an alternative model-dependent constraint.

While discussing optical flow in Section II.1.1, we already introduced the brightness constancy assumption as a source of errors, citing changes in lighting conditions as an example [165]. Other discrepancies can be mitigated by incorporating information regarding the origin of the images. In meteorology, for example, image-based velocimetry of the atmosphere has been improved by relating the radiance emitted by a material to its density [169], which results in a continuity equation for the intensity similar to that used in transmittance imagery [313]. In the same direction, [314] derived multiple intensity conservation equations corresponding to different image modalities for fluid flows (e.g. laser sheet imaging) by making as many approximations. We approach confocal imaging in a similar way. As per our framework, we also have a physical model of the underlying material, which gives us additional flexibility to derive a novel optical flow constraint.

The displacement depicted in images is only a projection of the behavior of the fluorescent material that we would like to observe. In particular, the fluorophores of a sample emit a 3D fluorescence that is picked up by a laser with a certain spread function and projected into 2D luminance, which is then cast to the image by the optical system (Figure III.1). This transformation needs to be taken in account in order to properly relate the material of interest with its digital representation. Here we show how to pass an initial diffusion equation of fluorophore concentration through the imaging system to obtain a modified conservation equation for the image intensity. The derivation is made in general dimensions not only for the sake of generality itself, but also to take profit of more comprehensive mathematical tools.

III.1.1 The local conservation differential form

Originally, the final intensity $I : \mathrm{O} \times \mathrm{T} \longrightarrow \mathbb{R}$ imprinted on an image $\mathrm{O} \subset \mathbb{R}^{d_\mathrm{O}}$ is related to the concentration $\Psi : \Omega \times \mathrm{T} \longrightarrow \mathbb{R}$ of fluorophores that are transported within the labelled material $\Omega \subset \mathbb{R}^{d_\Omega}$, $d_\Omega > d_\mathrm{O}$, over time $\mathrm{T} \subset \mathbb{R}$. Ideally, if we follow these fluorescent compounds moving in their reference frame, their concentration should not change except for a sink or loss by diffusion [314] : $D_t\Psi = B\Delta\Psi$. In the typical biological case of beads or polymer fibers, there is no practical diffusion ($B = 0$) and thus

$$D_t\Psi = 0. \tag{III.1}$$

When a laser is shone on the fluorophores inside the material, $\Psi(\mathbf{x}, t)$ fluoresces emitting a radiance that is received by the imaging system as luminance. This luminance $L(\mathbf{x}_\Pi, t)$ is defined on the projection $\mathbf{x}_\Pi \in \Omega_\Pi$ of the material-space on the reception (image) plane of dimension d_O, where $\Pi := \{1 \,..\, d_\mathrm{O}\} \subset \{1 \,..\, d_\Omega\}$ such that the space is split via the (external [315]) direct sum $\Omega_\Pi \bigoplus \Omega_{\Pi^c} = \Omega$ (see Figure III.1). More precisely, L is the integral of the fluorophore concentration over the orthogonal or projected dimensions Ω_{Π^c} pondered by a kernel $L_0(\mathbf{x})$ describing the distribution of the laser :

$$L(\mathbf{x}_\Pi, t) \propto \int_\Gamma L_0(\mathbf{x})\Psi(\mathbf{x}, t) d\Omega_{\Pi^c}, \tag{III.2}$$

where the integration spans the virtual domain $\Gamma(\mathbf{x}_\Pi) \subset \Omega_{\Pi^c}$. This control surface can either be taken to contain the whole domain of integration, or used to approximate the decaying range of $L_0(\mathbf{x}_\Pi, \mathbf{x}_{\Pi^c})$ as a sort of optical thickness $h \in \mathbb{R}^{d_{\Pi^c}}$ ($d_{\Pi^c} := \#\Pi^c$) if necessary.

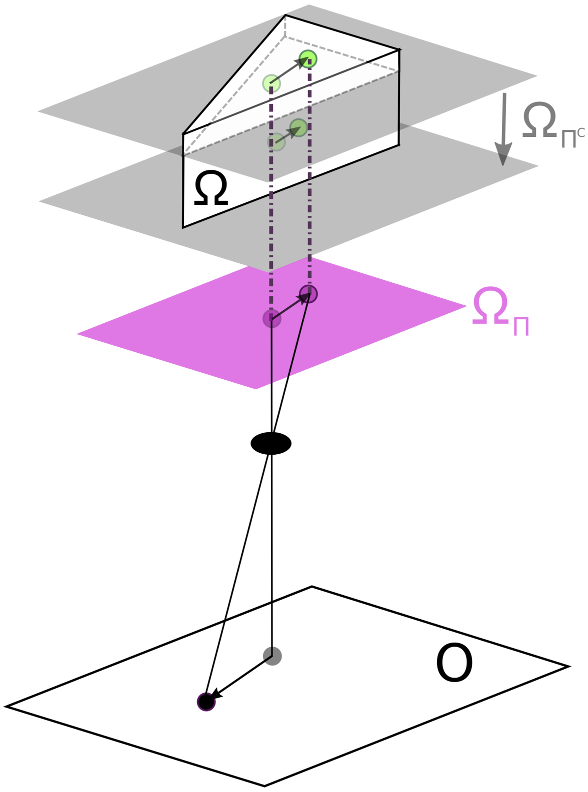

Figure III.1 – **Schematic of the projection of 3D fluorophores on a 2D image.** The fluorophore concentration Ψ (represented by a pair of green beads at different levels) in Ω (cake slice) emits a radiance that is projected (Ω_{Π^C}) by the laser sheet (grey surfaces mark example limits) into luminance on a plane Ω_Π. The optical set-up (black lens) casts it on the image O. The arrows show the difference between the real 3D movement in Ω (transparent beads correspond to the previous position) and the visible movement on the image O.

Using equations (III.1) and (III.2) we can derive (see Annex C) a conservation equation for the luminance that is valid up to first order in the orthogonal direction ($\mathbf{H}_{\Pi^c}\mathbf{u} = \mathbf{0}$) :

$$D_t l = l \nabla_{\Pi^c} \cdot \mathbf{u}_{\Pi^c}, \tag{III.3}$$

with $l := L/L_0(\mathbf{x}_\Pi, \hat{\mathbf{x}}_{\Pi^c})$ where $\hat{\mathbf{x}}_{\Pi^c} \in \Omega_{\Pi^c}$ is a byproduct of using the mean value theorem. That is the luminance is still advected, but it now has a source that depends on the out-of-'hyperplane' motion. In principle, the advection is driven by the fluoro-weighted average $\langle \mathbf{u}_\Pi \rangle$ over the projected variables (see Annex C), but if we also ignore the derivatives of $\mathbf{u}_\Pi$ in the orthogonal direction ($\mathbf{J}_{\Pi^c}\mathbf{u}_\Pi = \mathbf{0}$) then the advection only depends on $\mathbf{u}_\Pi$ itself.

Finally, the radiance received by the imaging system is cast on to the image plane by the optical system with a perspective projection $\mathbf{p} : \mathbf{x}_\Pi \in \Omega_\Pi \longrightarrow \mathbf{X} \in \mathrm{O}$ described by the collinearity equations [316, 317] in the $d_\Omega = 3$, $d_\mathrm{O} = 2$ case. More importantly, the intensity I recorded on the plane is directly proportional to the luminance if the solid angle of the camera is small [318] :

$$I(\mathbf{X}, t) \propto L(\mathbf{x}_\Pi, t). \tag{III.4}$$

Therefore (equations (III.3) and (III.4)), if we follow a pixel advected inside the image, its intensity does not change except for a source term :

$$D_t I = sI, \tag{III.5}$$

where $s(\mathbf{u}) = \nabla \cdot \mathbf{u} - \nabla_\Pi \cdot \mathbf{u}_\Pi$. In other words, the image brightness gains a source with respect to the fluorophore emission reflecting the changes due to out-of-plane motion. In the case of $d_\Omega = d_\mathrm{O}$, (III.5) reverts back to the seminal brightness constancy equation, i.e. $s_\Pi = 0$.

Even though equations (III.1) & (III.5) are expressed on different domains (Ω and O respectively), the latter holds in both (Ω_Π and O) coordinate systems because of the colinear transition $\mathbf{p} : \exists\, c \mid c\partial_{\mathbf{x}_\Pi} = \partial_{\mathbf{X}}$, $\mathbf{u}_\Pi = c\mathbf{U}$. Additionally, this means the optical flow recorded on the image by PDE (III.5) is representative of the displacement in the material up to a constant. In the rather usual case of an orthographic projection (notably in microscopy) this reduces to $\mathbf{x}_\Pi = \mathbf{X}$, $\mathbf{u}_\Pi = \mathbf{U}$ and we are no longer concerned about the constant. Since this case is the norm in microscopy from here on we write $\mathbf{x}$ instead of $\mathbf{X}$ without loss of generality.

III.1.2 The energy integral form

If we are interested in the sum over the whole domain of pixels, equation (III.5) implies minimising functional $\|D_t I - s_\Pi I\|^2_\mathrm{O}$. Our interest, however, lays on discrete displacements, not differential or continuous, and (III.5) is thus only the linear term. In fact, notice the expression involves velocity instead of displacement. This means that we need to adapt the strategy if we are to work with displacements that are not small.

First, we formulate the integrated equivalent (e.g. [319]) of equation (III.5). If we assume a constant velocity field over a time step then we can integrate the brightness equation over the pixels' trajectories as a first-order ODE :

$$I\left(\mathbf{x} + \mathbf{u}\Delta t, t + \Delta t\right) - I\left(\mathbf{x}, t\right) e^{s\Delta t} = 0, \tag{III.6}$$

where $\mathbf{u}$ is the displacement between two consecutive (Δt) time frames, $I_2 = I(\mathbf{x} + \mathbf{u}\Delta, t + \Delta t)$ and $I_1 = I(\mathbf{x}, t)$. However, this yields a highly non-linear expression and a non-convex minimisation : $\| I\left(\mathbf{x}+\Delta\mathbf{u}, t+\Delta t\right) exp\left(-s\Delta t\right) - I\left(\mathbf{x}, t\right)\|_{\mathrm{O}}^2$. Therefore, second, we linearise model (III.6) around $\mathbf{u}_w$ into a more tractable problem,

$$\mathcal{J}_{\mathrm{data}} = \|e^{-s_w}\left(\left(-I_w\nabla s_w + \nabla I_w\right)\cdot\left(\mathbf{u}-\mathbf{u}_w\right)+I_w\right) - I_1\|_{\mathrm{O}}^2, \tag{III.7}$$

where we set $\Delta t = 1$ without loss of generality and $I_w = I_2(x+\mathbf{u}_w, t+1)$, $s_w = s(\mathbf{u}_w)$. Alternatively, this is equivalent to considering $\mathbf{u}$ as a displacement, instead of a velocity, which is the point of view we will be taking hereafter. However, the expression is now valid only for small displacements. As in Chapter II, we adopt a multi-scale approach [189] to measure larger displacements : by iterating a mixture of anti-aliasing Gaussian filters and down-sampling, we obtain a pyramid of image resolutions. The displacements can then be propagated successively through all scales, from the coarsest (I_2, and $|\mathbf{u}_w|$ of the order of a pixel) until the finest (hopefully I_1, and $\mathbf{u}$). This is done by warping the image at each scale with the displacement $\mathbf{u}_w$ measured at the previous scale, i.e. by comparing I_w and I_1. Implementation details, including spline interpolation for warping and finite differences stencils, can be found in subsection III.3.3.8. We remark that with no source ($s = 0$) equation (III.7) reverts to the linearised optical flow equations, just as (III.5) reverts back to the brightness constancy equation.

III.1.3 Regularisation via PDE constraints

Notice that system (III.6) is under-determined : the problem is ill-posed. In order to solve this so-called aperture problem, in the field of optical flow it is customary to regularise the variational formulation by adding a smoothness constraint :

$$\mathcal{J}(\mathbf{u}) = \mathcal{J}_{\mathrm{data}}(\mathbf{u}) + \alpha\mathcal{J}_{\mathrm{feg}}(\mathbf{u}), \tag{III.8}$$

where $\alpha \in \mathbb{R}_{>0}$ is a parameter that controls the balance between data fidelity and imposed knowledge, and can vary with the multi-resolution scale k (e.g. $ln(\alpha) \propto -k$ emphasises smoothing at coarser levels [190]). For example, a classic approach is to require first-order spatial smoothness of the displacement [109] :

$$\mathcal{J}_{\mathrm{reg}}(\mathbf{u}) = \int_{\mathrm{O}} \nabla\mathbf{u} : \nabla\mathbf{u}\; d\Omega = \|\nabla\mathbf{u}\|_{\mathrm{O}}^2. \tag{III.9}$$

Here we propose a less arbitrary approach to regularise the problem : we incorporate our knowledge of the system's behavior in a way similar to [174, 175, 320]. As in Chapter II, we will constrain the observed motion to act like a continuum mechanics model of the observed material ; in this case a linearly elastic material. To present the model we first introduce Traction Force Microscopy.

III.2 Traction Force Microscopy

As exemplified in Section II.4 with E-cadherin-mediated adhesions, extracellular forces are essential to many biological functions. Traction Force Microscopy (TFM) is probably the most widely used approach to measure the forces exerted by cells on the extracellular substrate. Since we will illustrate our new framework by refomulating TFM, we begin by giving a short overview of the method. We then define the problem mathematically and propose an elastic model to describe the constitutive behavior of the substrate.

As was introduced in Chapter I (see Section I.2.3 in particular), cell-generated mechanical forces are essential to biological function. In this section we focus on traction forces exerted at the interface between the cell and the substrate or the ECM, which are transmitted through adhesion proteins such as integrin.

In general, forces cannot be measured directly, but rather have to be inferred from their measurable effects, for example from the deformation exerted on a calibrated material. This calibration is typically summarised in a system of constitutive equations that describe the physical response of the material. In this regard, the first documented effort to measure traction forces at a cellular scale (find a review in [321]) consisted in a thin elastic sheet that buckles under cellular traction [21]. While the approach is visually informative, the formation of wrinkles is a highly non-linear phenomenon and thus a precise quantification of the force is complicated by instabilities. A more quantitatively accessible method, known as Traction Force Microscope on soft elastic substrates (here S-TFM), was introduced in response [322, 323]. In this case, the substrate is a thick film made of a material that remains under a linear regime at the cellular-force scale, e.g. polyacrylamide. The forces can then be computed from the deformation of the material, which is typically seeded with fiduciary markers (e.g. fluorescent beads) to this purpose. To further facilitate the reconstruction of the traction, arrays of micropillars can be microfabricated to act as simple local strain gauges at the price of introducing an arbitrary substrate topography [324, 325, 326]. In an alternative direction, photo-quenching or Förster resonance energy transfer (FRET) allows to access forces at a molecular level by genetically engineering a linker whose fluorescence changes under strain [137]. This approach is very flexible regarding the microenvironment, but is remarkably hard to calibrate and is rather situational ; for example, it cannot measure macroscopic forces such as those between subcellular structures. It is worth remarking that TFM is not only useful in a biological context, but that also other disciplines such as experimental physics benefit from it [327].

Despite the constant evolution of the field, S-TFM remains the most used among TFM methods, likely because it offers the best value. More concretely : the experimental set-up is simple compared to microfabrication or genetic engineering ; the same approach adapts to a variety of substrates and is highly generalisable to different 2D or 3D[1] environments ; and the stress-strain relation is conceptually straightforward, yet still supported by extensive literature. Precisely, the large volume of literature on how to convert deformation into force reflects the interest of the method, but at the same time indicates that no approach has been definitive. Indeed, there exist a lot of methods to tackle this inverse problem [321]. Most approaches resort to Green's functions, inverting the problem either using the boundary element method [322, 323] or in Fourier space [328, 329, 327, 330, 331], a method known as FTTC. However, Green-based methods often need further assumptions : e.g. the cell cannot generate momentum, the material is incompressible, or the substrate is a half-plane (leading to Boussinesq's solution [178]). Alternatively, FEM-based approaches [332, 333] are gaining traction because they are more flexible to changes in geometry (e.g. 3D [334, 335]) and models (e.g. the non-linearity of more biologically relevant materials or big strains [336]). These include a PDE-constrained minimisation [337] reminiscent of our method in II.1, but decoupled from the velocimetry. Another approach is to inform the TFM problem with a cell model, notably by incorporating the position of adhesion and cytoskeletal proteins [229]. In principle, traction stress can also be reconstructed directly from the displacement field, but the derivatives involved in this strategy make it very sensitive to noisy data [338]. In fact, noisy data are an issue in all TFM methods because the problem is ill-posed[2]. That is small error-induced variations on the deformation field have great repercussion on the reconstructed traction [339, 321]. Therefore, the inverse problem needs to be regularised by adding *a priori* information, either via image [340] or reconstruction [341] filters, or à la Tikhonov [330]. In contrast, the impact of the imaging set-up (from the microscope to the beads) and the accuracy of the displacement field have been less investigated [164]. All in all, several fronts are still open.

Good part of reconstructing the map of traction forces accurately is obtaining reliable estimates of the deformation field. The displacement map can be extracted from a reference image, where the material is relaxed, and an image where the substrate is deformed by the cell. Depending on the density of fiduciary markers, the literature resorts to different PIV techniques ; most commonly, correlative-based tracking for higher densities, and multiple particle tracking for lower. However, recent studies have shown that methods based on the optical flow constraint obtain comparatively more accurate displacement estimates in TFM in particular [164], and in biological imaging in general [163]. While it might seem counter-intuitive that a technique looking for dense reconstructions outperforms techniques that exploit the sparsity of the fluorescent beads, the reality is that typical densities are high enough to maximally sample the domain at the microscospe's resolution and that the elasticity equations are smoothing. This also casts doubt on the necessity of purposefully seeding the material ; perhaps imaging the substrate with a 2-photon microscope or tagging[3] the polymers

---

[1] Though 3D dynamic imaging is still subpar in biology.

[2] For example, think of the long range $(1/r)$ of the Green's function in this context.

[3] In fact, gelified polyacrilamide is fluorescent when excited at 280 or $340nm$, with maximum emission at 340 and $460 - 520nm$. Its fluorescence can be greatly reduced by by adding dithiothreitol

directly might be enough in this respect.

All S-TFM methods have in common that PIV and force reconstruction are decoupled. While this allows for new developments in both disciplines to be integrated easily, the problem ends up being regularised twice. In addition, the two step process is keen on propagating uncertainties. Using our framework, we are able to regularise the inverse problem directly on the resulting force (i.e. only once), potentially reducing uncertainty propagation. Moreover, the FEM underlying our framework lets us work at the incompressibility limit, whereas the combination of Nitsche's method and adjoint-based minimisation allows us to introduce free boundary conditions because they can also be guessed from the image pair. For the same reasons, the method works in 3D out of the box, and extending it to non-linear models is conceptually straightforward. On a different note, our attempt at taking in account the image setting is threefold : out-of-plane motion via the modified conservation equation introduced in the previous section, trying to reduce the need for point-wise markers via a dense flow estimator like optical flow, and turning the method more global via multi-resolution. Another issue regarding S-TFM methods, is that uncertainty is not quantified. To our knowledge, no error bounds are ever provided for the reconstructed force except for those that result from averaging over many samples. In the incoming sections of the thesis we will also be proposing a way to go from pixel error all the way to traction error under the same framework.

The final remark of this short review on TFM methods concerns the experimental characterisation of the substrate's elasticity (through the constants of the constitutive equation) and is relegated to Annex D.

III.2.1 Definition of the problem to extract cellular tractions

Consider a cell in either of the two following cases : (i) a cell laying on a flat substrate and (ii) a cell either on a rugged surface or directly inside the extracellular matrix (EM). In both cases cells exert a traction force on their surrounding surface and the EM is deformed as a result. Even though (ii) is usually more informative and biologically relevant, (i) is much more used for its simplicity both on the computational and the experimental side (including both microscopy and wet lab). In any case, the EM is seeded with fluorescently labeled beads ; after a deformation of the material, the position of the beads change and can be compared to a resting state to obtain the displacement $\mathbf{u} : \Omega \longrightarrow \mathbb{R}^{d_\Omega}$, where $\Omega \subset \mathbb{R}^{d_\Omega}$ is the EM domain reflected in the field of view of the microscope. The cell has a domain $K \subset \Omega$, and stresses the substrate either (i) as a body force $\mathbf{f} : K \longrightarrow \mathbb{R}^{d_\Omega}$; or (ii) as a traction boundary condition $\mathbf{T} : \partial K \longrightarrow \mathbb{R}^{d_\Omega}$. Generally, the stresses can be further localised [229] as a subset of K because the cells do not adhere to their substrate continuously through their surface, but discretely through small patches called focal points. While the domain of adhesion is not readily available because it requires fluorescent labeling of a protein involved

---

or by replacing TEMED with sulphite [342].

in anchoring such as integrin or paxilin [343, 229], we note that the formulation can accommodate this information simply by considering these regions as K in place of the cell.

The problem then consists in recovering the forces $\mathbf{f}, \mathbf{T}$ exerted by the cell from a measurement of $\mathbf{u}$, i.e. an inverse problem. However, let us first introduce the forward problem : find $\mathbf{u}$ given $\mathbf{f}, \mathbf{T}$. That is we need constitutive equations that describe the physical response of the material that the cell is deforming.

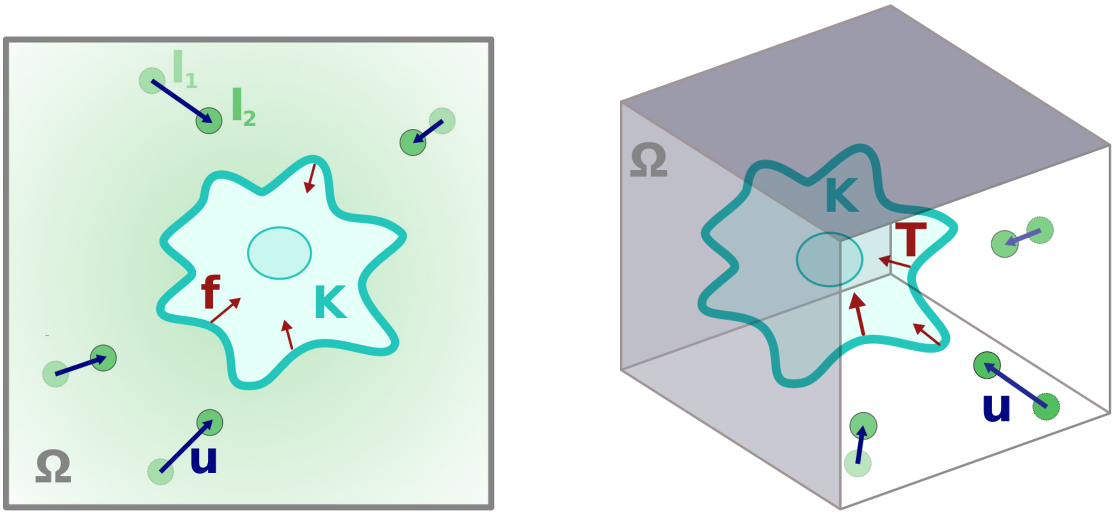

2D TFM

3D TFM

Figure III.2 – **Schema of TFM.**

III.2.2 Constitutive equations : a nearly-incompressible linearly elastic model

Many different polymers can be chosen to build EMs with properties ranging from elastic to viscoelastic. Conveniently, in most experimental set-ups the substrates used are comparatively soft and remain linear under cellular stress. Examples of these materials are polyacrilamide (PAA) gels [344] and polydimethylsiloxane (PDMS) gels [345]. With this consideration, in this section we present an isotropic linearly elastic model both for (ii) a general 3D situation and (i) its 2D plane-stress projection. Contrary to most TFM approaches, in this work we obtain a better control and stability of the model by formulating the would-be (see footnote 4) hydrostatic pressure and deviatoric stress as a coupled system of PDEs. This mixed formulation is also able to represent the incompressible limit, which is specially relevant for the stability of nearly incompressible materials such as PAA and PDMS. First, we present the differential form of the elastic equations. Second, we define the final forward problem (find $\mathbf{u}$ given $\mathbf{f}$, $\mathbf{g}$, $\mathbf{T}$) by deriving the weak form of this system and choosing suitable Hilbert spaces for the functions involved. Given the symmetries, the resulting formulation is equivalent to the principle of virtual work for a deformable body. We note that the framework developed in this paper can be adapted to any material model (e.g. non-linear elasticity) given its weak or energy form. And last, we use Nitsche's approach to control for the boundary conditions.

III.2.2.1 The local conservation differential form

An isotropic linearly elastic solid can be described with the Navier-Lamé (or -Cauchy) equations

$$(\lambda+\mu)\nabla\left(\nabla\cdot\mathbf{u}\right)+\mu\Delta\mathbf{u}+\mathbf{f}=0, \tag{III.10}$$

where $\lambda\in\mathbb{R}_{>0}$ and $\mu\in\mathbb{R}_{>0}$ are the Lamé coefficients, which are related to the more familiar Young's modulus E and Poisson's ratio ν as

$$\mu=\frac{E}{2\left(1+\nu\right)}\text{ and }\lambda=\frac{E\nu}{\left(1+\nu\right)\left(1-2\nu\right)}. \tag{III.11}$$

Although expression (III.10) is so far the standard in TFM, in this work we propose instead to split the original expression of the stress tensor $\boldsymbol{\varsigma}:\Omega\longrightarrow\mathbb{R}^{d_\Omega}\times\mathbb{R}^{d_\Omega}$ into what would be the hydrostatic and deviatoric components in the incompressible limit. That is, if $\boldsymbol{\varsigma}:=\lambda\,\mathrm{Tr}\left(\boldsymbol{\varepsilon}(\mathbf{u})\right)\mathbf{I}+2\mu\boldsymbol{\varepsilon}(\mathbf{u})$ is the tensor describing linear elasticity with the symmetric strain-rate gradient $\boldsymbol{\varepsilon}(\mathbf{u}):=1/2\left(\nabla\mathbf{u}+\nabla\mathbf{u}^T\right)$, we introduce an "artificial" pressure-like[4] variable p as a source term for the displacement in proportion to the incompressibility-like λ of the material : $\nabla\cdot\mathbf{u}+p/\lambda=0$. This yields

$$\boldsymbol{\varsigma}\left(\mathbf{u},p\right)=-p\mathbf{I}+2\mu\boldsymbol{\varepsilon}(\mathbf{u}) \tag{III.12}$$

for the stress, whose divergence is driven by the applied forces as

$$\begin{cases}\nabla\cdot\boldsymbol{\varsigma}=-\mathbb{1}_{\mathbf{f}|\mathrm{K}} & \text{in }\Omega\\ \nabla\cdot\mathbf{u}=-p/\lambda & \text{in }\Omega\\ \boldsymbol{\varsigma}\cdot\mathbf{n}=\mathbb{1}_{\mathbf{T}|\partial\mathrm{K}} & \text{on }\Gamma_{\mathbf{T}}\\ \mathbf{u}=\mathbf{g} & \text{on }\Gamma_{\mathbf{g}}\end{cases} \tag{III.13}$$

where $\mathbf{T}$ and $\mathbf{g}$ are the traction and displacement boundary conditions on boundary parts $\Gamma_{\mathbf{T}}$ and $\Gamma_{\mathbf{g}}$ respectively (here $\Gamma_{\mathbf{T}}\sqcup\Gamma_{\mathbf{g}}=\partial\Omega$ if the problem is to be well posed) ; and $\mathbb{1}_{\bullet|\bullet}$ are the extension with zeros of the cell forces and tractions to their respective supersets. The advantages of this choice of split formulation (III.12 & III.13) are

---

[4] p is only the real 3D hydrostatic pressure in the incompressible case [178, 346]. The real hydrostatic pressure is $-\boldsymbol{\varsigma}_{i,i}$ or $-(\lambda+2\mu/3)\mathbf{u}_{i,i}$, instead of $-\lambda\mathbf{u}_{i,i}$, but both agree at the limit $\lambda\to\infty$. This is better understood by expressing the stress tensor as a sum of hydrostatic compression and pure shear $\boldsymbol{\varsigma}_{i,j}=Bu_{k,k}\delta_{i,j}+(2\mu u_{i,j}-u_{k,k}\delta_{i,j}/3)$ with respective moduli B and μ, where $\lambda=B-2\mu/3$. Therefore λ does not seem to have a straightforward physical meaning other than being convenient to group the divergence and express near incompressibility. We note also that rigid motions constitute a singularity of the equation (see (III.10)).

threefold. First, it is natural to handle incompressible ($\lambda \to \infty$) materials, as opposed to simpler schemes such as (III.10), which typically underestimate the deformation (locking). Second, the divergence of the field can be independently monitored and embedded into the optical flow multi-resolution scheme through the variable p (see Section III.2.3). And third, the split approach is convenient to formulate and stabilise the weak variational problem (see Section III.2.2.3) [347, 348].

III.2.2.2 The 2D case : plane stress

While this and the forthcoming framework are formulated for the more general case of three-dimensional imaging data ($\Omega \subset \mathbb{R}^3$), we recognise that 3D cell microscopy is still not widely used in biology and often suffers from technical limitations. In this work, we adapt both the elasticity equations (III.13) (here) and the data assimiliation formulation (III.6) (Section III.1) to also consider a two-dimensional projection of the real problem.

Here, we consider a plane-stress model (similar to shallow-water) : we assume $\varsigma_{i,z} \approx 0$ as compared to the longitudinal internal stresses. Therefore, the in-plane strain tensor is uniform over the thickness [178] and we can integrate (or average) the 2D displacement $\mathbf{u}_{x,y}$ over the effective depth $h \sim 1\mu m$ of the microscope's field. Further derivation (that we adapt to (III.13)) shows the 3D equation of linear elasticity can then be reduced to its standard planar form (equation (III.13) with $\Omega \subset \mathbb{R}^2$) by adjusting its constants as

$$\bar{\mu} = \mu \text{ and } \bar{\lambda} = \frac{2\mu}{1 + \frac{2\mu}{\lambda}}, \tag{III.14}$$

where μ and λ are the original material parameters in (III.11). The original planar forces can then be recovered : $\mathbf{f} = h\bar{\mathbf{f}}$, where $\mathbf{f}$ is the traction at the surface. Finally, under the plane-stress paradigm, the full space divergence can be deduced from its flat projection :

$$2\mu\partial_z\mathbf{u}_z = -\bar{\lambda}\nabla_{x,y} \cdot \mathbf{u}_{x,y} = p, \tag{III.15}$$

where the subscript indicates the subset of components considered. To assess the adequacy [321] of this approximation we consider two main aspects. First, the plate is sufficiently thin : the cell is generally placed on top of a substrate which is $10 - 100$ fold wider/longer than it is thick. Alternatively, one can consider the 3D boundary conditions. Since the vertical displacement is comparatively smaller in experiments, $\partial_x\mathbf{u}_z$ can be neglected by (III.13) and thus the characteristic depth of the problem is also around $1\mu m \sim \mu\mathbf{u}_x/\mathbf{T}$ [337], i.e. of the same order as the microscope's depth of field.

III.2.2.3 The energy integral form

In order to solve these coupled linear elliptic partial differential equations (PDEs) via the Finite Elenement Method (FEM), we derive the weak formulation of (III.13).

We multiply the equations by respective test functions ($\mathbf{v}$ and q), integrate by parts, assume $\mathbf{g}$ is given as a Dirichlet condition, and exploit that the product of antisymmetric and symmetric tensors is zero. This process yields a bilinear, a_0, (containing the unknowns $\mathbf{u}$ and p) and a linear, l_0, variational forms :

$$\begin{aligned} a_0((\mathbf{u},p),(\mathbf{v},q)) &:= \langle \boldsymbol{\varsigma}(\mathbf{u},p), \boldsymbol{\varepsilon}(\mathbf{v})\rangle_\Omega \\ &- \frac{1}{\lambda}\langle p,q\rangle_\Omega - \langle \nabla\cdot\mathbf{u}, q\rangle_\Omega, \qquad \text{(III.16)} \\ l_0((\mathbf{v},q);(\mathbf{f},\mathbf{T})) &:= \langle \mathbf{f},\mathbf{v}\rangle_{\mathrm{K}} + \langle \mathbf{T},\mathbf{v}\rangle_{\partial\mathrm{K}} \qquad \text{(III.17)} \end{aligned}$$

$a_0 - l_0 = 0$ is then the weak equation and its solutions $(\mathbf{u},p)$ are called weak because the problem has been relaxed (they are only solutions with respect to the tests or, equivalently, in the sense of a distribution). However, many laws of physics are derived originally in their integral (as opposed to differential) form and thus the weak version is not that so : in this case, $\langle \boldsymbol{\varsigma}(\mathbf{u},p), \boldsymbol{\varepsilon}(\mathbf{v})\rangle_\Omega$ arises in the minimisation of elastic (strain) potential energy and l considers the work done on the system by the cell. To concretise the problem, we ought to choose proper spaces on Ω for the formulation. We can select a space F depending on the expected behavior of the traction forces $\mathbf{f}\in F$. Here, we have taken the Sobolev space $F = L^2 := W^{0,2}$ because it is a Hilbert space and fits in well with the required integrals[5]. This space is a standard choice both in the forward [349, 350] and inverse [351] cases, and is accompanied by an election of both the trial and test function spaces that makes finite all terms in (III.16) :

$$UP_{\mathbf{g}} := W^{1,2}_{\mathbf{g}|\Gamma_{\mathbf{g}}}\left(\Omega;\mathbb{R}^{d_\Omega}\right)\times W^{0,2}(\Omega;\mathbb{R}) \text{ and } VQ_{\mathbf{0}} := W^{1,2}_{\mathbf{0}|\Gamma_{\mathbf{g}}}\left(\Omega;\mathbb{R}^{d_\Omega}\right)\times W^{0,2}(\Omega;\mathbb{R}), \qquad \text{(III.18)}$$

where we write $\bullet|\Gamma_{\mathbf{g}}$ to express the respective boundary conditions [352, 353]. The forward problem can then be formulated formally as :

$$\text{find } (\mathbf{u},p)\in UP_{\mathbf{g}} \text{ such that } a_0 = l_0 \ \forall(\mathbf{v},q)\in VQ_{\mathbf{0}}. \qquad \text{(III.19)}$$

Once in this form, concepts of algebra can be used to show that both the differential and the weak formulation are equivalent [354] and to establish uniqueness, stability and regularity of the solutions [346, 355, 356]. Safe the term $\langle p,q\rangle_\Omega$, the setting resembles the classical Stokes problem. However, this extra integral is not detrimental and, in fact, helps stabilize the saddle point problem.

An extra mechanical equilibrium constrain can be added to the weak formulation to ensure that all forces integrate to zero $\int_\Omega \mathbf{f} = 0$. In this case, one would weight the integral with a scalar Lagrange multiplier and follow suit. However, we refrain from forcing the system into equilibrium as, for now, we do not want to exclude the possibility of working with cells that are half-way out of the image.

---

[5] **NOTATION :** we notate $\langle\bullet,\bullet\rangle_*$ the L^2-inner product of the appropriate dimension over a domain $*$, and $\|\bullet\|_*$ the induced norm ; e.g. $\langle\boldsymbol{\varepsilon}(\mathbf{u}),\boldsymbol{\varepsilon}(\mathbf{v})\rangle_\Omega = \int_\Omega \boldsymbol{\varepsilon}(\mathbf{u}) : \boldsymbol{\varepsilon}(\mathbf{v})\ d\Omega$ with the Frobenius tensor product $\boldsymbol{\varepsilon}(\mathbf{u})_{ij}\boldsymbol{\varepsilon}(\mathbf{v})_{ij}$, or $\langle\mathbf{u},\mathbf{v}\rangle_\Omega = \int_\Omega \mathbf{u}\cdot\mathbf{v}\ d\Omega$ with the dot product.

III.2.2.4 Weak boundary condition via Nitsche's approach

To have direct control over the boundary conditions $\mathbf{g}$ in the weak formulation we take Nitsche's approach [349, 357] [6]. We prefer $\mathbf{g}$ over $\mathbf{T}$ because we can regularise the former more naturally according to the optical flow constraint. We also remark that the real quantity of interest is still $\mathbf{f}$, and that controlling for $\mathbf{g}$ is mostly a computational requirement. Ideally, we would like to keep the system consistent, symmetric and "as coercive as possible". However, promoting the boundary term $\langle \mathbf{T}, \mathbf{v} \rangle_{\Gamma_\mathbf{g}}$ into its original bilinear form $-\langle \boldsymbol{\varsigma}(\mathbf{u}, p)\mathbf{n}, \mathbf{v} \rangle_{\Gamma_\mathbf{g}}$ breaks the symmetry. To compensate, a productive zero $(\mathbf{u} - \mathbf{g})|_{\Gamma_\mathbf{g}} = 0$ is added. While the system is then consistent and the bilinear form is symmetric, we add a final term $\langle \mathbf{u} - \mathbf{g}, \mathbf{v} \rangle_{\Gamma_\mathbf{g}}$ to be able to proof [7] existence and uniqueness using the inf-sup [361] or Ladyzhenskaya–Babus'ka–Brezzi (LBB) condition for saddle point problems [362, 363]. The resulting system is

$$a - l = 0 \tag{III.20}$$

where

$$\begin{aligned} a((\mathbf{u}, p), (\mathbf{v}, q)) := a_0((\mathbf{u}, p), (\mathbf{v}, q)) \qquad & - \langle \boldsymbol{\varsigma}(\mathbf{u}, p)\mathbf{n}, \mathbf{v} \rangle_{\Gamma_\mathbf{g}} \\ & - \langle \boldsymbol{\varsigma}(\mathbf{v}, q)\mathbf{n}, \mathbf{u} \rangle_{\Gamma_\mathbf{g}} + \frac{\xi}{h} \langle \mathbf{u}, \mathbf{v} \rangle_{\Gamma_\mathbf{g}}, \qquad \text{(III.21)} \\ l((\mathbf{v}, q); (\mathbf{f}, \mathbf{g}, \mathbf{T})) := l_0((\mathbf{v}, q); (\mathbf{f}, \mathbf{T})) \qquad & - \langle \boldsymbol{\varsigma}(\mathbf{v}, q)\mathbf{n}, \mathbf{g} \rangle_{\Gamma_\mathbf{g}} + \frac{\xi}{h} \langle \mathbf{g}, \mathbf{v} \rangle_{\Gamma_\mathbf{g}}. \qquad \text{(III.22)} \end{aligned}$$

This equation is formulated in the context of new spaces $(\mathbf{u}, p) \in UP$, $(\mathbf{v}, q) \in VQ$, which correspond to the old spaces $UP_\mathbf{g}$, $VQ_\mathbf{0}$ but without enforcing the boundary condition. In fact, the two spaces are now the same but we will differentiate them to keep the forthcoming formulation slightly more general. Contrary to typical problems with strong Dirichlet conditions, well-posedness of the discrete problem does not result as directly from that of the continuous problem because the spaces are not conforming in principle. Instead, the constant $\xi > 0$ has to be introduced to stabilise the discrete Galerkin approximation with respect to a mesh-dependent norm. To this end, ξ must be taken large enough with respect to the constant h that characterises the size of discretisation [364, 365].

Usually, we have no information regarding $\mathbf{T}$ and therefore we take $\Gamma = \Gamma_\mathbf{g}$, $\Gamma_\mathbf{T} = \emptyset$.

III.2.3 Formulation of a PDE-constrained inverse problem for TFM

Now that we have introduced the forward problem, let us formulate TFM. The corresponding inverse problem is to recover the traction $\mathbf{f}$ and boundary conditions $\mathbf{g}$ from a measurement of the substrate deformation $\mathbf{u}$. With this aim, an image of the

---

[6] Find some original references in [358] (German) or [359], and examples of applications to the Navier-Stokes equations in [360, 311].

[7] The task is complicated by the lack of boundary conditions in the test space.

system (either 2D or 3D) is taken before and after the deformation. In standard S-TFM, the displacement would be extracted from the before-after image pair using PIV techniques ; and the traction derived therefrom. Conversely, we propose to constrain optical flow to the linearly elastic PDEs describing the ECM.

In particular, we recall our modified optical flow conservation equation (III.7). Although the formulation of the framework will be general, we restrict its applications to real live-cell TFM : either with (i) $d_\Omega = 3$ (in fact we can use $d_\Omega = 2$), $d_{\mathrm{O}} = 2$ or (ii) $d_\Omega = d_{\mathrm{O}} = 3$. We first argue the 2D case. As detailed in Annex C, there can be two main reasons for our formulation to be more relevant than the standard approach : orthogonal variations of either the displacement or the fluorophore concentration. In the present context, both are worthy of consideration. First, there is movement along the z direction ; in fact, we have an expression for its derivative in (III.15). Second, the derivative of $\partial_z \Psi$ is non-zero. Indeed, as beads keep getting smaller (e.g. $0.5\mu m$ in 2009 [366], $0.2\mu m$ in 2019 [367]), the fluorescence gradient along the projection direction of the microscope becomes more relevant because the optical thickness is in the order of $\sim 1\mu m$. An additional note is that the 2D plane stress model results in a constant planar motion along the z-direction, i.e. $\partial_z \mathbf{u}_{x,y} = 0$, and therefore the approximation made in (III.1.1) holds exactly. Under this model, the source of the conservation equation (III.5) is $s = p/(2\mu)$. On the other hand, in 3D we have no source $s = 0$. Therefore, in practice (see Section C.1), we regain the original 3D brightness constancy equation.

The conservation equation relates the image intensity with the displacement, but it is under-determined. To regularise the expression and pose the inverse problem all at once, we use the linearly elastic PDEs of the substrate model. That is we require the displacement term $\mathbf{u}$ not only explains the data (equation (III.7)) but also fulfills the model (equations (III.13) or (III.20)). If we consider $\mathbf{f}$, $\mathbf{g}$ to be optimal control variables and $\mathbf{u}$, p optimal states, this idea can be formally expressed as solving (iteratively over the scales) the following problem :

$$\operatorname*{argmin}_{\mathbf{f},\mathbf{g}} \ \mathcal{J}(\mathbf{u}(\mathbf{f},\mathbf{g}),\mathbf{f},\mathbf{g}) \ := \ \mathcal{J}_{data}(\mathbf{u}) + \mathcal{J}_{reg}^{\bullet;\bullet}(\mathbf{f},\mathbf{g}) \text{ subject to (III.7)} \tag{III.23}$$

where $\mathcal{J}_{reg}^{\bullet;\bullet}(\mathbf{f},\mathbf{g}) = \mathcal{J}_{reg}^{\bullet}(\mathbf{f}) + \mathcal{J}_{reg}^{\bullet}(\mathbf{g})$ indicates the regularisation of $\mathbf{f}$ and $\mathbf{g}$ respectively. Hereafter we use $\mathbf{u}$ for either the full 2D or 3D displacement, and only use the material domain Ω because we can make it match with the image domain O. With all this strategy we obtain three main advantages : we can estimate physically relevant quantities (the goal here is to measure $\mathbf{f}$, and $\mathbf{g}$ allows us to not limit ourselves to zero boundary conditions) ; the model will "inpaint" local absences of information yielding highly-resoluted dense vector fields ; and we can regularise the system in a more plausible way. For example,

$$\mathcal{J}_{reg}^{L^2,L^2} := \alpha \|\mathbf{f}\|_{\mathrm{K}}^2 + \gamma \|\mathbf{g}\|_{\partial\mathrm{K}}^2 \tag{III.24}$$

with $\alpha, \gamma \in \mathbb{R}_{>0}$. Another option is to minimise the derivative of $\mathbf{g}$ normal to the boundary $\mathcal{J}_{reg}^{\mathbf{n}}(\mathbf{g}) := \gamma \|\nabla \mathbf{g} \cdot \mathbf{n}\|_{\partial\mathrm{K}}^2$. However, $\mathbf{g}$ is already regularised through the optical data term so it does not need much attention. Conversely, in subsection III.3.3.7 we present three continuous (almost everywhere) and convex regularisation terms on $\mathbf{f}$ that are inspired by different biological questions. In fact, we can even argue an appropriate range of values for the regularisation weight α (see Annex E). We remark that the final data and regularisation terms are convex and our constrain linear. Therefore the problem has a good chance of being well-posed.

An interesting addition to the data term is possible when we have multiple data for a common displacement field $\mathbf{u}$. For instance, we could image fluorescent beads of different wavelengths in respective channels [330] and obtain an indexed series I_1^j, I_2^j, $j \in J$ of pair-wise before-after images. The resulting data functional would simply be the sum : $\sum_J \omega_j \mathcal{J}_{data}(I_1^j, I_2^j)(\mathbf{u})$, possibly with some weights ω_j reflecting our confidence on each measurement. The generalisation of what follows to this alternative functional is straightforward. A last bio-inspired possibility would be to minimise the area where $\mathbf{f}$ is zero in an attempt to find cellular anchor points.

In the next section, we show how to approach the PDE-constrained minimisation of functional (III.23) via the adjoint method. In section III.4, we solve the equivalent problem under a Bayesian framework.

III.3 Deterministic PDE-constrained inverse problem

We take the opportunity of reformulating TFM to reinvent the framework proposed in II.1. In particular, our original method has some occasional stability and convergence issues that we tackle by posing the problem on more solid mathematical grounds. In this direction, we study the importance of the Hessian to our inverse problem and subsequently introduce Newton's method. In addition, we analyse all the linear systems and propose appropriate preconditioners to make the problem scalable, which is particularly interesting for our multi-resolution scheme. We also find that optimising with respect to the boundary conditions is easier after Nitsche's reformulation of the weak equations. Finally, we present different regularisations and their corresponding interpretations. In the particular case of L^2 regularisation, instead of resorting to iterative descent methods, we show that the inversion can be solved directly by addressing a coupled system of linear equations.

We approach the mathematical optimization problem by writing out the Lagrangian

$$\mathcal{L} = \mathcal{J}(\mathbf{u}, \mathbf{f}, \mathbf{g}) + a((\mathbf{u}, p), (\mathbf{v}, q)) - l((\mathbf{v}, q); (\mathbf{f}, \mathbf{g})), \tag{III.25}$$

while reusing the weighting function tuple $(\mathbf{v}, q)$ in the weak formulation to represent the multipliers. Given the big number of variables, the method of Lagrange multipliers comes at a large computational cost. A viable option is to calculate the gradient of the functional and to apply a gradient descent algorithm. However, since the total derivative of the functional with respect to the control variables $d\mathcal{J}/d(\mathbf{f}, \mathbf{g})$ has dependencies on the state variables through the elasticity PDEs, a finite difference approach would require a costly solve of equation (III.13) for each of the many directions. We propose to calculate the gradient by the adjoint method (a way to exploit the dual space of the PDE operator, see Annex A for some intuition) at the cost of only one additional solve of an equation akin to (III.13). Similarly, we can build the Hessian action of the functional by formulating two incremental systems (forward, and adjoint) that correspond to the second variations. Together, the four resulting PDEs can assemble a Newton system, which results in a descent direction that is exact up to quadratic expansion. Since the PDE constraint is linear, Newton's method should converge in a single step for L^2-based regularisation terms.

III.3.1 First order variations to construct the gradient

In order to illustrate the adjoint method we first derive the differential form of the Lagrangian

$$\delta\mathcal{L} = D_{(\mathbf{u},p)}\mathcal{L} \cdot (\tilde{\mathbf{u}}, \tilde{p}) + D_{(\mathbf{v},q)}\mathcal{L} \cdot (\tilde{\mathbf{v}}, \tilde{q}) + D_{(\mathbf{f},\mathbf{g})}\mathcal{L} \cdot (\tilde{\mathbf{f}}, \tilde{\mathbf{g}}) \tag{III.26}$$

where we write $\delta\mathcal{H}$ for the Gâteaux derivative of a functional $\mathcal{H}(s)$ in direction $\tilde{\boldsymbol{s}}$. Our original aim is to calculate the total derivative of $\mathcal{J}$. Notice that if the elastic equation is fulfilled, then $a = l$ and computing $\delta\mathcal{L}$ only involves derivatives with respect to the multipliers and controls. If we can eliminate the derivative with respect to the multipliers, calculating $\delta\mathcal{L}$ will be the same as computing $\delta\mathcal{J}$, the gradient of the functional. This is done by formulating the adjoint problem in the dual space of the forward problem. In this Section we derive a form of the gradient that only involves partial derivatives with respect to the controls precisely by imposing that both the forward and adjoint systems are satisfied simultaneously.

Forward problem. We set $D_{(\mathbf{v},q)}\mathcal{L}\cdot(\tilde{\mathbf{v}},\tilde{q}) = 0\ \forall(\tilde{\mathbf{v}},\tilde{q}) \in VQ$. By the linearity of a and l, this means finding the pair $(\mathbf{u}, p)$ such that

$$a((\mathbf{u},p),(\tilde{\mathbf{v}},\tilde{q})) = l((\tilde{\mathbf{v}},\tilde{q});(\mathbf{f},\mathbf{g})) \quad \forall(\tilde{\mathbf{v}},\tilde{q}) \in VQ, \tag{III.27}$$

which precisely reduces to satisfying the elasticity equation (III.13).

Adjoint problem. By imposing $D_{(\mathbf{u},p)}\mathcal{L}\cdot(\tilde{\mathbf{u}},\tilde{p}) = 0\ \forall(\tilde{\mathbf{u}},\tilde{p}) \in VQ$, we are looking for $(\mathbf{v}, q)$ that satisfy

$$a((\mathbf{v},q),(\tilde{\mathbf{u}},\tilde{p})) = -2\langle \boldsymbol{\varpi}\cdot(\mathbf{u}-\mathbf{u}_w) + (I_w e^{-s_w} - I_1), \boldsymbol{\varpi}\cdot\tilde{\mathbf{u}}\rangle_\Omega \quad \forall(\tilde{\mathbf{u}},\tilde{p}) \in VQ, \tag{III.28}$$

because a is linear and "self-adjoint", i.e. $a((\tilde{\mathbf{u}},\tilde{p}),(\mathbf{v},q)) = a((\mathbf{v},q),(\tilde{\mathbf{u}},\tilde{p}))\ \forall(\tilde{\mathbf{u}},\tilde{p})$, $(\mathbf{v},q) \in VQ$. Here $\boldsymbol{\varpi} = e^{-s_w}(\nabla I_w - I_w\nabla s_w)$ and $\mathbf{u}$ is the solution of the forward problem (III.27). The resulting equation is of the same form as the original weak formulation of the elasticity equation (III.27) but driven by a "force" that reflects the discrepancy with the data. Since (III.28) holds for all $(\tilde{\mathbf{u}},\tilde{p}) \in VQ$, this so-called adjoint equation can be formulated in its PDE strong form for comparison :

$$\begin{cases} \nabla\cdot\boldsymbol{\tau} = -2\left(\boldsymbol{\varpi}\cdot(\mathbf{u}-\mathbf{u}_w) + (I_w e^{-s_w} - I_1)\right)\boldsymbol{\varpi}^* & \text{in } \Omega \\ \nabla\cdot\mathbf{v} = -q/\lambda & \text{in } \Omega \\ \boldsymbol{\tau}\cdot\mathbf{n} = 0 & \text{on } \Gamma_{\mathbf{T}} \\ \mathbf{v} = 0 & \text{on } \Gamma_{\mathbf{g}}, \end{cases} \tag{III.29}$$

where $\boldsymbol{\tau} = -q\mathbf{I} + 2\mu\boldsymbol{\varepsilon}(\mathbf{v})$ is the adjoint stress tensor.

Gradient. We have $\delta\mathcal{J} = D_{(\mathbf{f},\mathbf{g})}\mathcal{L}\cdot(\tilde{\mathbf{f}},\tilde{\mathbf{g}})$ because the two other contributors of $\delta\mathcal{L}$ have been made zero, and thus we can evaluate the gradient with respect to the controls as

$$\delta\mathcal{J}(\mathbf{f},\mathbf{g})(\tilde{\mathbf{f}},\tilde{\mathbf{g}}) := D_{\mathbf{f}}\mathcal{J}_{reg}\cdot\tilde{\mathbf{f}} + D_{\mathbf{g}}\mathcal{J}_{reg}\cdot\tilde{\mathbf{g}} - \tilde{l}((\mathbf{v},q);(\tilde{\mathbf{f}},\tilde{\mathbf{g}})), \tag{III.30}$$

$$\tilde{l}((\mathbf{v},q);(\tilde{\mathbf{f}},\tilde{\mathbf{g}})) := \langle\mathbf{v},\tilde{\mathbf{f}}\rangle_K + \langle\frac{\xi}{h}\mathbf{v} - \boldsymbol{\varsigma}(\mathbf{v},q)\cdot\mathbf{n},\tilde{\mathbf{g}}\rangle_{\Gamma_{\mathbf{g}}}, \tag{III.31}$$

for all directions $\tilde{\mathbf{f}} \in F, \tilde{\mathbf{g}} \in V$ where $\mathbf{v}$, q is the solution of the adjoint equation (III.28). Therefore, the gradient consists of contributions from the regularisation functional and from the source term of the elastic equation, which is linear with respect to the controls.

Consider the case $\delta\mathcal{J}(\mathbf{f})(\tilde{\mathbf{f}}) = \langle 2\alpha\mathbf{f} - \mathbf{v}, \tilde{\mathbf{f}}\rangle_K$ where we only control for $\mathbf{f}$ and the regularisation is the standard L^2, i.e. $\mathcal{J}_{reg} = \alpha\langle\mathbf{f},\mathbf{f}\rangle_\Omega$. Notice here that $\delta\mathcal{J} = 0\ \forall\tilde{\mathbf{f}} \in F$

implies $\mathbf{f} = \mathbf{v}/2\alpha$ on K. Therefore, finding $\mathbf{f}$ is the result of solving the coupled system of elliptic partial differential equations formed by (III.13) and (III.29). In a similar way, if both $\mathbf{g}$ and $\mathbf{f}$ are regularised in a quadratic way the system is still linearly solvable when coupled : $\mathbf{f} = \mathbf{v}/2\alpha$, $\beta\mathbf{g} = (\xi/h)\mathbf{v} - \varsigma(\mathbf{v}, q)\mathbf{n}$ when $\mathcal{J}_{reg} = \alpha\langle\mathbf{f}, \mathbf{f}\rangle_\Omega + \beta\langle\mathbf{g}, \mathbf{g}\rangle_{\Gamma_\mathbf{g}}$.

However, in this work we use the Hessian as an alternative. If the functional term is indeed quadratic and the forward problem is linear, Newton method takes a single step. That is, using the Hessian involves solving 4 linear systems, which is not necessarily slower than solving the double-sized coupled system. Most importantly, computing the Hessian generalises to non-quadratic regularisations (e.g. here TV on $\mathbf{f}$), non-linear problems (e.g. viscoelastic models of collagen), and allows to estimate the errors of the reconstruction (see Sec. 5).

Let us summarise the steps to calculate the gradient at point $(\mathbf{f}, \mathbf{g})$: 1) solve (III.27) to get $(\mathbf{u}, p)$, 2) solve (III.28) to get $(\mathbf{v}, q)$, 3) compute gradient in direction $(\tilde{\mathbf{f}}, \tilde{\mathbf{g}})$ by solving (III.31).

III.3.2 Second order variations to build the Hessian action

In line with the first variations, we avoid using finite differences to compute the Hessian because there are too many possible sampling directions given the cost of evaluating the gradient (i.e. two PDEs per direction). Given $\mathbf{f}, (\mathbf{u}, p), (\mathbf{v}, q)$ and a direction $\tilde{\mathbf{f}}$, $\tilde{\mathbf{g}}$, we write down the meta-Lagrangian, which groups all the terms relevant to calculate the second variations. This will allow us to calculate the action of the Hessian in the specified direction.

$$\begin{aligned}
\mathcal{L}^H := & a((\mathbf{u}, p), (\tilde{\mathbf{v}}, \tilde{q})) - l((\tilde{\mathbf{v}}, \tilde{q}); (\mathbf{f}, \mathbf{g})) && \text{(III.32)}\\
& + a((\mathbf{v}, q), (\tilde{\mathbf{u}}, \tilde{p})) + 2\langle \boldsymbol{\mathscr{o}} \cdot (\mathbf{u} - \mathbf{u}_w) + (I_w e^{-s_w} - I_1), \boldsymbol{\mathscr{o}} \cdot \tilde{\mathbf{u}}\rangle_\Omega && \text{(III.33)}\\
& + D_\mathbf{f}\mathcal{J}^{\bullet}_{reg} \cdot \tilde{\mathbf{f}} + D_\mathbf{g}\mathcal{J}^{\bullet}_{reg} \cdot \tilde{\mathbf{g}} - \tilde{l}((\mathbf{v}, q); (\tilde{\mathbf{f}}, \tilde{\mathbf{g}})). && \text{(III.34)}
\end{aligned}$$

In this case, we anticipate that the bilinear forms for the incremental equations (both forward and adjoint) will be the same as in the original equations (respectively state and adjoint) because the forward problem is linear. In addition, the bilinear incremental forward and adjoint forms are exactly the same because the original a form is "self-adjoint". Therefore, all bilinear terms of the first and second variations are simply a ; and the only effect comes through the source terms that include effects from the force $\mathbf{f}$ variations, the boundary condition $\mathbf{g}$ variations, and the image pseudo-gradient $\boldsymbol{\mathscr{o}}$. Similarly, l is linear with respect to both the tests and the controls.

Incremental forward problem. We set $D_{(\mathbf{v},q)}\mathcal{L}^H\left(\tilde{\tilde{\mathbf{v}}}, \tilde{\tilde{q}}\right) = 0 \ \forall \left(\tilde{\tilde{\mathbf{v}}}, \tilde{\tilde{q}}\right) \in VQ$. By the linearity of a and l, this means finding the pair $(\tilde{\mathbf{u}}, \tilde{p})$ such that

$$a((\tilde{\mathbf{u}}, \tilde{p}), \left(\tilde{\tilde{\mathbf{v}}}, \tilde{\tilde{q}}\right)) = \tilde{l}(\left(\tilde{\tilde{\mathbf{v}}}, \tilde{\tilde{q}}\right); (\tilde{\mathbf{f}}, \tilde{\mathbf{g}})) \quad \forall \left(\tilde{\tilde{\mathbf{v}}}, \tilde{\tilde{q}}\right) \in VQ. \tag{III.35}$$

Incremental adjoint problem. By imposing $D_{(\mathbf{u},p)}\mathcal{L}^H \cdot \left(\tilde{\tilde{\mathbf{u}}}, \tilde{\tilde{p}}\right) = 0 \ \forall \left(\tilde{\tilde{\mathbf{u}}}, \tilde{\tilde{p}}\right) \in VQ$, we are looking for $(\tilde{\mathbf{v}}, \tilde{q})$ that satisfy

$$a((\tilde{\mathbf{v}}, \tilde{q}), \left(\tilde{\tilde{\mathbf{u}}}, \tilde{\tilde{p}}\right)) = -2\langle \mathcal{O} \cdot \tilde{\mathbf{u}}, \mathcal{O} \cdot \tilde{\tilde{\mathbf{u}}} \rangle_\Omega \quad \forall \left(\tilde{\tilde{\mathbf{u}}}, \tilde{\tilde{p}}\right) \in VQ, \tag{III.36}$$

because a is linear and "self-adjoint". Here $\tilde{\mathbf{u}}$ is the solution of (III.35).

Hessian. If the two incremental systems are satisfied, then $\delta\mathcal{L}^H = D_{(\mathbf{f},\mathbf{g})}\mathcal{L}^H \cdot (\tilde{\tilde{\mathbf{f}}}, \tilde{\tilde{\mathbf{g}}})$ where the action of the hessian reads very similar to the gradient because of all the linearities :

$$\langle (\tilde{\tilde{\mathbf{f}}}, \tilde{\tilde{\mathbf{g}}}), \delta^2 \mathcal{J}(\mathbf{f}, \mathbf{g})(\tilde{\mathbf{f}}, \tilde{\mathbf{g}}) \rangle := D^2_{\mathbf{f}} \mathcal{J}^{\bullet}_{reg} \cdot \tilde{\mathbf{f}} \cdot \tilde{\tilde{\mathbf{f}}} + D^2_{\mathbf{g}} \mathcal{J}^{\bullet}_{reg} \cdot \tilde{\mathbf{g}} \cdot \tilde{\tilde{\mathbf{g}}} - \tilde{l}((\tilde{\mathbf{v}}, \tilde{q}); (\tilde{\tilde{\mathbf{f}}}, \tilde{\tilde{\mathbf{g}}})), \tag{III.37}$$

$\forall \tilde{\tilde{\mathbf{f}}} \in F, \tilde{\tilde{\mathbf{g}}} \in V$ with $\tilde{\mathbf{v}}$, $\tilde{q}$ the solution of (III.36).

In the name of perspective, we recall the single control, L^2 scenario from the gradient computation where we find the same situation : $\langle \tilde{\tilde{\mathbf{f}}}, \delta^2 \mathcal{J}(\mathbf{f})(\tilde{\mathbf{f}}) \rangle = \langle 2\alpha\tilde{\mathbf{f}} - \tilde{\mathbf{v}}, \tilde{\tilde{\mathbf{f}}} \rangle_K$. The double control works likewise.

Newton. With the first and second order variations we can formulate Newton's method to minimise the PDE-constrained functional. That is, we find an update direction $\tilde{\mathbf{f}}$, $\tilde{\mathbf{g}}$ that reduces the value of $\mathcal{J}$ by solving the system

$$\langle (\tilde{\tilde{\mathbf{f}}}, \tilde{\tilde{\mathbf{g}}}), \delta^2 \mathcal{J}(\mathbf{f}, \mathbf{g})(\tilde{\mathbf{f}}, \tilde{\mathbf{g}}) \rangle = -\delta \mathcal{J}(\mathbf{f}, \mathbf{g})(\tilde{\tilde{\mathbf{f}}}, \tilde{\tilde{\mathbf{g}}}) \quad \forall \tilde{\tilde{\mathbf{f}}} \in F, \ \tilde{\tilde{\mathbf{g}}} \in V. \tag{III.38}$$

Since the first and second variations each take a pair of PDE solves, constructing the Newton system requires solving four PDEs. Following the same example, we have $\langle 2\alpha\tilde{\mathbf{f}} - \tilde{\mathbf{v}}, \tilde{\tilde{\mathbf{f}}} \rangle_K = -\langle 2\alpha\mathbf{f} - \mathbf{v}, \tilde{\tilde{\mathbf{f}}} \rangle_K$, which reduces to $\mathbf{f} + \tilde{\mathbf{f}} = (\mathbf{v} + \tilde{\mathbf{v}})/2\alpha$ on K.

III.3.3 Discretisation of the ∞-dimensional Newton's method

III.3.3.1 Galerkin approximation : a finite formulation of the ∞ dimensional weak equations

To solve the problem numerically it is necessary to discretise it. To this end, we introduce finite-dimensional subspaces $UP_h \subset UP$ and $VQ_h \subset VQ$ for the trial and test function spaces, notating the discrete counterparts of the infinite formulation with the subscript h. We also collect the variable pairs for readability, for example $\boldsymbol{U}_h = [\mathbf{u}_h, p_h]$, $\boldsymbol{V}_h = [\mathbf{v}_h, q_h]$. The sections that follow show how we formalise the discrete problem as a Galerkin approximation of the corresponding infinite formulation, covering from the forward system all the way to Newton's method. Under this formulation, we can clearly see the positive-definitness of the Hessian, which allows us to solve Newton's system via conjugate gradients. We also make use of this property to calculate the eigenvalues that reflect how well-informed is the inverse problem by the available data. The complete algorithm including all the image analysis steps, such as the pyramidal iterations and the warping, is described at the end.

III.3.3.2 The right finite elements avoid locking in the elastic equations

We solve the Galerkin-approximated version of problems III.42, III.43, III.46, III.47 using the Finite Element Method [185, 181]. To avoid locking[8] we choose a mixed formulation of Taylor-Hood elements that combine second and first order basis functions. We write each component of $\mathbf{u}_h$, $\mathbf{v}_h$ in a piece-wise (bi/tri)-quadratic basis of Lagrange finite-element functions, whereas p_h and q_h are a linear combination of piece-wise (bi/tri)-linear elements of Lagrange type. For example,

$$p_h = \sum_J p_j \phi_j(\mathbf{x}) \tag{III.39}$$

where $\{\phi_j\}_{j \in J}$ is the basis, $\#J$ is the number of nodes and p_j are the coefficients we solve for. The bases of $\mathbf{f}_h$ and $\mathbf{g}_h$ are determined according to the choice of regularisation. Replacing the ∞-dimensional test and trial functions with their discrete test (indexed by l) and trial (by j) counterparts in the weak formulations yields a variety of j, l linear systems. For example, the matrix resulting from discretising $\langle p, q\rangle_\Omega$ is the positive definite symmetric matrix $\langle \phi_j, \phi_l\rangle_\Omega$ known as mass matrix. In the following sections, we address discretisation in more detail.

To gauge the size of the problem, consider a square 256×256 2D image. Assume we use a regular triangular mesh to discretise it. Then the linearly-interpolated pressure field has 257^2 nodes or degrees of freedom (dof), and the displacement field $2(257+256)^2$. Together, the mixed space has close to $10^{5.5}$ dofs, which are squared when the matrix is constructed. Luckily, the resulting matrices are very sparse. Of course, the dofs grow cubically in 3D. For all reasons indicated above, in the text we emphasize size-aware approaches that exploit sparsity or avoid forming matrices altogether.

III.3.3.3 A discrete formulation transforms the problems into linear algebra

We begin by discretising the bilinear form a on the left-hand side of the elastic equations

$$A = \begin{bmatrix} W & B^T \\ B & M_p \end{bmatrix} \tag{III.40}$$

where W and M_p (i.e. the mass matrix of p) are symmetric matrices that result from the respective discretisations of $w(\mathbf{u}, \mathbf{v}) = \langle 2\mu\boldsymbol{\varepsilon}(\mathbf{u}), \boldsymbol{\varepsilon}(\mathbf{v})\rangle_\Omega - \langle 2\mu\boldsymbol{\varepsilon}(\mathbf{u})\mathbf{n}, \mathbf{v}\rangle_{\Gamma_\mathbf{g}} - \langle 2\mu\boldsymbol{\varepsilon}(\mathbf{v})\mathbf{n}, \mathbf{u}\rangle_{\Gamma_\mathbf{g}} + (\xi/h)\langle \mathbf{u}, \mathbf{v}\rangle_{\Gamma_\mathbf{g}}$ and $m_p(p, q) = -\frac{1}{\lambda}\langle p, q\rangle_\Omega$; and B stems from $b(u, q) = -\langle \nabla \cdot \mathbf{u}, q\rangle_\Omega + \langle q\mathbf{n}, \mathbf{u}\rangle_{\Gamma_\mathbf{g}}$. Therefore A is symmetric as expected from the "self-adjoint" behavior in the infinite dimensional formulation. However, we will keep the transpose notation A^T to showcase the origin of the terms. We also note that W is positive-definite for a big enough ξ and that M_p is negative-definite except in the incompressible limit where $M_p = 0$. On the right-hand side, we call L the discretisation of the

---

[8] That is we expect the same accuracy irrespectively of λ. An arbitrary combination of interpolations can lead to poor convergence and numerical performance. For example, the stresses can become very inaccurate and the displacements under-estimated.

linear form l (safe $\mathbf{T}$) :

$$L = \left[\begin{array}{cc} L_{\mathbf{f},\boldsymbol{V}} & L_{\mathbf{g},\boldsymbol{V}} \end{array}\right] := \left[\begin{array}{cc} L_{\mathbf{f},\mathbf{v}} & L_{\mathbf{g},\mathbf{v}} \\ 0 & L_{\mathbf{g},q} \end{array}\right], \tag{III.41}$$

with the matrices stemming from the following forms : $L_{\mathbf{f},\mathbf{v}}$ from $\langle \mathbf{v}, \mathbf{f} \rangle$; $L_{\mathbf{f},q} = 0$; $L_{\mathbf{g},\mathbf{v}}$ from $\langle (\xi/h)\mathbf{v} - 2\mu\boldsymbol{\varepsilon}(\mathbf{v})\mathbf{n}, \mathbf{g} \rangle$; and $L_{\mathbf{g},q}$ from $\langle q\mathbf{n}, \mathbf{g} \rangle$.

The discretised forward and adjoint linear systems are (in this order) :

$$A\boldsymbol{U}_h = \left[\begin{array}{cc} L_{\mathbf{f},\boldsymbol{V}} & L_{\mathbf{g},\boldsymbol{V}} \end{array}\right] \left[\begin{array}{c} \mathbf{f}_h \\ \mathbf{g}_h \end{array}\right] + \mathbf{T}_h \tag{III.42}$$

and

$$A^T \boldsymbol{V}_h = -2O^T O(\boldsymbol{U}_h - \boldsymbol{U}_{w_h}) + I_h, \tag{III.43}$$

with I_h the discretisation of $I_w e^{-s_w} - I_1$, $\boldsymbol{U}_{w_h}$ that of the displacement at the previous scale, and O such that the discretisation $J_{\mathbf{u},\mathbf{u}}$ of the optical flow source term $\langle \varnothing \otimes \varnothing\ \mathbf{u}, \tilde{\mathbf{u}} \rangle$ in

$$O^T O := \left[\begin{array}{cc} J_{\mathbf{u},\mathbf{u}} & 0 \\ 0 & 0 \end{array}\right]. \tag{III.44}$$

Leaving the gradient $\boldsymbol{g}$ to be

$$\left[\begin{array}{c} \boldsymbol{g}_{\mathbf{f}} \\ \boldsymbol{g}_{\mathbf{g}} \end{array}\right] = R \left[\begin{array}{c} \mathbf{f}_h \\ \mathbf{g}_h \end{array}\right] - \left[\begin{array}{c} L_{\mathbf{f},\boldsymbol{V}}^T \\ L_{\mathbf{g},\boldsymbol{V}}^T \end{array}\right] \boldsymbol{V}_h. \tag{III.45}$$

The incremental forward reads

$$A\tilde{\boldsymbol{U}}_h = \left[\begin{array}{cc} L_{\mathbf{f},\boldsymbol{V}} & L_{\mathbf{g},\boldsymbol{V}} \end{array}\right] \left[\begin{array}{c} \tilde{\mathbf{f}}_h \\ \tilde{\mathbf{g}}_h \end{array}\right]. \tag{III.46}$$

And we write the incremental adjoint as

$$A^T \tilde{\boldsymbol{V}}_h = -2O^T O\ \tilde{\boldsymbol{U}}_h. \tag{III.47}$$

Next, we discretise the action of the Hessian :

$$H \left[\begin{array}{c} \tilde{\mathbf{f}}_h \\ \tilde{\mathbf{g}}_h \end{array}\right] = \left[\begin{array}{cc} R_{\mathbf{f},\mathbf{f}} & 0 \\ 0 & R_{\mathbf{g},\mathbf{g}} \end{array}\right] \left[\begin{array}{c} \tilde{\mathbf{f}}_h \\ \tilde{\mathbf{g}}_h \end{array}\right] - \left[\begin{array}{c} L_{\mathbf{f},\boldsymbol{V}}^T \\ L_{\mathbf{g},\boldsymbol{V}}^T \end{array}\right] \tilde{\boldsymbol{V}}_h, \tag{III.48}$$

where $R_{\mathbf{f},\mathbf{f}}$ and $R_{\mathbf{g},\mathbf{g}}$ are the respective discretisations of $D^2_{\mathbf{g}}\mathcal{J}_{reg} \cdot \tilde{\mathbf{f}} \cdot \tilde{\tilde{\mathbf{f}}}$ and $D^2_{\mathbf{g}}\mathcal{J}_{reg} \cdot \tilde{\mathbf{g}} \cdot \tilde{\tilde{\mathbf{g}}}$. The resulting incremental system is of Karush-Kuhn-Tucker form. Lets collapse the full regularisation matrix under the term R. By substituting the two incremental systems (III.47), (III.46) into the action (III.48) we can extract an expression for the Hessian matrix,

$$H = R + H_{\text{data}}, \tag{III.49}$$

$$H_{\text{data}} := 2L^T A^{-T} O^T O A^{-1} L, \tag{III.50}$$

that brings out its positive definiteness. Indeed, the right-most term in (III.49) is positive semi-definite (product of a matrix with its transpose) and the regularisation matrices R will be positive-definite, eliminating the nullspace. The symmetry of H is also clear as both summands are symmetric. An alternative argument for positive definiteness is to notice that the infinite dimensional problem is itself a Gauss-Newton approximation of the Hessian because the second variations of the PDE with respect to $\boldsymbol{U}$, $(\mathbf{f}, \mathbf{g})$, and $(\mathbf{f}, \mathbf{g})$, $(\mathbf{f}, \mathbf{g})$ are zero. From this perspective, symmetry is granted because the result should be independent of the order of derivation.

III.3.3.4 Conjugate Gradient only requires matrix-free Hessian actions

Solving the resulting discretised Newton system,

$$H_h \begin{bmatrix} \tilde{\mathbf{f}}_h \\ \tilde{\mathbf{g}}_h \end{bmatrix} = - \begin{bmatrix} \boldsymbol{g}_{\mathrm{f}} \\ \boldsymbol{g}_{\mathrm{g}} \end{bmatrix}, \tag{III.51}$$

for $\tilde{\mathbf{f}}_h$, $\tilde{\mathbf{g}}_h$ provides a directional step that is guaranteed to descend by virtue of the positive definiteness of the Hessian. However, computing H involves dealing with large matrices that might become dense when inverted. To avoid building the hessian, we focus on its action on vectors, which can be calculated by solving the two incremental linear systems (III.46), (III.47).

Matrix-free direct solvers are scarce and often require constructing sparse matrices [368] or going random [369]. Alternatively, the iterative action of an operator is the basis of Krylov subspace methods. In particular, we are interested in the Conjugate Gradient (CG) method that applies to positive definite and symmetric matrices [370, 371, 372]. This algorithm takes successive steps that descend as close to the residual direction of the system as possible while ensuring H-orthogonality[9] with all the previous directions.

Some of the regularisation forms we will use are expected to converge in a single step $\mathbf{f} + \tilde{\mathbf{f}}$ because the problem is quadratic (the PDE is linear w.r.t. to the state and control variables) and Newton's method should be exact. Of course, this might not hold in practice, where round-off errors intervene. In other cases, solving Newton's system (III.51) too accurately might be pointless because we are implicitly making a quadratic approximation already. To prevent over-solving, we introduce an early-termination clause on the CG iterations that is most relevant when far from the minimum. In particular, we use Eisenstat's criterium [373], which is based on controlling the gradient. An additional criterium, Steinhaug's [374], stops the iterations if the curvature is ever negative, which might be relevant in TV.

Whereas normally the optimal step length is unitary, the resulting inexact Newton method can be globalised by line searching if necessary ; here we implement it using an Armijo back-tracking scheme [375]. Although Newton's method converges

---

[9] 9. Think of converting an elliptical space into a circle (as in [371] for the CG method), where convergence is immediate.

quadratically, any approximation might reduce the radius of this rate into a smaller neighbourhood around the solution. In terms of cost, each CG iteration requires a Hessian-vector product, and each such action takes a pair of linearized forward/adjoint solves.

III.3.3.5 Riesz-inspired preconditioner achieves mesh-independent convergence

In the absence of round-off errors, CG is guaranteed to converge in a number of iterations smaller than the size of the system. Specifically, the rate of convergence is a function of the condition number of the system matrix $\kappa(H)$ [371] :

$$\frac{\sqrt{\kappa(H)}-1}{\sqrt{\kappa(H)}+1}; \tag{III.52}$$

and thus can be improved by using a preconditioner P such that $\kappa(P^{-1}H) < \kappa(H)$. Here $\kappa(H) = |\lambda_+|/|\lambda_-|$ with the respective maximum and minimum eigenvalues[10] of H.

Choosing a preconditioner for CG is equivalent to choosing an inner product for the Hilbert space the control belongs to [376, 377]. In particular, the default choice (the identity) is implicitly enforcing the Euclidean product. The link between preconditioner and scalar product goes through the Riesz map. Indeed, the Riesz map acts precisely as the application of a preconditioner in the CG method when formulated (more generally) for Hilbert spaces [376] ; and in turn, the Riesz isomorphism is determined by the scalar product of the space[11]. In this work, we write our preconditioner as

$$P = \rho M + R, \tag{III.53}$$

where R is the regularisation matrix, and M is the mass matrix (FEM) that we add in proportion to a constant $\rho \in \mathbb{R}_{>0}$ to fill in the nullspace of R that might be singular (e.g. constant vectors if the regularisation is on the derivative of the control). In summary, our preconditioner is chosen to incorporate the inner product associated with the regularisation (e.g. L^2 or H^1 above), which specifies in which space we are looking for the solution[12], weighted by any possible grid irregularities, which are taken in account when building the (mass) matrix from the finite elements (see [378] for example).

---

[10] A symmetric real matrix is diagonalizable with real eigenvalues.

[11] Think for example of applying the derivative (defined in the dual space) of a functional to a given direction of the original space. The direction of steepest descent is precisely the one that minimises the resulting dual pairing. Now, if we apply the Riesz-Fréchet representation theorem to the derivative, we can find that evaluating the derivative in a given direction is equivalent to taking the inner product (associated to the space) of the same direction with the so-called Riesz representative of the derivative (here the Riesz map brings the derivative to the representative). Since we are now working with inner products we can directly deduce that the direction of steepest descent is precisely the representative by using Cauchy-Schwarz's inequality. The representative is known as the *gradient*

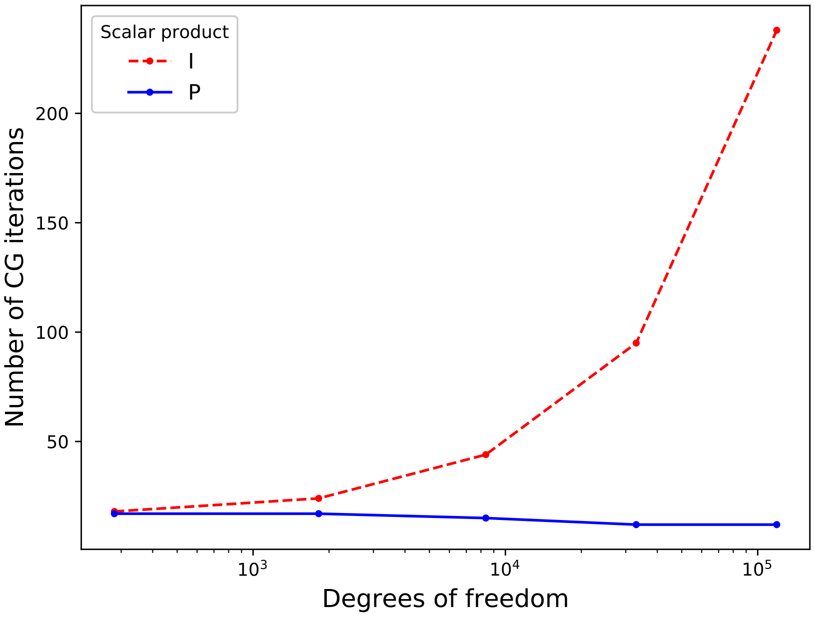

FIGURE III.3 – **The importance of choosing the appropriate inner product**. The figure displays the number of CG iterations to solve the inverse problem as a function of degrees of freedom when preconditioned with I (red) or P (blue). Choosing the right inner product P results in size-independent algorithms. The x-axis is log-scaled.

With an appropriate preconditioner/inner product we avoid mesh-dependent artifacts, notably in non-uniformly refined meshes [379, 380]. This can be understood intuitively : it is only by considering the correct measure of angles and distances that we will find the best descent directions. Indeed, we show in Figure III.3 that the total number of CG and Newton iterations of the problem is stable against mesh-size and parameter-space-size variations, as well as non-uniformity, when the system is preconditioned ; whereas taking $P = I$ results in the number of iterations increasing with the system size. This is specially severe when the elements of the mesh are of different sizes because the euclidean norm assigns equal weights to all of them. Conversely, the mass matrix reflects the importance of the elements more accurately. A related example regarding the importance of choosing an appropriate inner product is how, by choosing the Hessian in Newton's method, we drastically accelerate convergence with respect to steepest descent, which corresponds to the implicit choice of the identity.

The number of iterations when the system is preconditioned by the regularisation generally depends on how much of the parameter space is informed by the data. In fact, the data only informs a limited subset of directions in the control space, as shown later in Figure III.11. In other words, the method is algorithmically scalable : the cost of solving the (inverse) problem is independent of the mesh size (spatial discretisation)

---

of the function.

[12] Therefore estimating correctly the angles and distances of descent.

when measured in number of PDE solves[13].

This spectral property of the preconditioned Hessian misfit is specially interesting in light of our multi-scale approach to OF. In this way, we can better estimate the complexity of the problem at each scale because the PDE solves dominate the cost of the approach over other operations (e.g. inner products).

In this work, we take profit of the inherent multi-resolution nature of our problem (whereby optical flow displacements are sought from coarser to finer) to implement the preconditioner as an algebraic multi-grid (AMG) [381, 382] solver with whom it shares the mesh hierarchy. While the image could be easily made into a structured grid, it might be that we want to keep it unstructured. Two instances that are relevant to this work : integrating the cell domain to localise the traction forces, e.g. $\langle \mathbf{f}, \mathbf{f} \rangle$; and using a finer grid on the regions of the image with more information in order to better focus our efforts.

III.3.3.6 Multi-frontal LDL^T factorises all saddle-point systems at once

Working out the saddle-point forward and adjoint PDEs requires solving the corresponding linear systems. Once discretised using the FEM, the problem is large, sparse, and indefinite. More specifically, the size of the matrix is the number of degrees of freedom squared, of which the off-diagonals are filled up to a width proportional to the neighborhood graph-order of each node. Whereas these systems are normally approached/attacked with iterative solvers, the confluence of linearity and symmetry have originated 4 linear systems $Ax = b$ (III.42, III.43, III.46, III.47), all ruled by the same matrix A, but under different forcing terms b. To take advantage of this we use a direct solver that can factorise A into unitriangular matrices U^T (lower), U (upper) and block-diagonal (of order 1 or 2) matrix D as

$$A = U^T D U. \tag{III.54}$$

This factorisation[14], known as "LDL^T", takes advantage of the matrix symmetry to halve the cost of the more general "LU" factorisation. Once in this form, the problem can be quickly solved by forward ($U^T y = b$) and backward ($DUx = y$) substitution (for any b). To exploit the lower-dimensionality of sparse matrices, so-called frontal solvers [383] will divide the problem into a set of smaller dense matrices that avoid unnecessary zero-operations. The resulting blocks can then be factorised by standard pivoting. Precisely, the MUMPS library [384] automatises and parallelises this concept by taking a multi-frontal approach [385].

However, it is true that some image-derived meshes become too large for some sub-matrices to fit in memory. In this case, we would have to rely on iterative methods. Since the problems is indefinite (no CG), we use the minimal residual method

---

[13] Of course, at finer scales solving each PDE is bound to be more expensive ; it is only the number of PDE solves that stays constant.

[14] Instead of using the nomenclature LDL^T here we use $U^T DU$ because the former notation is already taken.

(MINRES) [386, 387] [15] with an incomplete factorisation as a preconditioner (e.g. Incomplete LU [16]), which can also be up-scaled from a lower resolution in the pyramid scheme.

III.3.3.7 Regularisation depends on the biological motive

We have experimented with three regularisations based on norms/semi-norms that we think might be suitable to represent different biological situations and that are also differentiable. We summarise L^2 and H^1 by writing

$$\mathcal{J}_{reg}^{H^1}(\mathbf{f}) := \alpha\langle \mathbf{f}, \mathbf{f}\rangle_K + \beta\langle \nabla\mathbf{f}, \nabla\mathbf{f}\rangle_K, \tag{III.55}$$

with some constants $\alpha, \beta \in \mathbb{R}_{\geq 0}$ that act as weights with respect to the data misfit. The first and second variations of the H^1 regularisation are as follows.

$$D_{\mathbf{f}}\mathcal{J}_{reg}^{H^1} \cdot \tilde{\mathbf{f}} = 2\alpha\langle \mathbf{f}, \tilde{\mathbf{f}}\rangle_K + 2\beta\langle \nabla\mathbf{f}, \nabla\tilde{\mathbf{f}}\rangle_K, \tag{III.56}$$

$$D_{\mathbf{f}}^2\mathcal{J}_{reg}^{H^1} \cdot \tilde{\mathbf{f}} \cdot \tilde{\tilde{\mathbf{f}}} = 2\alpha\langle \tilde{\mathbf{f}}, \tilde{\tilde{\mathbf{f}}}\rangle_K + 2\beta\langle \nabla\tilde{\mathbf{f}}, \nabla\tilde{\tilde{\mathbf{f}}}\rangle_K. \tag{III.57}$$

Here the parameter α acts as a low-pass filter of sorts (Annex E.1), and β works as a diffusion coefficient that smooths the control (Annex E.2). This approach is fit for studying the general distribution of traction forces exerted by a cell on the substrate or ECM.

Conversely, given a sufficiently good spatial resolution, total variation (TV) might be better suited to exactly localise the small focal adhesion patches that are generated by some cells [229]. To mimic the effect of TV in a vectorial setting [389], we minimise the Frobenius norm of the gradient $|\nabla\mathbf{f}|_{\mathrm{F}} = (\nabla\mathbf{f} : \nabla\mathbf{f})^{1/2}$ (we note $|$ for the norm as opposed to $\|$, which we used for the integral of the associated inner product over a domain) :

$$\mathcal{J}_{reg}^{\mathrm{TV}} := \alpha\int_K (\nabla\mathbf{f} : \nabla\mathbf{f})^{1/2}\ d\Omega = \alpha\int_K \sqrt{\mathrm{tr}\left(\nabla\mathbf{f}^T\nabla\mathbf{f}\right)}\ d\Omega; \tag{III.58}$$

whose variations are

$$D_{\mathbf{f}}\mathcal{J}_{reg}^{\mathrm{TV}} \cdot \tilde{\mathbf{f}} = \alpha\int_K \frac{\nabla\mathbf{f} : \nabla\tilde{\mathbf{f}}}{(\nabla\mathbf{f} : \nabla\mathbf{f})^{1/2}}\ d\Omega, \tag{III.59}$$

$$D_{\mathbf{f}}^2\mathcal{J}_{reg}^{\mathrm{TV}} \cdot \tilde{\mathbf{f}} \cdot \tilde{\tilde{\mathbf{f}}} = \alpha\int_K |\nabla\mathbf{f}|_{\mathrm{F}}^{-1}\nabla\tilde{\mathbf{f}}\left(\mathrm{I} - \frac{\nabla\mathbf{f}\otimes\nabla\mathbf{f}}{|\nabla\mathbf{f}|_{\mathrm{F}}^2}\right)\nabla\tilde{\tilde{\mathbf{f}}}\ d\Omega, \tag{III.60}$$

where we have used the linearity of the gradient and the sesquilinearity of the Frobenius product, or alternatively the cyclicity of the trace and its commutativity with respect to the derivative. In the second variation, we are thinking of the gradient matrices as stretched vectors and thus have used the outter product to make notation

---

[15] See also the generalised minimal residual method (GMRES) [388] if your matrix is non-symmetric.

[16] Alternatively, see Cholesky factorisation if your matrix is symmetric and positive-definite.

easier. In Annex E.3, we show how the operator in (III.60) acts as a non-linear anisotropic diffusor that prefers matrix directions that are Frobenius-perpendicular to $\nabla\mathbf{f}$ and therefore acts by somewhat preserving a common edge (with some directional "smearing") across the vectorial components.

Notice that the Frobenius norm is differentiable everywhere except at zero-gradients. In practice, we add an extra term $\epsilon \in \mathbb{R}_{>0}$ to stabilise the descent

$$\mathcal{J}^{\mathrm{TV}}_{reg} := \alpha \int_K \left(\nabla\mathbf{f} : \nabla\mathbf{f} + \epsilon\right)^{1/2} \, d\Omega, \tag{III.61}$$

at the price of some extra diffusion (of order ϵ^2) over the "edges". The first and second variations remain the same but with the perturbation appearing in all denominators. For smaller values of ϵ, the Hessian becomes more ill-conditioned as the relevance of the non-linear term increases, reducing the convergence radius of Newton's method. When far from the solution, we approximate the Hessian action by ignoring the non-linear anisotropic term as

$$D^2_{\mathbf{f}}\mathcal{J}^{\mathrm{TV}}_{reg} \cdot \tilde{\mathbf{f}} \cdot \tilde{\tilde{\mathbf{f}}} \approx \alpha \int_K \frac{\nabla\tilde{\mathbf{f}} : \nabla\tilde{\tilde{\mathbf{f}}}}{\left(\nabla\mathbf{f} : \nabla\mathbf{f} + \epsilon\right)^{1/2}} \, d\Omega, \tag{III.62}$$

i.e. demoting convergence to a linear rate, only to recover the original expression (III.60) in a small neighborhood near the minimum to finish quadratically. We remark that approximating the Hessian is not harmful (as far as the step size is controlled, e.g. à la back-tracking) because the direction is given by the gradient (again, think of approximating the Hessian as the Identity to recover steepest descent).

III.3.3.8 An automatic implementation to promote usage

The implementation scheme of the method can be found in algorithm 1. The final goal is automatisation to make the method accessible for the biological community. We expect the text will reflect this, but hope that it does not distract from the underlying methodology. The first step is to determine the subregion K whereto forces are constrained. As in Section II.1.3.6, this is achieved by solving another variational problem known as active contours (or snakes) that segments the cells automatically by progressively deforming an initial contour to minimise a given energy [63]. The resulting polygon is the reference of a pyramid of shapes that is obtained by down-sampling the vertices on the Fourier domain (in 2D, see Section III.3.3.9 for 3D). A hierarchy of meshes is also established. In this case, we take the image borders and the polygon as planar straight line graphs to perform a constrained Delaunay triangulation [198] (iterative refinement with Lloyd's relaxation algorithm [206]) at each scale. Accordingly, the image resolution is resized by recursively convoluting a size-varying low-pass filter (e.g. Gaussian), to avoid aliasing, and a continuous-domain filter (e.g. interpolation) [390] : $I_1^k(\mathbf{x}_h)$, $I_2^k(\mathbf{x}_h)$ $\forall k \in \{1 \, .. \, n\}$, where n is the number of scales. The coarsest level (n) of the sub-sampled dyadic pyramid is chosen to represent displacements of around a pixel [391, 189].

We recall that this coarser-to-finer iteration is needed to compensate the linearisation of the non-convex optical flow functional. Increasingly higher spatial-frequency components are taken in account by progressively subtracting the movement $\mathbf{u}_h^{k-1}$ detected in previous scales from the original image I_2 :

$$I_w^k(\mathbf{x}_h) := I_2^k(\mathbf{x}_h + \mathbf{u}_h^{k-1}). \tag{III.63}$$

Ideally, I_w should stabilise and gradually match with I_1 as we refine the scale, i.e. $k \to n$. To this end, we warp the image by mapping it onto the new coordinates at scale k via cubic spline interpolation. Notice that the multi-scaling doubles as a sort of remedy for Nyquist's limit. To evaluate $\mathcal{J}$, we also take the new image derivative $\nabla I_w^k(\mathbf{x}_h)$ by convolving with a five-point centered finite difference stencil as a kernel (order fourth accuracy). We use nearest-neighbors as an heuristic to fill in the differences at the border, but once the image is being warped we choose to avoid out-of-bound pixels altogether and cancel the data misfit term (as detected by the coordinate map). Finite elements are automatically cast on the mesh hierarchy using the FEniCS library [185, 347]. The matrices corresponding to the variational problems are then assembled by solving the integrals on the basis of piece-wise polynomia (Section III.3.3.2). The solution of the linear systems, Newton's method, Conjugate gradient and back-tracking has already been presented in Sections III.3.3.4-III.3.3.6. At each new scale, the algorithms are initialized with the solutions resulting from the previous step, but projected onto the new elements (up-scaled). In the interest of saving computation time, notice that many of the matrices can be pre-assembled because many variables are not inter-dependent.

The algorithm is implemented in Python 3 and acts as a wrapper to multiple routines, most of which are optimised in C++. The list of libraries we have used (directly or indirectly through other libraries) includes PIL, Matplotlib [392], NumPy [208], SciPy [209], FEniCS [185], mshr, CGAL [210], PETSc [212] (see their linear solver table), MUMPS [384], Trilinos [393], BLAS [394], LAPACK [395], MPI [396], and VTK (Kitware). We hope we were exhaustive in our acknowledgment. We also wish to thank hIPPYlib [397] and Moola [380] as great sources of inspiration. The code is open-sourced and will be available at `http://icy.bioimageanalysis.org/`.

Algorithm 1: Multi-scale TFM

```
Data: Reference image $I_1$ and image $I_2$, initial contours
Result: Estimates for $\mathbf{u}$, $\mathbf{f}$, $\mathbf{g}$
Segment cells automatically from initial contours;
Generate hierarchical n-mesh pyramid of cells and images;
$\mathbf{u}_h^0, \mathbf{f}_h^0, \mathbf{g}_h^0 = 0$;
from coarsest scale $(k = 1)$ to finest scale $(k = n)$
    Down-sample to $I_1^k$ and $I_2^k$;
    Warp $I_2^k$ with $-\mathbf{u}_h^{k-1}$ into $I_w^k$;
    Compute $\nabla I_w^k$;
    Project $(\mathbf{u}_h^{k-1}, \mathbf{f}_h^{k-1}, \mathbf{g}_h^{k-1})$ on FEM $k$-grid for initial condition;
    Newton's Method to minimize $\mathcal{J}^k$
        Solve adjoint PDE (III.43);
        Evaluate gradient (III.45);
        Preconditioner set-up (III.53);
        Conjugate Gradient
            Solve incremental forward PDE (III.46);
            Solve incremental adjoint PDE (III.47);
            Compute Hessian action (III.48);
        while $\sqrt{|\delta\mathcal{J}^k|/|\delta\mathcal{J}^1|} >$ CG tol.;
        Armijo back-tracking
            $\mathbf{f}_h^k, \mathbf{g}_h^k = \mathbf{f}_h^{k-1} + \tilde{\mathbf{f}}_h^k, \mathbf{g}_h^{k-1} + \tilde{\mathbf{g}}_h^k$;
            Solve forward PDE (III.42) : $\mathbf{u}_h^k$;
    while $|\delta\mathcal{J}^k| >$ N tol.
```

III.3.3.9 Computational hardships are mostly mesh-related in 3D

The method scales as-is to 3D on the theoretical side, but becomes computationally heavier as dimensions turn cubic. The most conceptually involved part is geometry. For example, down-scaling the 3D triangulated surface meshes representing the cells and images is specially difficult if the essential characteristics of the original shapes are to be conserved/preserved. To this end, one needs a measure, or cost function, that evaluates the resemblance between the coarser and finer meshes. Here we use the Lindstrom-Turk (LT) strategy [398]. In comparison to global error tracking methods (Section II.1.3.7), which consider the accumulated deviation from the initial surface [205], cost-driven methods such as LT measure the cost of collapsing individual edges by computing local deviations and progressing iteratively. The result are faster, though less accurate, algorithms. In LT specifically, the edges are pruned according to a combination of constraints that dictate the position of each resulting vertex by considering shape, volume, and boundary conservation. In this work, we use a memory-less version of

LT implemented in CGAL [210] by F. Cacciola. Another complex adaptation is active contours as it also concerned with mesh geometry.

In practice, the finite element method can be practically detached from dimensional considerations thanks to the abstract framework offered by the FEniCS library. Similarly, differentiating and warping are conceptually invariant, but need to be up-dimensioned and streamlined to deal with the computational overhead.

While we have implemented the algorithm and found the recovered force fields accurate, we will not devote extensive attention to 3D imaging because the modality is still not widely used in biology. Although the literature has emphasized the importance of a relevant 3D ECM to study cell behavior, the reality is that experiments are complicated, materials are not well characterised, acquisition speed and resolution lag behind, and image analysis is overwhelmed by the size of the resulting data. However, here we have set-up a highly scalable theory and implementation for the data to come. We note that this framework is also readily adaptable to the no-linear rheologies that will result from the quest for more biologically relevant materials (e.g. collagen).

III.3.4 Experiments and regularisation

We start by checking both the gradient and hessian. We compare the results of the adjoint-based computation to a finite difference approximation. That is we are expecting the error to be proportional to the step h :

$$\left|\frac{\mathcal{J}((\mathbf{f},\mathbf{g})+h(\tilde{\mathbf{f}},\tilde{\mathbf{g}}))-\mathcal{J}(\mathbf{f},\mathbf{g})}{h}-D_{\mathbf{f},\mathbf{g}}\mathcal{J}(\mathbf{f},\mathbf{g})(\tilde{\mathbf{f}},\tilde{\mathbf{g}})\right|=\mathcal{O}(h) \tag{III.64}$$

in any direction $(\tilde{\mathbf{f}},\tilde{\mathbf{g}})$; and the error of the Hessian to grow quadratically under functional differences, or linearly under a gradient difference scheme :

$$\left|\frac{D_{\mathbf{f},g}\mathcal{J}((\mathbf{f},\mathbf{g})+h(\tilde{\mathbf{f}},\tilde{\mathbf{g}}))-D_{\mathbf{f},g}\mathcal{J}(\mathbf{f},\mathbf{g})}{h}-D^2_{\mathbf{f},\mathbf{g}}\mathcal{J}(\mathbf{f},\mathbf{g})(\tilde{\mathbf{f}},\tilde{\mathbf{g}})\right|_{\infty}=\mathcal{O}(h) \tag{III.65}$$

In the regularisation instances where the problem is quadratic, the Hessian is exact and the error observed is the precision of the machine. The resulting curves are presented in Figure III.4.

We disclaim that the selection of the regularisation parameter α was done as per the next Section III.3.4.3 (accompanying Figure III.10) and is assumed throughout this one.

Next, we tested the mesh-dependence of the conjugate grandient and Newton's method. We found that the choice of preconditioner was key in ensuring that the number of iterations was constant across all possible sizes of the problem (Figure III.3). In turn, this allows us to accurately predict/anticipate the performance of the multi-scale approach.

To assess the accuracy of the inversion, we choose a force field $\mathbf{f}_*$ and boundary conditions $\mathbf{g}_*$ of appropriate regularity to simulate the forward problem by solving

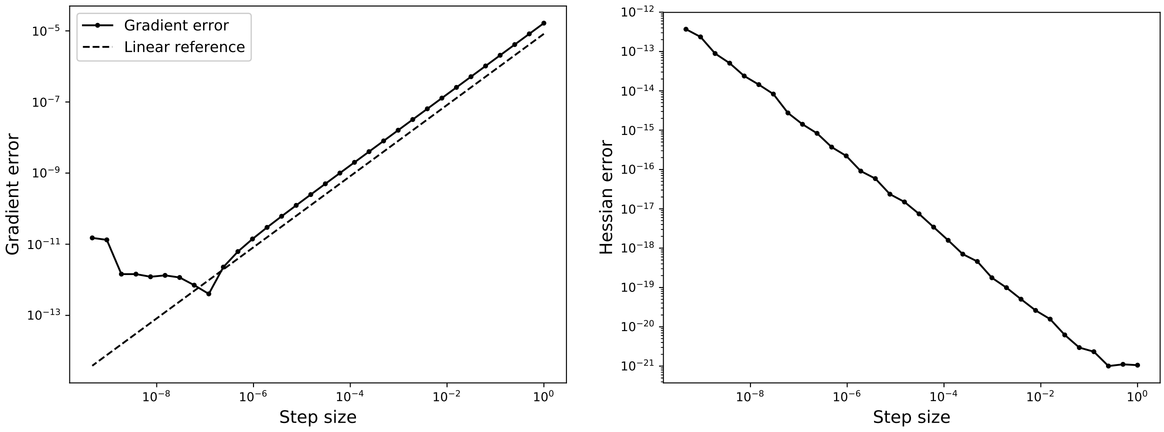

(a) (b)

Figure III.4 – **Checking the gradient and the Hessian by comparison to finite differences. a)** Error of the gradient as a function of the step h. **b)** Error of the ∞ norm of the Hessian as a function of the step h. The error values reflect machine precision because the Hessian is exact for quadratic problems. Both figures are in log-log scale.

$a_0 = l_0$ (III.19). The simulation results in a displacement field $\mathbf{u}_*$. We note that we simulate the problem on a different mesh size than we use for inversion, that we use $a = l$ instead, and that we add noise. Together, the three modifications should prevent an inverse crime. While this is enough to evaluate the direct inversion from displacement to force (Section III.3.4.1), our method aims at recovering force from a pair of images (Section III.3.4.2). To this end, the displacement $\mathbf{u}_*$ (simulated from $\mathbf{f}_*$) is used to warp a reference image I_1 into a deformed image I_2. In this case, the images are the only data used to inform the inverse problem. All errors are evaluated with a normalised L^2 norm :

$$\text{Error}(\mathbf{f}^*, \mathbf{f}_*) := \frac{\|\mathbf{f}^* - \mathbf{f}_*\|_\Omega}{\|\mathbf{f}_*\|_\Omega}, \tag{III.66}$$

where $\mathbf{f}^*$ is the inverted field.

III.3.4.1 Non-optical-flow preliminary test

First, we test the inversion by adding a percentage $\eta_\mathbf{u}$ of noise to the velocity field,

$$\mathbf{u}_d := \mathbf{u} + \eta_\mathbf{u} |\mathbf{u}|_\infty \mathrm{e}_\mathbf{u} \tag{III.67}$$

$\mathrm{e}_\mathbf{u} \sim \mathcal{N}(\mathbf{0}, \mathrm{I})$, and recovering the force field using the data term $\mathcal{J}^d_{data} := \|\mathbf{u} - \mathbf{u}_d\|^2_\Omega$. As shown in Figures III.5 and G.6, the original fields are well recovered, even under very noisy conditions. While the error of the recovered forces is higher than that of the displacement, both are robust to increasing noise (Figure III.6). This analysis allows us to have an idea of the range of errors we can expect in an ideal case and to verify that Newton's method is an adequate choice. For instance, the error of the force field is below the typical values upwards of 20 and 30 % reported in the literature ; these measurements are also inverted directly from a noisy displacement field, but countless details complicate any comparison.

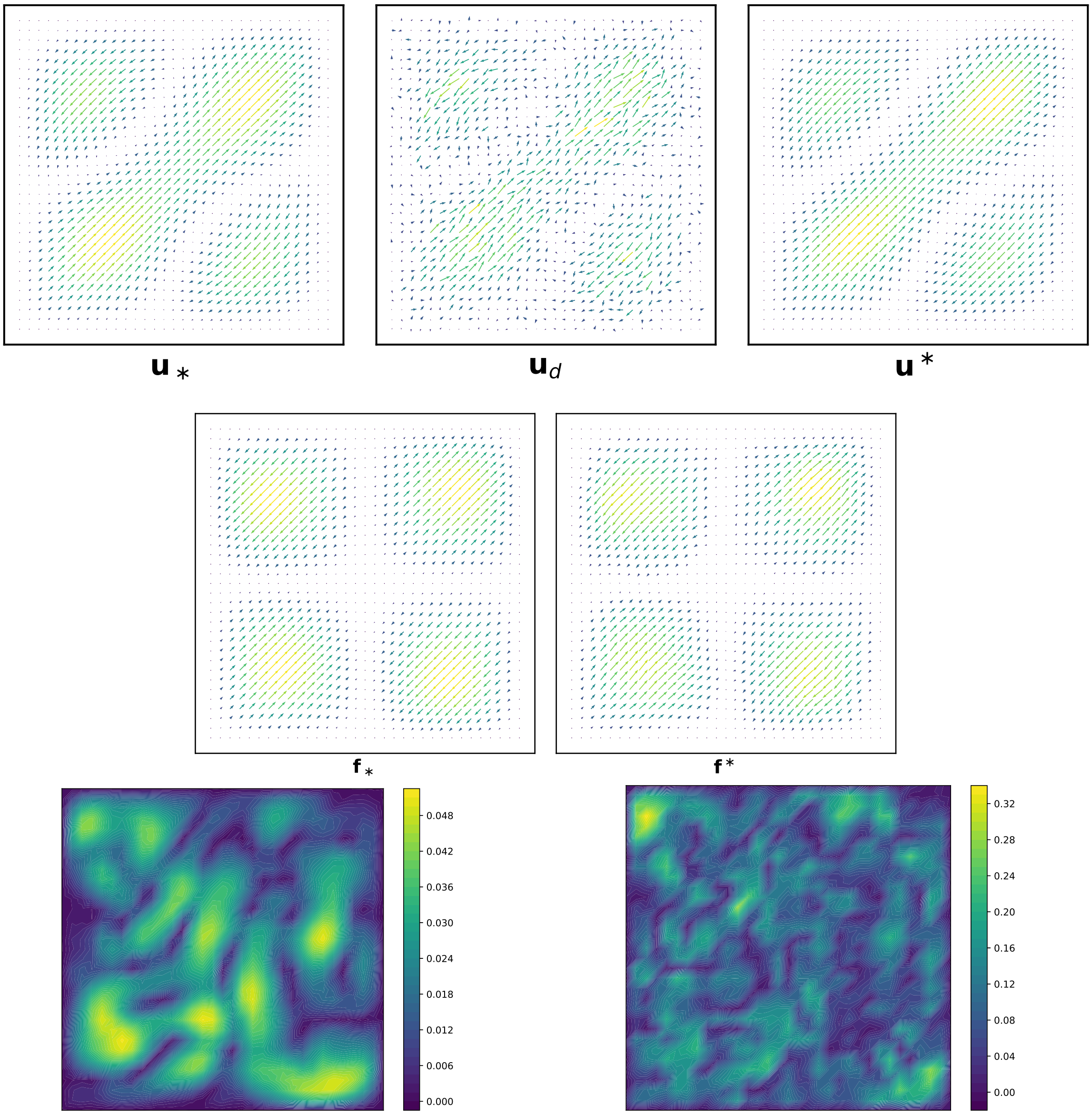

FIGURE III.5 – **Displacement and force reconstruction from noisy displacement data. Row 1)** True simulated displacement $\mathbf{u}_*$ (resulting from $\mathbf{f}_*$), displacement corrupted by $\eta_{\mathbf{u}}$ 20% noise, $\mathbf{u}_d$, and recovered displacement $\mathbf{u}^*$. **Row 2)** True imposed force $\mathbf{f}_*$ and recovered force $\mathbf{f}^*$. **Row 3)** Error map of the displacement $|\mathbf{u}^* - \mathbf{u}_*|_2 / \|\mathbf{u}_*\|_2$ and the force $|\mathbf{f}^* - \mathbf{f}_*|_2 / \|\mathbf{f}_*\|_2$. Violet (low) to yellow (high).

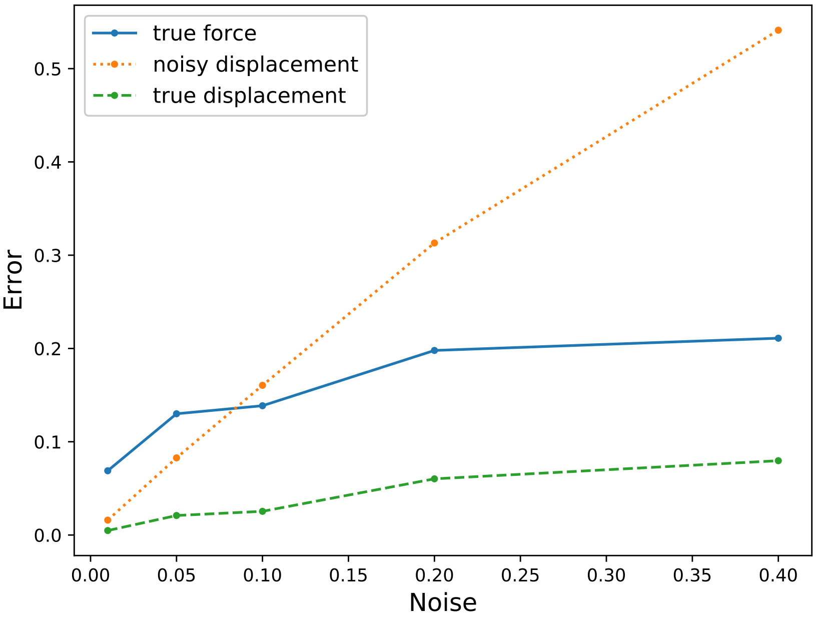

Figure III.6 – **Non-optical-flow : error of the inverted fields as a function of noise.** Error($\mathbf{f}^*, \mathbf{f}_*$) of the recovered force field as compared to the true imposed value ; Error($\mathbf{u}^*, \mathbf{u}_*$) of the displacement field compared to the true displacement (resulting from the true force) ; and Error($\mathbf{u}^*, \mathbf{u}_d$) of the displacement field compared to the erroneous data (notice the reasoning behind Morozov's criteria). All of them are a function of the percentage of error added $\eta_{\mathbf{u}}$.

III.3.4.2 Optical-flow test

The next step is to evaluate the modified optical flow inversion. With this aim, we add Gaussian noise to the image, and not to the velocity. We believe this approach to be closer to the conditions found in a real setting because the noise is modeled after that found on real images :

$$I_d := I_1 + \eta_I \mathrm{e}_I \tag{III.68}$$

$\mathrm{e}_I \sim \mathcal{N}(\mathbf{0}, \mathrm{I})$ with level η_I. For this purpose, we recover the original optical-flow-inspired $\mathcal{J}_{data}$. While real image noise is normally a mix of Poisson (photon counting) and Gaussian, here we focus on Gaussian noise for two reasons. One : it is most prevalent ; two : it is significantly easier to model when estimating the variance (Section III.4).

To determine whether our method has any effect on reducing noise sensitivity, in Figure III.7a we compare our PDE-constrained optimisation with a standard optical flow. The results show that regularising the underlying force with our method is more robust to noise than regularising the displacement directly. Indeed, the errors grow much faster in the standard approach than in the PDE-constrained approach (Figure III.7b). In addition, we remark that the elastic model we chose should be specially favorable to standard optical flow as the equations yield smooth displacement fields ; and that we accounted for neither out-of-plane flow nor for a restricted force zone $K \subset \Omega$ because both factors would give further edge to our method.

In our method, the displacement error stays below 10% down until a signal-to-noise ratio of 1.7 ; for comparison, typical confocal SNRs range between 25 and 50. Even when compared to the errors in Figure III.6, where the problem is "exact", our results still hold surprisingly well.

Therefore, we believe that TFM computations can greatly benefit from our approach : not only they account for out-of-plane flow, boundary conditions and near-incompressibility ; but they also promise to reduce error sensitivity. We will see in the up-coming Section III.4 that the method can also yield variance estimates by considering the image intensity uncertainty.

The force estimates of the PDE-constrained approach also fare well under noise (Figure III.8a), albeit worse than the displacement measures, as expected from the preliminary non-optical flow analysis (Figure III.6). We have also assessed the effect of multi-scaling in the recovery error. As the scale is refined, a progressively higher amount of information is considered, resulting in smaller reconstruction errors. However, the growing trend stops and plateaus (Figure III.8b). This behavior is a consequence, in part, of the effective rank of the hessian, which is showcased in Section III.3.4.4. In general, the force reconstruction appears much better than in the literature, but comparisons are hard for lack of detail. For example, at standard confocal SNR rates the error moves around 14% and hardly ever falls below 10%.

One of the advantages of this method is the fact that our knowledge of **f** can be used to regularise the problem more naturally. In Figure III.9, we show a comparison between L^2 and TV regularisation directly on the force field **f**. As expected, the TV method is much more accurate when recovering step functions ; for example, this might be the case of focal adhesions when enough resolution is available. It is worth noting that a force function of bounded variation does not correspond to a displacement function of bounded variation because the elastic equations are smoothing.

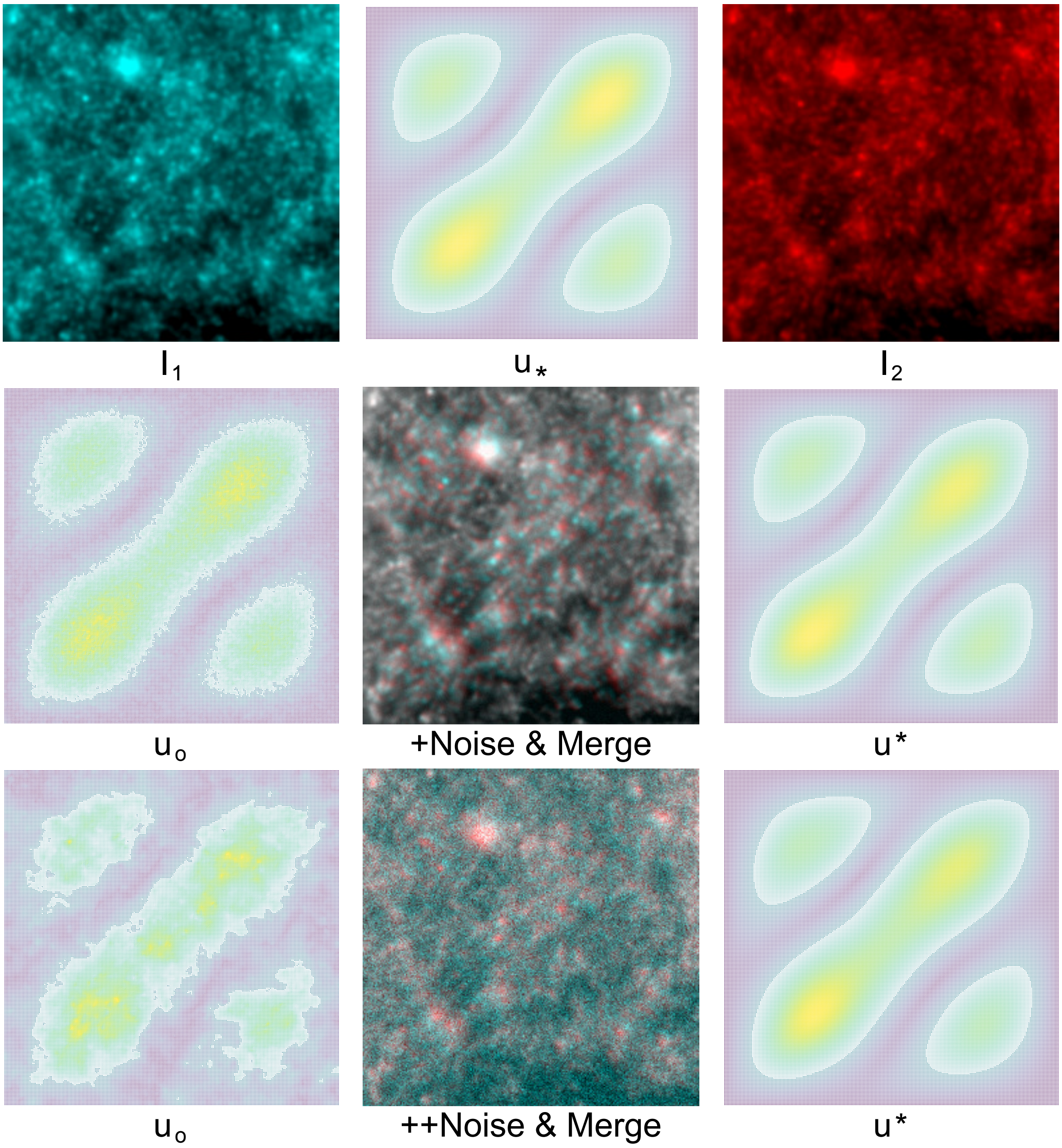

I_1 u_* I_2

u_o +Noise & Merge u^*

u_o ++Noise & Merge u^*

(a)

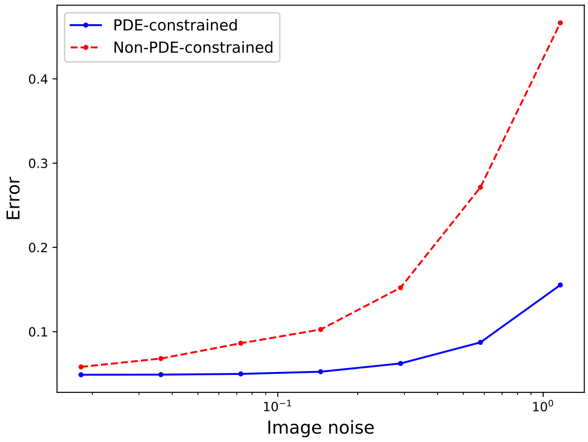

(b)

FIGURE III.7 – **Non-constrained optical flow vs PDE-constrained optical flow. a)** Row 1) The deformed image I_2 (red) after using the displacement field $\mathbf{u}_*$ to warp the reference image I_1 (cyan). Row 2) After adding noise (SNR 27.6) to both images the force is recovered with standard multi-scale optical flow ($\mathbf{u}_o$) and the PDE-constrained method ($\mathbf{u}^*$) ; the central image shows displacement in white as a superposition of both noisy images. Row 3) Same as (Row 2) but with a SNR of 1.7. All meshes (and thus the resolution of the displacement fields) are pixel sized ; the results shown in III.5 are from the same simulated system but coarser. Violet (low) to yellow (high). **b)** Error($\mathbf{u}^*, \mathbf{u}_*$) of the displacement field as a function of noise. The "image noise" parameter is the coefficient of variation, i.e. the reciprocal of the signal-to-noise (SNR) ratio. The SNRs of the points are 55.2, 27.6, 13.8, 6.9, 3.5, 1.7, 0.9. The displacement recovered by the regularised multi-scale optical flow is much more sensitive to noise than our multi-scale PDE-constrained approach. x-axis is log-scaled.

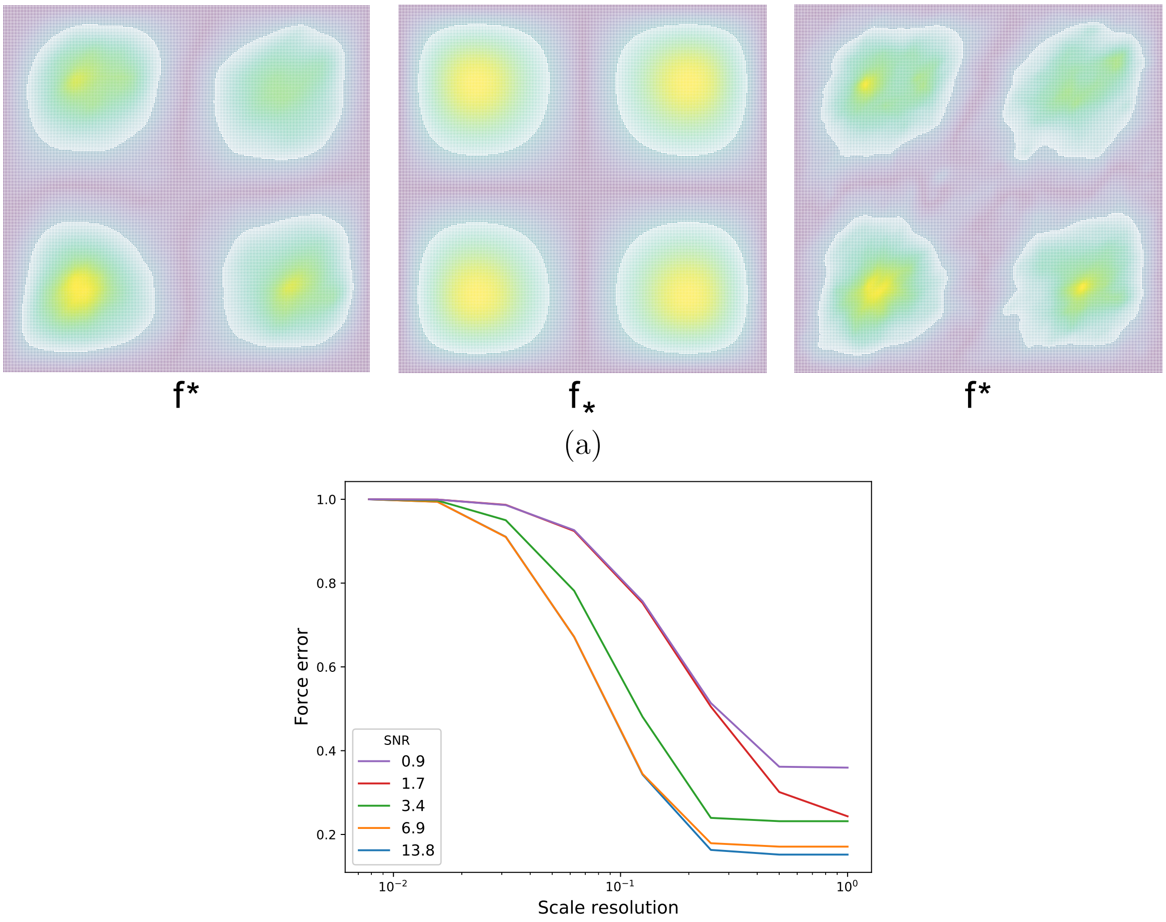

(a)

(b)

Figure III.8 – **PDE-reconstructed force. a)** Comparison of recovered force fields $\mathbf{f}^*$ (SNRs : 27.6 left, 1.7 right) with the true field $\mathbf{f}^*$ (middle). Find the corresponding velocity fields $\mathbf{u}^*$ and $\mathbf{u}$ in Figure III.7a. **b)** Error($\mathbf{f}^*, \mathbf{f}_*$) of the force field as a function of the scale (in the multi-resolution approach) for different values of the SNR. Typical confocal imaging SNRs range between 25 and 50. x-axis is log-scaled.

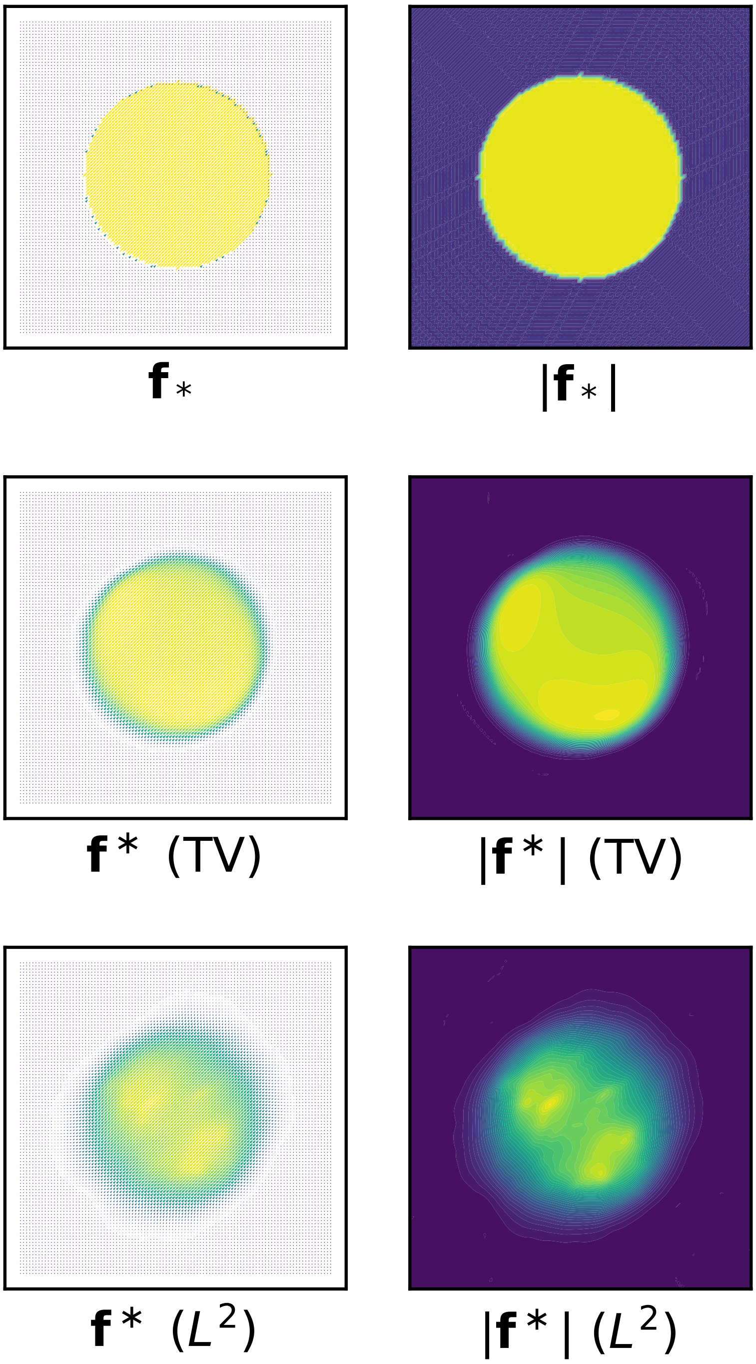

Figure III.9 – **TV vs L^2.** Vector fields (left column) and magnitudes (right column) for the true imposed force (top row), the force recovered using TV regularisation (middle row) and the force recovered using L^2 regularisation (bottom row). TV brings down the error from 30% to 20% and from 2% to 1% of the force and the displacement (respectively) as compared to L^2. Violet (low) to yellow (high).

III.3.4.3 The regularisation parameter should concur with the noise

We have shown (Annex E) the effect that the regularisation parameters (e.g. α) have on the solution : L^2 acts as a low-pass filter, and Tikhonov and Frobenius-TV respectively act as isotropic and anisotropic diffusors. While it is easier to find a suitable range of values armed with this intuition, the hunt for the perfect parameter requires some better-defined criteria. Based on the theory of residues, Morozov's discrepancy principle [399] states that the reconstruction is best when it recovers the noise norm δ, for example

$$\|\mathbf{u}^*(\alpha) - \mathbf{u}_d\|_\Omega \leq \delta_\mathbf{u}, \tag{III.69}$$

where $\mathbf{u}^*$ is the solution of the inverse problem, which we compare to the simulated displacement $\mathbf{u}_d$. In other words, the noise bounds the data misfit. Of course, a strong requirement is to be aware of the noise distribution. This is plausible in our computer-generated experiments, where we add noise ($\delta_\mathbf{u}$) to the displacement field, but less so in a real-world context. However, this possibility is not far-fetched as regards our experimental data. Indeed, we can have an educated idea of the noise δ_I within the images from the camera or the image settings. We can then use our original misfit (Figure III.10) to look for the ideal parameter :

$$\|I_2(\mathbf{x} + \mathbf{u}(\alpha)) - I_1(\mathbf{x})e^s\|_\Omega \leq \delta_I. \tag{III.70}$$

On another note, should we find ourselves completely blind, we can use the L-curve criterium [399]. In this alternative, one compares the data misfit to the regularisation effort in search for a compromise between being faithful to the data and providing an stable solution. Plotting both norms on a log-log scale yields a curve shaped like an L. The optimal parameter corresponds to the highest curvature of the L as it represents the tilting point where advancing in any direction is not a good trade-off.

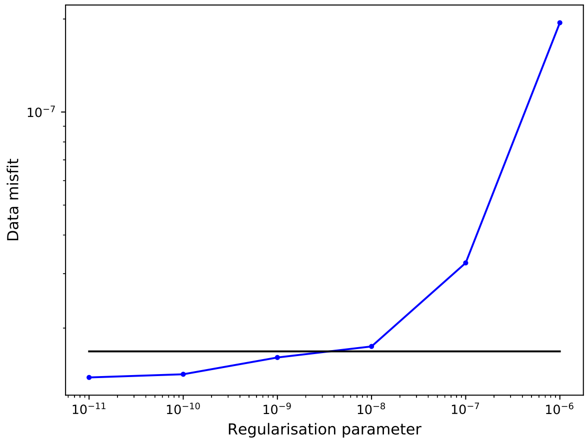

Figure III.10 – **Example of Morozov's principle in action.** Data misfit $\|I_2(\mathbf{x}+\mathbf{u}(\alpha)) - I_1(\mathbf{x})e^s\|_\Omega$ as a function of α. Black line marks the noise level δ_I. Morozov's principle suggests $\alpha = 10^{-9}$.

III.3.4.4 The spectrum of the Hessian reflects the influence of the data

To assess how well-informed the inverse problem is by the data, we analyse its eigenvectors [399] [17]. The question can be formalised into solving the following generalised hermitian eigenvalue problem (GHEP) : find some eigenvectors $(\hat{\mathbf{f}}_i, \hat{\mathbf{g}}_i)$ and corresponding eigenvalues λ_i such that

$$H_{\text{data}}(\hat{\mathbf{f}}_i, \hat{\mathbf{g}}_i) = \lambda_i R(\hat{\mathbf{f}}_i, \hat{\mathbf{g}}_i), \tag{III.71}$$

where we recall R, H_{data} are the regularisation and Hessian symmetric matrices, with $R + H_{\text{data}}$ positive definite. We have generalised the problem with the regularisation matrix for the same reasons as we chose the preconditioner in Newton's method : we need to properly represent the space of functions and inner product (Riesz). The dominant eigenvectors are the directions which are most informed by the data. To appreciate this intuitively, recall that the system is solved by "inverting" the Hessian and therefore the eigenvalues also get inverted. In fact, the function of the regulariser (proportional to α) is to lift the eigenvalues above the 1-threshold (Figure III.11b). If the problem is quadratic and we start with a zero guess, the eigenvectors (Figure III.12) directly conform the solution.

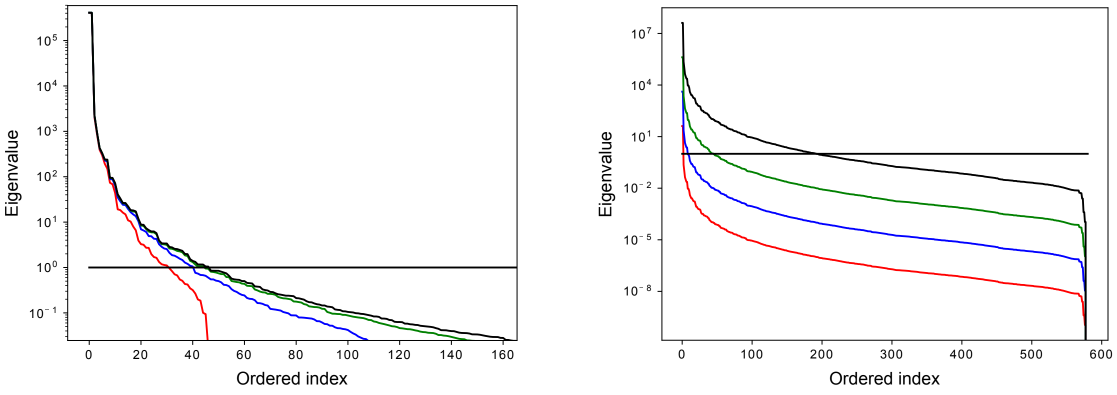

(a) (b)

Figure III.11 – **Hessian eigenvalues. a)** The dominant eigenvalues are independent of mesh dimension (increasing degrees of freedom or mesh size : red, blue, green, grey). **b)** The eigenvalues depend on the regularisation (increasing levels of α : red, blue, green, grey). In both figures the horizontal black line marks the 1-threshold. Both eigenvalues and eigenvectors are indexed in decreasing order.

To compute an approximation of the eigenmodes in feasible time, we use an algorithm based on random low-rank factorisation [404, 405]. In particular, we choose a double-pass algorithm because it only requires mat-vec products [404, 406]. There are

---

[17] Find an exemplary application in [400], and some recent website resources in [401, 402, 403]. I would like to take this opportunity to thank the 2018 Gene Golub Summer School for much important insight (details in Acknowledgments).

two fundamental ideas behind this approach. The first is to notice that $R^{-1}H_{\mathrm{data}}$ is not necessarily symmetric per se, but that it is symmetric with respect to the R inner product. The second is to adapt a randomized eigenvalue decomposition algorithm to a non-euclidean inner product [406]. Conceptually, randomised decompositions consist in constructing a relevant low-dimensional subspace Y of rank r by capturing the action of the matrix on a $r+p$ (p over-samples) Gaussian random matrix Θ, i.e. $Y = H_{\mathrm{data}}\Theta$ which is readily parallelisable. Y is then QR-factorised and eigen-decomposed. This process provides theoretical guarantees of convergence and a posteriori error measures, which are generally bounded by the eigenvalues left behind (i.e. dominated by λ_{r+p+1}). Our implementation is based on the algorithm proposed by Saibaba [406] for GHEP problems.

The number of generalised eigenvalues above 1 is called the effective rank of the Hessian misfit and its a reflection of the inherent dimension of the problem given the data available. In other words, the sparse observations we can make are only useful to a limited amount of modes of the infinite parameter field we are inverting for. Indeed, as is seen in Figure III.11a and is well-known as a spectral property of Hessian misfit expressions, the effective rank is independent of the spatial resolution (mesh size). In addition, the spectrum confirms that the Hessian is a compact operator with (rapidly) decaying eigenvalues, as is expected from an ill-posed problem. This property is behind the fast convergence of the CG method we have observed in Figure III.3.

Let us share some last intuition regarding the importance of the Hessian. The Hessian tells us how important (eigenvalue), or how informed by the data, is each direction (eigenvector) of the system. It is also in this sense that it helps Newton's method choose an ideal step and not only a direction. Think of an elliptic (rather than circular) quadratic potential energy, in which some directions matter more than others. The PDEs act here only as a linear constraint. If all directions matter the same, the Hessian is the identity and the algorithm becomes steepest descent. Riesz's interpretation is important here again to properly represent angles ; for this reason, we generalise the eigenvalue problem with the preconditioner matrix, which reflects our choice of inner product.

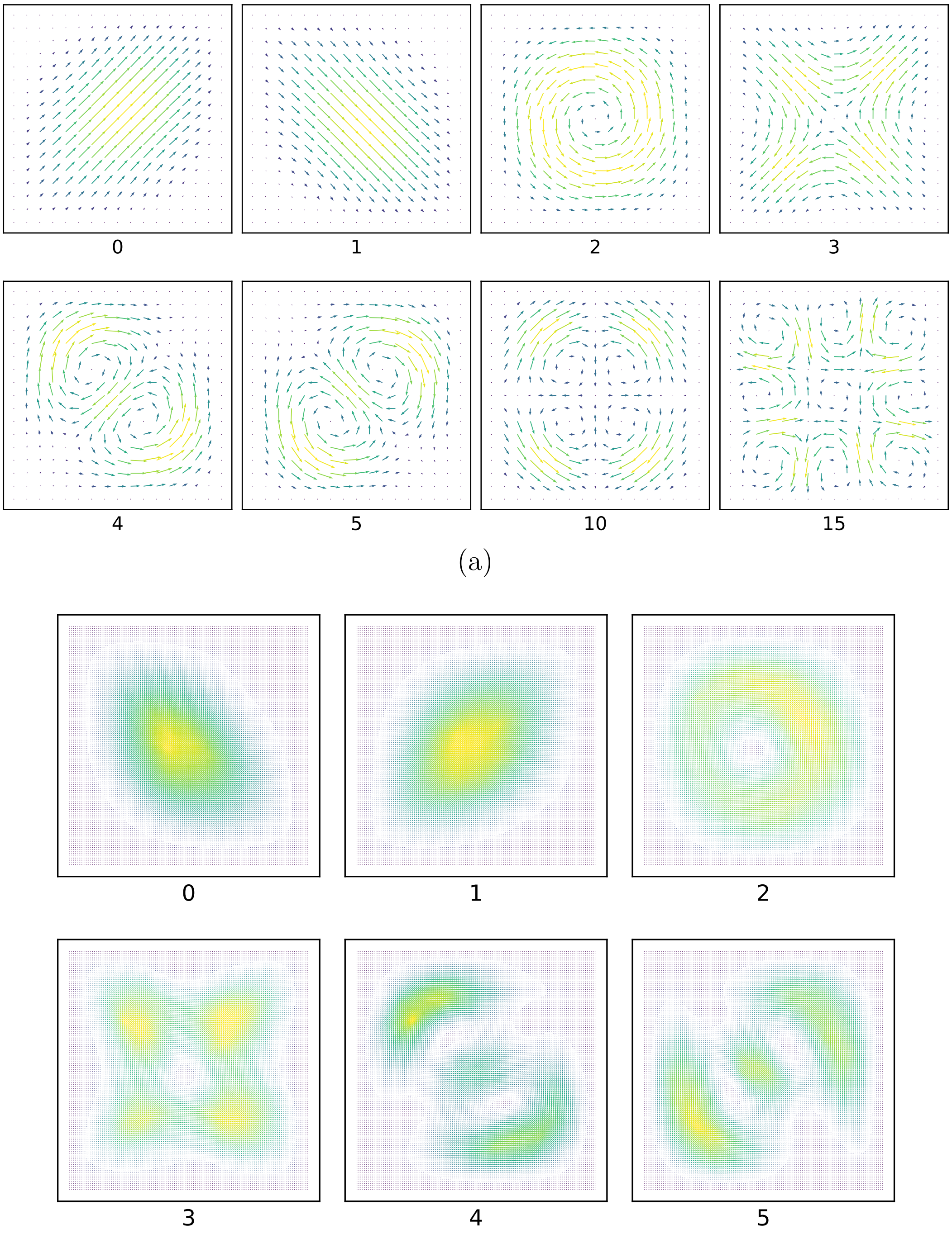

(a)

(b)

FIGURE III.12 – **Hessian eigenvectors.** a) Some eigenvectors $\hat{\mathbf{f}}_i$ for $i \in \{0, 1, 2, 3, 4, 5, 10, 15\}$ of the solution in Figure III.5. **b)** And $i \in \{0, 1, 2, 3, 4, 5\}$ of the solution in Figure III.8.

III.4 Adding uncertainty : Bayesian PDE-constrained inverse problem

The last part of the thesis extends the framework into a Bayesian setting. Inverting the deterministic PDE-constrained problem yields but single estimates of the quantities of interest. However, it is necessary to assess how reliable the reconstructions are because images are noisy. Indeed, a crucial duty of experimental science is to report measurement errors, yet (to our knowledge) a systematic method to quantify uncertainty has not been developed neither in PIV nor TFM. Under the Bayesian framework that we propose, the result is a posterior density that expresses the probability distribution of the traction force that was exerted by the cells on the substrate given that we observed our image sequence. To make such a large problem tractable we rely on a Laplacian approximation that yields a Gaussian posterior whose covariance is related to the Hessian of the problem, which we address using a low-rank approximation. We also model the experimental errors of the measured elastic modulus of the substrate by pre-marginalising the optical flow functional. Lastly, we propose to use the resulting error estimates to determine whether structures that appear on the recovered force field are actually significant or artifacts.

Inverting the deterministic PDE-constrained problem yields a single estimate of the force $\mathbf{f}$, the boundary condition $\mathbf{g}$, and the displacement field $\mathbf{u}$. However, it is necessary to assess how reliable the reconstructions are because our image measurements are not perfectly accurate. Indeed, a crucial duty of experimental science is to report measurement errors, yet (to our knowledge) a systematic method to quantify uncertainty has not been developed in neither PIV ($\mathbf{u}$) nor TFM ($\mathbf{f}$). While error estimates are sought, they normally consist on averaging many experiments. However, the patterns of force distribution on single experiments are much harder to assess under this frequentist approach. In this section, we show that the deterministic solution constitutes a good summary of the inversion problem as the point of maximum probability. We then compute the uncertainty associated with the reconstructed fields and provide confidence intervals.

To quantify the uncertainty of the inverse solution, we take a Bayesian approach [407, 408, 378] [18]. Under this framework, the result is a posterior density that expresses the probability distribution of $\mathbf{f}$ being the force that was exerted by the cells given that we observed images I_1 and I_2 under additive Gaussian noise. This distribution can be deduced from the combination of two other densities. 1) The likelihood, which talks about the opposite probability, i.e. "observe I_1, I_2 given a known force $\mathbf{f}$", and is

---

[18] See an example in [400], some website resources [401], and related libraries [409, 397]. I would like to take this opportunity to thank the 2018 Gene Golub Summer School for much important insight (details in Acknowledgments).

modeled by a noise-corrupted data functional $\mathcal{J}_{data}$. 2) And the prior density, which encodes *a priori* knowledge regarding **f** and is equivalent to the regularisation in the deterministic problem. In this part of the work, we focus on quantifying the uncertainty of **f** assuming **g** is the solution of the deterministic problem.

We recognise, of course, that Bayesian errors are subject to various assumptions, notably the prior distribution, and thus we recommend caution when interpreting the results of our method. However, standard PIV and TFM methods are not exempt of such predicament ; they also require prior knowledge in the form of a regulariser. In fact, PIV+TFM will often imply two regularisers.

To make such large problem tractable we rely (again) on linearising the data functional, which yields a Gaussian likelihood. Together with a Gaussian prior, this implies a Gaussian posterior, avoiding prohibitive sampling. We show that both the mean and the maximum *a posteriori* probability of the posterior distribution correspond to the deterministic solution when regularised with a norm equivalent to that used for the prior. We then compute the posterior covariance using a low-rank approximation. We also model the experimental errors of the measured elastic moduli by pre-marginalising the data functional. Lastly, we propose to use the resulting error estimates to determine whether structures that appear on the recovered force field are actually significant or are artifacts instead.

III.4.1 ∞-dimensional Bayesian inverse problem

In infinite dimension, Bayes' rule is formulated in terms of the Radon-Nikodym derivative because there is no analogue of Lebesgue's measure. It reads

$$\frac{d\nu_I}{d\nu_{\mathbf{f}}} \propto \pi(I_1|\mathbf{f}), \tag{III.72}$$

with the corresponding σ-finite measures ν_I, $\nu_{\mathbf{f}}$ in the place of conventional probability density functions (pdf). A second challenge is to ensure the well-posedness of the posterior distribution. To meet this requirement, in the literature there is not much room regarding the choice of a valid prior measure. In this work, we pick a Gaussian measure as a prior, with mean $\mathbf{f}_\star$ and a covariance operator $\mathcal{C}_{\mathbf{f}}$. As will be discussed in subsection III.4.1.1, priors based on inverse elliptic operators are most convenient as it is easy to verify that they satisfy the necessary regularity conditions for well-posedness [410]. In the Bayesian approach, the prior acts similarly to the regularisation term in the deterministic problem (see subsection III.4.2). Therefore, the choice of prior has great influence on the resulting reconstruction. Certainly, it is most important when the inverse problem is under-determined, but it can also be essential in over-determined systems if there is enough observational noise [410].

On the other hand, the likelihood is the result of both inflicting noise on the modified optical flow equation (III.6) and considering any modelling error. In particular, we model the image noise $\mathrm{e}_I \sim \mathcal{N}(\mathbf{0}, \mathrm{C}_I)$ as Gaussian additive, and postpone the proper introduction of a surrogate model error $\mathrm{e}_{\mu,\lambda}$ until Section III.4.3. Meanwhile, we call total error ($\mathrm{e}_{I,\mu,\lambda} := \mathrm{e}_I + \mathrm{e}_{\mu,\lambda}$) the sum of both error sources. Under this notation, the functional can be expressed as :

$$I\left(\mathbf{x} + \mathbf{u}(\mathbf{f}), t+1\right) e^{-s} = I\left(\mathbf{x}, t\right) + \mathrm{e}_{I,\mu,\lambda}. \tag{III.73}$$

In principle, the additive image noise is independent and identically distributed, i.e. $\mathrm{C}_I = \sigma_I^2 \mathrm{I}$ for some variance $\sigma_I \in \mathbb{R}_{\geq 0}$. Like the image error, the total error is also Gaussian because we approximate (Section III.4.3) the surrogate error as Gaussian. In particular, we account for the model reduction with a covariance $\mathrm{C}_{\mu,\lambda}$ and a possibly non-zero mean $\mathrm{e}_{\mu,\lambda,\star}$. Therefore, the likelihood of I_1 given $\mathbf{f}$ can be written as[19]

$$\pi(I_1|\mathbf{f}) \propto \exp\left(-\|I_2(\mathbf{x}+\mathbf{u})e^{-s} - I_1(\mathbf{x}) - \mathrm{e}_{\mu,\lambda,\star}\|^2_{\Omega,\mathrm{C}^{-1}}\right), \tag{III.74}$$

where $\mathrm{C} := \mathrm{C}_I + \mathrm{C}_{\mu,\lambda}$ because the covariances of two Gaussians sum, and the means sum too $\mathrm{e}_{\mu,\lambda,\star} = 0 + \mathrm{e}_{\mu,\lambda,\star}$. In other words, $\pi(I_1|\mathbf{f}) = \mathcal{N}(I_2(\mathbf{x}+\mathbf{u})e^{-s} - I_1(\mathbf{x}), \mathrm{C})$.

Even though the map $\mathbf{u}(\mathbf{f})$ is linear, $I_2(\mathbf{x}+\mathbf{u}(\mathbf{f}))$ is certainly not. This non-linearity results in a non-Gaussian likelihood distribution. However, we cannot afford to use sampling techniques such as Markov chain Monte Carlo (MCMC) methods because every sample is PDE-solve expensive. To make the problem tractable, we take the same linearisation as in (III.7), but directly on I_2 :

$$\pi(I_1|\mathbf{f}) \underset{\sim}{\propto} \exp\left(-\|e^{-s}\left((-I_2\nabla s + \nabla I_2)\cdot \mathbf{u} + I_2\right) - I_1 - \mathrm{e}_{\mu,\lambda,\star}\|^2_{\Omega,\mathrm{C}^{-1}}\right). \tag{III.75}$$

Alternatively, we have also attempted to follow the propagation of the error through the multi-scale analysis. For example, by propagating $\mathbf{f}$ to $\mathbf{u}$, and then $\mathbf{u}$ to the intensity of the warped image I_w. However, this is slow and it is not clear how to evaluate the errors incurred by certain operations (e.g. up-scaling). Therefore, we resort to the Laplacian approximation in (III.75). In the case where both prior and likelihood are Gaussian, the posterior is Gaussian with mean the maximum *a posteriori* (MAP) point, and covariance the Hessian of the negative-log posterior at that point.

III.4.1.1 Prior analysis for well-posedness and scalability

Whereas having access to non-Gaussian priors would be interesting to model edge-preserving regularisations such as TV, inverting ∞-dimensional fields in a Bayesian context is still a cutting-edge problem that merits active research. In the context of our work, the main obstacle is the combination of the high-dimensional parameter space and the cost of the PDE forward solve, which precludes reasonably-long sampling of the posterior via conventional approaches such as MCMC. This is the same problem we have just avoided by linearising the functional term.

---

[19] **NOTATION** : we use $\langle \bullet, \bullet \rangle_{*,\mathrm{M}}$ to notate the inner product weighted by a matrix (or operator) M over a domain $*$, and $\|\bullet\|_{*,\mathrm{M}}$ the induced norm. More visually, $\langle a, b\rangle_{*,\mathrm{M}}$ is $\langle \mathrm{M}^{1/2}a, \mathrm{M}^{1/2}b\rangle_*$ or $a^T\mathrm{M}b$.

In addition to non-Gaussianity, it has been shown that TV suffers from other problems in the Bayesian framework. Although it has worked on fixed discretisations [411, 412, 413], the fact that TV is not discretisation invariant [414] is specially relevant to our multi-scale method. To amend these short-comings while preserving the blocky reconstruction characteristic of TV regularisation, the literature proposes several alternatives such as Besov functions [415]. However, most remain non-Gaussian. Inspired by the asymptotical Gaussianity of TV, [416] uses Gaussian hyper-priors to recover blocky objects. Alternatively, [417] proposes a TV-G prior that includes a TV term, but uses Gaussian distributions as a reference measure. This strategy enables the use of MCMC-like algorithms developed for Gaussian priors that show dimension independence (e.g. preconditioned Crank-Nicolson). Given all subtleties and difficulties, adapting a TV-like prior to perform well under all our additional requirements will be the object of future research.

Common Gaussian priors in Bayesian inverse problems are defined in terms of ∞-dimensional covariance functions that result in dense matrices, which need to be built and later inverted. These computational hardships can be avoided by using inverse elliptic operators because they are fast to solve and do not require building the associated dense operator (we only need their action). Furthermore, [410] outlines an ∞-dimensional Bayesian framework that ensures well-posedness of the associated inverse problem given sufficient regularity of the prior such as in Laplacian-like operators[20]. Since it is first formulated on an infinite setting, this approach guarantees discretisation invariance for any finite approximation of the problem. We note that these methods are opposed to most classical approaches where the Bayesian framework is only introduced after discretisation (e.g. [407]). These analyses have to resort to capturing the limit of infinite resolution by modelling the error introduced by the finite approximation [418].

To represent the covariance operator of the Gaussian random field prior, we choose an inverse elliptic operator $\mathcal{C}_{\mathbf{f}}(\mathbf{f})$ defined as $(\alpha \mathrm{I} - \beta\Delta)^{-\nu}\,\mathbf{f}$ in K with a Neumann boundary condition $\beta\nabla\mathbf{f}\cdot\mathbf{n}$ on Γ, where $\mathbf{n}$ is the boundary normal and ν an exponent. Here $\alpha, \beta \in \mathbb{R}_{\geq 0}$ control the variance and the correlation length of the prior, respectively. Notice that for $\nu = 1$ the prior distribution is equivalent to Tikhonov H^1 regularisation as shown in (III.57)[21]. Unfortunately, the proposed operator is only trace class for $\nu > d_{\mathrm{O}}/2$. That is we can only guarantee that the ∞-dimensional Bayesian inverse problem is well-posed for $\nu > 1$ in 2D and $\nu > 3/2$ in 3D [410]. In other words, we need more regularity than in the deterministic counterpart, where $\nu = 1$ would generally suffice for well-posedness. Indeed, the resulting biharmonic operator for $\nu = 2$ is known to be very smoothing. This can be also seen from the point of view of the Green's functions of the associated elliptic PDE, which actually represents the co-

---

[20] [410] defines so-called Laplacian-like operators as positive-definite, invertible, self-adjoint, with eigenvalues (indexed by j) that grow like $|j^2|$; and with eigenfunctions that form an orthonormal basis of the overlaying Hilbert space, are bounded, and whose gradient grows like $|j|$.

[21] Think of discretising the operator with the FEM : integrating the Laplacian by parts yields a gradient product.

variance of the parameter field between two given points : in 2D and 3D they are bounded for the biharmonic operator but singular along the diagonal in the Laplacian (unbounded variance) [22]. In any case, the PDE imposes that the correlation of a point with its neighbours decreases (smoothly) with distance. We take $\nu = 2$ as the closest valid integer that guarantees bounded (point-wise) variance and well-posedness of the ∞-dimensional Bayesian inverse problem. With this operator it is easier to sample the Gaussian distribution because we have a fast and easy square root operator in $\mathcal{C}_{\mathbf{f}}^{1/2}$ as $(\alpha \mathrm{I} - \beta\Delta)^{-1}$.

The Gaussian prior can then be expressed as

$$\pi(\mathbf{f}) \propto \exp\left(-\|\mathcal{C}_{\mathbf{f}}^{-1/2}\left(\mathbf{f}-\mathbf{f}_\star\right)\|_\Omega^2\right) = \exp\left(-\|\mathbf{f}-\mathbf{f}_\star\|^2_{\Omega,\mathcal{C}_{\mathbf{f}}^{-1}}\right) \tag{III.76}$$

where $\mathbf{f}_\star$ is the prior mean (which we will set to zero $\mathbf{f}_\star = 0$). The first and second variations of the associated regularisation are

$$D_{\mathbf{f}}\mathcal{J}_{reg}^{\mathcal{C}_{\mathbf{f}}} \cdot \tilde{\mathbf{f}} = 2\mathcal{C}_{\mathbf{f}}^{-1}(\mathbf{f}-\mathbf{f}_\star), \tag{III.77}$$

$$D^2_{\mathbf{f}}\mathcal{J}_{reg}^{\mathcal{C}_{\mathbf{f}}} \cdot \tilde{\mathbf{f}} \cdot \tilde{\tilde{\mathbf{f}}} = 2\mathcal{C}_{\mathbf{f}}^{-1}(\tilde{\mathbf{f}}). \tag{III.78}$$

We recall the discrete regularisation for comparison :

$$D_{\mathbf{f}}\mathcal{J}_{reg}^{H^1} \cdot \tilde{\mathbf{f}} = 2\alpha\langle\mathbf{f},\tilde{\mathbf{f}}\rangle_K + 2\beta\langle\nabla\mathbf{f},\nabla\tilde{\mathbf{f}}\rangle_K, \tag{III.79}$$

$$D^2_{\mathbf{f}}\mathcal{J}_{reg}^{H^1} \cdot \tilde{\mathbf{f}} \cdot \tilde{\tilde{\mathbf{f}}} = 2\alpha\langle\tilde{\mathbf{f}},\tilde{\tilde{\mathbf{f}}}\rangle_K + 2\beta\langle\nabla\tilde{\mathbf{f}},\nabla\tilde{\tilde{\mathbf{f}}}\rangle_K. \tag{III.80}$$

III.4.2 Discretisation of Bayes' formula yields a Gaussian posterior

The finite-dimensional formulation of the Bayesian inverse problem requires subspaces akin to those introduced in its deterministic counterpart (here we only notate the pdfs with the h subscript, but leave the other variables as they are for readibility). Therefore, we focus on the discrete version of Bayes' law :

$$\pi_h(\mathbf{f}|I_1) \propto \pi_h(I_1|\mathbf{f})\pi_h(\mathbf{f}). \tag{III.81}$$

Collecting both prior and likelihood, we can write the posterior distribution

$$\begin{aligned}\pi_h(\mathbf{f}|I_1) \overset{\propto}{\sim} \exp(&-\|e^{-s}\left((-I_2\nabla s + \nabla I_2)\cdot\mathbf{u} + I_2\right) - I_1 - \mathrm{e}_{\mu,\lambda,\star}\|^2_{\Omega,\mathrm{C}^{-1}} \\ &- \|\mathbf{f}-\mathbf{f}_\star\|^2_{\Omega,\mathrm{C}_{\mathbf{f}}^{-1}}),\end{aligned} \tag{III.82}$$

which is the pdf that represents the probability of $\mathbf{f}$ given that we observed I_1. Notice that we have notated $\mathrm{C}_{\mathbf{f}}$ the finite-dimensional approximation (via FEM discretisation) of the covariance operator.

---

[22] Alternatively, think about what exponent is needed for the sum of the eigenvalues (trace) to be finite (e.g. $\sum_i 1/(1+i^2)$). The α terms makes the operator invertible.

The maximum *a posteriori* (MAP) probability estimate $\mathbf{f}^{\star}$ is the point that maximizes the posterior pdf (III.82), or minimizes its negative logarithm,

$$\mathbf{f}^{\star} := \underset{\mathbf{f}}{\operatorname{argmax}}\, \pi_h(\mathbf{f}|I_1) = \underset{\mathbf{f}}{\operatorname{argmin}}\, \mathcal{J}_h, \tag{III.83}$$

because the proportionality constant of the posterior does not depend on $\mathbf{f}$. This is precisely the result of the discretised version (minimise $\mathcal{J}_h$) of the deterministic inverse problem (III.23)[23], which we solved with multi-scaling and the adjoint method in Section III.3. That is $\mathbf{f}^{*} = \mathbf{f}^{\star}$ (notation from Section III.3.4). Notice also that the resulting posterior pdf (III.82) is normal because both the prior and the likelihood were chosen normal. Therefore, we also have that the MAP estimate is the mean $\mathbb{E}(\mathbf{f}) = \mathbf{f}^{\star}$. That is $\pi_h(\mathbf{f}|I_1) \sim \mathcal{N}(\mathbf{f}^{\star}, \mathrm{C}^{\mathbf{f}})$. This means that only the covariance $\mathrm{C}^{\mathbf{f}} \in \mathbb{R}^{n\times n}$ is left to fully characterise the posterior distribution, where n is the number of degrees of freedom of the discretised traction field $\mathbf{f}$. Completing squares and discarding any non-$\mathbf{f}$-dependent term to the proportionality constant, we can see that the posterior covariance $\mathrm{C}^{\mathbf{f}}$ is the inverse of the Hessian at $\mathbf{f}^{\star}$

$$\mathrm{C}^{\mathbf{f}} = \mathrm{H}^{-1}; \tag{III.84}$$

including the data misfit and the prior :

$$\mathrm{H} = \mathrm{H}_{\mathrm{data}}(\mathbf{f}^{\star}) + \mathrm{C}_{\mathbf{f}}^{-1}. \tag{III.85}$$

Due to size constraints, we use a low-rank approximation to compute a low-dimensional basis for the inverse of the Hessian. This is possible because the spectrum of the misfit decays fairly quickly. In other words, the eigenvalues collapse to zero or the Hessian misfit operator is compact. Similarly to section III.3.4.4, we use a randomized eigen-decomposition algorithm to extract the first r eigenvectors of a prior-generalised Hessian misfit from its matrix-free action on a random set of vectors. Then we use the matrix inversion identity on the full Hessian and obtain (Annex F) an approximation of the posterior covariance :

$$\mathrm{C}^{\mathbf{f}} \approx \mathrm{C}_{\mathbf{f}} - \mathrm{U}\Lambda\mathrm{U}^{T} \tag{III.86}$$

where $\mathrm{U} \in \mathbb{R}^{n\times r}$ is an r-ranked matrix corresponding to the $\mathrm{C}_{\mathbf{f}}^{-1}$-generalised Hessian misfit eigenvectors, and $\Lambda \in \mathbb{R}^{r\times r}$ is the diagonal matrix containing the corresponding eigenvalues. Expression (F.9) shows very visually how the data misfit reduces (the matrix stays semi positive-definite after the approximation) the uncertainty of the prior. All the details, as well as error estimates related to higher-ranked eigenvalues, can be found in Annex F.

---

[23] With some changes. First, the extra term coming from the mean surrogate error. Second, the norms of the forcing terms in the adjoint and incremental adjoint are now to be taken with respect to the C^{-1}-weighted inner product (e.g. $-2\langle \boldsymbol{\mathcal{O}} \cdot \tilde{\mathbf{u}}, \boldsymbol{\mathcal{O}} \cdot \tilde{\tilde{\mathbf{u}}}\rangle_{\Omega,\mathrm{C}^{-1}}$ or $-2O^{T}\mathrm{C}^{-1}O$ when discretised). And third, the covariance of the prior as presented in equations (III.76)-(III.78) and its relation with the discrete regularisation [408]. For example, the H^1 regularisation is akin to the elliptic operator we have introduced when $\nu = 1$. In this regard, the effect of σ_I weighting the data misfit term can be completely incorporated into the coefficients of the prior covariance, i.e. only the relative weights should matter to find the MAP.

III.4.3 Marginalisation can account for imperfections in the elastic modulus

Image noise is not the only source of uncertainty in our system. Parameters μ and λ, which describe the elastic behavior of the material, are also subject to error because they are measured experimentally. A possible solution to account for this uncertainty is to invert the problem for $\mathbf{f}$, μ and λ simultaneously, but such amount of unknowns is bound to be ill-posed and computationally prohibitive. Instead, we treat the elastic moduli as nuisance variables. In this manner, we can premarginalise over the moduli and propagate them to an additive term ; inverting only for $\mathbf{f}$. The result is a redefined likelihood with an associated error that takes in account both the original image noise and an approximation of the error induced by the elastic moduli. This is known as the Bayesian approximation error (BAE) approach [407, 418, 419], and is normally used to account for model uncertainties resulting from parameter-space-size reduction in surrogate models. For example, an alternative application in our context would be to consider the discrepancy introduced by a linear approximation of the non-linear response of 3D collagen matrices.

We recall (III.73) in order to specify the total noise term $\mathrm{e}_{I,\mu,\lambda}$. Take the original expression but considering μ and λ as unknowns. As before, suppose that our images are corrupted by some Gaussian noise $e_I \sim \mathcal{N}(\mathbf{0}, \sigma_I^2 \mathrm{I})$:

$$I_2\left(\mathbf{x}+\mathbf{u}(\mathbf{f},\mu,\lambda)\right) e^{-s(\mathbf{f},\mu,\lambda)} - I_1\left(\mathbf{x}\right) = \mathrm{e}_I. \tag{III.87}$$

We then propose our surrogate model. We reduce the parameter space by assuming the elastic moduli are fixed to some $\mu_\star$, $\lambda_\star$. In this case, we choose the experimental mean value of the moduli as were taken in the deterministic approach (Section III.3). We model the error $\mathrm{e}_{\mu,\lambda} := I_2\left(\mathbf{x}+\mathbf{u}(\mathbf{f},\mu_\star,\lambda_\star)\right) e^{-s} - I_2\left(\mathbf{x}+\mathbf{u}(\mathbf{f},\mu,\lambda)\right) e^{-s}$ incurred when using the simplified model as a Gaussian distribution $\mathrm{e}_{\mu,\lambda}|\mathbf{f} \sim \mathcal{N}$; where we have dropped the dependence in s for readability. Under all these conditions, the new functional

$$I_2\left(\mathbf{x}+\mathbf{u}(\mathbf{f},\mu_\star,\lambda_\star)\right) e^{-s(\mathbf{f},\mu_\star,\lambda_\star)} - I_1\left(\mathbf{x}\right) = \mathrm{e}_I + \mathrm{e}_{\mu,\lambda} \tag{III.88}$$

takes in account both the image error and the surrogate error. The next simplication gets us a step closer to a solvable problem : we consider that the surrogate error is independent of the force $\mathbf{f}$ and thus $\mathrm{e}_{\mu,\lambda} \sim \mathcal{N}(\mathrm{e}_{\mu,\lambda,\star}, \mathrm{C}_{\mu,\lambda})$ for some mean $\mathrm{e}_{\mu,\lambda,\star}$ and covariance $\mathrm{C}_{\mu,\lambda}$. The statistics of $\mathrm{e}_{\mu,\lambda}$ can be computed by calculating the mean and covariance of a large number of simulations. The cost of the simulations is very high, but they can be performed offline. While the surrogate approximation depends on the image, we have observed very similar values of the associated covariance matrix across images from the same source.

Finally, we can define the functional in (III.73) by working with a total error $\mathrm{e}_{I,\mu,\lambda} := \mathrm{e}_I + \mathrm{e}_{\mu,\lambda}$ with mean the sum of means $\mathrm{e}_{\mu,\lambda,\star} = 0 + \mathrm{e}_{\mu,\lambda,\star}$, and covariance the sum of covariances $\mathrm{C} = \mathrm{C}_I + \mathrm{C}_{\mu,\lambda}$; and setting $\mu_\star, \lambda_\star$ as in the deterministic inverse problem. The effect of each summand in the total covariance can be assessed by comparing the traces of the matrices $\mathrm{tr}(\mathrm{C}_I) < \mathrm{tr}(\mathrm{C}_{\mu,\lambda})$ [419]. In this way, one can determine whether it is significant to include either term. We would like to recall that we have made two approximations regarding the surrogate error in this Section III.4.3 : normalisation and independence.

As a last note, let us comment on the experimental significance underlying the surrogate errors we have just modeled. The experimental uncertainty intervals of the moduli are the result of averaging diverse substrate samples and thus are not necessarily representative of the possible variations within a single sample. However, we take these values for lack of better estimates. Other information such as the spatial length scale of the moduli variations, which might be related to polymer length, can be represented as (increasingly far) off-diagonal blocks of the covariance matrix.

III.4.4 Forward propagation of traction errors quantifies displacement uncertainty

After the posterior distribution of $\mathbf{f}$ has been computed, we can propagate the uncertainty [400] through the elastic equations to obtain the posterior distribution of the displacement $\mathbf{u}$. That is we need to solve a system of linearly elastic stochastic partial differential equations (SPDEs). Since the force-to-displacement map is linear (linear PDE), we have $\pi(\mathbf{u}|I_1) \sim \mathcal{N}(\mathbf{u}^*, C^{\mathbf{u}})$. It is clear that the mean and MAP point $\mathbf{u}^\star$ is the result of solving the forward PDE with the force term $\mathbf{f}^\star$ (and thus $\mathbf{u}^\star = \mathbf{u}^*$ also). Likewise, the displacement covariance $C^{\mathbf{u}}$ at the MAP $\mathbf{u}^\star$ is the result of filtering the force covariance $C^{\mathbf{f}}$ at the MAP $\mathbf{f}^\star$ through the linearly elastic PDEs :

$$\mathcal{C}^{\mathbf{u}} = \mathcal{A}^{-1}\mathcal{C}^{\mathbf{f}}\mathcal{A}^{-*} = \mathcal{A}^{-1}(\delta^2\mathcal{J})^{-1}\mathcal{A}^{-1}, \tag{III.89}$$

where we have used the expression for a linear transformation ($\mathcal{A}^{-1}$) of a Gaussian [420] (first equality), and both the "self-adjointness" of $\mathcal{A}$ and the non-discretised version of (III.84) (second equality). Both the force-to-displacement map $\mathcal{A}^{-1}$ and the Hessian are evaluated at $\mathbf{f}^\star$. Notice that expression (III.89) can be reformulated as $\left(\mathcal{A}\left(\delta^2\mathcal{J}\right)\mathcal{A}\right)^{-1}$. We could try to approximate (III.89) as we did with the Hessian, but we have no guarantees that it will turn out compact. Instead, let us re-summon the approximation of the hessian inverse (or posterior covariance) $\mathrm{H}_r^{-1} \in \mathbb{R}^{n\times n}$ to try and reduce computational expenses. First, we form the product $\mathrm{A}x_r^T = H_r^{-1}$ and solve it for an auxiliary variable x_r^T. Here again, $\mathrm{A} \in \mathbb{R}^{n\times m}$ is the discretisation of the operator $\mathcal{A}$, where m is the number of degrees of freedom of the discretised displacement $\mathbf{u}$. Next, we use x_r to pose the following linear system of equations : $\mathrm{A}y_r = x_r$. Solving for y_r produces an approximation $\mathrm{C}_r^{\mathbf{u}}$ of the discrete $\mathrm{C}^{\mathbf{u}}$ covariance $\mathcal{C}^{\mathbf{u}}$. This is yet to be implemented.

III.4.5 A null-hypothesis test to assign a significance to observed biological structures

Given that we now have the posterior distribution of the force, the floor is open to any kind of statistical inquiries. One in particular is motivated directly from biological considerations. Could we assess the significance of any structure revealed by TFM ? In other words, say we discover a force patch, could we determine whether it is real or an artifact ? Now that we have the posterior, we can use the covariance to attack this kind of problems ; that is to assess whether we are confident that a given structure is actually there and is not just a product of randomness. To this end, we propose a Bayesian hypothesis test [421], where we take the null hypothesis as H_0 : the structure is absent, and thus the complementary hypothesis is H_1 : the structure is present. This will divide the space of possible (solution) force fields into two : force fields that show the structure of interest (H_1), and force fields that do not. As usual, the aim is to reject H_0 in favor of H_1. This problem can be approached from Bayesian decision theory, for example as outlined in [421], where a reference set of "inpainted" solutions that substitute the potential structure by a more regular field is used as a reference. This is yet to be implemented.

III.4.6 Implementation and experiments

The Bayesian approach is summarised in Algorithm 2. The first step is to apply the deterministic Algorithm 1 in order to obtain the MAP estimate $\mathbf{f}^\star$ of the posterior distribution $\pi_h(\mathbf{f}|I_1, I_2)$ of the force. Next, inverting the Hessian at the MAP will yield the covariance matrix associated to the force pdf, which reflects the uncertainty of the reconstruction. The diagonal values correspond to the variance, whereas the off-diagonals reflect the covariance between parameters. A third step is to propagate the force covariance to obtain the covariance of the displacement distribution. This can be done using the force-to-displacement map $\mathcal{A}^{-1}$. Lastly, the posterior distribution of the force can be used to perform statistical tests on the significance of certain regions.

```
Algorithm 2: Uncertainty quantification in TFM
  Data: Reference image $I_1$ and image $I_2$, initial contours, pre-computed
        marginalisation of $\mu$ and $\lambda$, region of interest
  Result: Posterior distributions $\pi_h(\mathbf{f}|I_1, I_2)$, $\pi_h(\mathbf{u}|I_1, I_2)$, significance of region
  Apply Algorithm 1 : $\mathbf{u}^\star$, $\mathbf{f}^\star$, $\mathbf{g}^*$ ;
  Invert the Hessian via low-rank GHEP (F.9) : $\mathrm{C}^{\mathbf{f}}$, $\pi_h(\mathbf{f}|I_1, I_2)$;
  Propagate variance by solving SPDE (III.89) : $\mathrm{C}^{\mathbf{u}}$, $\pi_h(\mathbf{u}|I_1, I_2)$;
  Perform statistical test on region of interest : p-value
```

For the moment, we have only implemented the first and second steps. The covariance of the displacement is not particularly relevant in our context, where recovering forces is actually the final goal, and is expensive to compute. Contrarily, performing statistical tests to assess the significance of small patches of forces is biologically relevant. However, to explore this possibility we are awaiting experimental TFM data from our collaborators. Therefore, let us focus on computing the force covariance. The results are shown in Figures III.13 and III.14.

The variances displayed in Figure III.13 are computed by taking the diagonal values of the hessian inverse centered around the MAP point $\mathbf{f}^{\star}$ displayed in Figure III.5. This illustrates the problem of a direct inversion of the force from a displacement field (Section III.3.4.1). In this case, we can see how the boundaries are most uncertain in the prior distribution (indicating room for improvement in its choice). The data corrects (through the Hessian) the prior variance (remember expression (F.9)) fairly uniformly (but slightly less at the boundaries), decreasing its variance greatly. As a consequence, the posterior variance is quite low, i.e. the reconstruction is certain. This is further reflected in the samples as they barely deviate from the MAP (even when they have been exaggerated). Conversely, Figure III.14 focuses on the variance of our PDE-constrained optical flow method (Section III.3.4.2) centered around the MAP in Figure III.8. Here, the variance is reduced less in zones where the image intensity is homogeneous as compared to zones where it is heterogeneous (see Figure III.14c for comparison in the same color scale) because it is easier to distinguish movement with the optical flow functional.

Therefore, the results not only quantify the uncertainty of the recovered force from the image noise, but they also indicate what zones are most informative and thus might help in experiment design.

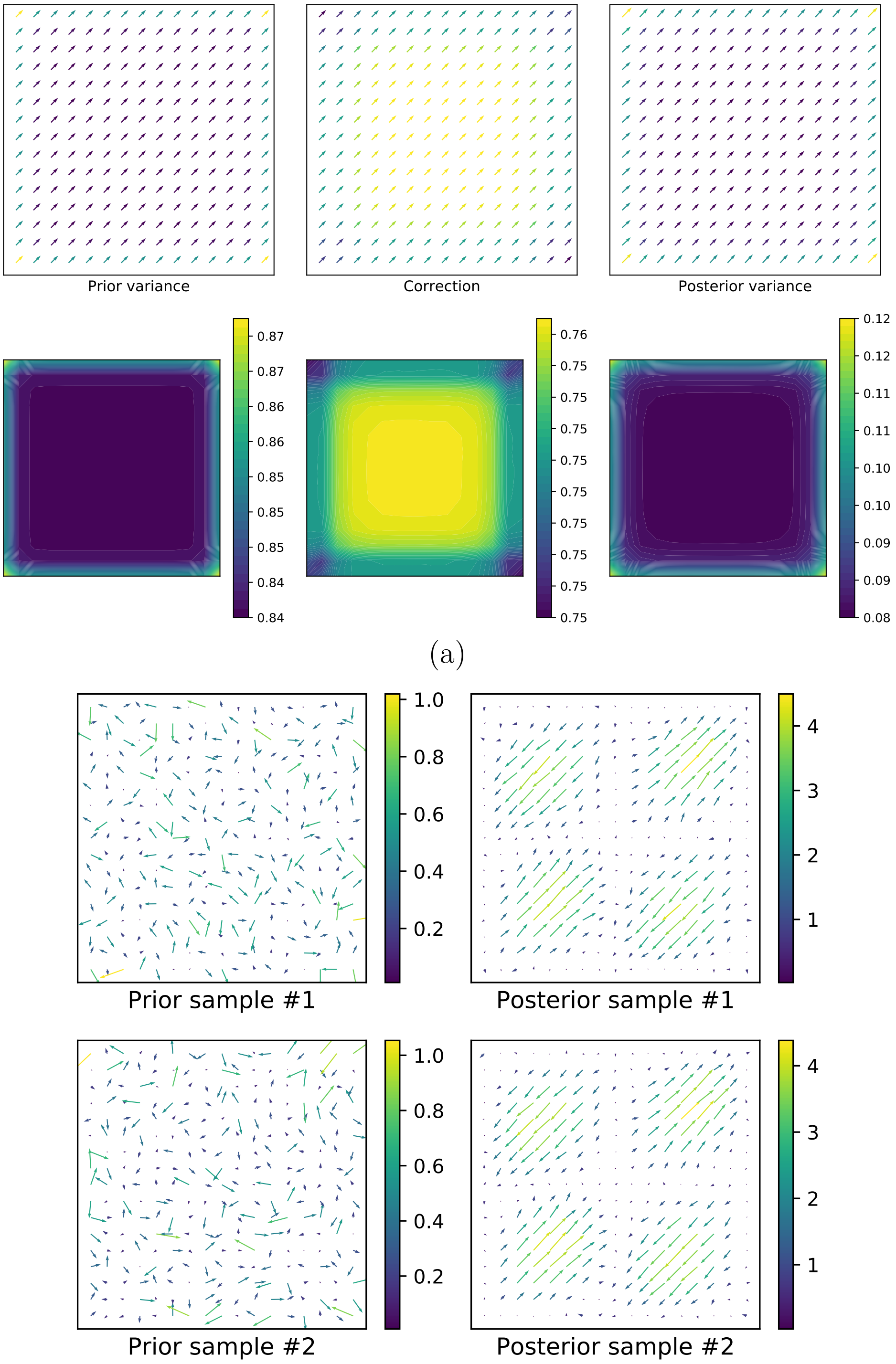

(b)

Figure III.13 – **Covariance and samples of the direct inversion. a)** Row 1) Left-to-right : diagonal of the covariance of the prior, the correction factor and the posterior. Row 2) Magnitudes corresponding to the vector fields in (Row 1). **b)** Two samples of both the prior (left column) and posterior (right column) force distributions. The samples were taken with an augmented variance to make differences noticeable. Everything is in relation to the MAP point $\mathbf{f}^\star$ in Figure III.5, but in a lower resolution.

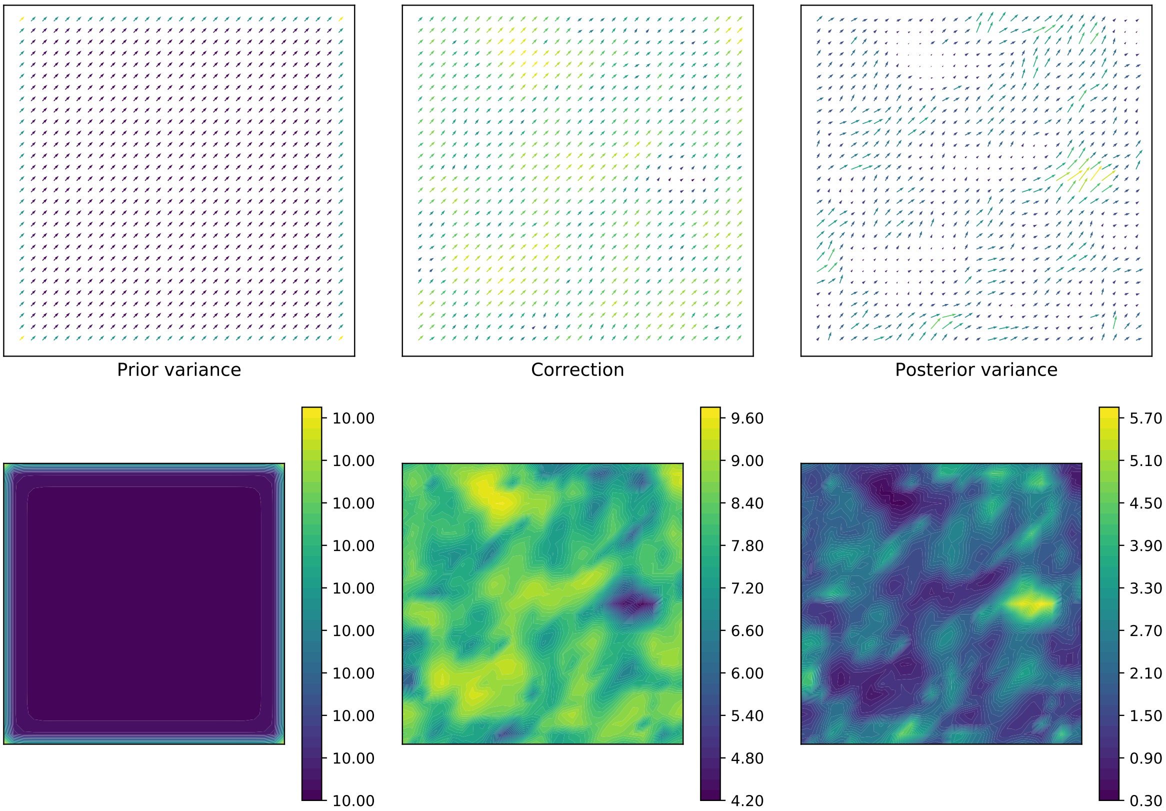
Prior variance
Correction
Posterior variance
10.00
10.00
10.00
10.00
10.00
10.00
10.00
10.00
10.00
10.00
9.60
9.00
8.40
7.80
7.20
6.60
6.00
5.40
4.80
4.20
5.70
5.10
4.50
3.90
3.30
2.70
2.10
1.50
0.90
0.30

(a)

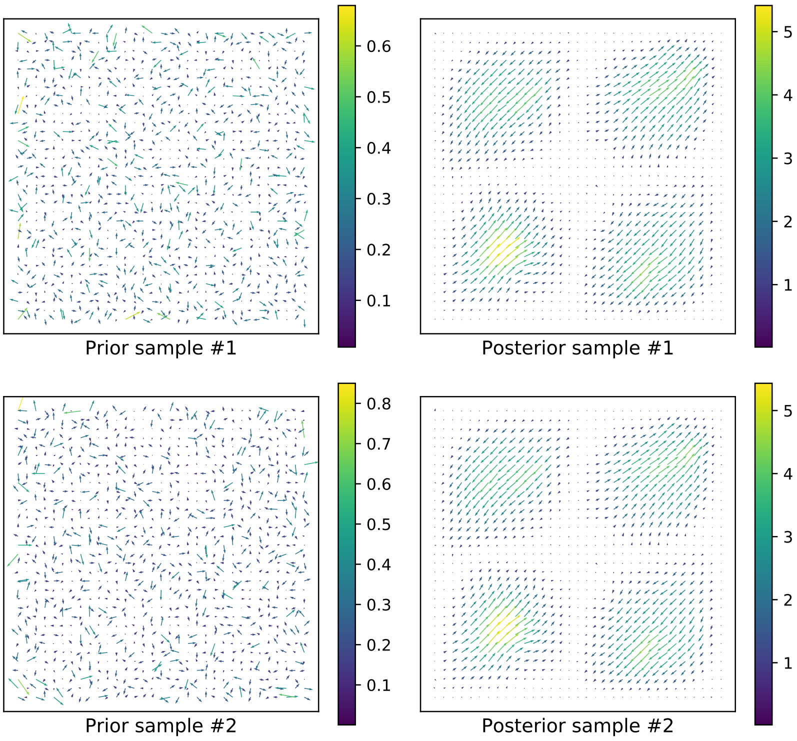
0.6
0.5
0.4
0.3
0.2
0.1
Prior sample #1
5
4
3
2
1
Posterior sample #1
0.8
0.7
0.6
0.5
0.4
0.3
0.2
0.1
Prior sample #2
5
4
3
2
1
Posterior sample #2

(b)

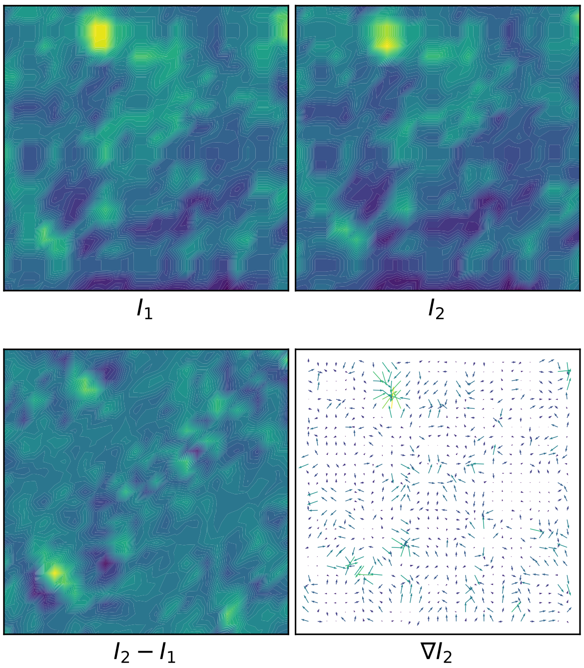

I_1 I_2

$I_2 - I_1$ ∇I_2

(c)

Figure III.14 – **Covariance and samples of the PDE-constrained optical flow inversion. a)** Row 1) Left-to-right : diagonal of the covariance of the prior, the correction factor and the posterior. Row 2) Magnitudes corresponding to the vector fields in (Row 1). **b)** Two samples of both the prior (left column) and posterior (right column) force distributions. **c)** Reference I_1 and deformed I_2 images, their difference, and the gradient of the deformed image. Everything is in relation to the MAP point $\mathbf{f}^\star$ in Figure III.8.

IV – Conclusion and future perspectives

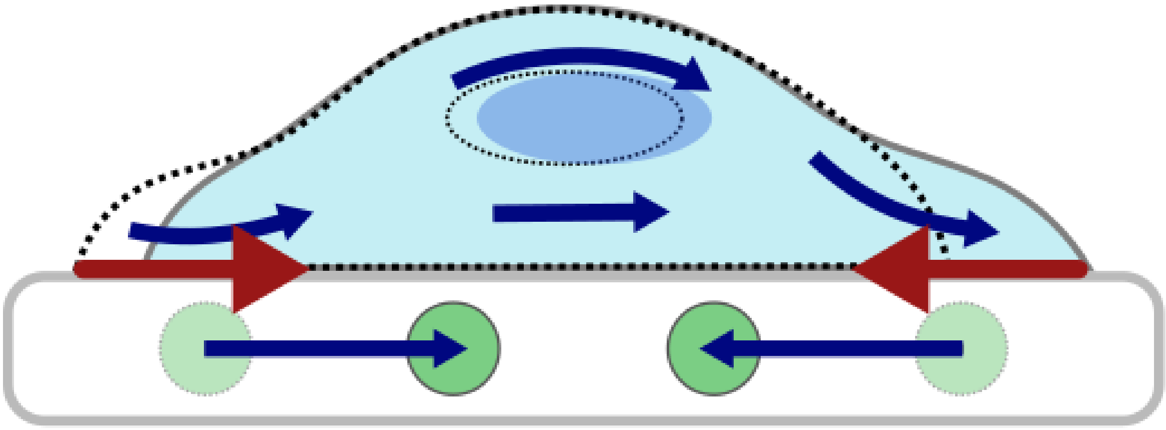

The leading aim of this work has been to develop a methodology that can assist in the boom of mechanobiology[1]. As in many other disciplines, improvements in the quality of experimental biophysical measurements have a history of turning into biological discoveries rather efficiently. In this regard, the central contribution of this thesis can be pinned down to the optimisation framework we have developed throughout the manuscript. Its three most relevant points to the cause are 1) non-invasiveness : it relies exclusively on standard microscopy ; 2) generality : 2D, 3D, intracellular, extracellular... presumably any theoretical model can be adapted ; and 3) uncertainty quantification : albeit Bayesian in origin, the error bounds are a good indicator of our confidence in the measurements. Because biology is eminently empirical, it might be surprising that we choose to bring up the third point. However, uncertainty is the elephant in the room of inverse problems in general, and (perhaps due to interdisciplinary miscommunication) of their bio-applications in particular ; this is the case of Traction Force Microscopy (TFM) for example. Even though an effort is present to average over many reconstructions (or measurements), many times conclusions are drawn from circumstantial force maps without a visible concern for possible artifacts. In fact, it is

---

[1] For a less digressive (and more factual) discussion of the thesis we refer the interested reader to Section .

precisely our rather-qualitative analysis on amoeboid motion that guilt-tripped us into uncertainty estimation.

Ultimately, all three points support the quest for biological significance. To illustrate our idea we opened two fronts : the first to introduce a novel way to look at intracellular physics, the second to reformulate extracellular TFM on alternative grounds. Even if the methodology was considerably expanded in the context of TFM during Chapter III, it is applicable to both problems. Quantifying intracellular forces and pressure gradients has helped us confirm and complement multiple hypotheses regarding amoeboid cell migration ; whereas the computed velocity fields are detailed enough to characterise cytoplasmic redistribution during bleb formation, and have motivated an advection-based tracking scheme that can follow dynamic molecular regions and allows defining integral measures. All these measurements are likely unprecedented, specially at this spatio-temporal resolution and extent (non-local), and everything without damaging the cell. On the other hand, extracellular measurements are more standardised, but we have been able to reduce noise sensitivity and provide error bounds in this respect. Other applications were found in the field of active nematics that also helped us test the relevance of the Stokes' equations to intracellular-like systems.

Throughout this thesis we have tried to emphasise the biological context of our work. Nevertheless, we believe the mathematical aspects are remarkably interesting, specially because we draw from several disciplines to build a framework that goes directly from pixels to measurements. That is we can take profit of the well controlled errors of the camera images to estimate the uncertainty of our reconstruction. This results in a big inverse problem that starts by formulating a PDE conservation model for the intensity and then requires that the underlying movement also abides by some PDE-based model. The idea can be formulated as an optimal control problem that we solve using variational calculus and complement with Bayesian estimates.

Software - For measurements to translate into discoveries, they have to be reproducible and easily accessible. If our hope is to tip the balance from expensive lab equipment to algorithms, it is imperative to provide working software. To both ends, we have implemented our methodology as an open-source module in the Icy platform. The concept has sparked interest in several communities, of which we are aware through direct contact or bug reports (!), and thus further investment should be profitable. In particular, there is much work to do in terms of user-friendliness, notably for very-end users. This is best done in close collaboration with the biology community, but also with software engineers. Indeed, programming solutions that can offer a good visual and interactive display are often in conflict with languages dedicated to scientific computing. Re-coding super-tested supported libraries, from say C++ into Java, would be gargantuan work. Therefore, we ask for bioimaging platforms to try and harness the potential of both worlds. This will also be a relevant point with the advent of deep learning techniques. Lastly, there is plenty to be optimised in our code that has not happened due to time constraints, specially in light of the late extensions introduced in Chapter III ; in other words, the implementation could be significantly faster.

Theory - From a theoretical standpoint, the Bayesian approach needs to be further developed. However, this is still a topic of active research in mathematical literaure. Taking in account the size of the problems we deal with, sampling with MCMC methods is prohibitive, which rules out the possibility of introducing non-linearities. Therefore, we are in need of either faster sampling methods, or linear regularisation schemes that can preserve discontinuous features such as TV. As of now, it seems like good theoretical guarantees for the infinite bayesian inverse problem involve rather smoothing regularisers (such as the Laplacian-like PDE we introduced) ; and that guarantees on the infinite formulation are needed to get discretisation invariance, which is particulary convenient in light of our multi-resolution scheme.

Other applications - A straightforward application that derives from the combination of Chapters II and III is to consider the full 3D picture of a cell navigating through the ECM (see Figure IV.1). In this case, complementary domains can be established for the inside and outside of the cell with respective fluid and elastic models. Of course, this gives rise to a big problem, but we have shown that L^2 regularisation can be turned into a coupled system of PDEs. In this case, we can move the parallelisation effort from considering many images pairs at once to solving the linear algebra problem derived from a single image pair (see MUMPS for example). This also permits to use the reconstructed displacement field to inform the segmentation of subsequent images.

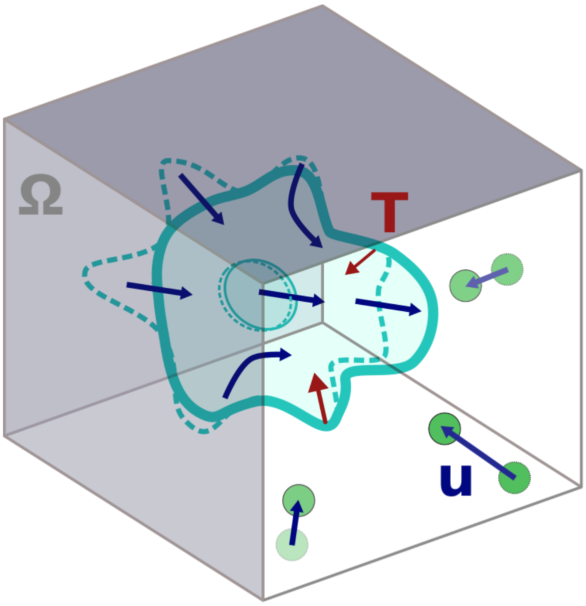

FIGURE IV.1 – **In and out : a 3D framework for cell-matrix interaction.**

An additional application is elastography (see Annex D). In principle, this problem is not linear and therefore reformulating it in a Bayesian setting is expensive. To make it more manageable, one could aim at partitioning the spatial map of elastic moduli into binary zones delimited by a parameterised curve or spline. Extracting only a few parameters (as opposed to a value for each spatial point) could be doable via an MCMC scheme. This should yield error estimates for the segmentation as well. While elastography aims at recovering the heterogeneous elastic properties of a material, it could also be applied to flowing fluids, i.e. to segment fluid regions of different viscosities that are invisible to the naked eye, for example cells in the blood stream. Alternatively, cell segmentation could exploit the optical refraction of light going through a cell by seeding fixed markers on the slide, potentially yielding a 3D map of the cell if the spatial resolution is enough to detect the smallest deviations.

To better represent the behavior of materials the fluid and elastic models have to be refined. In particular, biological fluids are better described by non-Newtonian viscoelastic models and cross-linked polymers such as the ECM also behave non-linearly. Section II.6 represents a first step in this direction, but this endeavour requires a lot of experimental support in the form of rheological probing and thus would be best reserved for a lab dedicated to the biophysical sciences.

A last possibility concerns the similarity of back-propagation to the adjoint approach or to reverse automatic differentiation : perhaps constraining deep learning to physical PDEs could help alleviate the dependence of variational formulations on energy weights, as well as on the physical constants of the model.

In a more biological direction, combining TFM experiments with intracellular analysis should help elucidate the essential details driving amoeboid motion, as well as the interaction and coordination between the inside and the outside of the cell.

A – Some intuition on the Adjoint method

A lot of ideas in this Annex come from [186] and [187, 188] (associated website http://www.dolfin-adjoint.org/en/release/documentation).

A.1 Discrete intuition

Let us illustrate the idea behind the adjoint method by taking the discrete approach, where we reason with matrices but know that a similar intuition holds in functional analysis. This is the avenue taken in Chapter II, specifically in Section II.1.3, from where we borrow the notation. First apply the chain rule to the functional $J(\theta(m), m)$ and PDE constraint $A(\theta, m) = 0$:

$$\frac{dJ(\theta(m), m)}{dm} = \frac{\partial J}{\partial \theta}\frac{d\theta}{dm} + \frac{\partial J}{\partial m}, \tag{A.1}$$

$$\frac{\partial A(\theta, m)}{\partial \theta}\frac{d\theta}{dm} = -\frac{\partial A(\theta, m)}{\partial m}, \tag{A.2}$$

where A could be the discretisation of $w - L$ via the FEM (see II.1.3), for example, and J that of the functional. Since the partial derivatives are simple to compute, the problem lies in computing the total derivatives. This can be achieved by solving the tangent linear system (A.2), where the partial derivatives w.r.t. to the controls act as source terms. However, $d\theta/dm$ is a large and dense matrix that scales badly with the size of the control space ; and in fact, we do not need all this information because we only care about a single functional. In this case, it is better to explore the dual space : instead of keeping the freedom of choosing the functional *a posteriori*, lets invert the roles with the controls and fix them *a posteriori* by taking the hermitian of the system. That is

$$\frac{dJ(\theta(m), m)}{dm} = -\lambda^* \frac{\partial A(\theta, m)}{\partial m} + \frac{\partial J}{\partial m}, \tag{A.3}$$

$$\left(\frac{\partial A(\theta, m)}{\partial \theta}\right)^* \lambda = \frac{\partial J}{\partial \theta}^*. \tag{A.4}$$

While (A.2) had a source term depending on the controls, the forcing term in (A.4) depends only on the functional. In other words, we avoid computing $d\theta/dm$ by first solving the so-called adjoint equation A.4 for λ, and then computing the final gradient via equation A.1. The change in dimension is also clear : $d\theta/dm$ is a matrix of dimensions state space times control space, whereas λ is a vector of the same dimension as the state space.

Notice here that the adjoint operator $(\partial A/\partial \theta)^*$ corresponds to the linearisation of the PDE A about the solution θ. Equation A.4 is therefore very similar to the forward PDE system, with the difference that the “propagation” of information is reversed by the transpose [1], plus a functional-dependant source term ; i.e. computing the gradient via the adjoint method only requires solving a linear PDE problem. This problem is akin to the forward model if such model is linear, and to the linearisation of the forward model if it is non-linear. The trade-off is clear in the duality : while the tangent linear space is convenient when the number of functionals to consider is big with respect to the controls, the adjoint approach works best when a functional is fixed but we have a large number of control parameters. This is perhaps best seen with the following equality

$$\frac{\partial J}{\partial \theta}\frac{d\theta}{dm} = -\lambda^* \frac{\partial A(\theta, m)}{\partial m}, \tag{A.5}$$

which is a direct consequence of duality in linear algebra. Therefore, the adjoint variables λ describe the influence of a given source term (here $-\partial A/\partial m$) on the functional through $-\lambda^* \partial A/\partial m$. Alternatively, the λ_i component of the adjoint is the value of the functional when the solution is the corresponding discrete Green’s function : $-\lambda^*(\partial A/\partial m)_i = \lambda_i = \partial J/\partial \theta (d\theta/dm)_i$, where the "discrete Green’s function" is the solution $(d\theta/dm)_i$ of (A.1) when the source term is precisely $-(\partial A/\partial m)_i$.

The same adjoint approach that was derived from the dual description, can also be derived from a Lagrangian perspective, i.e. using multipliers to write the constrained minimisation. Let L be the Lagrangian

$$L := J - \lambda^* A \tag{A.6}$$

whose perturbation is given by

$$dL = \frac{\partial J}{\partial \theta} d\theta + \frac{\partial J}{\partial m} dm - \lambda^* \frac{\partial A}{\partial \theta} d\theta - \lambda^* \frac{\partial A}{\partial m} dm. \tag{A.7}$$

If the derivative of the Lagrangian w.r.t. the state variables is zero and the forward equation $A = 0$ is satisfied, the total derivative of the Lagrangian w.r.t. the controls

$$dL = \left(\frac{\partial J}{\partial m} - \lambda^* \frac{\partial A}{\partial m} \right) dm = dJ \tag{A.8}$$

---

[1] E.g. advections reverse direction as transposing converts lower triangular matrices into upper triangular matrices. Similarly, in time-dependent problems time and causality are reversed.

is also the derivative of the functional w.r.t. to the controls $dJ = dL$. Setting the state derivatives to zero yields precisely the adjoint equation for λ :

$$\frac{\partial J}{\partial \theta} - \lambda^* \frac{\partial A}{\partial \theta} = 0. \tag{A.9}$$

Note that both these approaches work also for non-linear forward problems, in which case the adjoint equation is posed by the adjoint of the linearised problem. Under these frameworks, geometric constraints can be readily implemented by modifying the search direction of the controls, but state-dependent constraints such as $J_2(\theta) = 0$ are harder to incorporate because they require computing additional adjoints, which undermines the benefits of the adjoint approach. Instead, these are best included in a weak way in the original functional J.

A.2 Continuous intuition

Most of the intuition discussed for the discrete case applies directly to the continuous approach[2]. Instead of trying to solve the linearised PDE for $d\theta/dm$ in its weak form to evaluate the gradient functional $\int_\Omega (\partial J/\partial \theta)(d\theta/dm)d\mathbf{x}$, we look for the adjoint operator $(\partial A/\partial \theta)^*$ of the linearised PDE operator, $(\partial A/\partial \theta)$, as defined in functional analysis :

$$\int_\Omega \Lambda^* \left(\frac{\partial A}{\partial \theta}\right) \Theta \; d\mathbf{x} = \int_\Omega \left(\left(\frac{\partial A}{\partial \theta}\right)^* \Lambda\right)^* \Theta \; d\mathbf{x} \tag{A.10}$$

for all appropriate pair of functions Λ, Θ. If we then find a λ such that it solves the associated adjoint PDE system $(\partial A/\partial \theta)^* \lambda = (\partial J/\partial \theta)^*$ in its weak form, we can cheaply evaluate the gradient as

$$\int_\Omega \frac{\partial J}{\partial \theta} \frac{d\theta}{dm} d\mathbf{x} = \int_\Omega -\lambda^* \frac{\partial A}{\partial m} d\mathbf{x}. \tag{A.11}$$

This duality in functional analysis appears as a natural extension of the duality in linear algebra or linear programming. In this case, integration by parts to find the adjoint operator often reverses the sign, creating a similar effect to that of the transpose in the discrete case. For instance, the adjoint of the operator $\nabla\theta - \Delta\theta$ is $-\nabla\lambda - \Delta\lambda$. In this continuous case, it is specially important to keep track of boundary conditions as they have to be properly accounted for to solve the PDE associated to the adjoint system.

The same intuition also holds in terms of Green's functions. Concretely, the adjoint variable evaluated at a point $\mathbf{x}'$ is equal to the value of the functional when the solution is the Green's function evaluated at that same point. Indeed, consider the Green's function corresponding to the solution of the linearised PDE : $\theta(\mathbf{x}) = \int_\Omega -G(\mathbf{x}, \mathbf{x}') \frac{\partial A}{\partial m} d\mathbf{x}'$

---

[2] To emphasize this we heavily abuse the partial derivative notation, but these should rather be formulated and interpreted as Gâteaux derivatives (see Chapter III for a more formal treatment).

then

$$\int_\Omega \frac{\partial J}{\partial \theta}\theta(\mathbf{x})d\mathbf{x} = \int_\Omega -\frac{\partial J}{\partial \theta}G(\mathbf{x},\mathbf{x}')\frac{\partial A}{\partial m}d\mathbf{x}'d\mathbf{x} = \int_\Omega -\lambda^*(\mathbf{x}')\frac{\partial A}{\partial m}d\mathbf{x}' \tag{A.12}$$

and thus $\lambda^*(\mathbf{x}') = \int_\Omega \frac{\partial J}{\partial \theta}G(\mathbf{x},\mathbf{x}')d\mathbf{x}$.

As in the discrete case, the Lagragian way is also valid. Indeed, in Chapter III we take a continuous Lagrangian approach and show how it can be extended to second variations in order to compute a Hessian.

B – Derivation of the continuous Oldroyd-B model from a discrete damper/spring system

B.1 Discrete system

A third derivation of the Oldroyd B equations consists in building a continuum model starting from a discrete mass-less damper-spring system[1] , i.e. a linear combination (in series or parallel) of springs and dampers that respectively represent the elastic and viscous behavior of the material. This is somewhat analogous to building electrical circuits if the following correspondance is observed : voltage ↔ stress, current ↔ strain rate, capacitor ↔ spring because they store energy, and resistance ↔ damper because they dissipate it. In other words, the elastic stress σ_e is proportional to the strain acoording to Hooke's law :

$$\sigma_\mathrm{e} \propto \xi; \tag{B.1}$$

and the viscous stress σ_v to the strain rate as stated in Newton's law :

$$\sigma_\mathrm{v} \propto \dot{\xi}. \tag{B.2}$$

Series and parallel rules also apply to the total stress σ and strain ξ as a function of all the passive elements (indexed by i) in the circuit. Elements in parallel are under the same strain and add their stress, whereas a serial arrangement adds strain but shares a common stress applied through the system. More succinctly,

$$\text{in series : } \sigma = \sigma_i = \sigma_j,\ \xi = \sum_i \xi_i; \tag{B.3}$$

$$\text{in parallel : } \sigma = \sum_i \xi_i,\ \xi = \xi_i = \xi_j. \tag{B.4}$$

---

[1] **NOTATION :** to be consistent with previous notation, we keep $\mathbf{u}$ and $\epsilon(\mathbf{u})$ for velocity and strain rate ; and write $\mathbf{d}$, $\xi := \partial_\mathbf{x}\mathbf{d}$ for displacement and strain, where $\partial_\bullet$ denotes the partial derivative for example in $\mathbf{u} := \partial_t\mathbf{d}$. To keep it simpler, however, we will be using $\dot{\bullet}$ for the partial time derivative. We consider the stress σ as a scalar at first, and only tensorialise it after while also dividing it into hydrostatic and deviatoric.

However, notice that the rules are opposite to those in an electrical circuit. This contrast is a consequence of choosing voltage (which acts across elements), and stress (through elements) as respective excitators ; this role can be swapped from stress to strain by virtue of the excitation/response dualism in a linear system. In this case, the series/parallel rules of both circuits would be perfectly analogous at the expense of losing the direct and intuitive interpretation that the mechanical circuit is connected exactly as the associated mechanical system [422].

The most general form of these mechanical circuits, where an arbitrary number of elements in series and parallel is considered, is known as the Maxwell-Wiechert model. The viscoelastic materials described by this model can be solids or liquids, depending on whether all the deformations are reversible, which in turn is determined by whether there is any path of serial springs that can guarantee an instantaneous response. For example, a spring-damper system in series is called a Maxwell material and behaves like a liquid, but does not describe creep nor recovery. Conversely, if they are set in parallel as in a Kelving-Voigt material, they become solid (the deformation is entirely reversible) and can no longer display stress relaxation. Adding a serial spring to the latter system results in a material known as the standard solid model, which is the simplest setting that reproduces creep, recovery and relaxation. Conveniently, the equivalent fluid system, in which the serial spring is replaced by a damper (Figure II.30b), is the rheological model reported in the experimental study on the the cytoplasm of *Entamoeba histolytica* . It is known as three parameter fluid, or Jeffreys' model.

The three parameters : E_1 the elastic modulus of the parallel spring, and η_1, η_2 the respective viscosities of the parallel and serial dampers. The serial strain sum :

$$\dot{\xi} = \dot{\xi}_1 + \dot{\xi}_2; \tag{B.5}$$

and respective stress addition (in parallel) and conservation (in series) :

$$\sigma = E_1 \xi_1 + \eta_1 \dot{\xi}_1, \;\; \sigma = \eta_2 \dot{\xi}_2. \tag{B.6}$$

The combination of the three equations describes the evolution of the mechanical system more succinctly,

$$\lambda_2 \dot{\sigma} + \sigma = \eta_2 \left(\dot{\xi} + \lambda_1 \ddot{\xi} \right), \tag{B.7}$$

as a function of the retardation,

$$\lambda_1 := \frac{\eta_1}{E_1}, \tag{B.8}$$

and relaxation,

$$\lambda_2 := \frac{\eta_1 + \eta_2}{E_1}, \tag{B.9}$$

times. According to (B.7), having reached an equilibrium strain, as the viscosity kicks in, the stress will slowly *relax* in a time scale charaterised by λ_2 (see Figure II.29). On the other hand, the *retarded* onset of the elasticity response caused by the parallelised damper is described by λ_1. That is there is viscosity in every deformation, and no pure elastic response. For comparison, a Maxwell material has an instantaneous elastic response ($\eta_1 = 0$, $\lambda_1 = 0$), and a Voigt material cannot describe the relaxation behavior as the elastic response is always present and tends to the original state. If both relaxation and retardation share the same time scale, $\lambda_1 = \lambda_2$, the material behaves like a Newtonian fluid. This is most clear if we split the stress into a viscous and elastic part :

$$\sigma = \sigma_{\mathrm{v}} + \sigma_{\mathrm{e}}, \tag{B.10}$$

where the standard viscous stress is defined as usual

$$\sigma = 2\mu_s\dot{\xi}, \tag{B.11}$$

and the elastic stress is defined implicitly,

$$\lambda_2\dot{\sigma}_{\mathrm{e}} + \sigma_{\mathrm{e}} = 2\mu_{\mathrm{p}}\dot{\xi}. \tag{B.12}$$

With the stress split into two, the new variables μ_{s} and μ_{p} respectively act as the viscosities of the solvent (viscous) and polymeric (viscoelastic) components :

$$\mu_{\mathrm{s}} := \frac{\lambda_1}{\lambda_2}\eta_2 = \frac{\eta_1\eta_2}{\eta_1 + \eta_2}, \tag{B.13}$$

$$\mu_{\mathrm{p}} := \left(1 - \frac{\lambda_1}{\lambda_2}\right)\eta_2 = \eta_2 - \mu_{\mathrm{s}} = \frac{\eta_2^2}{\eta_1 + \eta_2}. \tag{B.14}$$

Where the elastic influence is reflected by λ_2 in (B.12). In fact, both viscosities only depend on the dampers, but both characteristic times include the elastic modulus. The sum of both, $\eta_2 = \mu_{\mathrm{s}} + \mu_{\mathrm{p}}$, acts as a sort of total viscosity.

B.2 Tensorialisation into continuum fluid dynamics

To start the transition to continuum fluid dynamics, we first switch strain for velocity in (B.12) :

$$\lambda_2\dot{\sigma}_{\mathrm{e}} + \sigma_{\mathrm{e}} = 2\mu_{\mathrm{p}}\partial_{\mathbf{x}}\mathbf{u}. \tag{B.15}$$

And then generalise the expression into a tensorial equation by assuming the stress is a symmetric tensor field τ, the velocity is divergence-free, and writing it in terms of the strain rate tensor $\epsilon(\mathbf{u})$:

$$\lambda_2\dot{\tau}_{\mathrm{e}} + \tau_{\mathrm{e}} = 2\mu_{\mathrm{p}}\epsilon \tag{B.16}$$

$$\tau_{\mathrm{v}} = 2\mu_{\mathrm{s}}\epsilon \tag{B.17}$$

$$\tau = \tau_{\mathrm{v}} + \tau_{\mathrm{e}} \tag{B.18}$$

$$\sigma = -p\mathrm{I} + \tau \tag{B.19}$$

However, equation (B.16) as a whole is not frame indifferent because the time derivative is not, but constitutive relations are expected to be an intrinsic property of a material and therefore independent of the observer. To be more precise, we not only want the equation to be invariant under any Euclidean transformation representing a frame change, but we also want the invariant to be frame independent. Similarly to how we need the material derivative (II.1) to guarantee the invariance of I in a moving image (or $\mathbf{u}$ in a fluid), we cannot carelessly generalise the time derivative of the stress to a tensorial setting if we want to be "physical". To translate the material derivative into the context of second-rank tensors, we consider a Lagrangian coordinate system that moves and deforms with the fluid so that the coordinates of a particular material point do not change with time regardless of rotations and stretches, including the base vectors, which also change along with the material as they are convected. The result is a set of frame-invariant time derivatives of a second-rank tensor in a moving fluid of which the so-called upper-convected time derivative[2] is the most used :

$$\overset{\nabla}{\bullet} := D_t \bullet - \Big((\nabla \mathbf{u})^T \cdot \bullet + \bullet \cdot (\nabla \mathbf{u}) \Big) . \tag{B.20}$$

A frame-invariant version of the equation describing the time evolution of the elastic tensor can be written as

$$\lambda_2 \overset{\nabla}{\tau_{\mathrm{e}}} + \tau_{\mathrm{e}} = 2\mu_{\mathrm{p}}\epsilon. \tag{B.21}$$

The ensemble of equations (B.21), (B.17), (B.18), (B.19) form a model known as Oldroyd B, which has been derived from the discrete spring/damper system found experimentally. While it is clear now that this relationship is known in the literature, I could not find the derivation written explicitly (perhaps it is considered trivial) so I leave it here as a reference in the hope of helping someone. The discrete-continuous equivalence of the parameters appears to be unavailable as well.

---

[2] See a derivation of the expression as a Lie derivative [423].

C – Derivation of the modified optical flow functional

If one has only a $d_{\text{O}}(< d_{\Omega})$-dimensional representation there is little hope of recovering the full d_{Ω}-dimensional representation of the movement. For example, we cannot integrate the fluorophore advection equation since it would require a d_{Ω}-dimensional initial condition. At best, one expects to obtain a concentration-weighted average of the movement :

$$\langle \mathbf{u}_{\Pi} \rangle_{\Gamma} = \int_{\Gamma} \mathbf{u}_{\Pi} \Psi d\Omega_{\Pi^C} / \int_{\Gamma} \Psi d\Omega_{\Pi^C}. \tag{C.1}$$

However, one can extract further information from the projected data if there exists a relation between the movement on spaces Ω_{Π^C} and Ω_{Π}, namely through a model.

Two main factors account for the different behavior of the movement in the image with respect to the original movement of the fluorophores, i.e. between respective equations (III.5) and (III.1). First, the fluorophore concentration varies along the complementary dimensions : otherwise $\nabla_{\Pi^C} \Psi = \mathbf{0}$. And second, there is movement along these dimensions : otherwise $\mathbf{u}_{\Pi^C} = \mathbf{0}$. In both exceptions no difference exists and (III.5) becomes $D_t I = 0$. The first relevant condition is a first order approximation. Therefore, let us neglect any derivative of order higher than one that does not lay on the projection Ω_{Π}.

We begin by using the mean value theorem on III.2,

$$L(\mathbf{x}_{\Pi}, t) \overset{\propto}{\sim} L_0(\mathbf{x}_{\Pi}) \int_{\Gamma} \Psi(\mathbf{x}, t) d\Omega_{\Pi^{\mathsf{c}}}, \tag{C.2}$$

and defining the normalised luminance $l := L/L_0$. Then 1) we take its time derivative, 2) differentiate under the integral sign in equation (C.2), 3) substitute in the fluorophore advection equation (III.1), 4) use the product rule for the divergence, and 5) split the space according to the projection . That is

$$\begin{aligned}
\partial_t l &\propto \int_\Gamma \partial_t \Psi \ d\Omega_{\Pi^c} \\
&= \int_\Gamma -\mathbf{u}\cdot\nabla\Psi \ d\Omega_{\Pi^c} \\
&= -\int_\Gamma \left(\nabla\cdot(\Psi\mathbf{u}) - \Psi\nabla\cdot\mathbf{u}\right) \ d\Omega_{\Pi^c} \\
&= -\int_\Gamma \left(\nabla_\Pi\cdot(\Psi\mathbf{u}_\Pi) - \Psi\nabla_\Pi\cdot\mathbf{u}_\Pi\right) \ d\Omega_{\Pi^c} \\
&\quad -\int_\Gamma \left(\nabla_{\Pi^c}\cdot(\Psi\mathbf{u}_{\Pi^c}) - \Psi\nabla_{\Pi^c}\cdot\mathbf{u}_{\Pi^c}\right) \ d\Omega_{\Pi^c}. \qquad \text{(C.3)}
\end{aligned}$$

The first terms in the last equation (C.3) can be expanded using the general Leibniz's integral rule (which we modify slightly to handle the divergence, see Section C.2 below) by considering the $(d_\Omega - d_O)$ −form $\Psi dx_{d_{O+1}} \wedge \ldots \wedge dx_{d_\Omega}$ over the Ω_Π-dependent chain Γ of the same dimension in d_Ω-space. Finally, one gets

$$\begin{aligned}
\int_\Gamma \nabla_\Pi\cdot(\Psi\mathbf{u}_\Pi) \ d\Omega_{\Pi^c} &= \nabla_\Pi\cdot\int_\Gamma \Psi\mathbf{u}_\Pi \ d\Omega_{\Pi^c} \qquad \text{(C.4)} \\
&\quad -\int_{\partial\Gamma} (\Psi\mathbf{u}_\Pi)\cdot\nabla_\Pi\Gamma\cdot d\Sigma, \\
\int_\Gamma \nabla_{\Pi^c}\cdot(\Psi\mathbf{u}_{\Pi^c}) \ d\Omega_{\Pi^c} &= -\int_{\partial\Gamma} (\Psi\mathbf{u}_\Pi)\cdot\nabla_{\Pi^c}\Gamma\cdot d\Sigma, \qquad \text{(C.5)}
\end{aligned}$$

where $d\Sigma$ is the infinitesimal surface element, and $\nabla_{\Pi^c}\Gamma = -\mathrm{I}$. Notice that the orthogonal (wrt to the projection) term vanishes because both integral and derivatives are taken over the same variables ; only the boundary terms are left. We can reformulate the first term on the right hand side of equation (C.4) in terms of the concentration-weighted velocity field and expanding the divergence :

$$\begin{aligned}
\nabla_\Pi\cdot\int_\Gamma \Psi\mathbf{u}_\Pi \ d\Omega_{\Pi^c} &\propto \nabla_\Pi\cdot(l\langle\mathbf{u}_\Pi\rangle_\Gamma) \\
&= \langle\mathbf{u}_\Pi\rangle_\Gamma\cdot\nabla_\Pi l + l\nabla_\Pi\cdot\langle\mathbf{u}_\Pi\rangle_\Gamma, \qquad \text{(C.6)}
\end{aligned}$$

with the same proportionality constant.

Assembling equations (C.4), (C.5) and (C.6) into (C.3) :

$$\begin{aligned}
\partial_t l &= -l\nabla_\Pi\cdot\langle\mathbf{u}_\Pi\rangle_\Gamma - \langle\mathbf{u}_\Pi\rangle_\Gamma\cdot\nabla_\Pi l \\
&\quad + k\int_\Gamma \left(\Psi\nabla_\Pi\cdot\mathbf{u}_\Pi + \Psi\nabla_{\Pi^c}\cdot\mathbf{u}_{\Pi^c}\right) \ d\Omega_{\Pi^c} \\
&\quad + k\int_{\partial\Gamma} (\Psi\mathbf{u})\cdot\nabla\Gamma\cdot d\Sigma, \qquad \text{(C.7)}
\end{aligned}$$

where k is the proportionality constant in in (III.4). Disregarding the second orders in the orthogonal direction, we get

$$\partial_t l = -\langle\mathbf{u}_\Pi\rangle_\Gamma\cdot\nabla_\Pi l + l\nabla_{\Pi^c}\cdot\mathbf{u}_{\Pi^c} + k\int_{\partial\Gamma} (\Psi\mathbf{u})\cdot\nabla\Gamma\cdot d\Sigma, \qquad \text{(C.8)}$$

where $\nabla_{\Pi^c} \cdot \mathbf{u}_{\Pi^c} = \nabla \cdot \mathbf{u} - \nabla_{\Pi} \cdot \mathbf{u}_{\Pi} \approx \nabla \cdot \mathbf{u} - \nabla_{\Pi} \cdot \langle \mathbf{u}_{\Pi} \rangle_{\Gamma}$. In addition, if we can also ignore the first derivatives of $\mathbf{u}_{\Pi}$ in the orthogonal direction (i.e. the Jacobian is null : $\mathbf{J}_{\Pi^c}\mathbf{u}_{\Pi} = \mathbf{0}_{d_{\mathrm{O}} \times d_{\Pi^c}}$), $\langle \mathbf{u}_{\Pi} \rangle_{\Gamma} \cdot \nabla_{\Pi} l = \mathbf{u}_{\Pi}$ and the previous expression can be simplified to

$$\partial_t l = -\mathbf{u}_{\Pi} \cdot \nabla_{\Pi} l + l \nabla_{\Pi^c} \cdot \mathbf{u}_{\Pi^c} + k \int_{\partial\Gamma} (\Psi \mathbf{u}) \cdot \nabla\Gamma \cdot d\Sigma, \tag{C.9}$$

which is much easier to link with our PDE model/constraint. Ideally, we could project our PDE equations onto the image plane, but the expressions would complicate greatly. Alternatively, our model can help to reformulate the only remnant of the orthogonal movement in (C.9), the divergence $\nabla_{\Pi^c} \cdot \mathbf{u}_{\Pi^c}$, in terms of the in-plane motion (see an example in Section III.2.3 with the elastic equations). Notice that the lose of symmetry between in-plane and out-of-plane variables happens because the integral is taken over the latter variables ; the consequences of this are clear when comparing (C.4) to (C.5), as the derivative of the integral disappears.

We now address the boundary terms in the last three equations. In the case where a 3D movement is projected onto 2D the boundary term reads $(\Psi \mathbf{u} \cdot \mathbf{n})|_{\Gamma}$ with $\mathbf{n}$ the boundary normal. In confocal microscopy, and more generally in laser sheet visualisation, it is reasonable to ignore the boundary terms. For example, one can consider that the flux in and out of the bounded region compensates (i.e. it does not accumulate in the region) or that the velocity is parallel to the control surfaces. However, part of the problem is cutting the space with the control surface Γ. Indeed, if we integrate over all space (controls Γ is placed at infinity) then the fluorophore concentration (as well as the velocity) decays to zero ; the only caveat being that greater care has to be taken when playing around with the integrals (e.g. mean value theorem, Leibniz, switching the limits in and outside the integrals, etc.) ; but L_0 and the other variables can be chosen well-behaved enough. This is particularly fruitful under the last approximation as there is no actual averaging. Certainly, the results should at least be good up to first order with the additional benefit of knowing the real form of the error sources, possibly leading to some sensible uncertainty quantification. If the boundary terms are neglected, the conservation equation can be written as

$$\partial_t l = -\mathbf{u}_{\Pi} \cdot \nabla_{\Pi} l + l \nabla_{\Pi^c} \cdot \mathbf{u}_{\Pi^c} ; \tag{C.10}$$

or in other words,

$$D_t l = l \nabla_{\Pi^c} \cdot \mathbf{u}_{\Pi^c} . \tag{C.11}$$

Since I is proportional to L, the equations above also hold for I.

C.1 Other situational conservation equations

In what follows we present three alternative conservation equations that also be deduced from this perspective on optical flow with the hope that they will be useful in different situations.

a) Diffusion. In cases where diffusion is not negligible $B \neq 0$ in equation (III.1), then the derivation remains the same, but equations (C.7), (C.8), (C.9) and (C.10) get two extra terms

$$B\Delta_\Pi l + [\text{B.T.}] \tag{C.12}$$

on their right hand side, where [B.T.] stands for boundary terms.

b) Beads. If the number of beads is really small it might be worth to consider them as a sum of Gaussians b_i, $i \in \{1 \,..\, m\}$, with mean $\mathbf{x}_{b_i}(t)$, defining the center of each bead, and σ_i, modelling its size. The scattering from the particles illuminated by the laser sheet is proportional to the number of particles [314], similarly to the fluorophore concentration Ψ in (III.4) ; and thus the form of the equations derived so far still holds. We can express the normalised luminance as

$$\sum_{i=1}^{m} b_i, \tag{C.13}$$

and readily substitute it into any of the equations (C.7), (C.8), (C.9), (C.10). For example

$$\sum_{i=1}^{m} \sigma_i^{-2} b_i \left(\mathbf{x}_\Pi - \mathbf{x}_{b_i}\right) \cdot \left(\mathbf{u}_\Pi - \dot{\mathbf{x}}_{b_i}\right) = -\sum_{i=1}^{m} b_i \nabla_{\Pi^c} \cdot \mathbf{u}_{\Pi^c} \tag{C.14}$$

using (C.10). In the limit where all σ_i go to zero at a similar rate, we have $\dot{\mathbf{x}}_{b_i} = \delta(\mathbf{x}_\Pi - \mathbf{x}_{b_i})\mathbf{u}_\Pi$.

c) 3D of 3D. Consider that we take 3D images of a 3D movement, as in a confocal z-stack. Notice that if we take $L_0 = \delta(\mathbf{x}_3 - z)$, we instantly get the seminal optical flow equation. Conversely, if we take an arbitrary L_0 we can derive an equation as a function of the velocity averaged in the z-direction along the laser zone Γ defined by control surfaces, i.e. $\langle \mathbf{u} \rangle$. In particular, by neglecting again the orthogonal (i.e. in the z direction because it is a z stack) second order derivatives (or equivalently the second order of the laser thickness) in the same fashion as before, we can derive the following expression for the 3D optical flow :

$$\partial_t l \approx -\langle \mathbf{u} \rangle \cdot \nabla l - l \nabla \langle \mathbf{u} \rangle + l \nabla \cdot \mathbf{u} \approx -\langle \mathbf{u} \rangle \cdot \nabla l, \tag{C.15}$$

modulo boundary terms. In this case, the orthogonal integration variables are only auxiliary during the derivation and the real orthogonal variables (the ones we take the final derivatives with respect to) are taken as the center of the integration domain.

C.2 Leibniz's general rule extended to the divergence

Let us define the d_{Π^c}−form $\omega = \Psi dx_{d_{\mathrm{O}+1}} \wedge \ldots \wedge dx_{d_\Omega}$. We would like to adapt the general Leibniz's rule (see equation 7.2 in [424]) to the divergence in equations (C.4) and (C.5). Let's proceed :

$$\nabla_\Pi \cdot \int_\Gamma \mathbf{u}_\Pi \, \omega = \sum_{i\in\Pi} \frac{\partial}{\partial x_i} \int_\Gamma u_i \omega \tag{C.16}$$

$$= \sum_{i\in\Pi} \int_\Gamma \frac{\partial}{\partial x_i} (u_i \omega) + \sum_{i\in Pi} \int_{\partial\Gamma} u_i \mathbf{v}_i \lrcorner\, \omega \tag{C.17}$$

$$= \int_\Gamma \sum_{i\in\Pi} \frac{\partial}{\partial x_i} (u_i \omega) + \int_{\partial\Gamma} \sum_{i\in\Pi} u_i \mathbf{v}_i \lrcorner\, \omega, \tag{C.18}$$

where $\lrcorner$ signals the interior product of the vector field $\mathbf{v}_i$ and the form ω; and the second equality is due to the the general Leibniz's rule. Typically $\mathbf{v}_i$ is the velocity describing the motion of the domain ($\mathbf{v} = \dot{\mathbf{x}}$), but here it describes the change of the control surface Γ. Therefore, $\mathbf{v}_i = \partial\Gamma/\partial x_i$, which has dimension d_{Π^c}.

$$\int_\Gamma \sum_{i\in\Pi} \frac{\partial}{\partial x_i} (u_i \omega) = \int_\Gamma \nabla_\Pi \cdot (\mathbf{u}_\Pi \Psi) \, dx_{d_{\mathrm{O}+1}} \wedge \ldots \wedge dx_{d_\Omega} \tag{C.19}$$

$$\int_{\partial\Gamma} \sum_{i\in\Pi} u_i \mathbf{v}_i \lrcorner\, \omega = \int_{\partial\Gamma} \mathbf{u}_\Pi \cdot \nabla_\Pi \Gamma \lrcorner\, \omega = \int_{\partial\Gamma} \mathbf{u}_\Pi \cdot \nabla_\Pi \Gamma \cdot d\Sigma. \tag{C.20}$$

Since the vector field and the form are of the same dimention, we can take a last step and multiply by a generic d_{Π^c}-dimensional vector representing the surface area. A similar derivation holds in the Π^c direction, but in such case we have $\nabla_{\Pi^c} \cdot \int_\Gamma \mathbf{u}_{\Pi^c} \omega = 0$. Putting together the two directions :

$$\nabla_\Pi \cdot \int_\Gamma \mathbf{u}_\Pi \Psi \, d\Omega_{\Pi^c} = \int_\Gamma \nabla \cdot (\mathbf{u}\Psi) \, d\Omega_{\Pi^c} + \int_{\partial\Gamma} (\mathbf{u}\Psi) \cdot \nabla\Gamma \lrcorner\, d\Omega_{\Pi^c} \tag{C.21}$$

with $d\Omega_{\Pi^c} = dx_{d_{\mathrm{O}+1}} \wedge \ldots \wedge dx_{d_\Omega}$.

D – Measuring elastic moduli

This section of the work was developed in collaboration with Samy Gobaa at Institut Pasteur and is published in [425].

Another experimental challenge in TFM is to characterise the elasticity of the material by measuring its constitutive parameters, namely the Lamé coefficients, i.e. the shear modulus μ and λ. While there exist calibration tables that relate stiffness to concentration for widely used materials (e.g polyacrylamide [426, 427]), the stiffness of many other materials is either not tabulated or not accurate enough. In addition, the standard rheological approaches to measure sample stiffness at the micro level require specialised set-ups such as atomic force microscopy, magnetic beads, cone-plate rheometers, spectrometers and uni-axial stretchers [336]. In this section, we try to look for alternatives that require little more than the microscope that is available at our facility. We also remark that this problem is not only of interest for cell biology, and that it encompasses multiple scales ; these considerations are out of the scope of the thesis, but we refer to [425] for further context.

D.1 Brownian microrheology

The first idea we considered was to insert beads into the elastic material and exploit their thermal energy as a microrheometer. The displacement of a particle undergoing thermally-powered Brownian motion within a viscous liquid is well characterised. Concretely, the standard deviation of the displacements d of the bead, or mean squared displacement (MSD, see Section I.2.2.3), is proportional to the time elapsed t : $< \Delta d^2 >= 4Dt$. The diffusion coefficient D depends on the shear viscosity of the fluid and therefore can be used as a gauge. Deviations from this linear relation typically reflect deviations of the viscous model into viscoelasticity. Is a similar approach possible for elastic materials ? In such case, the Brownian motion is constrained by elastic forces that respond immediately and thus the MSD is finite and independent of t [428]. In other words, the thermal energy $k_B T$ is up against springs :

$$< \Delta d^2 > \propto \frac{2k_B T}{rE}, \tag{D.1}$$

where k_B is Boltzmann's constant, T is the temperature in Kelvin, r is the radius of the bead or particle and E is the elastic modulus. This expression is perhaps best understood from the point of view of thermodynamics and statistical physics. In this regard, a thorough study on harmonic oscillators in heat baths can be found in [429]. The MSD can be computed after tracking the moving particles [430, 431]. However, the problem is that we are out of scale. Take $10nm$ as the best distance Δd we can resolve with a microscope and post-processing (e.g. fitting a PSF) , $r = 100nm$ a bead on the smaller size, and $T \approx 300K$. Then we could measure elastic moduli up to a maximum of $300Pa$. Whereas some techniques could yield better positional resolution, it would be hard to cover the necessary $0.1 - 10kPa$ range. Therefore, this method is not feasible in the context of TFM. In addition, while adding tracers in the form of beads to some materials is simple because they are polymerised from scratch, some others might result less accessible. Lastly, using a focused laser might help lengthen the stiffness range of this approach at a loss of simplicity.

D.2 Mechanical elastography

In [425], we explore an alternative method. In this case, we are not only looking for a single elasticity parameter but rather for the whole spatial distribution $\mu(\mathbf{x})$ of the shear modulus, a problem known as elastography. This can more accurately characterise the material sample. We propose to use our computational framework to extract elasticity measurements in biological materials, requiring only a standard microscopy set-up and a piezoelectric actuator [432] or, possibly, a chip with a vacuum chamber [433] (both commercially available). The scale of the resulting measurements is directly linked to the resolutive power of the microscope and thus can range across several scales. Even though in theory any type of imaging can be used, in the case of fluorescence microscopy some materials may require a label in the form of either fluorescent proteins or beads.

D.2.1 Experimental set-up.

More concretely, the experimental set-up (Fig. D.1) consists of a piezoelectric (PZT) actuator that moves a glass slide to compress the sample with great precision, either from the top or from the side, generating one or more boundary conditions. If necessary, the sample can be rotated to generate additional measurements (in this case, the resulting images can be registered). We note that these actuators and set-ups have been used to induce compression at different scales, generating displacements over a wide range of magnitudes within different samples [432, 434]. For example, the PZT ring actuator by Piezomechanik in [432] is able to induce up to 50% strain in step-wise micrometer-scale displacements on different synthetic and biological materials. Besides, more expensive models are able to offer nanometer accuracy. The strain induced within the sample can thus be regulated at almost any scale and is usually extracted by taking pictures before and after the compression is applied. These can be taken in a range of resolutions by using ultrasounds, optical coherence tomography or, as in the present case, conventional fluorescence microscopy.

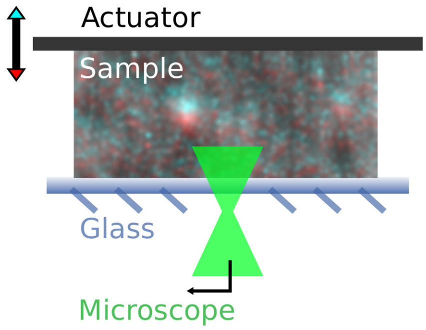

FIGURE D.1 – **Schematic of an experimental set-up.** The compression induced by the actuator on the sample can be finely regulated and can be imaged through a fluorescence microscope. An image of the sample is taken before (cyan) and after (red) the compression is applied.

D.2.2 Theoretical set-up

Since we are compressing a single side of the sample at a time, the deformation will reach the opposite side very weakly as compared to the noise. This situation is interesting as regards inverse problems because we have to combine multiple experiments, that is we have a problem with multiple PDE constraints.

a) Forward problem. We consider the sample to be a linearly elastic material with domain Ω described by its weak formulation $a(\mathbf{u}, \mathbf{w}; \mu) = 0 \;\forall\; \mathbf{w} \in H^1_{\mathbf{0}}(\Omega)$, where $\mathbf{u} \in H^1_{\mathbf{g}}$ is the displacement. The equations are exactly as presented for TFM during Chapter III (see Section III.2.2 in particular). However, here we do not control for the force $\mathbf{f}$ or the boundary condition $\mathbf{g}$, but for μ. In short, the forward problem is to find $\mathbf{u}$ given μ, with fixed $\mathbf{f}$ and $\mathbf{g}$.

b) Inverse problem. Our interest is to find a $\mu(\mathbf{x})$ that minimizes $J_{\text{data}}(I, \mathbf{u}; \mu) + J_{\text{reg}}$ subject to $a(\mathbf{u}, \mathbf{w}; \mu) = 0 \;\forall\; \mathbf{w} \in H^1_{\mathbf{0}}(\Omega)$. Here J_{data} is taken from (III.7), and we set $J_{\text{reg}} = \alpha \|\mu\|^2_{\Omega}$ for some weight $\alpha \in \mathbb{R}_{\geq 0}$. In the incompressible case, i.e. $\lambda \to +\infty$, inverting μ from $\mathbf{u}$ is a well-posed problem for certain boundary conditions [435]. However, several complications arise in practical situations. First, biological materials are often compressible. Second, the high levels of noise and the limited sampling in images make the problem very sensitive. Third, in order to conserve the integrity of the sample, only small displacements can be applied as boundary conditions. As a consequence, the displacement field over the sample can be hard to resolve, specially far from the source and in the presence of noise (see Fig. D.2a). For these reasons, we introduce a new functional

$$\mathcal{J}_{\text{data}} := \sum_{i=1}^{n} J_{\text{data}}(I_i, \mathbf{u}_i; \mu) \tag{D.2}$$

that incorporates n observations of the sample under different boundary conditions $\mathbf{g}_i$ that yield n different image pairs $I_i(\mathbf{x}, 0)$, $I_i(\mathbf{x}, 1)$. With this strategy, we aim at completing any lack of information stemming from the above-mentioned difficulties by accumulating independent observations. We also have to introduce the corresponding combined weak elastic equation :

$$\mathcal{A} = \sum_{i=1}^{n} a(\mathbf{u}_i, \mathbf{w}_i; \mu), \tag{D.3}$$

where $\mathbf{U} = (\mathbf{u}_1, \cdots, \mathbf{u}_n) \in \mathcal{U} := \bigtimes_i H^1_{\mathbf{g}_i}(\Omega)$ and $\mathbf{W} = (\mathbf{w}_1, \cdots, \mathbf{w}_n) \in \mathcal{W} := \bigtimes_i H^1_{\mathbf{0}}(\Omega)$. The final problem thus reads :

$$\underset{\mu}{\operatorname{argmin}}\ \mathcal{J}_{\text{data}} + J_{\text{reg}} \text{ subject to } \mathcal{A} = 0 \ \ \forall\, \mathbf{W} \in \mathcal{W}. \tag{D.4}$$

c) Minimisation. The optimisation problem has several PDE constraints (one per experiment or applied $\mathbf{g}_i$), making the computation of the derivatives particularly costly as the problem grows. We use the L-BGFS-B quasi-Newton method to solve the optimization problem (D.4) and compute the derivatives with the discrete adjoint method, exactly as in II.1.3. Importantly, $\mathcal{A}$ inherits the properties of linearity and "self-adjointness" (even if in a different space, $\mathcal{A}^*(W_1, W_2; \mu) = \mathcal{A}(W_1, W_2; \mu)$ $\forall\ W_1, W_2 \in \mathcal{W}$) by construction. Therefore the adjoint problem looks like the linear problem, which in turn looks like the original forward problem. In practice, it is better to take the change of variables $\mu = \exp(\beta)$ and minimise with respect to $\beta \in \mathbb{R}$ because the parameter $\mu \in \mathbb{R}_{>0}$ is to be kept positive.

d) Experiments. In order to test the methodology, we use different synthetic examples derived from real data, to which we apply simulated actuations. This allows us to work with fully controlled conditions. In particular, we use original microscopy images $I_i(\mathbf{x}, 0)$ of polyacrylamide gels, a well-studied linearly elastic material used widely in biology, and we use real values for the boundary conditions induced by a piezoelectric actuator, generating displacements like those observed in the literature. We also reproduce the noisy conditions of conventional fluorescence microscopy.

We start with a given modulus $\mu(\mathbf{x})$ map (Fig. D.2c) and solve the forward problem $\mathcal{A} = 0$ under different boundary conditions $\mathbf{g}_i$, $i \in \{1 \,..\, n\}$, to obtain the different displacement fields $\mathbf{u}_i$ (Fig. D.2b, $n = 1$). Then we use $\mathbf{u}_i$ to warp images $I_i(\mathbf{x}, 0)$ into images $I_i(\mathbf{x}, 1)$ (Fig. D.2a). Finally, we add noise at the level expected from a microscope and subsample the data to obtain the final pairs of images.

We remark that the magnitude of the displacements quickly decreases as one gets farther from the side where the boundary condition is applied. In fact, the added noise

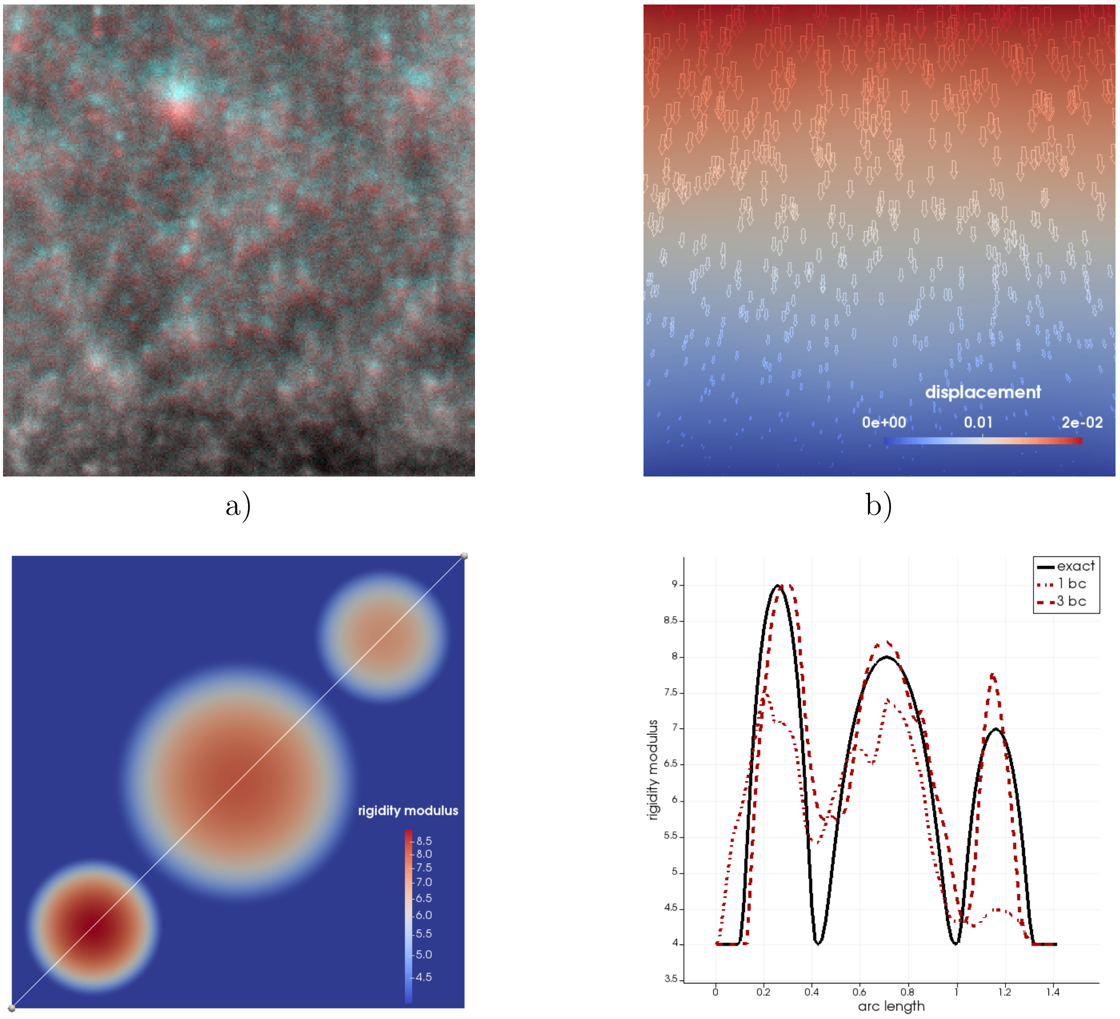

a) b) c) d)

Figure D.2 – **Numerical experiments. (a)** Two superimposed images of the polyacrylamide gel before (cyan) and after (red) applying an example of a uniform top boundary condition downwards and adding noise. Lack of movement is shown in white (cyan+red). **(b)** Displacement field applied to warp (a). **(c)** $\mu(\mathbf{x})$ with three occlusions. **(d)** Recovered $\mu(\mathbf{x})$ across the diagonal drawn in (c) for 1 and 3 different boundary conditions (dashed lines) as compared to the ground truth (solid line). The respective boundary conditions are compressing from the top, and compressing from the top and the two sides.

and the sampling amount to an almost complete loss of information at the opposite side (Fig. D.2a, white). In addition, the side of the image where the compression is applied is another source of error because the sample changes size slightly.

We work with a rigidity modulus (Fig. D.2c) that consists of three inclusions of different magnitude that partially occlude each other, making it more difficult to "see through". The results of the minimization (eq. D.4) are presented in Figure D.2d. By integrating data in the form of three different boundary conditions, $\mu(\mathbf{x})$ is much better recovered (as compared to using only one experiment) because the effects from warping the boundary are reduced and because the combination of the displacement fields samples the domain more extensively. In particular, including experiments where the sample is pressed from different sides reduces mismatches caused by the small values (relative to the noise) of the displacement field far from the boundary where the compression is applied. In this way, all three inclusions are resolved, localized and ordered in magnitude.

It is worth noting that the recovered values of μ are relative because the applied traction force is unknown. To obtain absolute values one must be aware of the force exerted on the sample or to layer it with a reference material of known properties.

E – Interpretation of the regularisation weights : filters and diffusers

E.1 L^2 regularisation behaves approximately as a low-pass filter

The filter effect is best seen by rescuing the coupled system of equation mentioned in Sec. (III.3.1), where we found $\mathbf{f} = \mathbf{v}/2\alpha$ on K. For simplicity, we resort to a standard data misfit term $(\mathbf{u} - \mathbf{u}_d)^2$, where $\mathbf{u}_d$ would be the measured displacement, instead of the modified optical flow functional. At lower dimension and under periodic boundary conditions we can write the simplified coupled system in the spatial Fourier domain as

$$\nu^2 \hat{\mathbf{u}} \propto \hat{\mathbf{v}}/\alpha, \tag{E.1}$$

$$\nu^2 \hat{\mathbf{v}} \propto \hat{\mathbf{u}}_d - \hat{\mathbf{u}}, \tag{E.2}$$

(here $\hat{\bullet}$ notates the amplitude) with the same proportionality constant ξ gathering the effects of μ and λ. This system is a low-pass filter that can be used to damp spatial frequencies that are indiscernible at the scale of the experiment : $\hat{\mathbf{u}}/\hat{\mathbf{u}}_d = (1 + \alpha\xi^2\nu^4)^{-1}$, where ν is the spatial frequency or wavenumber.

E.2 Tikhonov regularisation is a smoothing isotropic diffusor

In this case, the Newton iterations result in an isotropic diffusion regulated by β that smooths the control. This is most evident in the strong form of the Hessian action of the regulariser (III.57) :

$$-2\beta\Delta\tilde{\mathbf{f}}. \tag{E.3}$$

E.3 Frobenius TV operator acts via anisotropic diffusion

We address the action of the $(\mathrm{I} - \nabla \mathbf{f} \otimes \nabla \mathbf{f} / |\nabla \mathbf{f}|_{\mathrm{F}}^2)$ operator, where we disregard the ϵ perturbation. The gradient itself is a single eigenvector (eigenmatrix) of eigenvalue 0 ; and all the "frobenius-perpendicular" (the Frobenius product of two matrices is the sum of the inner products of their column vectors) vectors are of eigenvalue 1 and form a basis that spans the remaining space. The effect of this can be seen on the strong version of Newton's system, where the Hessian term becomes

$$- \nabla \cdot \left(\frac{\alpha}{|\nabla \mathbf{f}|_{\mathrm{F}}} \left(\mathrm{I} - \frac{\nabla \mathbf{f} \otimes \nabla \mathbf{f}}{|\nabla \mathbf{f}|_{\mathrm{F}}^2} \right) \nabla \tilde{\mathbf{f}} \right), \tag{E.4}$$

i.e. the Newton iterations act like an anisotropic diffusor. In one dimension this restricts the diffusion to progress along edges (perpendicular to the gradient), resulting in the characteristic sharp (piece-wise-like) transitions of TV regularisation. On flatter zones, the diffusion becomes isotropic. In the vectorial case, diffusion is only discouraged across the direction of the diagonal matrix. In addition, the definition of "edge" is not so clear-cut. Consider the image as a 2/3D manifold embedded in a **f**-dimensioned space [436, 437, 438] and let $\nabla \mathbf{f}^T \nabla \mathbf{f}$ be the metric tensor, a measure of the rate of change. Its eigenvectors (symmetric tensor) reflect the directions of maximal and minimal change. Accordingly, the vectorial edge should result from comparing the dissimilarity between the different (semi-positive) eigenvalues [439]. A suggestive approach would be to take the difference between maximum and minimum eigenvalues, but its very expensive and does not seem to have nice properties. The spectral and Frobenius norms are close alternatives. They are unitary invariant and convex, and hence Lipschitz and differentiable everywhere. They can be expressed in terms of the decreasingly-ordered eigenvalues λ_i, $i \in \{1 \,..\, d_\Omega\}$, of the metric as $|\nabla \mathbf{f}|_{\mathrm{F}} = \sqrt{\sum_i \lambda_i}$ and $|\nabla \mathbf{f}|_{\mathrm{s}} = \sqrt{\lambda_1}$. Continuing with the analysis of possible Schatten p-norms, after $p = 2$ and $p = \infty$, we considered $p = 1$, known as the nuclear norm $|\nabla \mathbf{f}|_{\mathrm{n}} = \sum_i \sqrt{\lambda_i}$; but discarded it because it requires taking the square root (or SVD) of a matrix. We also gave up on the spectral norm because it requires computing the dominant eigenvectors, which does not scale well to 3D dimensions [440]. The Frobenius norm is much simpler to handle and still couples the many components of the **f** vector [389]. The edge strength is weighted over all vectorial components so that common edges are not over-penalised, but the directions of the edge might be different for each component. This can introduce some "smearing" over the edges as shown by (E.4), but it is a good trade-off because this effect is not necessarily bad in the case of cellular traction forces. Aside from the coupling, TV acts on each component roughly as is expected. It is kind of a gradient sparsifier : it prefers monotonic functions[1] (as Tikhonov) but does not favor smooth changes, therefore preserving edges (blocky/stair effect) as are found in the data and being less penal when the function departs from the constant case.

---

[1] The seminal definition of total variation can be seen as the supremum of the sum of absolute differences of a one-varied function over any partition of a given interval.

E.3.1 Expressions for the TV Hessian action

$$D^2_{\mathbf{f}}\mathcal{J}^{\mathrm{TV}}_{reg} \cdot \tilde{\mathbf{f}} \cdot \tilde{\tilde{\mathbf{f}}} = \alpha \int_K \frac{\nabla \tilde{\mathbf{f}} : \nabla \tilde{\tilde{\mathbf{f}}}}{(\nabla \mathbf{f} : \nabla \mathbf{f} + \epsilon)^{1/2}}\, d\Omega - \alpha \int_K \frac{\left(\nabla \tilde{\mathbf{f}} : \nabla \mathbf{f}\right)\left(\nabla \mathbf{f} : \nabla \tilde{\tilde{\mathbf{f}}}\right)}{(\nabla \mathbf{f} : \nabla \mathbf{f} + \epsilon)^{3/2}}\, d\Omega, \tag{E.5}$$

$$D^2_{\mathbf{f}}\mathcal{J}^{\mathrm{TV}}_{reg} \cdot \tilde{\mathbf{f}} \cdot \tilde{\tilde{\mathbf{f}}} = \alpha \int_K (\nabla \mathbf{f} : \nabla \mathbf{f} + \epsilon)^{-1/2} \left(\nabla \tilde{\mathbf{f}} : \nabla \tilde{\tilde{\mathbf{f}}} - \frac{\left(\nabla \tilde{\mathbf{f}} : \nabla \mathbf{f}\right)\left(\nabla \mathbf{f} : \nabla \tilde{\tilde{\mathbf{f}}}\right)}{(\nabla \mathbf{f} : \nabla \mathbf{f} + \epsilon)} \right)\, d\Omega, \tag{E.6}$$

$$D^2_{\mathbf{f}}\mathcal{J}^{\mathrm{TV}}_{reg} \cdot \tilde{\mathbf{f}} \cdot \tilde{\tilde{\mathbf{f}}} = \alpha \int_K (\nabla \mathbf{f} : \nabla \mathbf{f} + \epsilon)^{-1/2}\, \nabla \tilde{\mathbf{f}} \left(\mathrm{I} - \frac{\nabla \mathbf{f} \otimes \nabla \mathbf{f}}{(\nabla \mathbf{f} : \nabla \mathbf{f} + \epsilon)} \right) \nabla \tilde{\tilde{\mathbf{f}}}\, d\Omega, \tag{E.7}$$

F – Low-rank approximation of the covariance

F.1 Covariance of the Gaussian posterior as the inverse of the Hessian

We have seen in Section III.4.2 that the posterior distribution can be expressed as

$$\begin{aligned}\pi_h(\mathbf{f}|I_1) \underset{\sim}{\propto} \exp(& - (y - G\theta)^T \, \mathrm{C}^{-1} \, (y - G\theta) \\ & - (\mathbf{f} - \mathbf{f}_\star)^T \, \mathrm{C}_{\mathbf{f}}^{-1} \, (\mathbf{f} - \mathbf{f}_\star)),\end{aligned} \tag{F.1}$$

with $y = I_2 e^{-s} - I_1 - \mathrm{e}_{\mu,\lambda,\star}$, $\theta = (\mathbf{f}, \mathbf{g})$ and $G = OA^{-1}L$, where O is the matrix resulting from the discretisation of the $\mathcal{O} = (-I_2 \nabla s + \nabla I_2)$ terms. By using the rules for both linear combinations and products regarding Gaussian densities [420], we can deduce that

$$\begin{aligned}\pi_h(\mathbf{f}|I_1) \underset{\sim}{\propto} \exp(- (\theta - (\mathbf{f}^\star, \mathbf{g}))^T & \\ & ((OA^{-1}L)^T \mathrm{C}^{-1} (OA^{-1}L) + \mathrm{C}_{\mathbf{f}}^{-1}) \\ (\theta - (\mathbf{f}^\star, \mathbf{g})) &\end{aligned} \tag{F.2}$$

because the MAP $\mathbf{f}^\star$ coincides with the mean under these circumstances, and constants can be absorbed into the exponential. Therefore, the covariance of the posterior is

$$\mathrm{C}^{\mathbf{f}} = ((OA^{-1}L)^T \mathrm{C}^{-1} (OA^{-1}L) + \mathrm{C}_{\mathbf{f}}^{-1})^{-1} = (\mathrm{H}_{\mathrm{data}} + \mathrm{C}_{\mathbf{f}}^{-1})^{-1} = \mathrm{H}^{-1}. \tag{F.3}$$

There should be a factor 2 here, but it can be transferred to the weights ; so we proceed more simply in this way. The size of the posterior covariance matrix $\mathrm{C}^{\mathbf{f}} \in \mathbb{R}^{n \times n}$ and the Hessian misfit $\mathrm{H}_{\mathrm{data}} \in \mathbb{R}^{n \times n}$ corresponds to the degrees of freedom n of the discretised traction force $\mathbf{f}$. Accordingly, C_I, $\mathrm{C}_{\mu,\lambda}$ and $\mathrm{C} = \mathrm{C}_I + \mathrm{C}_{\mu,\lambda}$ all belong to $\mathbb{R}^{l \times l}$, where l are the number of degrees of freedom of I.

F.2 Prior-generalised eigenvalue problem to low-rank approximate the Hessian inverse

When the forward model is expensive (PDE) and the number of parameters large (i.e. n is big), the Bayesian approach is intractable using conventional sampling techniques. If the problem is linear we can use the Hessian, otherwise, we can linearise it or marginalise it. As shown in the main text, in either case, an additive Gaussian noise model and a Gaussian prior density result in a Gaussian posterior density, which is fully described by its mean[1] and (Hessian-based) covariance. However, inverting the Hessian matrix is expensive. Specifically, the map A^{-1}, which brings the controls to $\mathbf{u}$, is dense and constructing it requires a PDE solve per parameter, in contrast to the deterministic approach.

However, the structure of the Hessian can be exploited towards fast approximations of its inverse with computable error bounds [441] (see applications in [442, 400]). In particular, one can construct a lower dimensional basis by using a low-rank approximation of the Hessian. This problem is tractable because the spectrum of the Hessian misfit decays rapidly, as only a low-dimension subspace of the parameter field is informed by the data (ill-posed problem). In other words, the Hessian misfit matrix is the discretisation of a compact operator. Only the modes of the parameter field that affect the displacement strongly are present in the dominant spectrum, whereas the rest (highly oscillatory) are negligible. Therefore, the range is finite dimensional (even before discretisation) and thus independent of mesh size.

Let's try to approximate the posterior covariance. Since it is also important to account for the prior, we present the posterior covariance as the prior covariance, but filtered through a data-based term :

$$\mathrm{C}^{\mathbf{f}} = \left(\mathrm{I} + \mathrm{C}_{\mathbf{f}}\mathrm{H}_{\mathrm{data}}\right)^{-1}\mathrm{C}_{\mathbf{f}}. \tag{F.4}$$

While the data misfit preconditioned with the prior $\mathrm{C}_{\mathbf{f}}\mathrm{H}_{\mathrm{data}}$ is not symmetric, it is so with respect to the $\mathrm{C}_{\mathbf{f}}^{-1}$ inner-product. In addition, the sum of the inverted prior and hessian misfit is positive definite because positive-definition is invariant under inversions. To factorise the prior-preconditioned data misfit $\mathrm{C}_{\mathbf{f}}\mathrm{H}_{\mathrm{data}}$, we first solve the corresponding generalised hermitian eigenvalue problem (see Section III.3.4.4)[2] : find the eigenvectors $\hat{\mathbf{f}}_i$ and corresponding eigenvalues λ_i such that

$$\mathrm{H}_{\mathrm{data}}\hat{\mathbf{f}}_i = \lambda_i \mathrm{C}_{\mathbf{f}}^{-1}\hat{\mathbf{f}}_i. \tag{F.5}$$

---

[1] The mean is the MAP estimate only in the linear case. The MAP results from solving the associated Tikhonov problem in both linear and non-linear cases.

[2] In that case, the preconditioner in the preconditioned misfit defined the inner product (angles) that best fitted the solution space (Riesz map). In a similar way, the prior acts here by informing the direction (angles) of the Hessian with *a priori* knowledge. This results in a sort of space were the data is weighted/guided by previous information.

By choosing the r most significant eigenvalues we can r-rank approximate the $n \times n$-sized misfit, and at the same time have bounds for the accuracy of said approximation :

$$\mathrm{H}_{\text{data}} = \left(\mathrm{C}_{\mathbf{f}}^{-1}\mathrm{U}\right) \mathrm{D} \left(\mathrm{C}_{\mathbf{f}}^{-1}\mathrm{U}\right)^{T} + \mathcal{O}\left(\sum_{i=r+1}^{n} \lambda_i\right) \tag{F.6}$$

where $\mathrm{D} \in \mathbb{R}^{r\times r}$ is a diagonal matrix containing the first (biggest) generalised eigenvalues λ_i, and $\mathrm{U} \in \mathbb{R}^{n\times r}$ contains the corresponding generalised eigenvectors and is $\mathrm{C}_{\mathbf{f}}^{-1}$-orthogonal. Notice that taking the largest eigenvalues of the GHEP is a way to maximise the so-called Rayleigh ratio,

$$\frac{\tilde{\mathbf{f}}^{T}\mathrm{H}_{\text{data}}\tilde{\mathbf{f}}}{\tilde{\mathbf{f}}^{T}\mathrm{C}_{\mathbf{f}}^{-1}\tilde{\mathbf{f}}}, \tag{F.7}$$

where $\tilde{\mathbf{f}}$ is any direction in the force space. In other words, for large eigenvalues the likelihood dominates over the prior. Using the matrix inversion lemma [420] on (F.6) to approximate the prior-modifier in (F.4), we obtain

$$\left(\mathrm{I} + \mathrm{C}_{\mathbf{f}}\mathrm{H}_{\text{data}}\right)^{-1} = \mathrm{I} - \mathrm{U}\Lambda\mathrm{U}^{T}\mathrm{C}_{\mathbf{f}}^{-T} + \mathcal{O}\left(\sum_{i=r+1}^{n} \frac{\lambda_i}{\lambda_i + 1}\right), \tag{F.8}$$

where the middle term on the right-hand side reflects the substraction (non-negative definite) effect the hessian data misfit exerts on the prior, i.e. lowering the covariance. The approximation retains the eigenvectors according to a compromise between data-fidelity and prior probability. Most clearly :

$$\mathrm{C}^{\mathbf{f}} = \mathrm{H}^{-1} \approx \mathrm{H}_{r}^{-1} := \mathrm{C}_{\mathbf{f}} - \mathrm{U}\Lambda\mathrm{U}^{T}, \tag{F.9}$$

where we have used that the inverse of a symmetric matrix is symmetric, and notated $\Lambda \in \mathbb{R}^{r\times r}$ the diagonal matrix with eigenvalues $\lambda_i / \left(\lambda_i + 1\right)$. We use expression (F.9) to approximate the posterior covariance. We note that this approximation is optimal in the sense described in [443]. As in section III.3.4.4, the approximation is computed via a randomised double-pass algorithm. In general, the less informative is the data, the faster the eigenvalues decay and thus a lower order approximation is adequate enough. Lastly, note that directions $\mathrm{C}_{\mathbf{f}}u_i$, with u_i an eigenvector, maximise the (relative) difference between the variance of the posterior and that of the prior.

G – Additional Figures

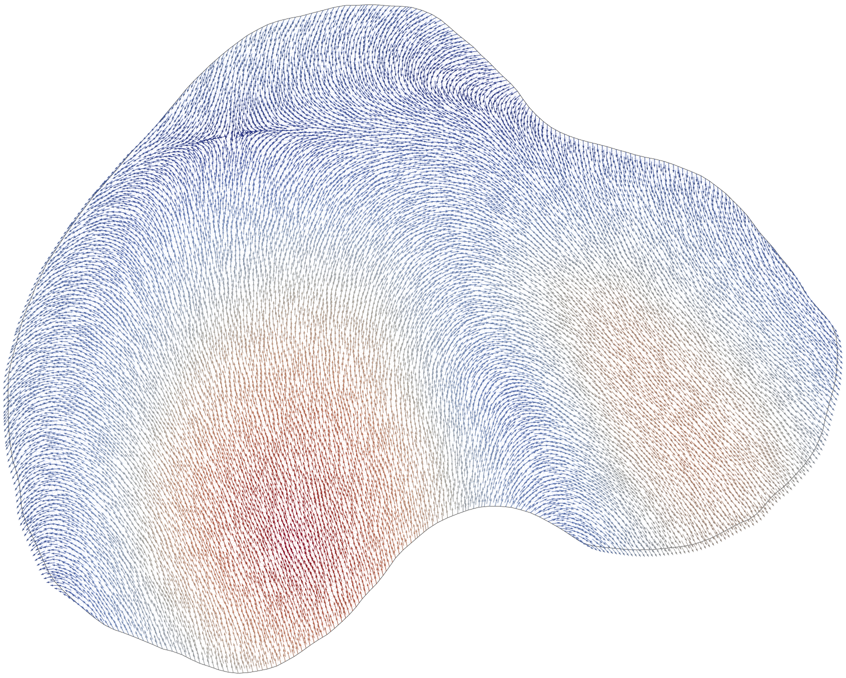

(a)

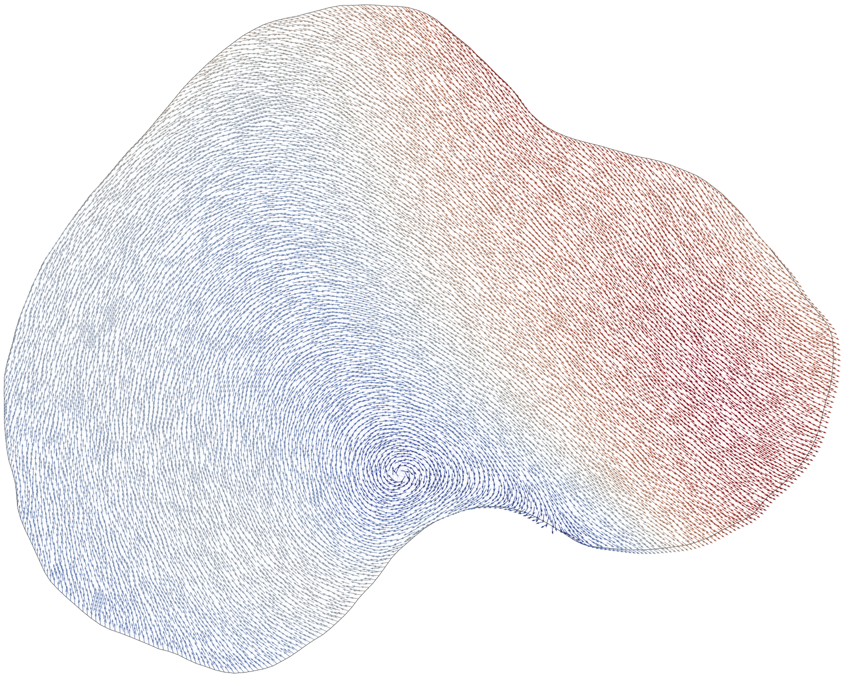

(b)

FIGURE G.1 – **BioFlow at full resolution** High (single-pixel) resolution maps of the intracellular forces (a) and velocity (b) presented in Figure II.3c with equivalent colour scale (NB : arrows are not scaled according to magnitude for better visualisation).

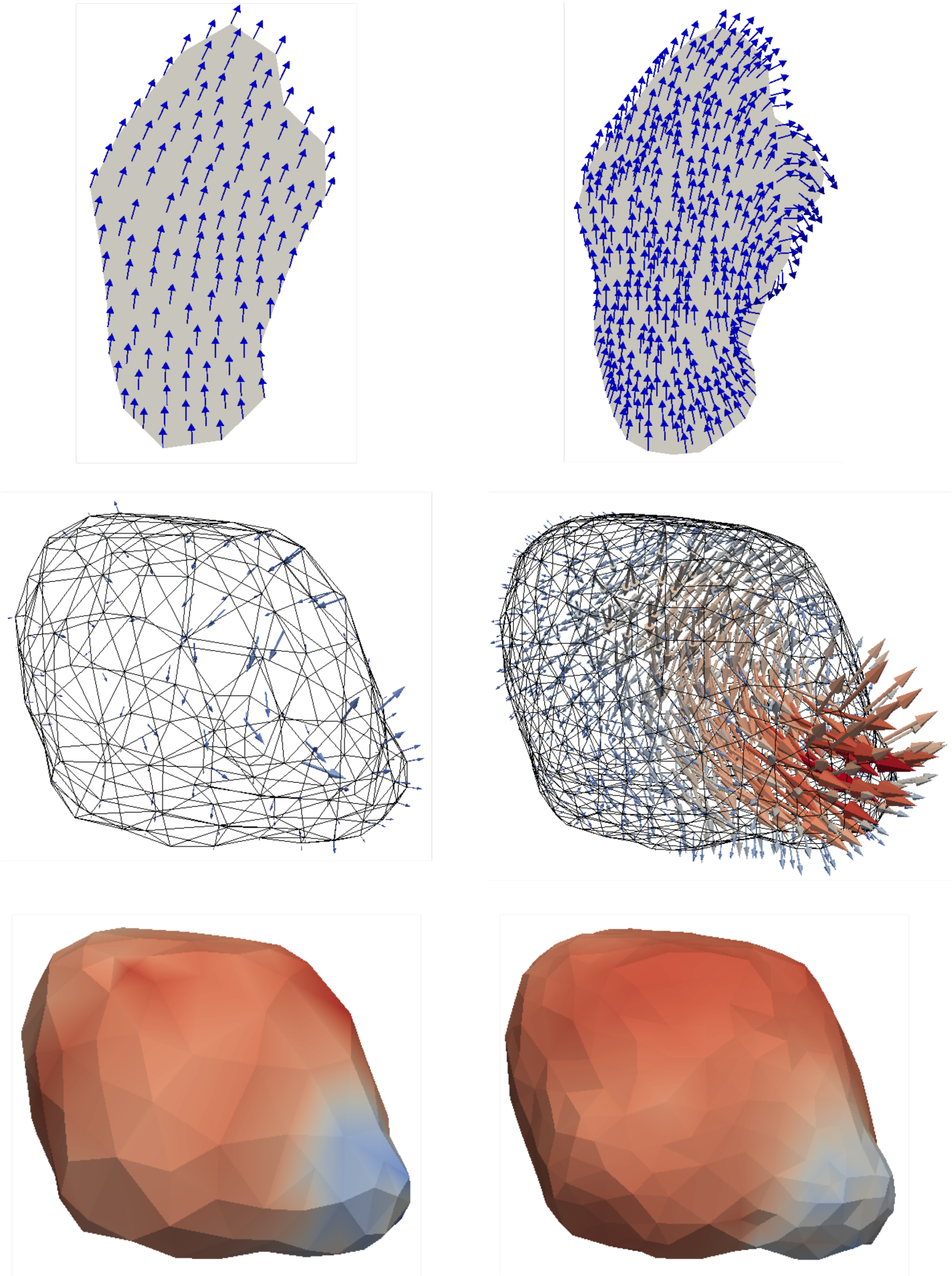

Figure G.2 – **Velocities (and pressure) along the multi-scale process.** All images correspond to scales 2 and 4 (out of 4) in Figure II.6. **Row 1)** 2D velocity becomes more accurate as the scale gets finer (arrows are not scaled or colored accordingly). **Row 2)** 3D velocity (arrows scaled and colored according to magnitude). **Row 3)** 3D pressure is colored from lower (blue) to higher (red).

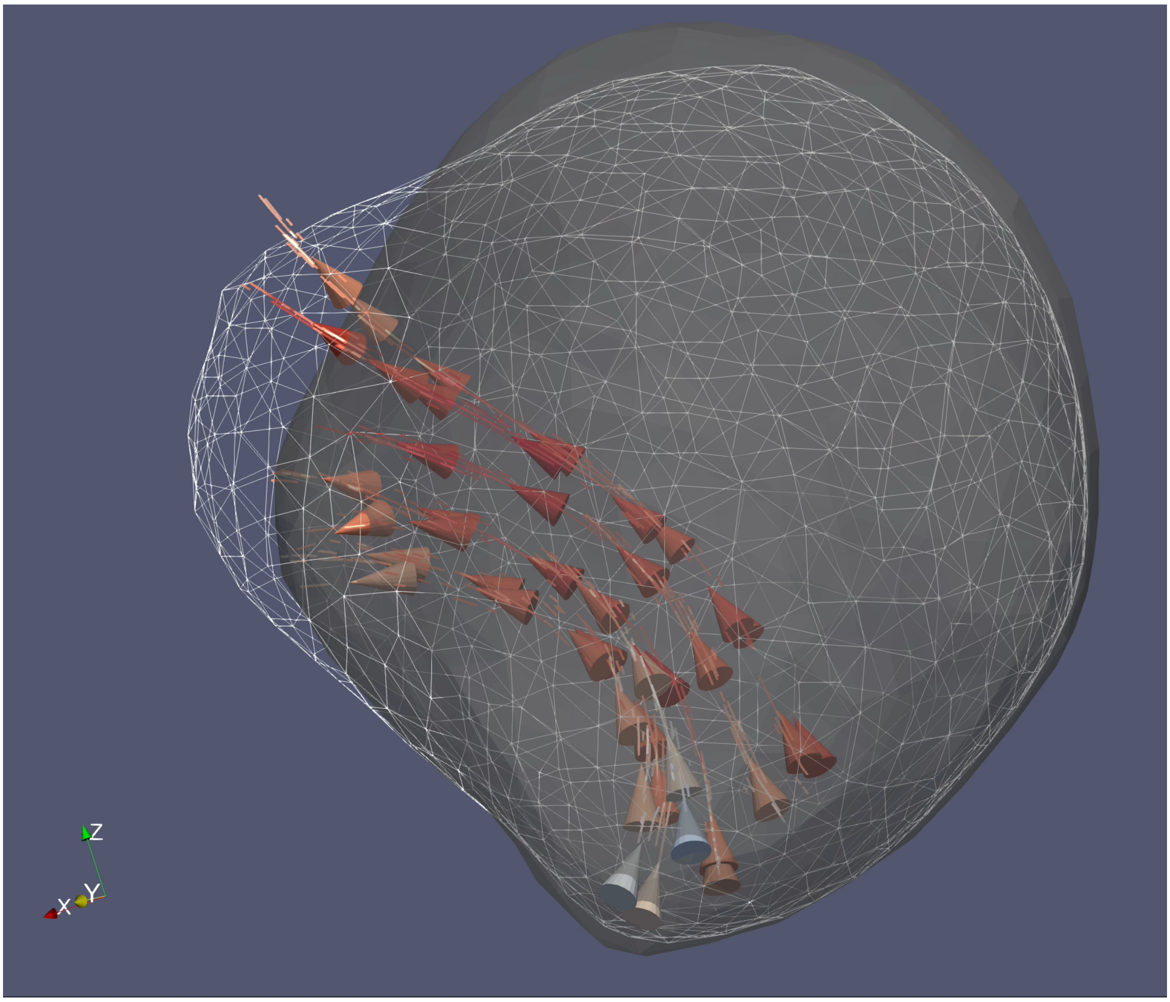

Figure G.3 – **3D streamlines in *E. histolytica*.** Solid cell volume shows the initial time point whereas white cell mesh indicates the following time point (see also Figure II.15), streamlines are colored from low (blue) to high (red) speed.

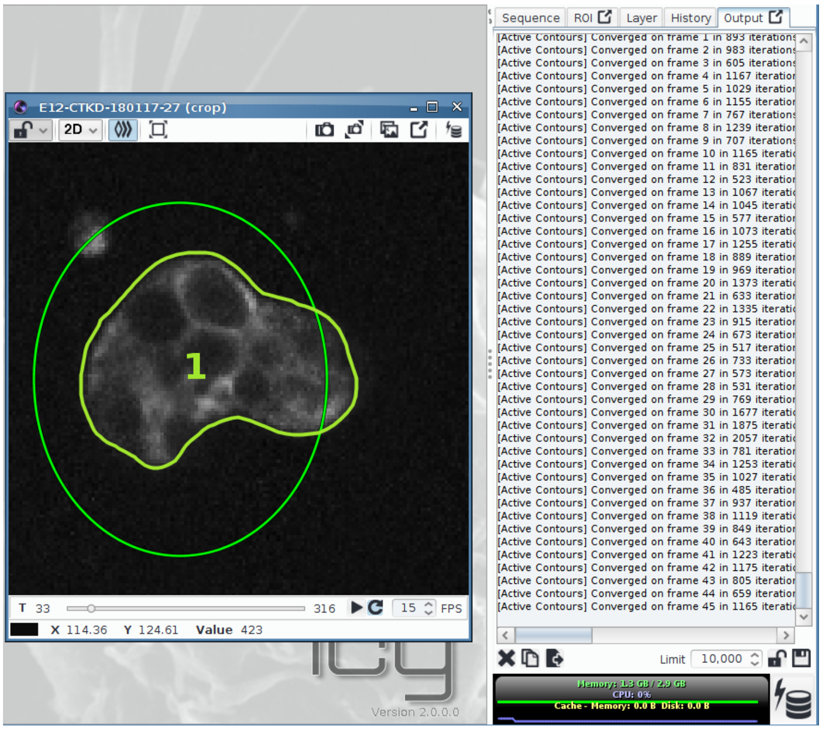

```
[Active Contours] Converged on frame 1 in 893 iterations
[Active Contours] Converged on frame 2 in 983 iterations
[Active Contours] Converged on frame 3 in 605 iterations
[Active Contours] Converged on frame 4 in 1167 iteration
[Active Contours] Converged on frame 5 in 1029 iteration
[Active Contours] Converged on frame 6 in 1155 iteration
[Active Contours] Converged on frame 7 in 767 iterations
[Active Contours] Converged on frame 8 in 1239 iteration
[Active Contours] Converged on frame 9 in 707 iterations
[Active Contours] Converged on frame 10 in 1165 iteratio
[Active Contours] Converged on frame 11 in 831 iteration
[Active Contours] Converged on frame 12 in 523 iteration
[Active Contours] Converged on frame 13 in 1067 iteratio
[Active Contours] Converged on frame 14 in 1045 iteratio
[Active Contours] Converged on frame 15 in 577 iteration
[Active Contours] Converged on frame 16 in 1073 iteratio
[Active Contours] Converged on frame 17 in 1255 iteratio
[Active Contours] Converged on frame 18 in 889 iteration
[Active Contours] Converged on frame 19 in 969 iteration
[Active Contours] Converged on frame 20 in 1373 iteratio
[Active Contours] Converged on frame 21 in 633 iteration
[Active Contours] Converged on frame 22 in 1335 iteratio
[Active Contours] Converged on frame 23 in 915 iteration
[Active Contours] Converged on frame 24 in 673 iteration
[Active Contours] Converged on frame 25 in 517 iteration
[Active Contours] Converged on frame 26 in 733 iteration
[Active Contours] Converged on frame 27 in 573 iteration
[Active Contours] Converged on frame 28 in 531 iteration
[Active Contours] Converged on frame 29 in 769 iteration
[Active Contours] Converged on frame 30 in 1677 iteratio
[Active Contours] Converged on frame 31 in 1875 iteratio
[Active Contours] Converged on frame 32 in 2057 iteratio
[Active Contours] Converged on frame 33 in 781 iteration
[Active Contours] Converged on frame 34 in 1253 iteratio
[Active Contours] Converged on frame 35 in 1027 iteratio
[Active Contours] Converged on frame 36 in 485 iteration
[Active Contours] Converged on frame 37 in 937 iteration
[Active Contours] Converged on frame 38 in 1119 iteratio
[Active Contours] Converged on frame 39 in 849 iteration
[Active Contours] Converged on frame 40 in 643 iteration
[Active Contours] Converged on frame 41 in 1223 iteratio
[Active Contours] Converged on frame 42 in 1175 iteratio
[Active Contours] Converged on frame 43 in 805 iteration
[Active Contours] Converged on frame 44 in 659 iteration
[Active Contours] Converged on frame 45 in 1165 iteratio
```

FIGURE G.4 – **BioFlow during active contours.**

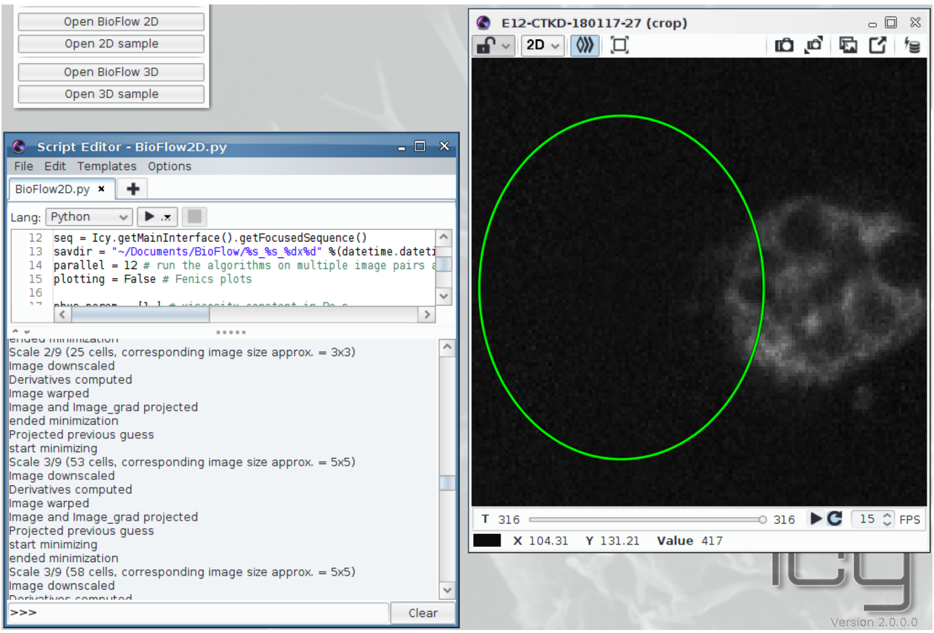

```python
seq = Icy.getMainInterface().getFocusedSequence()
savdir = "~/Documents/BioFlow/%s_%s_%dx%d" %(datetime.dateti
parallel = 12 # run the algorithms on multiple image pairs a
plotting = False # Fenics plots

```

```
ended minimization
Scale 2/9 (25 cells, corresponding image size approx. = 3x3)
Image downscaled
Derivatives computed
Image warped
Image and Image_grad projected
ended minimization
Projected previous guess
start minimizing
Scale 3/9 (53 cells, corresponding image size approx. = 5x5)
Image downscaled
Derivatives computed
Image warped
Image and Image_grad projected
Projected previous guess
start minimizing
ended minimization
Scale 3/9 (58 cells, corresponding image size approx. = 5x5)
Image downscaled
Derivatives computed
>>>
```

FIGURE G.5 – **BioFlow during functional minimisation (parallel iteration over scales).**

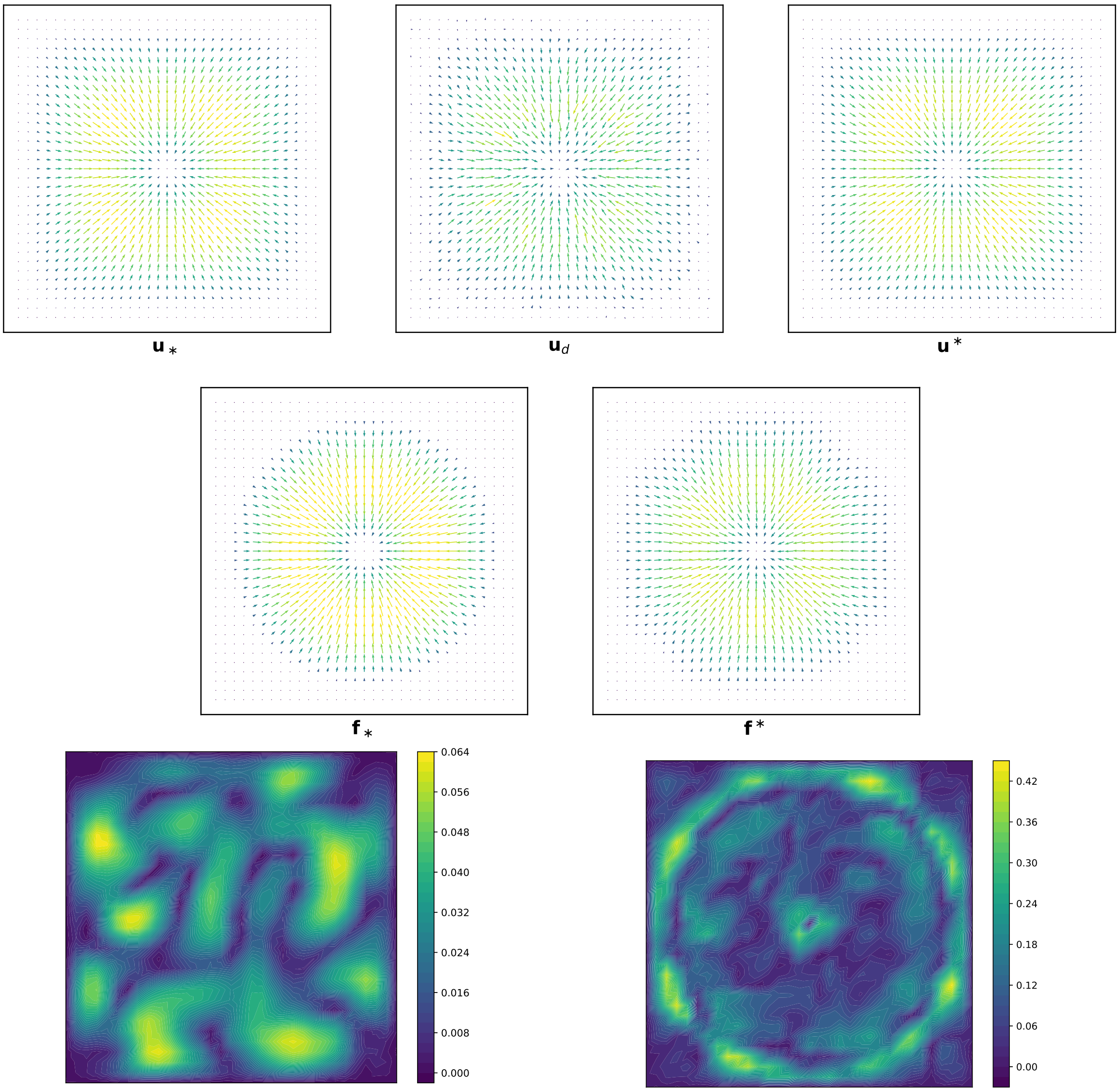

FIGURE G.6 – **Displacement and force reconstruction from noisy displacement data. Row 1)** True simulated displacement $\mathbf{u}_*$, displacement corrupted by 10% noise $\mathbf{u}_d$, and recovered displacement $\mathbf{u}^*$. **Row 2)** True simulated force $\mathbf{f}_*$ and recovered force $\mathbf{f}^*$. **Row 3)** Error map of the displacement $|\mathbf{u}^* - \mathbf{u}_*|_2/|\mathbf{u}_*|_2$ and the force $|\mathbf{f}^* - \mathbf{f}_*|_2/|\mathbf{f}_*|_2$. Blue/low to Yellow/high.

H – French summary

Approches variationnelles en problèmes inverses pour la caractérisation par imagerie de la dynamique cellulaire

Aleix Boquet Pujadas

Résumé

Nous proposons une méthode pour calculer des grandeurs physiques telles que les gradients de pressions ∇p, les forces $\mathbf{f}$ et les vitesses $\mathbf{u}$ nécessaires à la description des dynamiques cellulaires internes et externes et pour étudier les mécanismes biologiques qui les gouvernent. Cette méthode non invasive extrait le mouvement de l'objet biologique d'étude de son observation en microscopie à fluorescence conventionnelle, tout en inférant les variables d'un modèle physique décrivant son comportement. Cette idée est formulée comme un problème d'optimisation avec des dérivées partielles comme contrainte. Nous l'abordons par les méthodes adjointe et des éléments finis puis l'étendons dans un cadre bayésien pour en quantifier les incertitudes. Nous utilisons la dynamique des fluides pour décrire l'écoulement cytoplasmique et obtenons des estimations pour $\nabla p, \mathbf{f}, \mathbf{u}$ qui fédèrent et complètent des résultats précédents sur la mécanique de la migration cellulaire. Les forces sont validées par comparaison avec un système nématique incluant des moteurs moléculaires. Nous montrons aussi comment la vitesse obtenue peut être utilisée dans un shéma de *tracking* fondé sur l'advection, ce qui permet de suivre des régions moléculaires et de définir des mesures globales. Pour compléter l'étude intracellulaire avec des mesures extracellulaires, nous reformulons la microscopie de force de traction dans le cadre de la méthode proposée. Ceci permet une réduction de la propagation des incertitudes et fournit des barres d'erreur. Les logiciels et les outils de visualisation sont disponibles dans le programme *open-source* Icy.

Table des matières

1 Introduction **2**

2 Measures intracellulaires **3**
2.1 Bioflow . . . 3
2.2 Mesures biophysiques à l'intérieur de la cellule amiboïde . . . 5
2.3 Etude des champs de vecteurs . . . 5
2.4 Suivi des domaines intracellulaires diffus . . . 7
2.5 Forces moléculaires dans des systèmes nématiques qui imitent l'intérieur de la cellule . . . 9
2.6 La viscoélasticité du cytoplasme . . . 9

3 Measures extracellulaires **10**

3.1 Flux optique adapté 10
3.2 Microscopie à force de traction 11
3.3 Problème inverse déterministe sous contraintes d'EDPs 12
3.4 Ajoutant de l'incertitude : problème inverse bayésien sous contraintes d'EDPs 12

4 Conclusion et perspectives **12**

1 Introduction

La capacité des cellules à définir et à modifier leur forme, ainsi qu'à démarrer et à réguler leur mouvement est au cœur de nombreux processus biologiques fondamentaux tels que le développement, l'infection microbienne, la réponse immunitaire et les métastases du cancer. Les mécanismes sous-jacents à la forme et à la motilité des cellules impliquent des mécanismes moléculaires complexes qui déclenchent des signaux mécaniques. Par exemple, le réseau contractile d'actine-myosine est capable de générer des forces endogènes à la fois à l'intérieur et à l'extérieur de la cellule. Même si l'ensemble des moteurs moléculaires de myosine agissent localement et indépendamment, en exploitant les propriétés biophysiques de la cellule, leur coordination appropriée est capable d'exercer des forces de traction sur la matrice extracellulaire (ECM), ainsi que de la faire avancer. En passant par ces phases et d'autres, la cellule est capable de traduire la tension mécanique locale en mouvements qui concernent l'ensemble de la cellule et, éventuellement, en une migration globale. Par conséquent, déchiffrer la façon dont les cellules se déforment et se déplacent nécessite une meilleure compréhension des quantités biophysiques qui actionnent (et reflètent également) les dynamiques intracellulaires (IC) et extracellulaires (EC), telles que les forces et la pression IC et EC.

Malheureusement, beaucoup de ces quantités ne peuvent pas être mesurées directement avec les méthodologies actuelles, en particulier au niveau IC. Au lieu de cela, ils sont généralement estimés à l'aide de méthodes expérimentales invasives ou d'approches indirectes. Les méthodes directes permettent d'obtenir des mesures précises mais localisées aux dépens d'une installation expérimentale plus complexe et d'une perte de pertinence biologique. En effet, au stade actuel de miniaturisation, ces techniques entravent souvent les mouvements des cellules et risquent de les endommager. D'autre part, les méthodes indirectes offrent des mesures à une échelle plus globale, mais avec moins de précision et avec une résolution spatiale inférieure. Quelle que soit la méthode employée, de nombreuses mesures biophysiques restent insaisissables ou du moins rares et sont souvent limitées par des contraintes expérimentales. En résumé, il existe un besoin pour une méthode de mesure de quantités biophysiques reproductible, non invasive et généralisable, notamment à l'intérieur de la cellule.

Dans cette thèse, nous abordons ce défi du point de vue de l'imagerie non invasive. Nous examinons le quartet moderne de traitement d'image, à savoir les modèles stochastiques, l'analyse par ondelettes, les méthodes variationnelles et les équations aux dérivées partielles (EDP), afin de proposer un cadre qui tente de tirer le meilleur parti de toutes ces approches. Nous avons choisi les EDP comme point de départ ; non seulement parce qu'il sont connectées au reste des cadres, par exemple a l'approche variationnelle à l'aide des équations d'Euler-Lagrange ou de la formulation faible, mais également en raison de leur manière intuitive de décrire les phénomènes physiques. Concrètement, nous utilisons des PDE pour modéliser directement le monde physique, qui ne se reflète que plus tard sur une séquence d'images. La première PDE est donc utilisée pour décrire l'équation de transport scalaire de l'objet émetteur de lumière vu à travers l'objectif du microscope. C'est essentiellement un problème d'enregistrement. Comme le système est sous-déterminé, nous le réécrivons en langage variationnel. Sous ces termes, nous pouvons essayer de rendre le problème plus spécifique en contrôlant l'espace des solutions. Entrez le deuxième système d'EDP. Ces deuxièmes équations modélisent le mouvement physique réel capturé par la caméra, par exemple en utilisant la mécanique des milieux continus pour décrire le cytoplasme à l'intérieur d'une cellule. Au total, les seuls candidats pour résoudre le premier problème variationnel sont des fonctions qui satisfont (également) le deuxième modèle physique. Notez que de cette manière, au lieu de restreindre directement l'espace des mappes d'enregistrement, nous pouvons maintenant réduire l'espace des variables physiques inconnues en utilisant le second ensemble d'EDPs. Il y a deux avantages. Premièrement, la régularisation peut avoir lieu de manière physiquement pertinente. Deuxièmement, les quantités physiques peuvent être estimées directement à partir des images. Comme nous le verrons dans la section suivante, il s'agit du sujet principal de la thèse : les progrès en analyse d'images sont les bienvenus, mais notre véritable intérêt est de prendre des mesures physiques. Ensuite, nous exploitons les connexions existantes entre les quatre perspectives du traitement d'image. Pas assez local ? Nous limitons l'espace à travers la perspective variationnelle, par exemple en considérant uniquement les fonctions physiques à variation bornée. Pas assez global ? Nous adoptons une approche multi-résolution à la ondelette. Sommes-nous certains de nos mesures ? Entrez la stochasticité par inférence bayésienne. Nous pouvons interpréter la régularisation physique comme une information à priori, la fonctionnelle variationnelle comme une énergie et quantifier les incertitudes de nos mesures à l'aide du théorème de Bayes.

2 Measures intracellulaires

2.1 Bioflow

Nous commençons par présenter une méthode qui extrait des mesures IC partout dans des cellules qui se déplacent librement en utilisant imagerie en direct. Ceci est réalisé en extrayant le mouvement du matériel IC (principalement du cytoplasme) observé en utilisant de la microscopie à fluorescence, tout en déduisant simultanément les variables d'une description physique de l'intérieur de la cellule. Plus spécifiquement, nous intégrons le flux optique, une méthode de traitement d'image qui extrait des informations de mouvement à partir de séquences d'images, dans un cadre d'assimilation de données. Tout est formulé selon une approche variationnelle. Notamment, nous minimisons une fonction décrivant le mouvement de l'intensité des pixels dans les images contrainte par un système d'EDPs décrivant la relation entre le mouvement du matériau observé et ses paramètres d'intérêt. La même idée fonctionne à la fois en 2D et en 3D. Même si nous avons mis au point la méthode décrite ci-dessus pour mesurer l'IC, son cadre est très général et s'étend facilement à différents modèles, y compris l'EC.

Dans un premier cas, la description théorique du matériau intracellulaire est choisie comme un modèle en dynamique des fluides. En particulier, l'intérieur de la cellule est bien décrit par un régime de Stokes ($Re \ll 1$) car l'inertie joue peu de rôle à l'échelle de la cellule. Dans ce cas, les quantités d'intérêt sont la vitesse IC, la pression IC et les forces IC (IC-upf) ; tandis que les images de microscopie à fluorescence, qui reflet le mouvement du matériau IC, constituent les observations du modèle (voir Figures 1 et 2). Du point de vue du contrôle optimal, les contrôles du système sont à la fois la force et les conditions aux limites de la vitesse ; alors que les variables d'état, c'est-à-dire la pression et la vitesse, sont entièrement déterminées par les équations de la dynamique des fluides. A leur tour, les variables d'état apparaissent dans la fonctionnelle de flux optique (c'est-à-dire avec les images) et, par conséquent, toute dérivée de la fonctionnelle par rapport aux variables de contrôle doit prendre en compte les variations introduites par les EDPs du fluide.

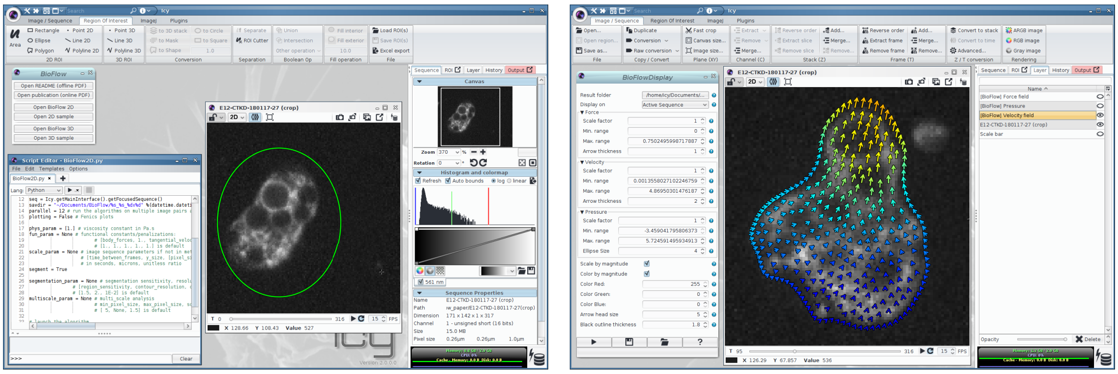

(a) (b)

FIGURE 1 – **Logiciel Bioflow et modules d'affichage. a)** BioFlow fonctionnant sur le logiciel Icy. Étapes à suivre pour exécuter le logiciel : 1) ouvrir la séquence vidéo ; 2) dessinez une région d'intérêt autour de la cellule comme référence pour la segmentation ; 3) ouvrir BioFlow ; 4) exécuter. **b)** BioFlow Display est associé au logiciel BioFlow et permet d'afficher des champs vectoriels et scalaires sur la séquence d'origine. Les résultats sont présentés sous forme de couches de vitesse, de pression et de force pouvant être activées ou désactivées à volonté.

Le problème d'optimisation est résolu numériquement avec la descente itérative de Broyden–Fletcher–Goldfarb–Shanno où le gradient est calculé via la méthode adjointe. Contrairement à l'utilisation d'un schéma de différences finies, où la fonctionnelle contrainte à l'EDP doit être évaluée dans toutes les nombreuses directions possibles des variables de contrôle (chacune au prix d'une EDP), l'approche adjointe exploite l'espace dual pour formuler le gradient en tant que solution d'un seul système d'EDPs linéaires dit adjointe. À un niveau plus bas, les espaces de fonctions discrètes sont écrits en bases d'éléments finis afin de faciliter la résolution des EDPs sous leur formulation faible. Afin de rendre convexe le problème d'optimisation, la fonctionnelle de flux optique est généralement pré-linéarisé et ne peut donc récupérer que des champs de vitesse faibles. Pour généraliser la méthode, nous l'intégrons dans un schéma multi-résolution, dans lequel le problème est progressivement optimisé depuis les mouvements les plus grossiers jusqu'à l'échelle d'un pixel. En d'autres termes, nous pouvons rendre compte de grandes vitesses en résolvant non pas un mais plusieurs problèmes qui satisfont l'approximation linéaire.

Afin de définir le problème sur le domaine approprié, nous segmentons la cellule dans l'image donnée à l'aide d'un modèle de contour actif. Comme avec l'image elle-même, une pyramide à plusieurs échelles doit être construite à partir du contour segmenté. En 2D, nous pouvons ré-échantillonner le contour polygonal sur le domaine de Fourier. Cependant, la même stratégie n'est pas satisfaisante lorsqu'elle est appliquée à un maillage de surface 3D. Au lieu de cela, nous utilisons une méthode d'approximation de forme variationnelle pour tenter de préserver la forme et les caractéristiques saillantes.

Chaque étape a été automatisée dans un logiciel allant des séquences d'images directement aux estimations physiques. Le programme est disponible sur la plateforme à code source ouvert Icy (voir Figure 1).

2.2 Mesures biophysiques à l'intérieur de la cellule amiboïde

Nous illustrons et validons l'efficacité de cette approche dans le contexte de la migration de cellules amiboïdes. En particulier, nous utilisons notre méthode pour étudier le stade trophozoïte du parasite unicellulaire *Entamoeba histolytica*. Ces amibes se caractérisent par l'émission de bosses (blebs) à la surface cellulaire qui se transforment en protubérances et se remplissent via un flux cytoplasmique induit par les forces de contraction de l'acto-myosine. Leur grande motilité et la nature principalement visqueuse de leur cytoplasme constituent un modèle attrayant du point de vue biophysique. Nous montrons qu'en utilisant uniquement un marqueur cytoplasmique et de la microscopie confocale, notre méthode permet d'obtenir des mesures spatiotemporelles IC-upf partout dans des cellules migrant sur un substrat conventionnel *in vitro*. Ces mesures corroborent et étendent plusieurs études théoriques et expérimentales. Notre contribution est remarquable sous deux aspects. Premièrement, nous rapportons pour la première fois une description quantitative complète des phases de mouvement du parasite, confirmant plusieurs prédictions telles que le flux cytoplasmique induit par la pression ou la rétraction de l'arrière de la cellule au moyen de forces moléculaires (voir Figures 2 et 3). Et deuxièmement, nous dévoilons une dynamique à double périodicité dans *Entamoeba histolytica* : $7.9 \pm 0.4s$ entre deux protubérances consécutives, et $4.6 \pm 1.1s$ qui caractérise le flux cytoplasmique.

2.3 Etude des champs de vecteurs

Les détails dans lesquels le flux cytoplasmique est capturé par notre méthode ont motivé le développement d'outils de visualisation qui sont proposés en tant qu'add-ons

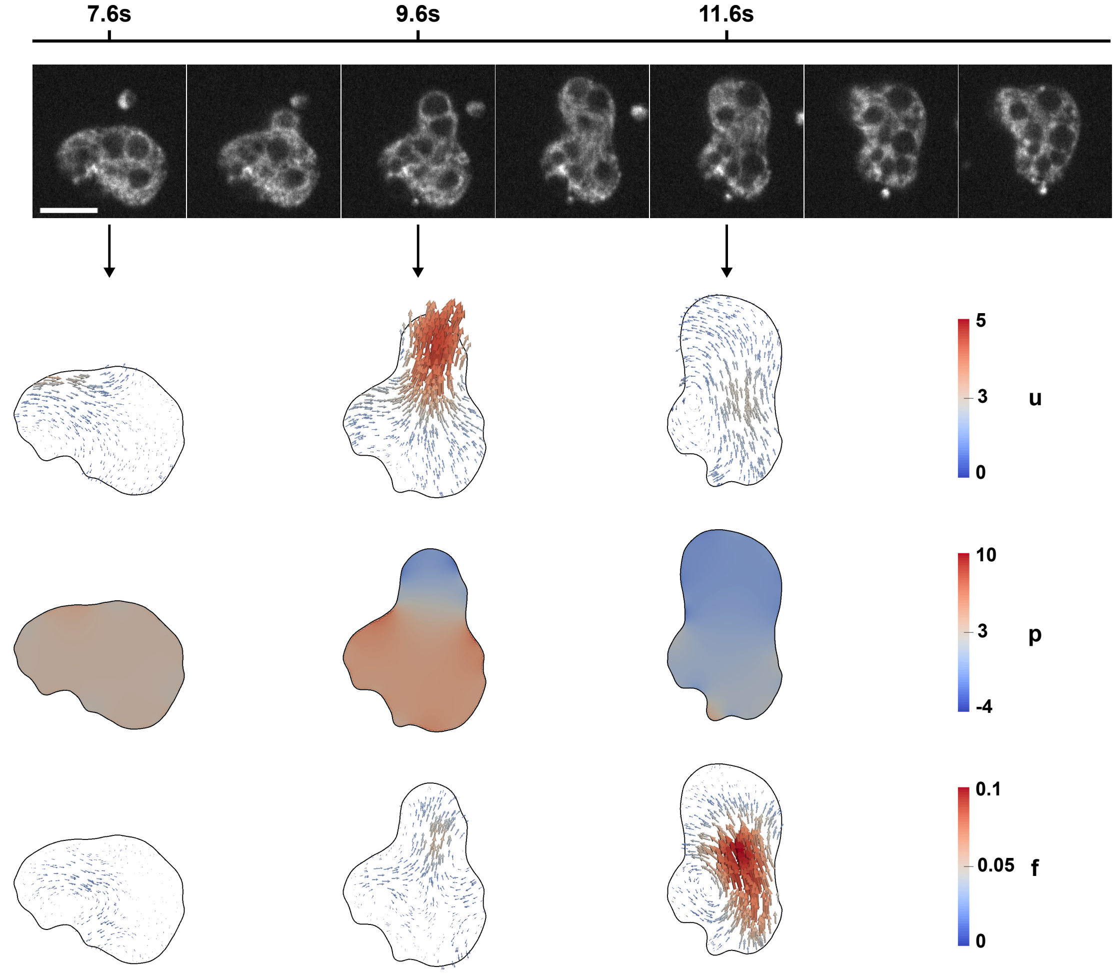

FIGURE 2 – **Vitesse, pression et forces intracellulaires lors d'une protubérance cellulaire.** En haut : instantanés d'une séquence de vidéo-microscopie 2D ; En bas (par ordre décroissant) : vitesse intracellulaire estimée $\mathbf{u}$ ($\mu m/s$), pression p (Pa) et force $\mathbf{f}$ ($nN/\mu m^2$) avant ($t = 7.6s$), pendant ($t = 9.6s$) et après ($t = 11.6s$) la protubérance, respectivement.

au logiciel. Ceux-ci incluent des champs de vecteurs superposés, ainsi que des lignes de courant et des trajectoires de particules à la fois en 2- et 3-D. En collaboration avec Mohammad Goudarzi et Erez Raz, nous utilisons ces outils pour visualiser et quantifier le rôle précis du flux cytoplasmique au cours de la formation de blebs *in vivo*. Le modèle accepté est qu'une redistribution du cytoplasme interne ne suffit pas pour gonfler les blebs et qu'un afflux d'eau de l'extérieur via les protéines dites aquaporines est nécessaire. Au contraire, en utilisant des cellules germinales primordiales de poisson-zèbre (PGCs) et de la microscopie à une résolution spatio-temporelle de pointe, nous montrons que : (i) le knockdown de certaines aquaporines au moyen des morpholinos ne semble pas affecter la formation des blebs ; (ii) les changements de volume cellulaire ne sont pas liés aux blebs ; (iii) les blebs sont principalement remplies par une redistribution du cytoplasme à partir de l'arrière des cellules ; et (iv) les modèles précédents surestimaient l'énergie élastique requise par le flux cytoplasmique pour étirer la membrane car ils ne tenaient pas compte des plis et des invaginations de la membrane.

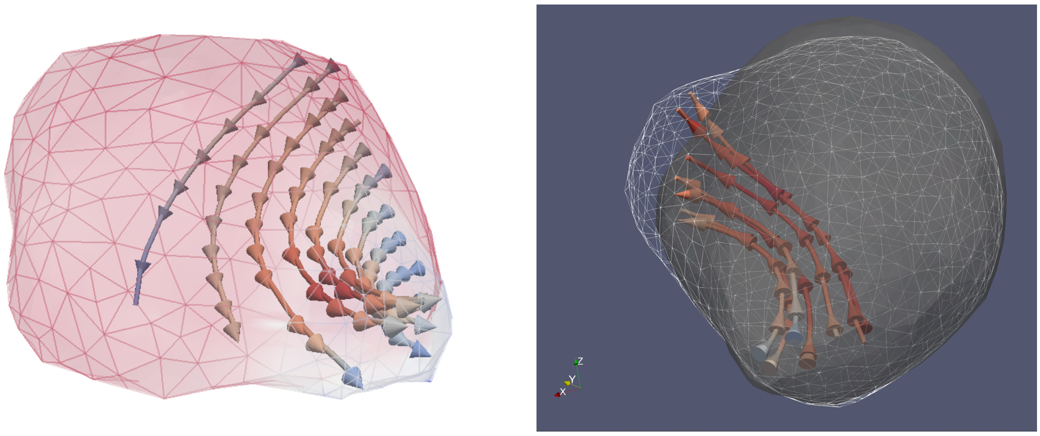

(a) (b)

Figure 3 – **Des lignes de courant en 2D and 3D montrent la redistribution du matériel vers une protubérance cellulaire. a)** Des lignes de courant 3D dans *E. histolytica*. La pression est utilisée pour colorer le maillage (plus haut en rouge à l'arrière, plus bas en blanc à l'avant). **b)** Des lignes de courant 3D dans *E. histolytica*, le volume solide indique le point temporel initial, tandis que le maillage blanche indique le point temporel suivant. Les flèches se superposent aux lignes de courant et sont codées par couleur. Tout est affiché dans le logiciel ParaView.

2.4 Suivi des domaines intracellulaires diffus

Une redistribution contrôlée du matériel dans la cellule est essentielle aux fonctions biologiques : les molécules doivent être synchronisées dans le temps et bien placées dans l'espace pour remplir leur rôle dans le contexte de la coordination de la cellule entière. Cette organisation spatio-temporelle est fait par de multiples processus chimiques et physiques. La diffusion peut transporter passivement des biomolécules le long de gradients de concentration, mais elle est limitée en vitesse et ne fonctionne que dans un seul sens. Par conséquent, d'autres mécanismes complémentaires plus actifs, tels que le flux cytoplasmique et le transport motorisé, ont dû s'engager aux dépens de l'énergie. La spécificité et la diversité de ces solutions reflètent l'importance du transport moléculaire dans un large éventail de systèmes, par exemple dans la division cellulaire. Malgré son importance, la redistribution moléculaire reste difficile à étudier quantitativement. L'approche standard en biologie commence par l'imagerie vidéo de la protéine d'intérêt marquée par fluorescence et se déroule de l'une des deux manières suivantes : soit par projections d'intensité maximale, où le temps est projeté sur une seule image ; soit par kymographes d'intensité, qui se concentrent sur l'évolution temporelle d'une seule dimension spatiale. Des informations de mouvement peuvent être extraites de ces deux visualisations, mais elles sont intrinsèquement biaisées car elles ignorent une dimension de manière arbitraire. Les réponses de la communauté d'analystes d'image ont toujours été les algorithmes de suivi, qu'on appelle de *tracking*. Cependant, la région d'intérêt des molécules advectées est souvent trop diffuse pour être segmentée de manière constant dans la pratique. Dans certains cas, l'utilisation de microscopie s*peckle* peut simplifier le problème et permettre d'utiliser de *tracking* multi-particule.

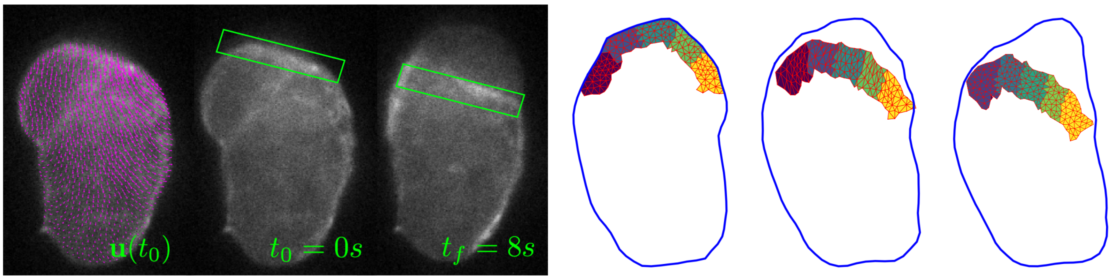

(a) (b)

Figure 4 – **Exemples d'une région moléculaire diffuse, de l'advection d'une maille et du re-maillage. a)** Le bord de la protéine qui se déplace en arrière est approximativement délimité par le rectangle vert à $0s$ et $8s$. Le champ de vitesse à $0s$ est affiché en magenta. **b)** Évolution de chaque partition triangulée (maillage rouge) (couleurs différentes) à mesure que la cellule (contour bleu) se déplace. Sur l'image la plus à droite, les partitions ont été remodelées car la qualité avait diminué. Les cellules en (a) et (b) sont différentes.

Nous montrons comment utiliser les champs de vitesse extraits par la méthode présentée dans la section 2.1 pour construire un schéma de suivi basé sur l'advection qui est capable de suivre des régions moléculaires diffuses. Ceci est fait en résolvant l'équation différentielle ordinaire posée par le champ sur une région initialement délimitée, et en corrigeant les erreurs éventuelles avec l'équation de Laplace. La région advectée est représentée par une maille qui peut être divisé encore en sous-régions d'intérêt. Des éléments finis peuvent ensuite être posés sur le maillage et utilisés pour calculer des intégrales de ligne de manière transparente, ce qui permet de définir plusieurs mesures. En collaboration avec Cecilia Grimaldi et Erez Raz, nous utilisons ce système de suivi pour étudier le rôle de l'E-cadhérine dans la migration cellulaire *in vivo*. Cette protéine est impliquée dans l'adhérence cellule-cellule. L'observation principale est qu'une réduction de l'E-cadhérine diminue la persistance (dit aussi "directionnellite") des cellules qui se déplacent dans un embryon de poisson zèbre, mais ne diminue pas leur vitesse. Il semble que l'E-cadhérine stabilise les structures riches en actine à l'avant de la cellule (appelées brosses d'actine) en réduisant le flux «naturel» d'actine vers l'arrière des cellules. En conséquence, les brosses recrutent plus de myosine, ce qui affaiblit le cortex et favorise donc la formation de blebs à l'avant de la cellule. Pour tester cette hypothèse, nous avons voulu quantifier la stabilisation de l'actine sous différents degrés d'expression de l'E-cadhérine. Notre nouvelle méthode de suivi nous permet non seulement de suivre les brosses d'actine avec précision même si elles sont très diffuses, mais également de définir une mesure de quantification appropriée. Dans le cas de ce travail, nous quantifions la dépolarisation des brosses le long de l'axe avant-arrière de la cellule en présence ou en absence d'E-cadhérine afin de confirmer notre hypothèse.

2.5 Forces moléculaires dans des systèmes nématiques qui imitent l'intérieur de la cellule

En raison de leur nouveauté et de leur nature théorique, les forces estimées par la méthode proposée sont difficiles à valider expérimentalement. En collaboration avec Jérôme Hardoüin, nous étudions un système nématique ressemblant au cytosquelette composé d'un mélange de microtubules et de kinésine en suspension à une interface eau-huile. La nature active des molécules de kinésine (alimentées par l'hydrolisis d'ATP) induit des forces dans le système qui peuvent être déduites de l'orientation des filaments à travers les équations de la nématohydrodynamique. Comme ces forces se répercutent à leur tour sur l'eau sous-jacente, elles peuvent être comparées à celles extraites du cadre présenté dans la Section 2.1, mais avec des termes de régularisation différents. La comparaison de la magnitude des forces peut également aider à calibrer la viscosité ou le coefficient d'activité, ce qui s'est révélé particulièrement difficile à déterminer expérimentalement. En outre, le calcul de la pression et des contraintes déviatoriques semble prometteur pour l'étude de la nucléation de défauts de la matière active dits topologiques, et le calcul des exposants de Lyapunov du champ d'écoulement pourrait aider à analyser les instabilités du système.

2.6 La viscoélasticité du cytoplasme

Le modèle de Stokes intracellulaire n'est valable qu'à certaines échelles de temps, qui dépendent du type de cellule et de son mouvement. Pour remplacer le modèle newtonien visqueux du cytoplasme par une représentation plus précise, nous tirons parti de plusieurs expériences rhéologiques rapportées dans la littérature. En particulier, le cytoplasme des cellules amiboïdes a été décrit à plusieurs reprises comme un fluide viscoélastique bien modelé par les équations de Jeffreys. Bien qu'il s'agisse d'un système mécanique discret composé de ressorts et d'amortisseurs, son extension à la mécanique des milieux continus est connue sous le nom de modèle Oldroyd B. En déduisant explicitement le dernier modèle du premier, nous reproduisons le lien exact entre les constantes des ressorts et des amortisseurs, décrites dans les articles, et les paramètres viscoélas-

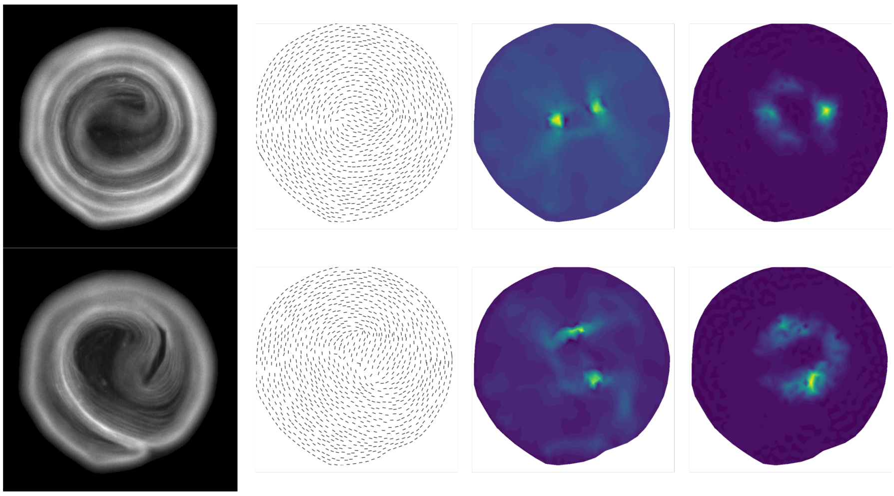

Figure 5 – **Comparaison entre les forces nématiques actives et les forces dans le fluide. Colonne 1)** Deux images d'une séquence montrant un mélange de microtubules et de kinésine se déplaçant spontanément. **Colonne 2)** Champ directeur extrait des images de la (col. 1) reflétant l'orientation des filaments. **Colonne 3)** Force calculée à partir du champ d'orientation présenté dans la (col. 2). **Colonne 4)**. Force dans le fluide extraite de la séquence d'images comme indiqué dans la Section 2.5 ; à comparer avec (col. 3). Les dernières forces sont représentées par le carré de la magnitude car elles sont beaucoup plus régulières. Lorsque les forces sont générées plus près du mur, la précision de la reconstruction se dégrade.

tiques qui régissent le mouvement d'un fluide Oldroyd. Cependant, contrairement aux autres modèles viscoélastiques, les fluides Oldroyd B souffrent de plusieurs problèmes de convergence. Pour stabiliser la formulation faible du problème, nous avons recours à une combinaison de la méthode *streamline upwind*, qui ajoute un terme diffusif, et de l'approche *discrete elastic viscous split stress*. Le pas de temps est alors implémenté avec un schéma *backwards* et la non-linéarité du modèle est attaquée avec la méthode de Newton. Une fois que le problème direct a convergé, nous adaptons la fonctionnelle liée aux données et les termes de régularisation, tous deux introduits dans la section 2.1, à ce problème dépendant du temps, notamment en introduisant un terme reflétant le travail effectué par le système. Bien que l'approche adjointe visant à minimiser le système résultant soit décrite dans la thèse, nous ne l'avons pas utilisée en raison de l'absence de données biologiques pertinentes.

3 Measures extracellulaires

3.1 Flux optique adapté

Nous avons également exploré l'extracellulaire. À cette fin, nous avons d'abord réévalué la fonctionnelle standard du flux optique. Le lien entre le mouvement 2D réfléchi sur l'intensité de l'image et le mouvement 3D original du matériau n'est pas simple. Pour corriger la divergence, nous avons développé une reformulation du flux optique qui clarifie la relation entre le mouvement réel et le mouvement perçu dans le contexte de l'imagerie confocale. Au lieu d'imposer une conservation stricte de l'intensité, la nouvelle expression incorpore un terme source qui reflète la divergence du flux (déduite d'un modèle physique) et qui est proportionnelle à l'intensité elle-même. De cette manière, nous sommes en mesure de prendre en compte les mouvements hors du plan au premier ordre.

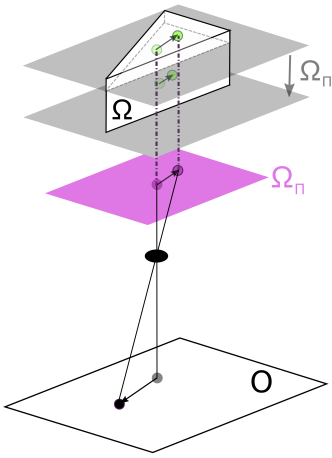

FIGURE 6 – **Schéma de la projection de fluorophores 3D sur une image 2D.** La concentration de fluorophores 3D (représentée par une paire de perles vertes à différents niveaux) dans le matériau d'origine Ω (tranche de gâteau) émet un rayonnement qui est projeté (Ω_{Π^C}) par le laser comme luminance sur un plan Ω_{Π}. La configuration optique (lentille noire) le projette ensuite sur le plan de l'image O. Les flèches indiquent la différence entre le mouvement 3D réel dans Ω (les perles transparentes correspondent à la position précédente) et le mouvement visible sur l'image O.

3.2 Microscopie à force de traction

Comme cela a été illustré avec les adhérences médiées par E-cadhérine dans la Section 2.4, les forces extracellulaires sont essentielles à de nombreuses fonctions biologiques. La microscopie à force de traction (TFM) mesure les forces exercées par les cellules sur le substrat extracellulaire en observant sa déformation, par exemple en suivant le mouvement de marqueurs fluorescents intégrés tels que des billes. Nous reformulons la TFM dans notre cadre. Dans ce cas, les quantités biophysiques d'intérêt sont le déplacement EC et les forces de traction EC ; tandis que le mouvement du substrat EC capturé sur des images de microscopie constitue l'observation du modèle, qui est considéré comme un continuum linéairement élastique. Cette refonte de la TFM promet plusieurs avantages : réduction de la sensibilité au bruit, prise en compte du mouvement hors du plan (grâce au flux optique adapté), extension plus facile à la 3D, flexibilité du modèle élastique et réduction du besoin des mesures ponctuelles (c.-à-d. les billes fluorescentes dans le substrat), ainsi que la possibilité de prendre en compte des systèmes à force non équilibrée et des conditions aux limites non nulles. Dans ce contexte, le flux optique modifié est particulièrement important car les marqueurs fluorescents deviennent nettement plus petits que la profondeur de champ du microscope confocal typique. De plus, les modèles élastiques de contrainte plane satisfont l'approximation du premier ordre et les expressions résultant de notre flux optique adapté sont donc exactes.

3.3 Problème inverse déterministe sous contraintes d'EDPs

Nous avons profité de la reformulation de TFM pour réinventer également le cadre proposé dans la section 2.1. En particulier, notre méthode originale a quelques problèmes occasionnels de stabilité et de convergence que nous avons résolus en posant le problème sur des bases mathématiques plus solides. Dans cette direction, nous étudions l'importance du hessien pour notre problème inverse et puis introduisons la méthode de Newton. De plus, nous analysons tous les systèmes linéaires et proposons des préconditionneurs appropriés afin que le problème ne dépende pas de l'échelle ou de la taille des variables, ce qui est particulièrement intéressant pour notre approche multi-résolution. Nous trouvons également que l'optimisation par rapport aux conditions aux limites est mieux abordée par la méthode dite de Nitsche. Enfin, nous présentons différentes régularisations et leurs interprétations correspondantes. Dans le cas particulier de la régularisation L^2, au lieu de recourir à des méthodes de descente itérative, nous montrons que l'inversion peut être résolue directement en s'occupant d'un système couplé d'équations linéaires. Par ailleurs, la régularisation TV est non linéaire mais permet de mieux préserver les contours.

3.4 Ajoutant de l'incertitude : problème inverse bayésien sous contraintes d'EDPs

La dernière partie de la thèse étend la méthode dans un cadre bayésien. L'inversion du problème déterministe sous contrainte d'EDP ne produit qu'une seule estimation des quantités d'intérêt. Cependant, il est nécessaire d'évaluer la fiabilité des reconstructions car les images sont bruitées. En effet, l'une des tâches cruciales de la science expérimentale est de signaler les erreurs de mesure. Pourtant, à notre connaissance, aucune méthode systématique de quantification de l'incertitude n'a été mise au point ni dans PIV ni dans TFM. Dans le cadre bayésien que nous proposons, l'estimation résultante est une densité postérieure exprimant la distribution de probabilité de la force de traction exercée par les cellules sur le substrat lors de l'observation d'une séquence d'images. Pour résoudre un problème aussi grand, nous nous appuyons sur une approximation laplacienne qui donne un postérieur gaussien dont la covariance est liée à la hessienne du problème, que nous abordons ensuite à l'aide d'une approximation matricielle de bas rang. Nous modélisons également les erreurs expérimentales du module d'élasticité du substrat en pré-marginalisant la fonctionnelle de flux optique. Enfin, nous proposons d'utiliser les estimations d'erreur résultantes pour déterminer si les structures apparaissant sur le champ de force récupéré sont réellement significatives ou s'il s'agit d'artefacts.

4 Conclusion et perspectives

L'objectif principal de ce travail a été de développer une méthodologie qui puisse aider à l'essor de la mécanobiologie. Comme dans de nombreuses autres disciplines,

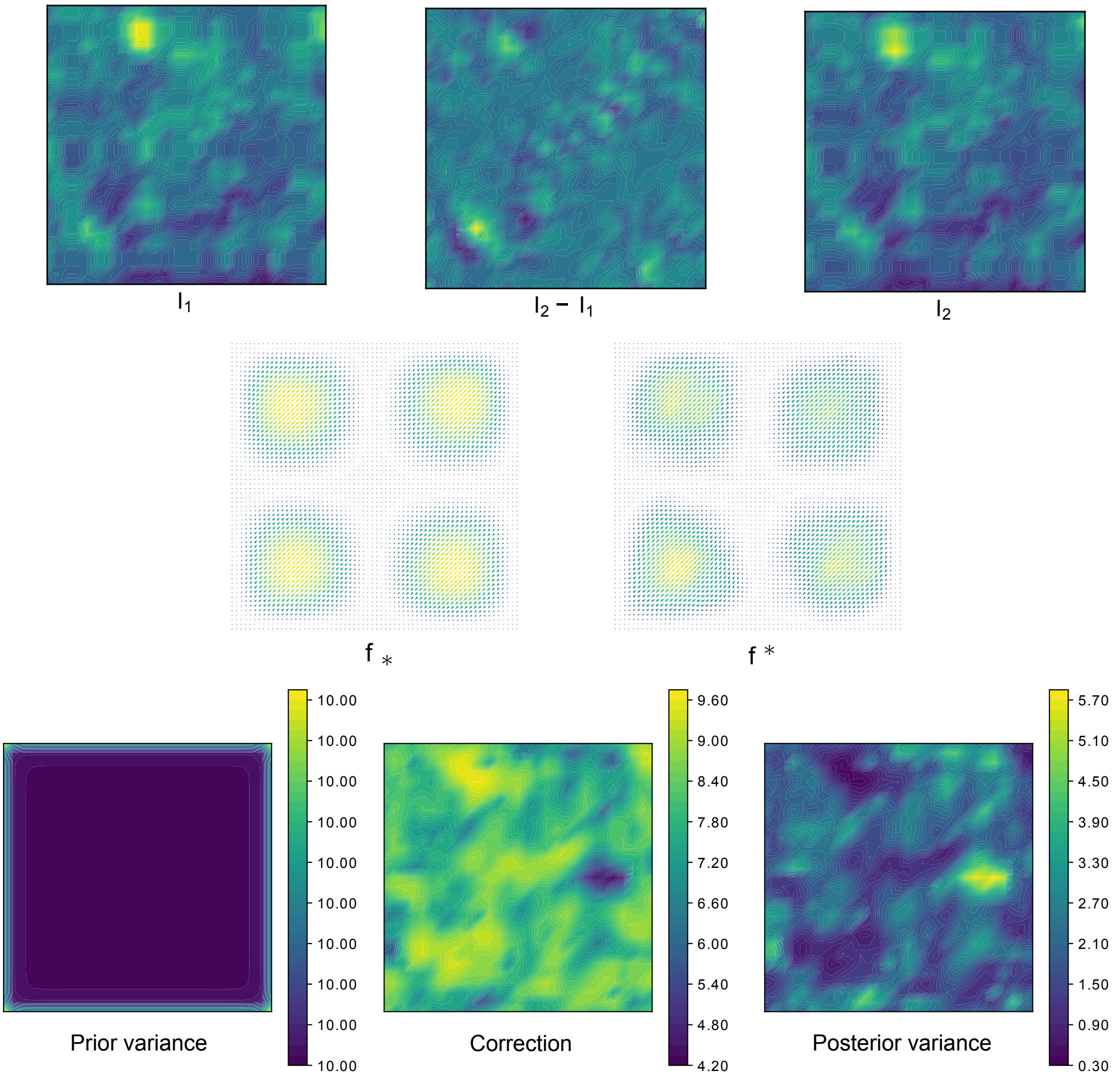

FIGURE 7 – **Problème inverse déterministe et bayésien pour la TFM. Rangée du haut)** Image avant (I_1) et après (I_2) ayant été déformée par une force de traction. **Rangée du milieu)** La force simulée $\mathbf{f}_*$ et la force ont récupéré $\mathbf{f}^*$ à un RSB de 27.6 (violet 0 à jaune 5) à une échelle légèrement supérieure. La solution au problème déterministe $\mathbf{f}^*$ correspond au point maximum *a posteriori* de la distribution de probabilité de la $\mathbf{f}$ dans le problème bayésien. **Rangée du bas)** La variance *a priori* de la $\mathbf{f}$ est corrigé par les données d'image entraînant une variance *a posteriori* inférieure. Il semble que là où l'image a plus de texture, la variance diminue davantage ; c'est-à-dire que l'on est plus certain du résultat.

l'amélioration de la qualité des mesures biophysiques expérimentales a toujours permis de se transformer en découvertes biologiques de manière assez efficace. À cet égard, l'apport central de cette thèse peut s'articuler autour du cadre d'optimisation que nous avons développé tout au long du manuscrit. Ses trois points les plus pertinents pour la cause sont : 1) le caractère non invasif des mesures : elles reposent exclusivement sur la microscopie standard ; 2) la généralité : 2D, 3D, intracellulaire, extracellulaire ... vraisemblablement tout modèle théorique peut être adapté ; et 3) la quantification de l'incertitude : bien que d'origine bayésienne, les limites d'erreur sont un bon indicateur de notre confiance dans les mesures. Comme la biologie est éminemment empirique, il pourrait être surprenant que nous choisissions d'évoquer le troisième point. Cependant, l'incertitude est le non-dit évident des problèmes inverses en général et (peut-être en raison d'une mauvaise communication interdisciplinaire) de leurs applications biologiques en particulier ; c'est le cas de la microscopie à force de traction (TFM) par exemple. Même si un effort est présent pour faire la moyenne sur plusieurs reconstructions (ou mesures), des conclusions sont parfois tirées de champs de force circonstanciels sans se soucier des éventuels artefacts. En fait, c'est précisément notre analyse plutôt qualitative sur le mouvement amiboïde qui nous a incités à nous lancer dans l'estimation de l'incertitude.

En fin de compte, les trois points contribuent à la lutte pour une recherche biologiquement pertinente. Pour illustrer notre idée, nous avons ouvert deux fronts : le premier pour introduire une nouvelle façon de regarder la physique intracellulaire, le second pour reformuler la TFM extracellulaire sur des bases alternatives. Même si la méthodologie a été considérablement développée dans le contexte de TFM lors de la section 3, elle est applicable aux deux problèmes. La quantification des forces intracellulaires et des gradients de pression nous a aidés à confirmer et à compléter de nombreuses hypothèses concernant la migration des cellules amiboïdes ; tandis que les champs de vitesse calculés sont suffisamment détaillés pour caractériser la redistribution cytoplasmique lors de la formation des blebs, et ont aussi motivé un schéma de *tracking* basé sur l'advection qui peut suivre les régions moléculaires dynamiques et permet de définir des mesures intégrales. Toutes ces mesures sont probablement sans précédent, en particulier à cette résolution et à cette étendue spatio-temporelles (non locales) ; et tout se passe sans endommager la cellule. En revanche, les mesures extracellulaires sont plus standardisées, mais nous avons pu réduire la sensibilité au bruit et fournir des limites d'erreur à cet égard. D'autres applications ont été trouvées dans le domaine de la nématique active, ce qui nous a également permis de tester la pertinence des équations de Stokes pour des systèmes de type intracellulaire.

Tout au long de cette thèse, nous avons essayé de souligner le contexte biologique de notre travail. Néanmoins, nous pensons que les aspects mathématiques sont remarquablement intéressants, notamment parce que nous nous appuyons sur plusieurs disciplines pour créer un cadre allant directement des pixels aux mesures. C'est-à-dire que nous pouvons tirer profit des erreurs bien contrôlées des images de microscopie pour estimer l'incertitude de notre reconstruction. Il en résulte un gros problème inverse qui commence par la formulation d'un modèle aux EDPs de conservation pour l'intensité, puis exige que le mouvement sous-jacent respecte également un modèle de continuum aussi basé sur les EDPs. L'idée peut être formulée comme un problème de contrôle optimal que nous résolvons à l'aide du calcul variationnel et que nous complétons avec des estimations bayésiennes.

Pour que les mesures se traduisent en découvertes, elles doivent être reproductibles et facilement accessibles. Si notre espoir est de remplacer les coûteux équipements de laboratoire par des algorithmes, il est impératif de fournir un logiciel fonctionnel. Dans les deux cas, nous avons mis en œuvre notre méthodologie en tant que logiciel open source sur la plate-forme Icy. Cependant, il reste beaucoup à faire en termes de convivialité, notamment pour les utilisateurs finaux.

D'un point de vue théorique, l'approche bayésienne doit encore être développée. Cependant, cela reste un sujet de recherche active dans la littérature mathématique. Compte tenu de la taille des problèmes traités, l'échantillonnage avec les méthodes de Monte-Carlo par chaînes de Markov est prohibitif, ce qui exclut la possibilité d'introduire des non-linéarités. Par conséquent, nous avons besoin de méthodes d'échantillonnage plus rapides ou de systèmes de régularisation linéaires capables de préserver les caractéristiques discontinues telles que la TV.

Une application simple qui découle de la combinaison des sections 2 et 3 consiste à considérer l'image 3D complète d'une cellule naviguant dans l'ECM. Dans ce cas, des domaines complémentaires peuvent être établis pour l'intérieur et l'extérieur de la cellule avec des modèles fluides et élastiques respectifs. D'autre part, les modèles doivent être affinés pour mieux représenter le comportement des matériaux biologiques. En particulier, les fluides biologiques sont mieux décrits par des modèles viscoélastiques non newtoniens et les polymères réticulés tels que le ECM ont également un comportement non linéaire. La section 2.6 représente un premier pas dans cette direction, mais cet effort nécessite beaucoup de support expérimental sous forme des sondages rhéologiques et serait donc mieux réservé à un laboratoire dédié aux sciences biophysiques.

Bibliographie

[1] J. J. Shen ; «Inpainting and the Fundamental Problem of Image Processing» ; SIAM News **36** (2003). 20

[2] T. F. Chan & J. Shen ; *Image processing and analysis : variational, PDE, wavelet, and stochastic methods* (Society for Industrial and Applied Mathematics) (2005) ; ISBN 9780898715897. 20

[3] P. Burt & E. Adelson ; «The Laplacian Pyramid as a Compact Image Code» ; IEEE Transactions on Communications **31**, p. 532–540 (1983). ISSN 0096-2244. `http://ieeexplore.ieee.org/document/1095851/`. 20

[4] A. Chambolle, R. A. DeVore, N. Y. Lee & B. J. Lucier ; «Nonlinear wavelet image processing : Variational problems, compression, and noise removal through wavelet shrinkage» ; IEEE Transactions on Image Processing **7**, p. 319–335 (1998). ISSN 10577149. 20

[5] G. Steidl, J. Weickert, T. Brox, P. Mrázek & M. Welk ; «On the equivalence of soft wavelet shrinkage, total variation diffusion, total variation regularization, and SIDEs» ; SIAM Journal on Numerical Analysis **42**, p. 686–713 (2004). ISSN 00361429. 20

[6] L. Alvarez, F. Guichard, P. L. Lions & J. M. Morel ; «Axioms and fundamental equations of image processing» ; Archive for Rational Mechanics and Analysis **123**, p. 199–257 (1993). ISSN 14320673. 20

[7] V. Bruni, B. Piccoli & D. Vitulano ; «Wavelets and partial differential equations for image denoising» ; ELCVIA Electronic Letters on Computer Vision and Image Analysis **6**, p. 36 (2007). 20

[8] G. Aubert & P. Kornprobst ; *Mathematical Problems in Image Processing : Partial Differential Equations and the Calculus of Variations (Applied Mathematical Sciences (Springer)) (v. 147)* (Springer) (2001) ; ISBN 0387953264. `http://www.amazon.com/exec/obidos/redirect?tag=citeulike07-20{&}path=ASIN/0387953264`. 20, 42

[9] D.H.Hubel & T.N.Wiesel ; «Receptive fields, binocular interaction and functional architecture in the cat's visual cortex.» ; The Journal of physiology **160**, p. 106–54 (1962)ISSN 0022-3751. `http://www.ncbi.nlm.nih.gov/pubmed/14449617{%}0Ahttp://www.pubmedcentral.nih.gov/articlerender.fcgi?artid=PMC1359523`. 21

[10] A. N. Tikhonov ; «Regularization of Incorrectly Posed Problems» ; Soviet Mathematics Doklady **4** (1963). 22

[11] P. Friedl & K. Wolf ; «Plasticity of cell migration : A multiscale tuning model» ; (2010). 23, 25, 26

[12] L. K. Fritz-Laylin, S. J. Lord & R. D. Mullins ; «WASP and SCAR are evolutionarily conserved in actin-filled pseudopod-based motility» ; Journal of Cell Biology **216**, p. 1673–1688 (2017). ISSN 15408140. 23

[13] J. Y. Lee & B. Goldstein ; «Mechanisms of cell positioning during C. elegans gastrulation» ; Development **130**, p. 307–320 (2003). ISSN 09501991. 23

[14] R. N. Germain, E. A. Robey & M. D. Cahalan ; «A Decade of imaging cellular motility and interaction dynamics in the immune system» ; (2012). 23

[15] M. Bockhorn, R. K. Jain & L. L. Munn ; «Active versus passive mechanisms in metastasis : do cancer cells crawl into vessels, or are they pushed ?» ; (2007). 23

[16] et al. Janeway CA Jr, Travers P, Walport M ; *Immunobiology : The Immune System in Health and Disease* ; 5^{e} édition (Garland Science, New York) (2001). 23

[17] T. D. Palmer, W. J. Ashby, J. D. Lewis & A. Zijlstra ; «Targeting tumor cell motility to prevent metastasis» ; Advanced Drug Delivery Reviews **63**, p. 568–581 (2011). ISSN 0169409X. 23

[18] R. Ananthakrishnan & A. Ehrlicher ; «The forces behind cell movement» ; (2007). 24

[19] J. T. Finer, R. M. Simmons & J. A. Spudich ; «Single myosin molecule mechanics : Piconewton forces and nanometre steps» ; Nature **368**, p. 113–119 (1994). ISSN 00280836. 24

[20] C. A. Brunner, A. Ehrlicher, B. Kohlstrunk, D. Knebel, J. A. Käs & M. Goegler ; «Cell migration through small gaps» ; European Biophysics Journal **35**, p. 713–719 (2006). ISSN 01757571. 24

[21] A. K. Harris, P. Wild & D. Stopak ; «Silicone rubber substrata : A new wrinkle in the study of cell locomotion» ; Science **208**, p. 177–179 (1980). ISSN 00368075. 24, 126

[22] G. W. Brodland ; «How computational models can help unlock biological systems» ; (2015). 24

[23] B. M. Slepchenko, J. C. Schaff, J. H. Carson & L. M. Loew ; «Computational cell biology : Spatiotemporal simulation of cellular events» ; (2002). 24

[24] H. Coskun & H. Coskun ; «Cell Physician : Reading Cell Motion A Mathematical Diagnostic Technique Through Analysis of Single Cell Motion» ; Bulletin of Mathematical Biology **73**, p. 658–682 (2011). ISSN 00928240. 24

[25] F. Pampaloni, E. G. Reynaud & E. H. K. Stelzer ; «The third dimension bridges the gap between cell culture and live tissue» ; (2007). 24

[26] J. M. Muthinja, J. Ripp, T. Krüger, A. Imle, T. Haraszti, O. T. Fackler, J. P. Spatz, M. Engstler & F. Frischknecht ; «Tailored environments to study motile cells and pathogens» ; (2018). 24

[27] E. Meijering, A. E. Carpenter, H. Peng, F. A. Hamprecht & J. C. Olivo-Marin ; «Imagining the future of bioimage analysis» ; Nature Biotechnology **34**, p. 1250–1255 (2016). ISSN 15461696. 24

[28] D. A. T. Shirley, L. Farr, K. Watanabe & S. Moonah; «A review of the global burden, new diagnostics, and current Therapeutics for amebiasis»; Open Forum Infectious Diseases **5** (2018). ISSN 23288957. 24

[29] J. A. Goldbogen, J. Calambokidis, A. S. Friedlaender, J. Francis, S. L. DeRuiter, A. K. Stimpert, E. Falcone & B. L. Southall; «Underwater acrobatics by the world's largest predator : 360 rolling manoeuvres by lunge-feeding blue whales»; Biology Letters **9** (2013). ISSN 1744957X. 24

[30] D. E. Cade, A. S. Friedlaender, J. Calambokidis & J. A. Goldbogen; «Kinematic Diversity in Rorqual Whale Feeding Mechanisms»; Current Biology **26**, p. 2617–2624 (2016). ISSN 09609822. 24

[31] M. Sakai, K. Aoki, K. Sato, M. Amano, R. W. Baird, D. L. Webster, G. S. Schorr & N. Miyazaki; « Swim Speed and Acceleration Measurements of Short-Finned Pilot Whales (Globicephala macrorhynchus) in Hawai'i »; Mammal Study **36**, p. 55–59 (2011). ISSN 1343-4152. 24

[32] E. M. Purcell; «Life at low Reynolds number»; American Journal of Physics **45**, p. 3–11 (1977). ISSN 0002-9505. 24, 26, 32, 46

[33] P. Devreotes & A. R. Horwitz; «Signaling networks that regulate cell migration»; Cold Spring Harbor Perspectives in Biology **7** (2015). ISSN 19430264. 25

[34] A. B. Jaffe & A. Hall; «RHO GTPASES : Biochemistry and Biology»; Annual Review of Cell and Developmental Biology **21**, p. 247–269 (2005). ISSN 1081-0706. 25

[35] K. Pavnková, D. Rösel, M. Novotný & J. Brábek; «The molecular mechanisms of transition between mesenchymal and amoeboid invasiveness in tumor cells»; (2010). 25

[36] M. L. Taddei, E. Giannoni, A. Morandi, L. Ippolito, M. Ramazzotti, M. Callari, P. Gandellini & P. Chiarugi; «Mesenchymal to amoeboid transition is associated with stem-like features of melanoma cells»; Cell Communication and Signaling **12** (2014). ISSN 1478811X. 25

[37] Cell Migration Consortium; «Cell Migration Gateway»; `http://www.cellmigration.org/science/{#}stasis`. 25

[38] K. Hu, L. Ji, K. T. Applegate, G. Danuser & C. M. Waterman-Storer; «Differential transmission of actin motion within focal adhesions»; Science **315**, p. 111–115 (2007). ISSN 00368075. 25

[39] E. K. Paluch & E. Raz; «The role and regulation of blebs in cell migration»; (2013). 25

[40] J. B. Wyckoff, S. E. Pinner, S. Gschmeissner, J. S. Condeelis & E. Sahai; «ROCK- and Myosin-Dependent Matrix Deformation Enables Protease-Independent Tumor-Cell Invasion In Vivo»; Current Biology **16**, p. 1515–1523 (2006). ISSN 09609822. 25

[41] G. Charras & E. Paluch; «Blebs lead the way : How to migrate without lamellipodia»; (2008). 25

[42] G. T. Charras, M. Coughlin, T. J. Mitchison & L. Mahadevan; «Life and times of a cellular bleb»; Biophysical Journal **94**, p. 1836–1853 (2008). ISSN 15420086. 25, 66, 71

[43] G. T. Charras, C. K. Hu, M. Coughlin & T. J. Mitchison ; «Reassembly of contractile actin cortex in cell blebs» ; Journal of Cell Biology **175**, p. 477–490 (2006). ISSN 00219525. 26

[44] I. Lavi, M. Piel, A. M. Lennon-Duménil, R. Voituriez & N. S. Gov ; «Deterministic patterns in cell motility» ; Nature Physics **12**, p. 1146–1152 (2016). ISSN 17452481. 26, 32

[45] Y. Cao, E. Ghabache & W.-J. Rappel ; «Plasticity of cell migration resulting from mechanochemical coupling» ; bioRxiv p. 644880 (2019). `https://www.biorxiv.org/content/10.1101/644880v1`. 26

[46] D. Flores-Robles, C. Rosales, J. L. Rosales-Encina & P. Talamás-Rohana ; «Entamoeba histolytica : A $\beta 1$ integrin-like fibronectin receptor assembles a signaling complex similar to those of mammalian cells» ; Experimental Parasitology **103**, p. 8–15 (2003). ISSN 00144894. 26

[47] E. Labruyère, C. Zimmer, V. Galy, J. C. Olivo-Marin & N. Guillén ; «EhPAK, a member of the p21-activated kinase family, is involved in the control of Entamoeba histolytica migration and phagocytosis» ; (2003). 26

[48] J. Marquay Markiewicz, S. Syan, C.-C. Hon, C. Weber, D. Faust & N. Guillen ; «A proteomic and cellular analysis of uropods in the pathogen Entamoeba histolytica.» ; PLoS neglected tropical diseases **5**, p. e1002 (2011). ISSN 1935-2735. `http://www.ncbi.nlm.nih.gov/pubmed/21483708http://www.pubmedcentral.nih.gov/articlerender.fcgi?artid=PMC3071361`. 26

[49] R. Thibeaux, P. Avé, M. Bernier, M. Morcelet, P. Frileux, N. Guillén & E. Labruyère ; «The parasite Entamoeba histolytica exploits the activities of human matrix metalloproteinases to invade colonic tissue» ; Nature Communications **5** (2014). ISSN 20411723. 26, 36

[50] S. Blazquez, C. Zimmer, G. Guigon, J. C. Olivo-Marin, N. Guillén & E. Labruyère ; «Human tumor necrosis factor is a chemoattractant for the parasite Entamoeba histolytica» ; Infection and Immunity **74**, p. 1407–1411 (2006). ISSN 00199567. 26

[51] B. Ladoux & R. M. Mège ; «Mechanobiology of collective cell behaviours» ; Nature Reviews Molecular Cell Biology **18**, p. 743–757 (2017). ISSN 14710080. 26

[52] V. Lecaudey, G. Cakan-Akdogan, W. H. J. Norton & D. Gilmour ; «Dynamic Fgf signaling couples morphogenesis and migration in the zebrafish lateral line primordium» ; Development **135**, p. 2695–2705 (2008). ISSN 09501991. 26

[53] A. Brugués, E. Anon, V. Conte, J. H. Veldhuis, M. Gupta, J. Colombelli, J. J. Muñoz, G. W. Brodland, B. Ladoux & X. Trepat ; «Forces driving epithelial wound healing» ; Nature Physics **10**, p. 683–690 (2014). ISSN 17452481. 26

[54] A. Labernadie, T. Kato, A. Brugués, X. Serra-Picamal, S. Derzsi, E. Arwert, A. Weston, V. González-Tarragó, A. Elosegui-Artola, L. Albertazzi, J. Alcaraz, P. Roca-Cusachs, E. Sahai & X. Trepat ; «A mechanically active heterotypic E-cadherin/N-cadherin adhesion enables fibroblasts to drive cancer cell invasion» ; Nature Cell Biology **19**, p. 224–237 (2017). ISSN 14764679. 26

[55] X. Trepat & E. Sahai ; «Mesoscale physical principles of collective cell organization» ; (2018). 26

[56] J. A. Park, J. H. Kim, D. Bi, J. A. Mitchel, N. T. Qazvini, K. Tantisira, C. Y. Park, M. McGill, S. H. Kim, B. Gweon, J. Notbohm, R. Steward, S. Burger, S. H. Randell, A. T. Kho, D. T. Tambe, C. Hardin, S. A. Shore, E. Israel, D. A. Weitz, D. J. Tschumperlin, E. P. Henske, S. T. Weiss, M. L. Manning, J. P. Butler, J. M. Drazen & J. J. Fredberg ; «Unjamming and cell shape in the asthmatic airway epithelium» ; Nature Materials **14**, p. 1040–1048 (2015). ISSN 14764660. 26

[57] C. Zheng & K. Ahmad ; «The segmentation of images of biological cells-A survey of methods and systems» ; Rapport technique. 27

[58] S. Beucher & C. Lantuéjoul ; «Use of Watersheds in Contour Detection» ; Rapport technique (1979). 27

[59] R. Cilla, V. Mechery, B. Hernandez de Madrid, S. Del Signore, I. Dotu & V. Hatini ; «Segmentation and tracking of adherens junctions in 3D for the analysis of epithelial tissue morphogenesis» ; PLoS Computational Biology **11** (2015). ISSN 15537358. 29

[60] T. Pock, D. Cremers, H. Bischof & A. Chambolle ; «Global Solutions of Variational Models with Convex Regularization» ; SIAM Journal on Imaging Sciences **3**, p. 1122–1145 (2010). 29

[61] T. F. Chan & L. A. Vese ; «Active contours without edges» ; IEEE Transactions on Image Processing **10**, p. 266–277 (2001). ISSN 10577149. 29, 58

[62] S. Mukherjee & S. T. Acton ; «Region based segmentation in presence of intensity inhomogeneity using legendre polynomials» ; IEEE Signal Processing Letters **22**, p. 298–302 (2015). ISSN 10709908. 29

[63] A. Dufour, R. Thibeaux, E. Labruyère, N. Guillén & J.-C. Olivo-Marin ; «3-D active meshes : fast discrete deformable models for cell tracking in 3-D time-lapse microscopy.» ; IEEE transactions on image processing : a publication of the IEEE Signal Processing Society **20**, p. 1925–37 (2011). ISSN 1941-0042. `http://www.ncbi.nlm.nih.gov/pubmed/21193379`. 29, 58, 147

[64] P. Arhets, J. C. Olivo, P. Gounon, P. Sansonetti & N. Guillén ; «Virulence and functions of myosin II are inhibited by overexpression of light meromyosin in Entamoeba histolytica.» ; Molecular biology of the cell **9**, p. 1537–47 (1998). ISSN 1059-1524. `http://www.ncbi.nlm.nih.gov/pubmed/9614192http://www.pubmedcentral.nih.gov/articlerender.fcgi?artid=PMC25380`. 30

[65] T. Lagache, A. Grassart, S. Dallongeville, O. Faklaris, N. Sauvonnet, A. Dufour, L. Danglot & J. C. Olivo-Marin ; «Mapping molecular assemblies with fluorescence microscopy and object-based spatial statistics» ; Nature Communications **9** (2018). ISSN 20411723. 30

[66] A. Zaritsky, U. Obolski, Z. Gan, C. R. Reis, Z. Kadlecova, Y. Du, S. L. Schmid & G. Danuser ; «Decoupling global biases and local interactions between cell biological variables» ; eLife **6** (2017). ISSN 2050084X. 30

[67] M. Manich, N. Hernandez-Cuevas, J. D. Ospina-Villa, S. Syan, L. A. Marchat, J. C. Olivo-Marin & N. Guillén ; «Morphodynamics of the actin-rich cytoskeleton in Entamoeba histolytica» ; Frontiers in Cellular and Infection Microbiology **8** (2018). ISSN 22352988. 30

[68] J. C. Olivo-Marin ; «Extraction of spots in biological images using multiscale products» ; Pattern Recognition **35**, p. 1989–1996 (2002). ISSN 00313203. 30

[69] W. Stein & D. F. Bronner ; *Cell shape : determinants, regulation, and regulatory role* (Academic Press) (1989). 30

[70] A. Haupt & N. Minc ; «How cells sense their own shape - mechanisms to probe cell geometry and their implications in cellular organization and function» ; (2018). 30

[71] E. Karsenti ; «Self-organization in cell biology : A brief history» ; (2008). 30

[72] J. Lobo, E. Y. S. See, M. Biggs & A. Pandit ; «An insight into morphometric descriptors of cell shape that pertain to regenerative medicine» ; (2016). 31

[73] Image Metrology ; «SPIP : Reference Guide, Shape Measurement Parameters» ; `http://www.imagemet.com/WebHelp6/Default.htm{#}PnPParameters/Measure{_}Shape{_}Parameters.htm`. 31

[74] H. Elliott, R. S. Fischer, K. A. Myers, R. A. Desai, L. Gao, C. S. Chen, R. S. Adelstein, C. M. Waterman & G. Danuser ; «Myosin II controls cellular branching morphogenesis and migration in three dimensions by minimizing cell-surface curvature» ; Nature Cell Biology **17**, p. 137–147 (2015). ISSN 14764679. 31

[75] M. M. Bagonis, L. Fusco, O. Pertz & G. Danuser ; «Automated profiling of growth cone heterogeneity defines relations between morphology and motility» ; Journal of Cell Biology **218**, p. 350–379 (2019). ISSN 15408140. 31

[76] C. H. Brechbuhler, G. Gerig & O. Kubler ; «Parametrization of closed surfaces for 3-D shape description» ; Computer Vision and Image Understanding **61**, p. 154–170 (1995). ISSN 10773142. 31

[77] J.-P. Antoine & P. Vandergheynst ; «Wavelets on the 2-Sphere : A Group-Theoretical Approach» ; Applied and Computational Harmonic Analysis **7**, p. 262–291 (1999). ISSN 10635203. 31

[78] R. Tournemenne, C. Ducroz, J.-C. Olivo-Marin & A. Dufour ; «3D shape analysis using overcomplete spherical wavelets : Application to BLEB detection in cell biology» ; dans «2014 IEEE 11th International Symposium on Biomedical Imaging (ISBI)», p. 365–368 (IEEE) (2014) ; ISBN 978-1-4673-1961-4. `http://ieeexplore.ieee.org/document/6867884/`. 31

[79] D. B. Petropolis, D. M. Faust, G. Deep Jhingan & N. Guillen ; «A New Human 3D-Liver Model Unravels the Role of Galectins in Liver Infection by the Parasite Entamoeba histolytica» ; PLoS Pathogens **10** (2014). ISSN 15537374. 31

[80] S. Blazquez, M. C. Rigothier, M. Huerre & N. Guillén ; «Initiation of inflammation and cell death during liver abscess formation by Entamoeba histolytica depends on activity of the galactose/N-acetyl-d-galactosamine lectin» ; International Journal for Parasitology **37**, p. 425–433 (2007). ISSN 00207519. 31

[81] K. Khairy, J. Foo & J. Howard ; «Shapes of Red Blood Cells : Comparison of 3D Confocal Images with the Bilayer-Couple Model» ; Cellular and Molecular Bioengineering **1**, p. 173–181 (2008). ISSN 1865-5025. 31

[82] A. Dufour, T. Y. Liu, C. Ducroz, R. Tournemenne, B. Cummings, R. Thibeaux, N. Guillen, A. Hero & J. C. Olivo-Marin ; «Signal processing challenges in quantitative 3-D cell morphology : More than meets the eye» ; (2015). 31

[83] C. Sommer & D. W. Gerlich ; «Machine learning in cell biology-teaching computers to recognize phenotypes» ; Journal of Cell Science **126**, p. 5529–5539 (2013). ISSN 00219533. 31

[84] E. S. Welf, M. K. Driscoll, K. M. Dean, C. Schäfer, J. Chu, M. W. Davidson, M. Z. Lin, G. Danuser & R. Fiolka ; «Quantitative Multiscale Cell Imaging in Controlled 3D Microenvironments» ; Developmental Cell **36**, p. 462–475 (2016). ISSN 18781551. 32

[85] M. K. Driscoll & G. Danuser ; «Quantifying Modes of 3D Cell Migration» ; (2015). 32

[86] E. Rodolà, Z. Lähner, A. M. Bronstein, M. M. Bronstein & J. Solomon ; «Functional Maps on Product Manifolds» ; dans T. Ju & A. Vaxman (rédacteurs), «Symposium on Geometry Processing 2018- Posters», (2018). 32

[87] L. Bertot, A. Grassart, T. Lagache, G. Nardi, C. Basquin, J. C. Olivo-Marin & N. Sauvonnet ; «Quantitative and Statistical Study of the Dynamics of Clathrin-Dependent and -Independent Endocytosis Reveal a Differential Role of EndophilinA2» ; Cell Reports **22**, p. 1574–1588 (2018). ISSN 22111247. 32

[88] H. Qian, M. P. Sheetz & E. L. Elson ; «Single particle tracking. Analysis of diffusion and flow in two-dimensional systems» ; Biophysical Journal **60**, p. 910–921 (1991). ISSN 00063495. 32

[89] P. Maiuri, E. Terriac, P. Paul-Gilloteaux, T. Vignaud, K. McNally, J. Onuffer, K. Thorn, P. A. Nguyen, N. Georgoulia, D. Soong, A. Jayo, N. Beil, J. Beneke, J. C. Hong Lim, C. Pei-Ying Sim, Y. S. Chu, A. Jiménez-Dalmaroni, J. F. Joanny, J. P. Thiery, H. Erfle, M. Parsons, T. J. Mitchison, W. A. Lim, A. M. Lennon-Duménil, M. Piel & M. Théry ; «The first World Cell Race» ; (2012). 32

[90] G. B. Bailey, G. J. Leitch & D. B. Day ; «Chemotaxis by Entamoeba histolytica.» ; The Journal of protozoology **32**, p. 341–6 (1985)ISSN 0022-3921. `http://www.ncbi.nlm.nih.gov/pubmed/2861283`. 32

[91] E. Franco, J. Vazquez-Prado & I. Meza ; «Fibronectin-Derived Fragments as Inducers of Adhesion and Chemotaxis of "Entamoeba histolytica" Trophozoites» ; `https://www.jstor.org/stable/30106877`. 32

[92] M. Zaki, N. Andrew & R. H. Insall ; «Entamoeba histolytica cell movement : a central role for self-generated chemokines and chemorepellents.» ; Proceedings of the National Academy of Sciences of the United States of America **103**, p. 18 751–6 (2006). ISSN 0027-8424. `http://www.ncbi.nlm.nih.gov/pubmed/17132728http://www.pubmedcentral.nih.gov/articlerender.fcgi?artid=PMC1693734`. 32

[93] S. Blazquez, G. Guigon, C. Weber, S. Syan, O. Sismeiro, J. Y. Coppée, E. Labruyère & N. Guillén ; «Chemotaxis of Entamoeba histolytica towards the pro-inflammatory cytokine TNF is based on PI3K signalling, cytoskeleton reorganization and the Galactose/N-acetylgalactosamine lectin activity» ; Cellular Microbiology **10**, p. 1676–1686 (2008). ISSN 14625814. 32

[94] O. Bénichou, C. Loverdo, M. Moreau & R. Voituriez ; «Intermittent search strategies» ; Reviews of Modern Physics **83**, p. 81–129 (2011). ISSN 00346861. 32

[95] P. Maiuri, J. F. Rupprecht, S. Wieser, V. Ruprecht, O. Bénichou, N. Carpi, M. Coppey, S. De Beco, N. Gov, C. P. Heisenberg, C. Lage Crespo, F. Lautenschlaeger, M. Le Berre, A. M. Lennon-Dumenil, M. Raab, H. R. Thiam, M. Piel, M. Sixt & R. Voituriez ; «Actin flows mediate a universal coupling between cell speed and cell persistence» ; Cell **161**, p. 374–386 (2015). ISSN 10974172. 32

[96] N. Chenouard, I. Bloch & J. C. Olivo-Marin ; «Multiple hypothesis tracking for cluttered biological image sequences» ; IEEE Transactions on Pattern Analysis and Machine Intelligence **35**, p. 2736–2750 (2013). ISSN 01628828. 32

[97] E. Meijering, I. Smal & G. Danuser ; «Tracking in molecular bioimaging» ; IEEE Signal Processing Magazine **23**, p. 46–53 (2006). ISSN 10535888. 32

[98] F. De Chaumont, R. D. S. Coura, P. Serreau, A. Cressant, J. Chabout, S. Granon & J. C. Olivo-Marin ; «Computerized video analysis of social interactions in mice» ; Nature Methods **9**, p. 410–417 (2012). ISSN 15487091. 32

[99] A. Weissbrod, A. Shapiro, G. Vasserman, L. Edry, M. Dayan, A. Yitzhaky, L. Hertzberg, O. Feinerman & T. Kimchi ; «Automated long-term tracking and social behavioural phenotyping of animal colonies within a semi-natural environment» ; Nature Communications **4** (2013). ISSN 20411723. 32

[100] F. de Chaumont, E. Ey, N. Torquet, T. Lagache, S. Dallongeville, A. Imbert, T. Legou, A. M. Le Sourd, P. Faure, T. Bourgeron & J. C. Olivo-Marin ; «Real-time analysis of the behaviour of groups of mice via a depth-sensing camera and machine learning» ; Nature Biomedical Engineering (2019). ISSN 2157846X. 32

[101] G. Pasqual, A. Chudnovskiy, J. M. Tas, M. Agudelo, L. D. Schweitzer, A. Cui, N. Hacohen & G. D. Victora ; «Monitoring T cell-dendritic cell interactions in vivo by intercellular enzymatic labelling» ; Nature **553**, p. 496–500 (2018). ISSN 14764687. 33

[102] J. Y. Tinevez, N. Perry, J. Schindelin, G. M. Hoopes, G. D. Reynolds, E. Laplantine, S. Y. Bednarek, S. L. Shorte & K. W. Eliceiri ; «TrackMate : An open and extensible platform for single-particle tracking» ; Methods **115**, p. 80–90 (2017). ISSN 10959130. 33

[103] C. Wolff, J. Y. Tinevez, T. Pietzsch, E. Stamataki, B. Harich, L. Guignard, S. Preibisch, S. Shorte, P. J. Keller, P. Tomancak & A. Pavlopoulos ; «Multi-view light-sheet imaging and tracking with the MaMuT software reveals the cell lineage of a direct developing arthropod limb» ; eLife **7** (2018). ISSN 2050084X. 33

[104] E. Coudrier, F. Amblard, C. Zimmer, P. Roux, J.-C. Olivo-Marin, M.-C. Rigothier & N. Guillén ; «Myosin II and the Gal-GalNAc lectin play a crucial role in tissue invasion by Entamoeba histolytica.» ; Cellular microbiology **7**, p. 19–27 (2005). ISSN 1462-5814. `http://www.ncbi.nlm.nih.gov/pubmed/15617520`. 33

[105] R. E. Goldstein & J. W. van de Meent ; «A physical perspective on cytoplasmic streaming» ; Interface Focus **5** (2015). ISSN 20428901. 33, 87

[106] B. Nitzsche, V. Bormuth, C. Bräuer, J. Howard, L. Ionov, J. Kerssemakers, T. Korten, C. Leduc, F. Ruhnow & S. Diez ; «Studying kinesin motors by optical 3D-nanometry in gliding motility assays.» ; Methods in cell biology **95**, p. 247–71 (2010). ISSN 0091-679X. `http://www.ncbi.nlm.nih.gov/pubmed/20466139`. 33, 87

[107] P. Vallotton, G. Danuser, S. Bohnet, J. J. Meister & A. B. Verkhovsky ; «Tracking retrograde flow in keratocytes : News from the front» ; Molecular Biology of the Cell **16**, p. 1223–1231 (2005). ISSN 10591524. 33, 88

[108] D. Dabiri ; «Cross-correlation digital particle image velocimetry - A review» ; dans A. S. Freire, A. Liha & B. Breidenthal (rédacteurs), «Turbulencia», p. 155–99 (Rio de Janeiro) (2006). 33

[109] B. K. Horn & B. G. Schunck ; «Determining optical flow» ; Artificial Intelligence **17**, p. 185–203 (1981). ISSN 00043702. `https://linkinghub.elsevier.com/retrieve/pii/0004370281900242`. 33, 44, 125

[110] E. K. Paluch, C. M. Nelson, N. Biais, B. Fabry, J. Moeller, B. L. Pruitt, C. Wollnik, G. Kudryasheva, F. Rehfeldt & W. Federle ; «Mechanotransduction : use the force(s).» ; BMC biology **13**, p. 47 (2015). ISSN 1741-7007. `http://www.ncbi.nlm.nih.gov/pubmed/26141078http://www.pubmedcentral.nih.gov/articlerender.fcgi?artid=PMC4491211`. 34

[111] M. K. L. Han & J. de Rooij ; «Converging and Unique Mechanisms of Mechanotransduction at Adhesion Sites.» ; Trends in cell biology **26**, p. 612–623 (2016). ISSN 1879-3088. `http://www.ncbi.nlm.nih.gov/pubmed/27036655`. 34

[112] C. V. B. de Gusmão & W. D. Belangero ; «HOW DO BONE CELLS SENSE MECHANICAL LOADING ?» ; Revista Brasileira de Ortopedia (English Edition) **44**, p. 299–305 (2009). ISSN 22554971. 34

[113] H. Sackin ; «Stretch-activated ion channels» ; dans «Kidney International», , tome 48p. 1134–1147 (Nature Publishing Group) (1995) ; ISSN 00852538. 34

[114] M. L. Rodriguez, P. J. McGarry & N. J. Sniadecki ; «Review on cell mechanics : Experimental and modeling approaches» ; Applied Mechanics Reviews **65** (2013). ISSN 00036900. 34

[115] J. Brugués, B. Maugis, J. Casademunt, P. Nassoy, F. Amblard & P. Sens ; «Dynamical organization of the cytoskeletal cortex probed by micropipette aspiration» ; Proceedings of the National Academy of Sciences of the United States of America **107**, p. 15 415–15 420 (2010). ISSN 00278424. 34, 36, 77, 120

[116] R. Gómez-Martínez, A. M. Hernández-Pinto, M. Duch, P. Vázquez, K. Zinoviev, E. J. De La Rosa, J. Esteve, T. Suárez & J. A. Plaza ; «Silicon chips detect intracellular pressure changes in living cells» ; Nature Nanotechnology **8**, p. 517–521 (2013). ISSN 17483395. 34

[117] R. J. Petrie & H. Koo ; «Direct measurement of intracellular pressure» ; Current Protocols in Cell Biology (2014). ISSN 19342616. 34

[118] S. M. Kelly & P. T. Macklem ; «Direct measurement of intracellular pressure» ; American Journal of Physiology-Cell Physiology **260**, p. C652–C657 (1991). ISSN 0363-6143. `http://www.physiology.org/doi/10.1152/ajpcell.1991.260.3.C652`. 34

[119] B. H. Blehm, T. A. Schroer, K. M. Trybus, Y. R. Chemla & P. R. Selvin ; «In vivo optical trapping indicates kinesin's stall force is reduced by dynein during intracellular transport» ; Proceedings of the National Academy of Sciences of the United States of America **110**, p. 3381–3386 (2013). ISSN 00278424. 34

[120] F. M. Fazal & S. M. Block ; «Optical tweezers study life under tension» ; (2011). 35

[121] D. Gao, W. Ding, M. Nieto-Vesperinas, X. Ding, M. Rahman, T. Zhang, C. T. Lim & C. W. Qiu ; «Optical manipulation from the microscale to the nanoscale : Fundamentals, advances and prospects» ; Light: Science and Applications **6** (2017). ISSN 20477538. 35

[122] R. J. Adrian ; «Twenty years of particle image velocimetry» ; dans «Experiments in Fluids», , tome 39p. 159–169 (2005) ; ISSN 07234864. 35

[123] A. Mogilner ; «Mathematics of cell motility : Have we got its number ?» ; (2009). 35

[124] R. Lockley, G. Ladds & T. Bretschneider ; «Image based validation of dynamical models for cell reorientation» ; Cytometry Part A **87**, p. 471–480 (2015). ISSN 15524930. 35, 40

[125] R. Niwayama, H. Nagao, T. S. Kitajima, L. Hufnagel, K. Shinohara, T. Higuchi, T. Ishikawa & A. Kimura ; «Bayesian Inference of Forces Causing Cytoplasmic Streaming in Caenorhabditis elegans Embryos and Mouse Oocytes» ; PloS one **11**, p. e0159 917 (2016). ISSN 19326203. 35, 40

[126] O. Du Roure, A. Saez, A. Buguin, R. H. Austin, P. Chavrier, P. Siberzan & B. Ladoux ; «Force mapping in epithelial cell migration» ; Proceedings of the National Academy of Sciences of the United States of America **102**, p. 2390–2395 (2005). ISSN 00278424. 35

[127] H. Delanoë-Ayari, J. P. Rieu & M. Sano ; «4D traction force microscopy reveals asymmetric cortical forces in migrating dictyostelium cells» ; Physical Review Letters **105** (2010). ISSN 00319007. 35

[128] J. C. del Álamo, R. Meili, B. Álvarez-González, B. Alonso-Latorre, E. Bastounis, R. Firtel & J. C. Lasheras ; «Three-Dimensional Quantification of Cellular Traction Forces and Mechanosensing of Thin Substrata by Fourier Traction Force Microscopy» ; PLoS ONE **8** (2013). ISSN 19326203. 35

[129] W. J. Polacheck & C. S. Chen ; «Measuring cell-generated forces : A guide to the available tools» ; (2016). 35

[130] P. Roca-Cusachs, V. Conte & X. Trepat ; «Quantifying forces in cell biology» ; (2017). 35

[131] O. Campàs, T. Mammoto, S. Hasso, R. A. Sperling, D. O'connell, A. G. Bischof, R. Maas, D. A. Weitz, L. Mahadevan & D. E. Ingber ; «Quantifying cell-generated mechanical forces within living embryonic tissues» ; Nature Methods **11**, p. 183–189 (2014). ISSN 15487105. 35

[132] M. Tozluolu, A. L. Tournier, R. P. Jenkins, S. Hooper, P. A. Bates & E. Sahai ; «Matrix geometry determines optimal cancer cell migration strategy and modulates response to interventions» ; Nature Cell Biology **15**, p. 751–762 (2013). ISSN 14657392. 36

[133] O. L. Lewis, S. Zhang, R. D. Guy & C. A. Juan ; «Coordination of contractility, adhesion and flow in migrating Physarum amoebae» ; Journal of the Royal Society Interface **12** (2015)`http://rsif.royalsocietypublishing.org/content/12/106/20141359`. 36, 40, 77

[134] B. Maugis, J. Brugués, P. Nassoy, N. Guillen, P. Sens & F. Amblard ; «Dynamic instability of the intracellular pressure drives bleb-based motility» ; Journal of Cell Science **123**, p. 3884–3892 (2010). ISSN 00219533. 36, 57, 66, 71, 73, 78

[135] C. Rivière, S. Marion, N. Guillén, J. C. Bacri, F. Gazeau & C. Wilhelm ; «Signaling through the phosphatidylinositol 3-kinase regulates mechanotaxis induced by local low magnetic forces in Entamoeba histolytica» ; Journal of Biomechanics **40**, p. 64–77 (2007). ISSN 00219290. 36

[136] S. Marion, N. Guillen, J. C. Bacri & C. Wilhelm ; «Acto-myosin cytoskeleton dependent viscosity and shear-thinning behavior of the amoeba cytoplasm» ; European Biophysics Journal **34**, p. 262–272 (2005). ISSN 01757571. 36, 46, 65, 77, 110, 111, 120

[137] A. L. Cost, P. Ringer, A. Chrostek-Grashoff & C. Grashoff ; «How to Measure Molecular Forces in Cells : A Guide to Evaluating Genetically-Encoded FRET-Based Tension Sensors» ; Cellular and Molecular Bioengineering **8**, p. 96–105 (2015). ISSN 18655033. 36, 126

[138] D. Eder, K. Basler & C. M. Aegerter ; «Challenging FRET-based E-Cadherin force measurements in Drosophila» ; Scientific Reports **7** (2017). ISSN 20452322. 36

[139] L. Hodgson, F. Shen & K. Hahn ; «Biosensors for characterizing the dynamics of Rho family GTPases in living cells» ; Current Protocols in Cell Biology p. 14 111–141 126 (2010). ISSN 19342616. 36

[140] S. Alam, D. B. Lovett, R. B. Dickinson, K. J. Roux & T. P. Lele ; «Nuclear forces and cell mechanosensing.» ; Progress in molecular biology and translational science **126**, p. 205–15 (2014). ISSN 1878-0814. `http://www.ncbi.nlm.nih.gov/pubmed/25081619http://www.pubmedcentral.nih.gov/articlerender.fcgi?artid=PMC4261915`. 36

[141] J. Barrila, A. Crabbé, J. Yang, K. Franco, S. D. Nydam, R. J. Forsyth, R. R. Davis, S. Gangaraju, C. Mark Ott, C. B. Coyne, M. J. Bissell & C. A. Nickerson ; «Modeling host-pathogen interactions in the context of the microenvironment : Three-dimensional cell culture comes of age» ; Infection and Immunity **86** (2018). ISSN 10985522. 36

[142] S. L. Burgess & W. A. Petri ; «The Intestinal Bacterial Microbiome and E. histolytica Infection» ; (2016). 36

[143] N. Guillén ; «The interaction between Entamoeba histolytica and enterobacteria shed light on an ancient antibacterial response» ; (2019). 36

[144] C. A. Nickerson, C. Mark Ott, S. J. Mister, B. J. Morrow, L. Burns-Keliher & D. L. Pierson ; «Microgravity as a novel environmental signal affecting Salmonella enterica serovar Typhimurium virulence» ; Infection and Immunity **68**, p. 3147–3152 (2000). ISSN 00199567. 36

[145] C. P. Ng, B. Hinz & M. A. Swartz ; «Interstitial fluid flow induces myofibroblast differentiation and collagen alignment in vitro» ; Journal of Cell Science **118**, p. 4731–4739 (2005). ISSN 00219533. 36

[146] A. Grassart, V. Malardé, S. Gobaa, A. Sartori-Rupp, J. Kerns, K. Karalis, B. Marteyn, P. Sansonetti & N. Sauvonnet ; «Bioengineered Human Organ-on-Chip Reveals Intestinal Microenvironment and Mechanical Forces Impacting Shigella Infection» ; Cell Host Microbe **26**, p. 435 – 444.e4 (2019). ISSN 1931-3128. `http://www.sciencedirect.com/science/article/pii/S1931312819304160`. 37

[147] C. Bonnans, J. Chou & Z. Werb ; «Remodelling the extracellular matrix in development and disease» ; (2014). 37

[148] R. Thibeaux, A. Dufour, P. Roux, M. Bernier, A. C. Baglin, P. Frileux, J. C. Olivo-Marin, N. Guillén & E. Labruyère ; «Newly visualized fibrillar collagen scaffolds dictate Entamoeba histolytica invasion route in the human colon» ; Cellular Microbiology **14**, p. 609–621 (2012). ISSN 14625814. 37

[149] A. Ravichandran, Y. Liu & S. H. Teoh ; «Review : bioreactor design towards generation of relevant engineered tissues : focus on clinical translation» ; (2018). 37

[150] G. Rossi, A. Manfrin & M. P. Lutolf ; «Progress and potential in organoid research» ; (2018). 37

[151] B. Zhang, A. Korolj, B. F. L. Lai & M. Radisic ; «Advances in organ-on-a-chip engineering» ; (2018). 37

[152] N. Ji, H. Shroff, H. Zhong & E. Betzig ; «Advances in the speed and resolution of light microscopy» ; (2008). 37

[153] B. C. Chen, W. R. Legant, K. Wang, L. Shao, D. E. Milkie, M. W. Davidson, C. Janetopoulos, X. S. Wu, J. A. Hammer, Z. Liu, B. P. English, Y. Mimori-Kiyosue, D. P. Romero, A. T. Ritter, J. Lippincott-Schwartz, L. Fritz-Laylin, R. D. Mullins, D. M. Mitchell, J. N. Bembenek, A. C. Reymann, R. Böhme, S. W. Grill, J. T. Wang, G. Seydoux, U. S. Tulu, D. P. Kiehart & E. Betzig ; «Lattice light-sheet microscopy : Imaging molecules to embryos at high spatiotemporal resolution» ; Science **346** (2014). ISSN 10959203. 37

[154] M. Liebling, A. S. Forouhar, M. Gharib, S. E. Fraser & M. E. Dickinson ; «Four-dimensional cardiac imaging in living embryos via postacquisition synchronization of nongated slice sequences» ; Journal of Biomedical Optics **10**, p. 054 001 (2005). ISSN 10833668. 37

[155] K. G. Chan, S. J. Streichan, L. A. Trinh & M. Liebling ; «Simultaneous Temporal Superresolution and Denoising for Cardiac Fluorescence Microscopy» ; IEEE Transactions on Computational Imaging **2**, p. 348–358 (2016). 37

[156] T. Iskratsch, H. Wolfenson & M. P. Sheetz ; «Appreciating force and shape-the rise of mechanotransduction in cell biology» ; (2014). 37

[157] P. Romani, I. Brian, G. Santinon, A. Pocaterra, M. Audano, S. Pedretti, S. Mathieu, M. Forcato, S. Bicciato, J. B. Manneville, N. Mitro & S. Dupont ; «Extracellular matrix mechanical cues regulate lipid metabolism through Lipin-1 and SREBP» ; Nature Cell Biology **21**, p. 338–347 (2019). ISSN 14764679. 38

[158] T. Bertero, W. M. Oldham, K. A. Cottrill, S. Pisano, R. R. Vanderpool, Q. Yu, J. Zhao, Y. Tai, Y. Tang, Y. Y. Zhang, S. Rehman, M. Sugahara, Z. Qi, J. Gorcsan, S. O. Vargas, R. Saggar, R. Saggar, W. D. Wallace, D. J. Ross, K. J. Haley, A. B. Waxman, V. N. Parikh, T. De Marco, P. Y. Hsue, A. Morris, M. A. Simon, K. A. Norris, C. Gaggioli, J. Loscalzo, J. Fessel & S. Y. Chan ; «Vascular stiffness mechanoactivates YAP/TAZ-dependent glutaminolysis to drive pulmonary hypertension» ; Journal of Clinical Investigation **126**, p. 3313–3335 (2016). ISSN 15588238. 38

[159] A. Tajik, Y. Zhang, F. Wei, J. Sun, Q. Jia, W. Zhou, R. Singh, N. Khanna, A. S. Belmont & N. Wang ; «Transcription upregulation via force-induced direct stretching of chromatin» ; Nature Materials **15**, p. 1287–1296 (2016). ISSN 14764660. 38

[160] A. Boquet-Pujadas, T. Lecomte *et al.* ; «BioFlow : a non-invasive, image-based method to measure speed, pressure and forces inside living cells» ; Scientific Reports **7**, p. 9178 (2017). ISSN 2045-2322. 39, 50, 51, 57, 66, 67, 70, 72, 74, 76

[161] O. Talagrand & P. Courtier ; «Variational Assimilation of Meteorological Observations With the Adjoint Vorticity Equation. I : Theory» ; Quarterly Journal of the Royal Meteorological Society **113**, p. 1311–1328 (1987). ISSN 00359009. `http://doi.wiley.com/10.1002/qj.49711347812`. 40, 54

[162] F. De Chaumont, S. Dallongeville, N. Chenouard, N. Hervé, S. Pop, T. Provoost, V. Meas-Yedid, P. Pankajakshan, T. Lecomte, Y. Le Montagner, T. Lagache, A. Dufour & J. C. Olivo-Marin ; «Icy : An open bioimage informatics platform for extended reproducible research» ; (2012). 40, 61

[163] D. Vig, A. Hamby *et al.* ; «On the Quantification of Cellular Velocity Fields» ; Biophysical Journal **110**, p. 1469–1475 (2016). ISSN 0006-3495. 42, 88, 127

[164] C. N. Holenstein, U. Silvan & J. G. Snedeker ; «High-resolution traction force microscopy on small focal adhesions-Improved accuracy through optimal marker distribution and optical flow tracking» ; Scientific Reports **7** (2017). ISSN 20452322. 42, 127

[165] S. Negahdaripour & C.-H. Yu ; «A generalized brightness change model for computing optical flow» ; dans «1993 (4th) International Conference on Computer Vision», p. 2–11 (IEEE Computer Society Press) ; ISBN 0-8186-3870-2. `http://ieeexplore.ieee.org/document/378241/`. 43, 122

[166] M. Mattavelli & A. Nicoulin ; «Motion estimation relaxing the constancy brightness constraint» ; dans «Proceedings - International Conference on Image Processing, ICIP», , tome 2p. 770–774 (IEEE Computer Society) (1994) ; ISSN 15224880. 43

[167] T. Corpetti, E. Mémin & P. Pérez ; «Adaptation of standard optic methods to fluid motion» ; dans «Int. Symposium on Flow Visualization», paper 62 ; p. 1–10 (Edinburgh, Scotland) (2000). 43

[168] T. Corpetti, E. Mémin & P. Pérez ; «Estimating fluid optical flow» ; dans «IAPR Int. Conf. on Pattern Recognition, ICPR 2000», , tome 3p. 1045–1049 (Barcelone, Espagne) (2000). 44

[169] T. Corpetti, É. Mémin & P. Pérez ; «Dense estimation of fluid flows» ; IEEE Transactions on Pattern Analysis and Machine Intelligence **24**, p. 365–380 (2002). ISSN 01628828. 44, 122

[170] T. G. Laure Blanc-Feraud, Michel Barlaud ; «Motion estimation involving discontinuities in multiresolution scheme» ; Optical Engineering **32**, p. 1475 – 1482 – 8 (1993). `https://doi.org/10.1117/12.138647`. 44

[171] R. Deriche, P. Kornprobst & G. Aubert ; «Optical-flow estimation while preserving its discontinuities : A variational approach» ; dans S. Z. Li, D. P. Mital, E. K. Teoh & H. Wang (rédacteurs), «Recent Developments in Computer Vision», p. 69–80 (Springer Berlin Heidelberg, Berlin, Heidelberg) (1996) ; ISBN 978-3-540-49448-5. 44

[172] G. Aubert & P. Kornprobst ; «A Mathematical Study of the Relaxed Optical Flow Problem in the Space BV()» ; SIAM J. MATH. ANAL **30**, p. 1282–1308 (1999). 44

[173] D. Heitz, E. Mémin & C. Schnörr ; «Variational fluid flow measurements from image sequences : Synopsis and perspectives» ; Experiments in Fluids **48**, p. 369–393 (2010). ISSN 07234864. 44

[174] P. Héas, E. Mémin, N. Papadakis & A. Szantai ; «Layered estimation of atmospheric mesoscale dynamics from satellite imagery» ; dans «IEEE Transactions on Geoscience and Remote Sensing», , tome 45p. 4087–4104 (2007) ; ISSN 01962892. 44, 125

[175] P. Ruhnau, A. Stahl & C. Schnörr ; «Variational estimation of experimental fluid flows with physics-based spatio-temporal regularization» ; Measurement Science and Technology **18**, p. 755–763 (2007). ISSN 13616501. 44, 125

[176] M. D. Gunzberger ; *Perspectives in Flow Control and Optimization (Advances in Design and Control)* (2003) ; ISBN 978-0898715279. 44, 52

[177] S. Marion, C. Wilhelm, H. Voigt, J.-C. Bacri & N. Guillén ; «Overexpression of myosin IB in living Entamoeba histolytica enhances cytoplasm viscosity and reduces phagocytosis.» ; Journal of cell science **117**, p. 3271–3279 (2004). ISSN 0021-9533. 46

[178] L. D. L. D. Landau, E. M. E. M. Lifshits, A. M. Kosevich & L. P. L. P. Pitaevskii ; *Theory of elasticity* (Butterworth-Heinemann) (1986) ; ISBN 9780750626330. 50, 127, 130, 131

[179] D. J. Tritton ; *Physical Fluid Dynamics* (Springer, Dordrecht) (1977). `http://www.springerlink.com/index/10.1007/978-94-009-9992-3{_}1`. 50

[180] F. Brezzi ; «On the existence, uniqueness and approximation of saddle-point problems arising from lagrangian multipliers» ; ESAIM : Mathematical Modelling and Numerical Analysis **8**, p. 129–51 (1974). 53

[181] F.-J. Sayas ; «A gentle introduction to the Finite Element Method» ; Rapport technique (2015). 53, 140

[182] V. Girault & P.-A. Raviart ; *Finite Element Methods for Navier-Stokes Equations : theory and algorithms* (Springer) (1986) ; ISBN 978-3-642-61623-5. 53

[183] C. Taylor & P. Hood ; «A numerical solution of the Navier-Stokes equations using the finite element technique» ; Computers & Fluids **1**, p. 73–100 (1973). ISSN 00457930. 53

[184] A. Logg & G. N. Wells ; «DOLFIN : Automated Finite Element Computing» ; ACM Trans. Math. Soft. **37** (2010). ISSN 0098-3500. 54, 93, 117

[185] A. Logg, K.-A. Mardal & G. Wells ; «Automated solution of differential equations by the finite element method – the FEniCS book» ; (2012). `http://dx.doi.org/10.1007/978-3-642-23099-8`. 54, 62, 91, 140, 148

[186] M. B. Giles & N. A. Pierce ; «An introduction to the adjoint approach to design» ; Flow, Turbulence and Combustion **65**, p. 393–415 (2000). ISSN 13866184. 54, 181

[187] P. Farrell, D. Ham, S. Funke & M. Rognes ; «Automated derivation of the adjoint of high-level transient finite element programs» ; SIAM Journal on Scientific Computing **35**, p. C369–C393 (2013). ISSN 1064-8275. `http://arxiv.org/abs/1204.5577`. 55, 119, 181

[188] S. W. Funke & P. E. Farrell ; «A framework for automated PDE-constrained optimisation» ; CoRR **abs/1302.3894** (2013)`http://arxiv.org/abs/1302.3894` ; 1302.3894. 55, 119, 181

[189] N. Papenberg, A. Bruhn, T. Brox, S. Didas & J. Weickert ; «Highly Accurate Optic Flow Computation with Theoretically Justified Warping» ; International Journal of Computer Vision **67**, p. 141–158 (2006). 56, 125, 147

[190] H. Zimmer, A. Bruhn & J. Weickert ; «Optic flow in harmony» ; International Journal of Computer Vision **93**, p. 368–388 (2011). ISSN 09205691. 57, 125

[191] R. P. Brent ; *Algorithms for Minimization Without Derivatives* (Dover Books) (2013). 57

[192] D. Mumford & J. Shah ; «Optimal approximations by piecewise smooth functions and associated variational problems» ; Communications on Pure and Applied Mathematics **42**, p. 577–685 (1989). ISSN 00103640. `http://doi.wiley.com/10.1002/cpa.3160420503`. 58

[193] V. Caselles, R. Kimmel & G. Sapiro ; «Geodesic Active Contours» ; International Journal of Computer Vision **22**, p. 61–79 (1997). ISSN 09205691. 58

[194] M. Kass, A. Witkin & D. Terzopoulos ; «Snakes : Active contour models» ; (1988). 59

[195] C. Zimmer & S. Member ; «Coupled Parametric Active Contours» ; IEEE Transactions on Pattern Analysis and Machine Intelligence **27**, p. 1838–1842 (2005). 59

[196] T. F. Chan, S. Esedoglu & M. Nikolova ; «Algorithms for finding global minimizers of image segmentation and denoising models» ; SIAM Journal on Applied Mathematics **66**, p. 1632–1648 (2006). ISSN 00361399. 59

[197] E. S. Brown, T. F. Chan & X. Bresson ; «Completely convex formulation of the Chan-Vese image segmentation model» ; International Journal of Computer Vision **98**, p. 103–121 (2012). ISSN 09205691. 59

[198] L. Rineau & M. Yvinec ; «A generic software design for Delaunay refinement meshing» ; Computational Geometry: Theory and Applications **38**, p. 100–110 (2007). ISSN 09257721. 59, 147

[199] J. Ruppert ; «A delaunay refinement algorithm for quality 2-dimensional mesh generation» ; Journal of Algorithms **18**, p. 548–585 (1995). ISSN 01966774. 59

[200] J. R. Shewchuk ; «What is a Good Linear Element ? Interpolation, Conditioning, and Quality Measures» ; Proceedings of the 11th International Meshing Roundtable (2002)ISSN 1130-1473. 59, 92

[201] L. Chen ; «MESH SMOOTHING SCHEMES BASED ON OPTIMAL DELAUNAY TRIANGULATIONS» ; Rapport technique. 59

[202] P. Alliez, D. Cohen-Steiner, M. Yvinec & M. Desbrun ; «Variational tetrahedral meshing» ; dans «ACM SIGGRAPH 2005 Papers on - SIGGRAPH '05», p. 617 (ACM Press, New York, New York, USA) (2005). `http://portal.acm.org/citation.cfm?doid=1186822.1073238`. 59

[203] J. Tournois, C. Wormser, P. Alliez & M. Desbrun ; «Interleaving Delaunay refinement and optimization for practical isotropic tetrahedron mesh generation» ; dans «ACM SIGGRAPH 2009 papers on - SIGGRAPH '09», p. 1 (ACM Press, New York, New York, USA) (2009) ; ISBN 9781605587264. `http://portal.acm.org/citation.cfm?doid=1576246.1531381`. 59

[204] S.-W. Cheng, T. K. Dey, H. Edelsbrunner, M. A. Facello & S.-H. Teng ; «Sliver exudation» ; dans «Proceedings of the fifteenth annual symposium on Computational geometry - SCG '99», p. 1–13 (ACM Press, New York, New York, USA) (1999) ; ISBN 1581130686. `http://portal.acm.org/citation.cfm?doid=304893.304894`. 59

[205] D. Cohen-Steiner, P. Alliez & M. Desbrun ; «Variational shape approximation» ; dans «ACM SIGGRAPH 2004 Papers, SIGGRAPH 2004», p. 905–914 (2004). 59, 61, 149

[206] S. P. Lloyd ; «Least Squares Quantization in PCM» ; IEEE Transactions on Information Theory **28**, p. 129–137 (1982). ISSN 15579654. 61, 147

[207] A. Dufour, V. Meas-Yedid & J.-C. Olivo-Marin ; «Automated quantification of cell endocytosis using active contours and wavelets» ; dans «IAPR International Conference on Pattern Recognition», (Tampa, FL, USA) (2008). 61

[208] S. van der Walt, S. C. Colbert & G. Varoquaux ; «The NumPy Array : A Structure for Efficient Numerical Computation» ; Computing in Science & Engineering **13**, p. 22–30 (2011). ISSN 1521-9615. 62, 93, 148

[209] T. E. Oliphant ; «Python for Scientific Computing» ; Computing in Science & Engineering **9**, p. 10–20 (2007). ISSN 1521-9615. 62, 93, 148

[210] A. Fabri & S. Pion ; «CGAL : The Computational Geometry Algorithms Library» ; dans «Proceedings of the 17th ACM SIGSPATIAL International Conference on Advances in Geographic Information Systems», p. 538–539 (ACM, New York, NY, USA) (2009) ; ISBN 978-1-60558-649-6. 62, 92, 148, 150

[211] S. Balay, W. D. Gropp, L. C. McInnes & B. F. Smith ; «Efficient Management of Parallelism in Object Oriented Numerical Software Libraries» ; dans E. Arge, A. M. Bruaset & H. P. Langtangen (rédacteurs), «Modern Software Tools in Scientific Computing», p. 163–202 (Birkhäuser Press) (1997). 62

[212] S. Balay, S. Abhyankar, M. Adams, J. Brown, P. B. Buschelman, Kris, L. Dalcin, A. Dener, V. Eijkhout, W. G. Karpeyev, Dmitry, D. Kaushik, M. Knepley, D. May, L. C. M. Mills, R. Tran, T. Munson, K. Rupp, P. S. Smith, Barry˜F., S. Zampini, H. Zhang & H. Zhang ; «PETSc Users Manual» ; Rapport technique ANL-95/11 - Revision 3.11 ; Argonne National Laboratory (2019). `https://www.mcs.anl.gov/petsc`. 62, 148

[213] S. Balay, S. Abhyankar, M. Adams, J. Brown, P. B. Buschelman, Kris, L. Dalcin, A. Dener, V. Eijkhout, W. G. Karpeyev, Dmitry, D. Kaushik, M. Knepley, D. May, L. C. M. Mills, R. Tran, T. Munson, K. Rupp, P. S. Smith, Barry˜F., S. Zampini, H. Zhang & H. Zhang ; «PETSc Web page» ; https ://www.mcs.anl.gov/petsc (2019). `https://www.mcs.anl.gov/petsc`. 62

[214] B. He, K. Doubrovinski, O. Polyakov & E. Wieschaus ; «Apical constriction drives tissue-scale hydrodynamic flow to mediate cell elongation.» ; Nature **508**, p. 392–6 (2014). ISSN 1476-4687. `http://www.ncbi.nlm.nih.gov/pubmed/24590071`. 65

[215] J. G. Goetz, E. Steed, R. R. Ferreira, S. Roth, C. Ramspacher, F. Boselli, G. Charvin, M. Liebling, C. Wyart, Y. Schwab & J. Vermot ; «Endothelial cilia mediate low flow sensing during zebrafish vascular development» ; Cell Reports **6**, p. 799–808 (2014). ISSN 22111247. 65

[216] T. Nozaki & A. Bhattacharya ; *Amebiasis. Biology and Pathogenesis of Entamoeba* (Springer) (2015) ; ISBN 978-4-431-55200-0. 66

[217] L. Vayssié, M. Vargas, C. Weber & N. Guillén ; «Double-stranded RNA mediates homology-dependant gene silencing of γ-tubulin in the human parasite Entamoeba histolytica» ; Molecular and Biochemical Parasitology **138**, p. 21–28 (2004). ISSN 01666851. 66

[218] C. G. Clark, U. C. M. Alsmark, M. Tazreiter, Y. Saito-Nakano, V. Ali, S. Marion, C. Weber, C. Mukherjee, I. Bruchhaus, E. Tannich, M. Leippe, T. Sicheritz-Ponten, P. G. Foster, J. Samuelson, C. J. Noël, R. P. Hirt, T. M. Embley, C. A. Gilchrist, B. J. Mann, U. Singh, J. P. Ackers, S. Bhattacharya, A. Bhattacharya, A. Lohia, N. Guillén, M. Duchêne, T. Nozaki & N. Hall ; «Structure and Content of the Entamoeba histolytica Genome» ; Advances in Parasitology **65**, p. 51–190 (2007). ISSN 0065308X. 66

[219] R. D. Allen & N. Kamiya (rédacteurs) ; *Primitive Motile Systems in Cell Biology* (Elsevier Academic Press) (1964) ; ISBN 9780323161428. `http://www.sciencedirect.com/science/book/9780123956811`. 66

[220] K. Matsumoto, S. Takagi & T. Nakagaki ; «Locomotive mechanism of Physarum plasmodia based on spatiotemporal analysis of protoplasmic streaming.» ; Biophysical journal **94**, p. 2492–504 (2008). ISSN 1542-0086. `http://www.pubmedcentral.nih.gov/articlerender.fcgi?artid=2267142&tool=pmcentrez&rendertype=abstract`. 66

[221] H. Keller & P. Eggli ; «Protrusive activity, cytoplasmic compartmentalization, and restriction rings in locomoting blebbing walker carcinosarcoma cells are related to detachment of cortical actin from the plasma membrane» ; Cell Motility and the Cytoskeleton **41**, p. 181–193 (1998). ISSN 08861544. 66

[222] J. V. Small, T. Stradal, E. Vignal & K. Rottner ; «The lamellipodium : Where motility begins» ; Trends in Cell Biology **12**, p. 112–120 (2002). ISSN 09628924. 66

[223] F. Y. Lim, Y. L. Koon & K.-H. Chiam ; «A computational model of amoeboid cell migration.» ; Computer methods in biomechanics and biomedical engineering **16**, p. 1085–95 (2013). ISSN 1476-8259. `http://www.ncbi.nlm.nih.gov/pubmed/23342988`. 66, 68

[224] A. Taloni, E. Kardash, O. U. Salman, S. Zapperi & C. a. M. L. Porta ; «Volume changes during active shape fluctuations in cells» ; Physical Review Letters **114**, p. 1–12 (2015). ISSN 0031-9007. 66, 83, 85

[225] W. Strychalski & R. D. Guy ; «Intracellular pressure dynamics in blebbing cells» ; Biophysical journal **110**, p. 1168–79 (2016). ISSN 15420086. `http://dx.doi.org/10.1016/j.bpj.2016.01.012`. 66

[226] J. F. Casella, M. D. Flanagan & S. Lin ; «Cytochalasin D inhibits actin polymerization and induces depolymerization of actin filaments formed during platelet shape change» ; Nature **293**, p. 302–5 (1981). 66

[227] U. S. Schwarz, N. Q. Balaban, D. Riveline, A. Bershadsky, B. Geiger & S. A. Safran ; «Calculation of Forces at Focal Adhesions from Elastic Substrate Data : The Effect of Localized Force and the Need for Regularization» ; Biophysical Journal **83**, p. 1380–1394 (2002). ISSN 0006-3495. `http://dx.doi.org/10.1016/S0006-3495(02)73909-X`. 68

[228] C. Franck, S. a. Maskarinec, D. a. Tirrell & G. Ravichandran ; «Three-dimensional traction force microscopy : a new tool for quantifying cell-matrix interactions.» ; PloS one **6**, p. e17 833 (2011). ISSN 1932-6203. `http://www.pubmedcentral.nih.gov/articlerender.fcgi?artid=3066163&tool=pmcentrez&rendertype=abstract`. 68

[229] J. R. D. Soiné, C. a. Brand, J. Stricker, P. W. Oakes, M. L. Gardel & U. S. Schwarz ; «Model-based Traction Force Microscopy Reveals Differential Tension in Cellular Actin Bundles» ; PLOS Computational Biology **11**, p. e1004 076 (2015). ISSN 1553-7358. `http://dx.plos.org/10.1371/journal.pcbi.1004076`. 68, 127, 128, 129, 146

[230] O. C. Zienkiewicz, R. L. Taylor & P. Nithiarasu ; «Biofluid Dynamics» ; dans «The Finite Element Method for Fluid Dynamics», 7^{e} édition ; chapitre 14, p. 451–84 (Elsevier) (2014). 71

[231] S. Butterworth ; «On the Theory of Filter Amplifiers» ; Wireless Engineer **7**, p. 536–541 (1930). 73

[232] N. Morone, T. Fujiwara, K. Murase, R. S. Kasai, H. Ike, S. Yuasa, J. Usukura & A. Kusumi ; «Three-dimensional reconstruction of the membrane skeleton at the plasma membrane interface by electron tomography» ; Journal of Cell Biology **174**, p. 851–862 (2006). ISSN 00219525. 77

[233] K. Aoki, F. Maeda, T. Nagasako, Y. Mochizuki, S. Uchida & J. Ikenouchi ; «A RhoA and Rnd3 cycle regulates actin reassembly during membrane blebbing.» ; Proceedings of the National Academy of Sciences of the United States of America **113**, p. 1863–71 (2016). ISSN 1091-6490. `http://www.pnas.org/content/113/13/E1863.full`. 77

[234] R. Bharadwaj, R. Arya, M. Shahid mansuri, S. Bhattacharya & A. Bhattacharya ; «EhRho1 regulates plasma membrane blebbing through PI3 kinase in Entamoeba histolytica» ; Cellular Microbiology **19** (2017). ISSN 14625822. 77

[235] K. Tarbashevich, M. Reichman-Fried, C. Grimaldi & E. Raz ; «Chemokine-dependent pH elevation at the cell front sustains polarity in directionally migrating zebrafish germ cells» ; Current Biology **25**, p. 1096–1103 (2015). ISSN 09609822. 77

[236] H. Blaser, M. Reichman-Fried, I. Castanon, K. Dumstrei, F. Marlow, K. Kawakami, L. Solnica-Krezel, C. P. Heisenberg & E. Raz ; «Migration of Zebrafish Primordial Germ Cells : A Role for Myosin Contraction and Cytoplasmic Flow» ; Developmental Cell **11**, p. 613–627 (2006). ISSN 15345807. 77, 87

[237] G. I. Taylor ; «Stability of a Viscous Liquid Contained between Two Rotating Cylinders» ; Proceedings of the Royal Society A: Mathematical, Physical and Engineering Sciences **102**, p. 541–542 (1923). ISSN 1364-5021. `http://rspa.royalsocietypublishing.org/cgi/doi/10.1098/rspa.1923.0013`. 78, 110

[238] M. Goudarzi, A. Boquet-Pujadas *et al.* ; «Fluid dynamics during bleb formation in migrating cells in vivo» ; PLoS ONE **14** (2019)ISSN 19326203 (ISSN). 79, 83, 84, 85, 87

[239] J. C. Butcher ; «A history of Runge-Kutta methods» ; Applied Numerical Mathematics **20**, p. 247–260 (1996). ISSN 0168-9274. 81

[240] M. Köprunner, C. Thisse, B. Thisse & E. Raz ; «A zebrafish nanos-related gene is essential for the development of primordial germ cells» ; Genes & Development **15**, p. 2877–2885 (2001). ISSN 0890-9369. 84

[241] K. Tarbashevich, M. Reichman-Fried, C. Grimaldi & E. Raz ; «Chemokine-dependent pH elevation at the cell front sustains polarity in directionally migrating zebrafish germ cells» ; Current Biology **25**, p. 1096–1103 (2015). ISSN 09609822. 84

[242] H. Blaser, S. Eisenbeiss, M. Neumann, M. Reichman-Fried, B. Thisse, C. Thisse & E. Raz ; «Transition from non-motile behaviour to directed migration during early PGC development in zebrafish» ; Journal of Cell Science **118**, p. 4027–4038 (2005). ISSN 00219533. 85

[243] M. Goudarzi, K. Tarbashevich, K. Mildner, I. Begemann, J. Garcia, A. Paksa, M. Reichman-Fried, H. Mahabaleshwar, H. Blaser, J. Hartwig, D. Zeuschner, M. Galic, M. Bagnat, T. Betz & E. Raz ; «Bleb Expansion in Migrating Cells Depends on Supply of Membrane from Cell Surface Invaginations» ; Developmental Cell **43**, p. 577–587.e5 (2017). ISSN 18781551. 85

[244] A. Boquet-Pujadas, C. Grimaldi, E. Raz & J. Olivo-Marin ; «Tracking and line integration of diffuse cellular subdomains by mesh advection» ; dans «Proc. IEEE Eng. Med. Biol. Soc. (EMBC)», p. 6018–6021 (2019). 87, 88, 91, 93

[245] M. Mittasch, P. Gross *et al.* ; «Non-invasive perturbations of intracellular flow reveal physical principles of cell organization» ; Nature Cell Biology **20**, p. 344–351 (2018). ISSN 1476-4679. 87

[246] N. Chenouard, I. Smal, F. De Chaumont, M. Mavska, I. F. Sbalzarini, Y. Gong, J. Cardinale, C. Carthel, S. Coraluppi, M. Winter, A. R. Cohen, W. J. Godinez, K. Rohr, Y. Kalaidzidis, L. Liang, J. Duncan, H. Shen, Y. Xu, K. E. Magnusson, J. Jaldén, H. M. Blau, P. Paul-Gilloteaux, P. Roudot, C. Kervrann, F. Waharte, J. Y. Tinevez, S. L. Shorte, J. Willemse, K. Celler, G. P. Van Wezel, H. W. Dan, Y. S. Tsai, C. O. De Solórzano, J. C. Olivo-Marin & E. Meijering ; «Objective comparison of particle tracking methods» ; Nature Methods **11**, p. 281–289 (2014). ISSN 15487091. 88

[247] O. Sorkine, D. Cohen-Or *et al.*; «Laplacian Surface Editing»; dans «Proceedings of the 2004 Eurographics/ACM SIGGRAPH Symposium on Geometry Processing», p. 175–184 (ACM, NY, USA) (2004); ISBN 3-905673-13-4. 93

[248] I. E. Sutherland & G. W. Hodgman; «Reentrant Polygon Clipping»; Commun. ACM **17**, p. 32–42 (1974). ISSN 0001-0782. 93

[249] M. S. Alnaes, J. Blechta *et al.*; «The FEniCS Project Version 1.5»; Archive of Numerical Software **3** (2015). 93

[250] E. Kardash, M. Reichman-Fried *et al.*; «A role for Rho GTPases and cell–cell adhesion in single-cell motility in vivo»; Nature Cell Biology **12**, p. 47 (2009). 94, 95, 96

[251] M. Doitsidou, M. Reichman-Fried, J. Stebler, M. Köprunner, J. Dörries, D. Meyer, C. V. Esguerra, T. Leung & E. Raz; «Guidance of Primordial Germ Cell Migration by the Chemokine SDF-1»; Cell **111**, p. 647 – 659 (2002). ISSN 0092-8674. `http://www.sciencedirect.com/science/article/pii/S0092867402011352`. 95

[252] M. Reichman-Fried, S. Minina & E. Raz; «Autonomous Modes of Behavior in Primordial Germ Cell Migration»; Developmental Cell **6**, p. 589 – 596 (2004). ISSN 1534-5807. `http://www.sciencedirect.com/science/article/pii/S1534580704000747`. 95

[253] P. G. DE GENNES & J. PROST; *The Physics of Liquid Crystals*; 2e édition (1993). 98, 101

[254] A. Doostmohammadi, J. Ignés-Mullol, J. M. Yeomans & F. Sagués; «Active nematics»; (2018). 98, 99, 100

[255] H. Gruler, U. Dewald & M. Eberhardt; «Nematic liquid crystals formed by living amoeboid cells»; The European Physical Journal B **11**, p. 187 (1999). ISSN 14346028. `http://link.springer.de/link/service/journals/10051/bibs/9011001/90110187.htm`. 98

[256] R. Kemkemer, D. Kling, D. Kaufmann & H. Gruler; «Elastic properties of nematoid arrangements formed by amoeboid cells»; The European Physical Journal E **1**, p. 215 (2000). ISSN 12928941. `http://link.springer.com/10.1007/s101890050024`. 98

[257] D. Volfson, S. Cookson, J. Hasty & L. S. Tsimring; «Biomechanical ordering of dense cell populations»; Proceedings of the National Academy of Sciences of the United States of America **105**, p. 15 346–15 351 (2008). ISSN 00278424. 99

[258] A. Doostmohammadi, M. F. Adamer, S. P. Thampi & J. M. Yeomans; «Stabilization of active matter by flow-vortex lattices and defect ordering»; Nature Communications **7** (2016). ISSN 20411723. 99, 100

[259] T. B. Saw, A. Doostmohammadi, V. Nier, L. Kocgozlu, S. Thampi, Y. Toyama, P. Marcq, C. T. Lim, J. M. Yeomans & B. Ladoux; «Topological defects in epithelia govern cell death and extrusion»; Nature **544**, p. 212–216 (2017). ISSN 14764687. 99

[260] F. J. Nédélec, T. Surrey, A. C. Maggs & S. Leibler; «Self-organization of microtubules and motors»; Nature **389**, p. 305–308 (1997). ISSN 00280836. 99

[261] T. Sanchez, D. T. Chen, S. J. Decamp, M. Heymann & Z. Dogic ; «Spontaneous motion in hierarchically assembled active matter» ; Nature **491**, p. 431–434 (2012). ISSN 00280836. 99

[262] G. Henkin, S. J. DeCamp, D. T. Chen, T. Sanchez & Z. Dogic ; «Tunable dynamics of microtubule-based active isotropic gels» ; Philosophical Transactions of the Royal Society A: Mathematical, Physical and Engineering Sciences **372** (2014). ISSN 1364503X. 99

[263] P. Guillamat, J. Ignés-Mullol & F. Sagués ; «Taming active turbulence with patterned soft interfaces» ; Nature Communications **8** (2017). ISSN 20411723. 99, 100

[264] S. Ramaswamy & M. Rao ; «Active-filament hydrodynamics : instabilities, boundary conditions and rheology» ; New Journal of Physics **9**, p. 423–423 (2007). 99

[265] R. Aditi Simha & S. Ramaswamy ; «Hydrodynamic Fluctuations and Instabilities in Ordered Suspensions of Self-Propelled Particles» ; Phys. Rev. Lett. **89**, p. 058 101 (2002). `https://link.aps.org/doi/10.1103/PhysRevLett.89.058101`. 99

[266] R. Voituriez, J. F. Joanny & J. Prost ; «Spontaneous flow transition in active polar gels» ; Europhysics Letters **70**, p. 404–410 (2005). ISSN 02955075. 99

[267] L. Giomi, M. J. Bowick, X. Ma & M. C. Marchetti ; «Defect annihilation and proliferation in active Nematics» ; Physical Review Letters **110** (2013). ISSN 00319007. 99

[268] P. Guillamat, J. Ignés-Mullol, S. Shankar, M. C. Marchetti & F. Sagués ; «Probing the shear viscosity of an active nematic film» ; Physical Review E **94** (2016). ISSN 24700053. 100

[269] A. Opathalage, M. M. Norton, M. P. N. Juniper, B. Langeslay, S. A. Aghvami, S. Fraden & Z. Dogic ; «Self-organized dynamics and the transition to turbulence of confined active nematics» ; Proceedings of the National Academy of Sciences **116**, p. 4788–4797 (2019). ISSN 0027-8424. `https://www.pnas.org/content/116/11/4788` ; `https://www.pnas.org/content/116/11/4788.full.pdf`. 100, 103

[270] D. Marenduzzo, E. Orlandini & J. M. Yeomans ; «Hydrodynamics and rheology of active liquid crystals : A numerical investigation» ; Physical Review Letters **98** (2007). ISSN 00319007. 100

[271] P. W. Ellis, D. J. Pearce, Y. W. Chang, G. Goldsztein, L. Giomi & A. Fernandez-Nieves ; «Curvature-induced defect unbinding and dynamics in active nematic toroids» ; Nature Physics **14**, p. 85–90 (2018). ISSN 17452481. 101

[272] J. Weickert ; «Coherence-Enhancing Diffusion Filtering» ; International Journal of Computer Vision **31**, p. 111–127 (1999). `http://link.springer.com/10.1023/A:1008009714131`. 101

[273] P. Kelly ; «Engineering Solid Mechanics» ; dans «Mechanics Lecture Notes», chapitre Plate theory (University of Auckland, Auckland) (2018). 105

[274] S. Wiggins ; *Normally hyperbolic invariant manifolds in dynamical systems* (Springer-Verlag) (1994) ; ISBN 9780387942056. 105

[275] S. C. Shadden ; «Lagrangian Coherent Structures» ; dans «Transport and Mixing in Laminar Flows : From Microfluidics to Oceanic Currents», p. 59–89 (Wiley-VCH) (2011) ; ISBN 9783527410118. 105

[276] S. C. Shadden, F. Lekien & J. E. Marsden ; «Definition and properties of Lagrangian coherent structures from finite-time Lyapunov exponents in two-dimensional aperiodic flows» ; Physica D: Nonlinear Phenomena **212**, p. 271–304 (2005). ISSN 01672789. 107

[277] S. Hendabadi, J. Bermejo, Y. Benito, R. Yotti, F. Fernández-Avilés, J. C. del Álamo & S. C. Shadden ; «Topology of Blood Transport in the Human Left Ventricle by Novel Processing of Doppler Echocardiography» ; Annals of Biomedical Engineering **41**, p. 2603–2616 (2013). ISSN 1573-9686. `https://doi.org/10.1007/s10439-013-0853-z`. 107

[278] A. Morozov & S. E. Spagnolie ; «Introduction to Complex Fluids» ; dans «Complex Fluids in Biological Systems», p. 3–52 (2015). 108, 119

[279] R. D. Guy & B. Thomases ; «Computational Challenges for Simulating Strongly Elastic Flows in Biology» ; dans «Complex Fluids in Biological Systems», p. 359–397 (2015). 108, 111

[280] R. G. Owens & T. N. Phillips ; *Computational Rheology* (PUBLISHED BY IMPERIAL COLLEGE PRESS AND DISTRIBUTED BY WORLD SCIENTIFIC PUBLISHING CO.) (2002). 109, 114, 117

[281] F. P. Baaijens ; «Mixed finite element methods for viscoelastic flow analysis : A review» ; Journal of Non-Newtonian Fluid Mechanics **79**, p. 361–385 (1998). ISSN 03770257. 109

[282] A. R. Terrel & University of Chicago. ; *Finite element method automation for non-Newtonian fluid models.* (2010) ; ISBN 9781124198125. 109

[283] R. Guénette & M. Fortin ; «A new mixed finite element method for computing viscoelastic flows» ; Journal of Non-Newtonian Fluid Mechanics **60**, p. 27–52 (1995). ISSN 03770257. 109, 112

[284] W. Feneberg, M. Westphal & E. Sackmann ; «Dictyostelium cells' cytoplasm as an active viscoplastic body.» ; European biophysics journal : EBJ **30**, p. 284–94 (2001)ISSN 0175-7571. `http://www.ncbi.nlm.nih.gov/pubmed/11548131`. 110, 111

[285] J. F. Berret ; «Local viscoelasticity of living cells measured by rotational magnetic spectroscopy» ; Nature Communications **7**, p. 10 134 EP – (2016)`https://doi.org/10.1038/ncomms10134`. 110

[286] J. Oldroyd ; «On the formulation of rheological equations of state» ; Proceedings of the Royal Society of London. Series A. Mathematical and Physical Sciences **200**, p. 523–541 (1950). ISSN 2053-9169. 111

[287] J. M. Marchal & M. J. Crochet ; «A new mixed finite element for calculating viscoelastic flow» ; Journal of Non-Newtonian Fluid Mechanics **26**, p. 77–114 (1987). ISSN 03770257. 114

[288] M. J. Crochet & V. Legat ; «The consistent streamline-upwind/Petrov-Galerkin method for viscoelastic flow revisited» ; Journal of Non-Newtonian Fluid Mechanics **42**, p. 283–299 (1992). ISSN 03770257. 114

[289] M. J. Crochet, V. Delvaux & J. M. Marchal ; «On the convergence of the streamline-upwind mixed finite element» ; Journal of Non-Newtonian Fluid Mechanics **34**, p. 261–268 (1990). ISSN 03770257. 114

[290] X. L. Luo & R. I. Tanner ; «A decoupled finite element streamline-upwind scheme for viscoelastic flow problems» ; Journal of Non-Newtonian Fluid Mechanics **31**, p. 143–162 (1989). ISSN 03770257. 114

[291] R. I. Tanner & H. Jin ; «A study of some numerical viscoelastic schemes» ; Journal of Non-Newtonian Fluid Mechanics **41**, p. 171–196 (1991). ISSN 03770257. 114

[292] J. Baranger, D. Sandri & L. Baranger ; «A FORMULATION OF STOKES'S PROBLEM AND THE LINEAR ELASTICITY EQUATIONS SUGGESTED BY THE OLDROYD MODEL FOR VISCOELASTIC FLOW» ; Rapport technique. `http://www.numdam.org/`. 114

[293] M. Fortin & R. Pierre ; «On the convergence of the mixed method of Crochet and Marchal for viscoelastic flows» ; Computer Methods in Applied Mechanics and Engineering **73**, p. 341–350 (1989). ISSN 00457825. 114, 115

[294] M. G. N. Perera & K. Walters ; «Long-range memory effects in flows involving abrupt changes in geometry. Part I : flows associated with I-shaped and T-shaped geometries» ; Journal of Non-Newtonian Fluid Mechanics **2**, p. 49–81 (1977). ISSN 03770257. 114

[295] M. A. Mendelson, P. W. Yeh, R. A. Brown & R. C. Armstrong ; «Approximation error in finite element calculation of viscoelastic fluid flows» ; Journal of Non-Newtonian Fluid Mechanics **10**, p. 31–54 (1982). ISSN 03770257. 114

[296] D. Rajagopalan, R. C. Armstrong & R. A. Brown ; «Finite element methdos for calculation of steady, viscoelastic flow using constitutive equations with a Newtonian viscosity» ; Journal of Non-Newtonian Fluid Mechanics **36**, p. 159–192 (1990). ISSN 03770257. 114

[297] R. Guénette & M. Fortin ; «A new mixed finite element method for computing viscoelastic flows» ; Journal of Non-Newtonian Fluid Mechanics **60**, p. 27–52 (1995). ISSN 03770257. 114

[298] M. Fortin, R. Guénette & R. Pierre ; «Numerical analysis of the modified EVSS method» ; Computer Methods in Applied Mechanics and Engineering **143**, p. 79–95 (1997). ISSN 00457825. 115, 116

[299] P. Constantin & M. Kliegl ; «Note on Global Regularity for Two-Dimensional Oldroyd-B Fluids with Diffusive Stress» ; Archive for Rational Mechanics and Analysis **206**, p. 725–740 (2012). ISSN 00039527. 115

[300] J. Y. Chemin & N. Masmoudi ; «About lifespan of regular solutions of equations related to viscoelastic fluids» ; SIAM Journal on Mathematical Analysis **33**, p. 84–112 (2001). ISSN 00361410. 115

[301] F.-H. Lin, C. Liu & P. Zhang ; «On hydrodynamics of viscoelastic fluids» ; Communications on Pure and Applied Mathematics **58**, p. 1437–1471 (2005). ISSN 0010-3640. 115

[302] J. M. Rallison & E. J. Hinch ; «Do we understand the physics in the constitutive equation ?» ; Journal of Non-Newtonian Fluid Mechanics **29**, p. 37–55 (1988). ISSN 03770257. 115

[303] B. Thomases & M. Shelley ; «Emergence of singular structures in Oldroyd-B fluids» ; Physics of Fluids **19** (2007). ISSN 10706631. 115

[304] M. Behr, M. Behr, D. Arora & M. Pasquali ; «STABILIZED FINITE ELEMENT METHODS OF GLS TYPE FOR OLDROYD-B VISCOELASTIC FLUID» ; (2004)http://citeseerx.ist.psu.edu/viewdoc/summary?doi=10.1.1.64.8041. 117

[305] Y. Cao, X. G. Ren, X. W. Guo, M. Wang, Q. Wang, X. H. Xu & X. J. Yang ; «A new method to simulate free surface flows for Viscoelastic fluid» ; Advances in Materials Science and Engineering **2015** (2015). ISSN 16878442. 117

[306] T. J. Craven, J. M. Rees & W. B. Zimmerman ; «Stabilised finite element modelling of oldroyd-B viscoelastic flows» ; Proceedings of the COMSOL Users Conference p. 137–150 (2006)http://static2.comsol.co.in/papers/1563/download/Zimmerman.pdf. 117

[307] S. Meng, K. L. Xin & G. Evans ; «Numerical simulation of Oldroyd-B fluid in a contraction channel» ; Journal of Supercomputing **22**, p. 29–43 (2002). ISSN 09208542. 117

[308] C. Chauvière & R. G. Owens ; «How accurate is your solution ? Error indicators for viscoelastic flow calculations» ; Journal of Non-Newtonian Fluid Mechanics **95**, p. 1–33 (2000). ISSN 03770257. 117

[309] H. S. Dou & N. Phan-Thien ; «The flow of an Oldroyd-B fluid past a cylinder in a channel : adaptive viscosity vorticity (DAVSS-ω) formulation» ; Journal of Non-Newtonian Fluid Mechanics **87**, p. 47–73 (1999). ISSN 03770257. 117

[310] G. H. McKinley, R. C. Armstrong & R. A. Brown ; «The wake instability in viscoelastic flow past confined circular cylinders» ; Philosophical Transactions - Royal Society of London, A **344**, p. 265–304 (1993). 117

[311] S. W. Funke, M. Nordaas, Ø. Evju, M. S. Alnæs & K. A. Mardal ; «Variational data assimilation for transient blood flow simulations : Cerebral aneurysms as an illustrative example» ; International Journal for Numerical Methods in Biomedical Engineering **35** (2019). ISSN 20407947. 118, 133

[312] P. Stumm & A. Walther ; «New algorithms for optimal online checkpointing» ; SIAM Journal on Scientific Computing **32**, p. 836–854 (2010). ISSN 10648275. 119

[313] J. M. Fitzpatrick ; «The existence of geometrical density-image transformations corresponding to object motion» ; Computer Vision, Graphics, and Image Processing **44**, p. 155 – 174 (1988). ISSN 0734-189X. http://www.sciencedirect.com/science/article/pii/S0734189X88800033. 122

[314] T. Liu & L. Shen ; «Fluid flow and optical flow» ; Journal of Fluid Mechanics (2008). ISSN 00221120. 122, 192

[315] N. Dunford & J. T. Schwartz ; *Linear Operators, Parts I and II* (Wiley-Interscience) (1988) ; ISBN 978-0-471-60847-9. http://eu.wiley.com/WileyCDA/WileyTitle/productCd-0471608475.html. 122

[316] E. M. Mikhail, J. S. Bethel & J. C. McGlone ; *Introduction to modern photogrammetry* (Wiley) (2001) ; ISBN 9780471309246. 124

[317] C. S. Fraser ; «Photogrammetric Camera Component Calibration : A Review of Analytical Techniques» ; dans «Calibration and Orientation of Cameras in Computer Vision», p. 95–121 (2001). 124

[318] T. Liu ; «Geometric and kinematic aspects of image-based measurements of deformable bodies» ; (2004). 124

[319] T. Corpetti, D. Heitz, G. Arroyo, E. Mémin & A. Santa-Cruz ; «Fluid experimental flow estimation based on an optical-flow scheme» ; Experiments in Fluids **40**, p. 80–97 (2006). ISSN 07234864. 124

[320] N. Papadakis, T. Corpetti & E. Mémin ; «Dynamically consistent optical flow estimation» ; dans «Proceedings of the IEEE International Conference on Computer Vision», (2007). 125

[321] U. S. Schwarz & J. R. Soiné ; «Traction force microscopy on soft elastic substrates : A guide to recent computational advances» ; (2015). 126, 127, 131

[322] M. Dembo, T. Oliver, A. Ishihara & K. Jacobson ; «Imaging the traction stresses exerted by locomoting cells with the elastic substratum method» ; Biophysical Journal **70**, p. 2008–2022 (1996). ISSN 00063495. 126, 127

[323] M. Dembo & Y. L. Wang ; «Stresses at the cell-to-substrate interface during locomotion of fibroblasts» ; Biophysical Journal **76**, p. 2307–2316 (1999). ISSN 00063495. 126, 127

[324] J. L. Tan, J. Tien, D. M. Pirone, D. S. Gray, K. Bhadriraju & C. S. Chen ; «Cells lying on a bed of microneedles : An approach to isolate mechanical force» ; Proceedings of the National Academy of Sciences of the United States of America **100**, p. 1484–1489 (2003). ISSN 00278424. 126

[325] L. Trichet, J. Le Digabel, R. J. Hawkins, S. R. K. Vedula, M. Gupta, C. Ribrault, P. Hersen, R. Voituriez & B. Ladoux ; «Evidence of a large-scale mechanosensing mechanism for cellular adaptation to substrate stiffness» ; Proceedings of the National Academy of Sciences of the United States of America **109**, p. 6933–6938 (2012). ISSN 00278424. 126

[326] S. Ghassemi, G. Meacci, S. Liu, A. A. Gondarenko, A. Mathur, P. Roca-Cusachs, M. P. Sheetz & J. Hone ; «Cells test substrate rigidity by local contractions on submicrometer pillars» ; Proceedings of the National Academy of Sciences of the United States of America **109**, p. 5328–5333 (2012). ISSN 00278424. 126

[327] R. W. Style, R. Boltyanskiy, G. K. German, C. Hyland, C. W. Macminn, A. F. Mertz, L. A. Wilen, Y. Xu & E. R. Dufresne ; «Traction force microscopy in physics and biology» ; (2014). 126, 127

[328] J. P. Butler, I. M. Tolić-Norrelykke, B. Fabry & J. J. Fredberg ; «Traction fields, moments, and strain energy that cells exert on their surroundings.» ; American journal of physiology. Cell physiology **282**, p. 595–605 (2002). ISSN 0363-6143. `http://www.ncbi.nlm.nih.gov/pubmed/11832345`. 127

[329] B. Sabass, M. L. Gardel, C. M. Waterman & U. S. Schwarz ; «High resolution traction force microscopy based on experimental and computational advances.» ; Biophysical journal **94**, p. 207–20 (2008). ISSN 1542-0086. `http://www.pubmedcentral.nih.gov/articlerender.fcgi?artid=2134850&tool=pmcentrez&rendertype=abstract`. 127

[330] S. V. Plotnikov, B. Sabass, U. S. Schwarz & C. M. Waterman ; «High-Resolution Traction Force Microscopy» ; dans «Methods in Cell Biology», , tome 123p. 367–394 (Academic Press Inc.) (2014). 127, 135

[331] J. L. Martiel, A. Leal, L. Kurzawa, M. Balland, I. Wang, T. Vignaud, Q. Tseng & M. Théry ; «Measurement of cell traction forces with ImageJ» ; Methods in Cell Biology **125**, p. 269–287 (2015). ISSN 0091679X. 127

[332] Z. Yang, J.-S. Lin, J. Chen & J. H.-C. Wang ; «Determining substrate displacement and cell traction fields–a new approach.» ; Journal of theoretical biology **242**, p. 607–16 (2006). ISSN 0022-5193. `http://www.ncbi.nlm.nih.gov/pubmed/16782134`. 127

[333] S. S. Hur, Y. Zhao, Y. S. Li, E. Botvinick & S. Chien ; «Live Cells Exert 3-Dimensional Traction Forces on Their Substrata» ; Cellular and Molecular Bioengineering **2**, p. 425–436 (2009). ISSN 18655025. 127

[334] W. R. Legant, J. S. Miller, B. L. Blakely, D. M. Cohen, G. M. Genin & C. S. Chen ; «Measurement of mechanical tractions exerted by cells in three-dimensional matrices.» ; Nature methods **7**, p. 969–71 (2010). ISSN 1548-7105. `http://www.pubmedcentral.nih.gov/articlerender.fcgi?artid=3056435&tool=pmcentrez&rendertype=abstract`. 127

[335] T. M. Koch, S. Münster, N. Bonakdar, J. P. Butler & B. Fabry ; «3D Traction forces in cancer cell invasion.» ; PloS one **7**, p. e33 476 (2012). ISSN 1932-6203. `http://www.pubmedcentral.nih.gov/articlerender.fcgi?artid=3316584&tool=pmcentrez&rendertype=abstract`. 127

[336] J. Steinwachs, C. Metzner, K. Skodzek, N. Lang, I. Thievessen, C. Mark, S. Münster, K. E. Aifantis & B. Fabry ; «Three-dimensional force microscopy of cells in biopolymer networks» ; Nature Methods **13**, p. 171–176 (2016). ISSN 15487105. 127, 195

[337] D. Ambrosi ; «Cellular Traction as an Inverse Problem» ; (2006). `https://www.jstor.org/stable/40233361`. 127, 131

[338] E. Bar-Kochba, J. Toyjanova, E. Andrews, K. S. Kim & C. Franck ; «A Fast Iterative Digital Volume Correlation Algorithm for Large Deformations» ; Experimental Mechanics **55**, p. 261–274 (2015). ISSN 17412765. 127

[339] A. Kirsch ; *An Introduction to the Mathematical Theory of Inverse Problems* (Springer) (2011). 127

[340] H. Tanimoto & M. Sano ; «Dynamics of Traction Stress Field during Cell Division» ; Phys. Rev. Lett. **109**, p. 248 110 (2012). `https://link.aps.org/doi/10.1103/PhysRevLett.109.248110`. 127

[341] J. Huang, L. Qin, X. Peng, T. Zhu, C. Xiong, Y. Zhang & J. Fang ; «Cellular traction force recovery : An optimal filtering approach in two-dimensional Fourier space» ; Journal of Theoretical Biology **259**, p. 811 – 819 (2009). ISSN 0022-5193. `http://www.sciencedirect.com/science/article/pii/S0022519309002306`. 127

[342] Z. Deyl & J. Hovrejvsí ; «Chapter 6. Electromigration techniques» ; dans Z. Deyl (rédacteur), «Separation Methods», , *New Comprehensive Biochemistry*, tome 8p. 415 – 496 (Elsevier) (1984). `http://www.sciencedirect.com/science/article/pii/S0167730608602227`. 128

[343] I. Thievessen, P. M. Thompson, S. Berlemont, K. M. Plevock, S. V. Plotnikov, A. Zemljic-Harpf, R. S. Ross, M. W. Davidson, G. Danuser, S. L. Campbell & C. M. Waterman ; «Vinculin–actin interaction couples actin retrograde flow to focal

adhesions, but is dispensable for focal adhesion growth» ; The Journal of Cell Biology **202**, p. 163–177 (2013). ISSN 0021-9525. `http://jcb.rupress.org/content/202/1/163`; `http://jcb.rupress.org/content/202/1/163.full.pdf`. 129

[344] C. E. Kandow, P. C. Georges, P. A. Janmey & K. A. Beningo ; «Polyacrylamide Hydrogels for Cell Mechanics : Steps Toward Optimization and Alternative Uses» ; dans «Cell Mechanics», , *Methods in Cell Biology*, tome 83p. 29 – 46 (Academic Press) (2007). `http://www.sciencedirect.com/science/article/pii/S0091679X07830020`. 129

[345] C. M. Cesa, N. Kirchgessner, D. Mayer, U. S. Schwarz, B. Hoffmann & R. Merkel ; «Micropatterned silicone elastomer substrates for high resolution analysis of cellular force patterns» ; Review of Scientific Instruments **78** (2007). `https://doi.org/10.1063/1.2712870`. 129

[346] T. J. R. Hughes ; «Chapter 4 : Mixed and Penalty Methods, Reduced and Selective Integration, and Sundry Variational Crimes» ; dans «The Finite Element Method : Linear Static and Dynamic Finite Element Analysis», (Dover Civil and Mechanical Engineering) (2000). 130, 132

[347] H. P. Langtangen & A. Logg ; *Solving PDEs in Python* (Springer International Publishing) (2016). 131, 148

[348] K.-A. Mardal ; «Lecture 22 : Linear elasticity» ; dans «FEniCS Course», (2017). `https://folk.uio.no/kent-and/sommerskole/material/lecture{_}22{_}linear{_}elasticity.pdf`. 131

[349] R. Becker, E. Burman & P. Hansbo ; «A Nitsche extended finite element method for incompressible elasticity with discontinuous modulus of elasticity» ; Computer Methods in Applied Mechanics and Engineering **198**, p. 3352–3360 (2009). ISSN 00457825. 132, 133

[350] B. P. Lamichhane ; «A mixed finite element method for nearly incompressible elasticity and Stokes equations using primal and dual meshes with quadrilateral and hexahedral grids» ; Journal of Computational and Applied Mathematics **260**, p. 356–363 (2014). ISSN 03770427. 132

[351] G. Vitale, L. Preziosi & D. Ambrosi ; «Force traction microscopy : An inverse problem with pointwise observations» ; Journal of Mathematical Analysis and Applications **395**, p. 788–801 (2012). ISSN 0022247X. 132

[352] P. G. Ciarlet & C. Mardare ; «An Introduction to Shell Theory» ; dans «Differential Geometry : Theory and Applications», p. 94–184 (Higher Education Press & World Scientific) (2008). 132

[353] C. Mardare ; «Mathematical methods in elasticity» ; Rapport technique (2019). `https://www.ljll.math.upmc.fr/MathModel/enseignement/polycopies/mardare.pdf`. 132

[354] T. J. R. Hughes ; «Chapter 2 : Formulation of Two- and Three-Dimensional Boundary-Value Problems» ; dans «The Finite Element Method : Linear Static and Dynamic Finite Element Analysis», (Dover Civil and Mechanical Engineering) (2000). 132

[355] J. T. Oden & G. F. Carey ; *Finite elements : Mathematical Aspects* (Prentice-Hall) (1981) ; ISBN 9780133170818. 132

[356] G. Duvaut & J. L. Lions ; *Inequalities in Mechanics and Physics* (Springer Berlin Heidelberg) (1976) ; ISBN 9783642661655. 132

[357] C. Clason ; «What is the general idea of Nitsche's method in numerical analysis ?» ; (2015). `https://scicomp.stackexchange.com/questions/19910/what-is-the-general-idea-of-nitsches-method-in-numerical-analysis`. 133

[358] J. Nitsche ; «Über ein Variationsprinzip zur Lösung von Dirichlet-Problemen bei Verwendung von Teilräumen, die keinen Randbedingungen unterworfen sind» ; Abhandlungen aus dem Mathematischen Seminar der Universität Hamburg **36**, p. 9–15 (1971). ISSN 18658784. 133

[359] J. Freund & R. Stenberg ; «On weakly imposed boundary conditions for second order problems» ; (1995). 133

[360] R. Mekhlouf, A. Baggag & L. Remaki ; «Assessment of Nitsche's Method for Dirichlet Boundary Conditions Treatment» ; Journal of Fluid Flow, Heat and Mass Transfer **4**, p. 54–63 (2017). 133

[361] L. Chen ; «INF-SUP CONDITIONS» ; (2014)`https://www.math.uci.edu/{~}chenlong/226/infsup.pdf`. 133

[362] K. J. Bathe ; «Inf-sup condition and its evaluation for mixed finite element methods» ; Computers and Structures **79**, p. 243–252 (2001). ISSN 00457949. 133

[363] K.-J. Bathe ; «Chapter 4 : Formulation of the Finite Element Method-Linear Analysis in Solid and Structural Mechanics» ; dans «Finite Element Procedures», (2007) ; ISBN 978-0979004902. `https://www.amazon.com/Finite-Element-Procedures-K-J-Bathe/dp/097900490X`. 133

[364] P. Hansbo ; «Nitsche's method for interface problems in computational mechanics» ; GAMM-Mitteilungen **28**, p. 183–206 (2005). 133

[365] F. Chouly, P. Hild & Y. Renard ; «Symmetric and non-symmetric variants of Nitsche's method for contact problems in elasticity : theory and numerical experiments» ; Mathematics of Computation **84**, p. 1089–1112 (2014). ISSN 0025-5718. 133

[366] X. Trepat, M. R. Wasserman, T. E. Angelini, E. Millet, D. A. Weitz, J. P. Butler & J. J. Fredberg ; «Physical forces during collective cell migration» ; Nature Physics **5**, p. 426–430 (2009). ISSN 17452481. 134

[367] M. Uroz, A. Garcia-Puig, I. Tekeli, A. Elosegui-Artola, J. F. Abenza, A. Marín-Llauradó, S. Pujals, V. Conte, L. Albertazzi, P. Roca-Cusachs, Á. Raya & X. Trepat ; «Traction forces at the cytokinetic ring regulate cell division and polyploidy in the migrating zebrafish epicardium» ; Nature Materials (2019). ISSN 14764660. 134

[368] J. Xia ; «Matrix-free sparse direct solvers» ; Rapport technique (2013). 142

[369] J. Xia ; «Randomized sparse direct solvers» ; SIAM Journal on Matrix Analysis and Applications **34**, p. 197–227 (2012). ISSN 08954798. 142

[370] M. Hestenes & E. Stiefel ; «Methods of conjugate gradients for solving linear systems» ; Journal of Research of the National Bureau of Standards **49**, p. 409 (1952). ISSN 0091-0635. 142

[371] J. R. Shewchuk ; «An Introduction to the Conjugate Gradient Method Without the Agonizing Pain» ; Rapport technique (1994). 142, 143

[372] D. Rich ; «What is an intuitive explanation of what the conjugate gradient method is ?» ; (2017). https://www.quora.com/What-is-an-intuitive-explanation-of-what-the-conjugate-gradient-method-is. 142

[373] S. C. Eisenstat & H. F. Walker ; «Choosing the forcing terms in an inexact Newton method» ; SIAM Journal of Scientific Computing **17**, p. 16–32 (1996). ISSN 10648275. 142

[374] R. S. Dembo, S. C. Eisenstat & T. Steihaug ; «Inexact Newton Methods» ; (1982). https://www.jstor.org/stable/2156954. 142

[375] L. Armijo ; «Minimization of functions having lipschitz continuous first partial derivatives» ; Pacific Journal of Mathematics **16**, p. 1–3 (1966). ISSN 00308730. 142

[376] A. Gunnel, R. Herzog & E. Sachs ; «A note on preconditioners and scalar products in Krylov subspace methods for self-adjoint problems in Hilbert space» ; Electron. Trans. Numer. Anal. **41**, p. 13–20 (2014). 143

[377] J. Schöberl & W. Zulehner ; «Symmetric indefinite preconditioners for saddle point problems with applications to PDE-constrained optimization problems» ; SIAM Journal on Matrix Analysis and Applications **29**, p. 752–773 (2007). ISSN 08954798. 143

[378] T. Bui-Thanh, O. Ghattas, J. Martin & G. Stadler ; «A computational framework for infinite-dimensional bayesian inverse problems part I : The linearized case, with application to global seismic inversion» ; SIAM Journal on Scientific Computing **35** (2013). ISSN 10648275. 143, 163

[379] T. Schwedes, S. W. Funke & D. A. Ham ; «An iteration count estimate for a mesh-dependent steepest descent method based on finite elements and Riesz inner product representation» ; ArXiv p. 1–13 (2016)http://arxiv.org/abs/1606.08069 ; 1606.08069. 144

[380] M. Nordaas & S. W. Funke ; «The Moola optimisation package» ; (2016). https://github.com/funsim/moola. 144, 148

[381] K. Stüben ; «A review of algebraic multigrid» ; Journal of Computational and Applied Mathematics **128**, p. 281–309 (2001). ISSN 03770427. 145

[382] Y. Shapira ; «Algebraic Multigrid» ; dans «Matrix-Based Multigrid : Theory and Applications», (2003). 145

[383] B. M. Irons ; «A frontal solution program for finite element analysis» ; International Journal for Numerical Methods in Engineering **2**, p. 5–32 (1970). ISSN 10970207. 145

[384] P. R. Amestoy, I. S. Duff, J.-Y. L'Excellent & J. Koster ; «A Fully Asynchronous Multifrontal Solver Using Distributed Dynamic Scheduling» ; SIAM Journal on Matrix Analysis and Applications **23**, p. 15–41 (2001). ISSN 0895-4798. http://epubs.siam.org/doi/abs/10.1137/S0895479899358194. 145, 148

[385] P. R. Amestoy, I. S. Duff & J. Y. L'Excellent ; «Multifrontal parallel distributed symmetric and unsymmetric solvers» ; Computer Methods in Applied Mechanics and Engineering **184**, p. 501–520 (2000). ISSN 00457825. 145

[386] C. C. Paige & M. A. Saunders ; «Solution of Sparse Indefinite Systems of Linear Equations» ; (1975). https://www.jstor.org/stable/2156178. 146

[387] C. C. Paige, B. N. Parlett & H. A. van der Vorst ; «Approximate solutions and eigenvalue bounds from Krylov subspaces» ; Numerical Linear Algebra with Applications **2**, p. 115–133 (1995). ISSN 10991506. 146

[388] Y. Saad & M. H. Schultz ; «GMRES : A Generalized Minimal Residual Algorithm for Solving Nonsymmetric Linear Systems» ; SIAM Journal on Scientific and Statistical Computing **7**, p. 856–869 (1986). ISSN 0196-5204. 146

[389] X. Bresson & T. F. Chan ; «Fast dual minimization of the vectorial total variation norm and applications to color image processing» ; Inverse Problems and Imaging **2**, p. 455–484 (2008). ISSN 19308345. 146, 202

[390] D. Schumacher ; «GENERAL FILTERED IMAGE RESCALING» ; dans «Graphics Gems III (IBM Version)», p. 8–16 (Elsevier) (1992). `https://linkinghub.elsevier.com/retrieve/pii/B9780080507552500129`. 147

[391] P. Ruhnau, T. Kohlberger, C. Schnörr & H. Nobach ; «Variational optical flow estimation for particle image velocimetry» ; Experiments in Fluids **38**, p. 21–32 (2005). ISSN 07234864. 147

[392] J. D. Hunter ; «Matplotlib : A 2D graphics environment» ; Computing in Science & Engineering **9**, p. 90–95 (2007). 148

[393] M. A. Heroux, R. A. Bartlett, V. E. Howle, R. J. Hoekstra, J. J. Hu, T. G. Kolda, R. B. Lehoucq, K. R. Long, R. P. Pawlowski, E. T. Phipps, A. G. Salinger, H. K. Thornquist, R. S. Tuminaro, J. M. Willenbring, A. Williams & K. S. Stanley ; «An overview of the trilinos project» ; (2005). 148

[394] C. L. Lawson, R. J. Hanson, D. R. Kincaid & F. T. Krogh ; «Basic Linear Algebra Subprograms for Fortran Usage» ; ACM Transactions on Mathematical Software (TOMS) **5**, p. 308–323 (1979). ISSN 15577295. 148

[395] E. Anderson, Z. Bai, C. Bischof, L. S. Blackford, J. Demmel, J. Dongarra, J. Du Croz, A. Greenbaum, S. Hammarling, A. McKenney & D. Sorensen ; *LAPACK Users' Guide* (Society for Industrial and Applied Mathematics) (1999) ; ISBN 978-0-89871-447-0. `http://epubs.siam.org/doi/book/10.1137/1.9780898719604`. 148

[396] The MPI Forum ; «MPI : a message passing interface» ; dans «Proceedings of the 1993 ACM/IEEE conference on Supercomputing - Supercomputing '93», p. 878–883 (ACM Press, New York, New York, USA) (1993) ; ISBN 0818643404. `http://portal.acm.org/citation.cfm?doid=169627.169855`. 148

[397] U. Villa, N. Petra & O. Ghattas ; «hIPPYlib : An Extensible Software Framework for Large-Scale Inverse Problems Governed by PDEs ; Part I : Deterministic Inversion and Linearized Bayesian Inference» ; (2019)`https://hippylib.github.io/` ; `1909.03948`. 148, 163

[398] P. Lindstrom & G. Turk ; «Evaluation of memoryless simplification» ; IEEE Transactions on Visualization and Computer Graphics **5**, p. 98–115 (1999). ISSN 10772626. 149

[399] C. R. Vogel ; *Computational Methods for Inverse Problems* (Society for Industrial and Applied Mathematics) (2002). 159, 160

[400] T. Isaac, N. Petra, G. Stadler & O. Ghattas ; «Scalable and efficient algorithms for the propagation of uncertainty from data through inference to prediction for large-scale problems, with application to flow of the Antarctic ice sheet» ; Journal of Computational Physics **296**, p. 348–368 (2015). ISSN 10902716. 160, 163, 170, 206

[401] O. Ghattas, Y. Marzouk, M. Parno, N. Petra, G. Stadler & U. Villa ; «Inverse Problems : Systematic Integration of Data with Models under Uncertainty» ; (2018). `http://g2s3.com`. 160, 163

[402] O. Ghattas ; «Computational and Variational Inverse Problems» ; (2015). `https://users.oden.utexas.edu/{~}omar/inverse{_}problems/index.html`. 160

[403] U. Villa ; «Computational and Variational Inverse Problems» ; (2015). `https://uvilla.github.io/inverse15/`. 160

[404] N. Halko, P. G. Martinsson & J. A. Tropp ; «Finding structure with randomness : Probabilistic algorithms for constructing approximate matrix decompositions» ; SIAM Review **53**, p. 217–288 (2011). ISSN 00361445. 160

[405] N. Kishore Kumar & J. Schneider ; «Literature survey on low rank approximation of matrices» ; Linear and Multilinear Algebra **65**, p. 2212–2244 (2017). ISSN 15635139. 160

[406] A. K. Saibaba, J. Lee & P. K. Kitanidis ; «Randomized algorithms for generalized Hermitian eigenvalue problems with application to computing Karhunen-Loève expansion» ; Numerical Linear Algebra with Applications **23**, p. 314–339 (2016). ISSN 10991506. 160, 161

[407] J. P. Kaipio & E. Somersalo ; «Statistical and computational inverse problems» ; dans «Applied Mathematical Sciences (Switzerland)», , tome 160p. i–339 (Springer) (2005). 163, 166, 169

[408] T. Bui-Thanh ; «A Gentle Tutorial on Statistical Inversion using the Bayesian Paradigm» ; Rapport technique (2012). `http://citeseerx.ist.psu.edu/viewdoc/summary?doi=10.1.1.716.9306`. 163, 168

[409] M. Parno, P. Conrad, A. Davis & Y. Marzouk ; «MIT uncertainty quantification (MUQ) library» ; (2014)`http://muq.mit.edu`. 163

[410] A. M. Stuart ; «Inverse problems : A Bayesian perspective» ; (2010). 164, 166

[411] J. P. Kaipio, V. Kolehmainen, E. Somersalo & M. Vauhkonen ; «Statistical inversion and Monte Carlo sampling methods in electrical impedance tomography» ; Inverse Problems **16**, p. 1487–1522 (2000). ISSN 02665611. 166

[412] S. Siltanen, V. Kolehmainen, S. Järvenpää, J. P. Kaipio, P. Koistinen, M. Lassas, J. Pirttilä & E. Somersalo ; «Statistical inversion for medical x-ray tomography with few radiographs : I. General theory» ; (2003). 166

[413] V. Kolehmainen, S. Siltanen, S. Järvenpää, J. P. Kaipio, P. Koistinen, M. Lassas, J. Pirttilä & E. Somersalo ; «Statistical inversion for medical x-ray tomography with few radiographs : II. Application to dental radiology» ; Physics in Medicine and Biology **48**, p. 1465–1490 (2003). ISSN 00319155. 166

[414] M. Lassas & S. Siltanen ; «Can one use total variation prior for edge-preserving Bayesian inversion ?» ; Inverse Problems **20**, p. 1537–1563 (2004). ISSN 02665611. 166

[415] M. Lassas, E. Saksman & S. Siltanen ; «Discretization-invariant Bayesian inversion and Besov space priors» ; (2009)`http://arxiv.org/abs/0901.4220` ; `0901.4220`. 166

[416] D. Calvetti & E. Somersalo ; «A Gaussian hypermodel to recover blocky objects» ; Inverse Problems **23**, p. 733–754 (2007). ISSN 02665611. 166

[417] Z. Yao, Z. Hu & J. Li ; «A TV-Gaussian prior for infinite-dimensional Bayesian inverse problems and its numerical implementations» ; Inverse Problems **32** (2016). ISSN 13616420. 166

[418] J. Kaipio & E. Somersalo ; «Statistical inverse problems : Discretization, model reduction and inverse crimes» ; Journal of Computational and Applied Mathematics **198**, p. 493–504 (2007). ISSN 03770427. 166, 169

[419] J. Kaipio & V. Kolehmainen ; «Chapter 32 : Approximate marginalization over modelling errors and uncertainties in inverse problems» ; dans «Bayesian Theory and Applications», p. 644–672 (Oxford University Press) (2013). 169, 170

[420] K. Brandt Petersen & M. Syskind Pedersen ; «The Matrix Cookbook» ; Rapport technique ; Technical University of Denmark (2012). 170, 205, 207

[421] A. Repetti, M. Pereyra & Y. Wiaux ; «Scalable Bayesian Uncertainty Quantification in Imaging Inverse Problems via Convex Optimization» ; SIAM Journal on Imaging Sciences **12**, p. 87–118 (2019). `https://doi.org/10.1137/18M1173629`. 171

[422] N. W. Tschoegl ; «Representation of Linear Viscoelastic Behavior by Series-Parallel Models» ; dans «The Phenomenological Theory of Linear Viscoelastic Behavior», p. 69–156 (Springer Berlin Heidelberg, Berlin, Heidelberg) (1989). `http://www.springerlink.com/index/10.1007/978-3-642-73602-5{_}3`. 186

[423] T. Matolcsi & P. Ván ; «Absolute time derivatives» ; Journal of Mathematical Physics **48**, p. 053 507–053 507 (2007). `math-ph/0608065`. 188

[424] H. Flanders ; «Differentiation Under the Integral Sign» ; The American Mathematical Monthly **80**, p. 615 (1973). ISSN 00029890. 192

[425] A. Boquet-Pujadas & J.-C. Olivo-Marin ; «Multiple variational image assimilation for accessible micro-elastography» ; Journal of Physics: Conference Series **1131**, p. 012 014 (2018). ISSN 1742-6588. 195, 196

[426] T. Yeung, P. C. Georges, L. A. Flanagan, B. Marg, M. Ortiz, M. Funaki, N. Zahir, W. Ming, V. Weaver & P. A. Janmey ; «Effects of substrate stiffness on cell morphology, cytoskeletal structure, and adhesion» ; Cell Motility and the Cytoskeleton **60**, p. 24–34 (2005). ISSN 08861544. 195

[427] T. Boudou, J. Ohayon, C. Picart & P. Tracqui ; «An extended relationship for the characterization of Young's modulus and Poisson's ratio of tunable polyacrylamide gels.» ; Biorheology **43**, p. 721–8 (2006)ISSN 0006-355X. `http://www.ncbi.nlm.nih.gov/pubmed/17148855`. 195

[428] D. Wirtz ; «Particle-Tracking Microrheology of Living Cells : Principles and Applications» ; Annual Review of Biophysics **38**, p. 301–326 (2009). ISSN 1936-122X. 195

[429] S. F. Norrelykke & H. Flyvbjerg ; «Harmonic oscillator in heat bath : Exact simulation of time-lapse-recorded data and exact analytical benchmark statistics» ; Physical Review E - Statistical, Nonlinear, and Soft Matter Physics **83** (2011). ISSN 15393755. 196

[430] T. Savin & P. S. Doyle ; «Static and dynamic errors in particle tracking microrheology.» ; Biophysical journal **88**, p. 623–638 (2005). ISSN 0006-3495. `http://www.scopus.com/inward/record.url?eid=2-s2.0-11244278527&partnerID=tZOtx3y1`. 196

[431] T. Maier & T. Haraszti ; «Python algorithms in particle tracking microrheology» ; Chemistry Central Journal **6** (2012). ISSN 1752153X. 196

[432] K. M. Kennedy, L. Chin, R. A. McLaughlin, B. Latham, C. M. Saunders, D. D. Sampson & B. F. Kennedy ; «Quantitative micro-elastography : Imaging of tissue elasticity using compression optical coherence elastography» ; Scientific Reports **5** (2015). ISSN 20452322. 196

[433] D. Huh, B. D. Matthews, A. Mammoto, M. Montoya-Zavala, H. Yuan Hsin & D. E. Ingber ; «Reconstituting organ-level lung functions on a chip» ; Science **328**, p. 1662–1668 (2010). ISSN 00368075. 196

[434] S. Es'haghian, K. M. Kennedy, P. Gong, D. D. Sampson, R. A. McLaughlin & B. F. Kennedy ; « Optical palpation in vivo : imaging human skin lesions using mechanical contrast » ; Journal of Biomedical Optics **20**, p. 016 013 (2015). ISSN 1083-3668. 196

[435] P. E. Barbone & J. C. Bamber ; «Quantitative elasticity imaging : What can and cannot be inferred from strain images» ; Physics in Medicine and Biology **47**, p. 2147–2164 (2002). ISSN 00319155. 197

[436] S. Di Zenzo ; «A note on the gradient of a multi-image» ; Computer Vision, Graphics and Image Processing **33**, p. 116–125 (1986). ISSN 0734189X. 202

[437] G. Sapiro & D. L. Ringach ; «Anisotropic diffusion of multivalued images with applications to color filtering» ; IEEE Transactions on Image Processing **5**, p. 1582–1586 (1996). ISSN 10577149. 202

[438] G. Sapiro ; «Vector-valued active contours» ; dans «Proceedings CVPR IEEE Computer Society Conference on Computer Vision and Pattern Recognition», p. 680–685 (1996). 202

[439] A. Cumani ; «Edge detection in multispectral images» ; CVGIP: Graphical Models and Image Processing **53**, p. 40–51 (1991). ISSN 10499652. 202

[440] B. Goldluecke & D. Cremers ; «An approach to vectorial total variation based on geometric measure theory» ; dans «Proceedings of the IEEE Computer Society Conference on Computer Vision and Pattern Recognition», p. 327–333 (2010) ; ISBN 9781424469840 ; ISSN 10636919. 202

[441] A. Borzì & V. Schulz ; *Computational Optimization of Systems Governed by Partial Differential Equations* (Society for Industrial and Applied Mathematics) (2011). 206

[442] H. P. Flath, L. C. Wilcox, V. AkçElik, J. Hill, B. Van Bloemen Waanders & O. Ghattas ; «Fast algorithms for bayesian uncertainty quantification in large-scale linear inverse problems based on low-rank partial hessian approximations» ; SIAM Journal on Scientific Computing **33**, p. 407–432 (2011). ISSN 10648275. 206

[443] A. Spantini, A. Solonen, T. Cui, J. Martin, L. Tenorio & Y. Marzouk ; «Optimal low-rank approximations of Bayesian linear inverse problems» ; SIAM Journal on Scientific Computing **37**, p. A2451–A2487 (2015). ISSN 10957200. 207

Aleix BOQUET PUJADAS **26 novembre 2019**

Sujet : Approches variationnelles en problèmes inverses pour la caractérisation par imagerie de la dynamique cellulaire

Résumé : Nous proposons une méthode pour calculer des grandeurs physiques telles que les gradients de pressions ∇p, les forces $\mathbf{f}$ et les vitesses $\mathbf{u}$ nécessaires à la description des dynamiques cellulaires interne et externe et pour étudier les mécanismes biologiques qui les gouvernent. Cette méthode non invasive extrait le mouvement de l'objet biologique d'étude de son observation en microscopie de fluorescence conventionelle, tout en inférant les variables d'un modèle physique décrivant son comportement. Cette idée est formuleé comme un problème d'optimisation avec des dérivées partielles comme contraint. Nous l'abordons par les méthodes adjoint et des éléments finis puis l'étendons dans un cadre Bayesian pour en quantifier les incertitudes. Nous utilisons la dynamique des fluides pour décrire l'écoulement cytoplasmique et obtenons des estimations pour $\nabla p, \mathbf{f}, \mathbf{u}$ qui fédèrent et complètent des résultats précédents sur la mécanique de la migration cellulaire. Les forces sont validées par comparaison avec un système nématique incluant des moteurs moléculaires. Nous montrons aussi comment la vitesse obtenu peut être utilisé dans un shéma de *tracking* fondé sur l'advection, ce qui permet de suivir des regions moléculaires et de definir mesures globales. Pour compléter l'étude interne avec des mesures extracellulaires, nous reformulons la microscopie de force de traction dans le cadre de la méthode proposée. Ceci permet une réduction de la propagation des incertitudes et fournit des barres d'erreur. Les logiciels et les outils de visualisation sont disponibles dans le programme *open-source* Icy.

Mots clés : problème inverse, biophysique, imagerie, mechanobiologie, cytoplasme, méthode adjoint, assimilation variationnelle, flux optique, dynamique fluides, mechanique, incertitude

Subject : Variational approaches in inverse problems for image-based characterisation of cellular dynamics

Abstract: We propose a computational imaging framework that estimates 2D or 3D biophysical quantities such as pressure gradients ∇p, forces $\mathbf{f}$ and velocity $\mathbf{u}$ that are required to characterise cell dynamics in and outside the cell and to model the biological mechanisms that govern it. The method works non-invasively by extracting the motion of the biological object of interest observed using conventional fluorescence microscopy, while simultaneously inferring the variables of a physical model describing its constitutive behavior. This idea is formulated as a PDE-constrained optimisation, which we approach with the finite element and adjoint methods, and is subsequently extended into a Bayesian setting to allow for uncertainty quantification. We use a fluid dynamics model to describe cytoplasmic streaming in amoeboid cells, obtaining intracellular estimates of $\nabla p, \mathbf{f}, \mathbf{u}$ that reconcile and extend multiple reports on the mechanics of cell migration. The forces are validated by comparison with an active nematic system that includes molecular motors. We also show how the computed velocity field can be used in an advection-based tracking scheme that is able to follow dynamic molecular regions and allows defining integral measures. To complement the internal insight with extracellular measurements, we reformulate the standard traction force microscopy within our proposed framework, reducing uncertainty propagation and providing error bounds. Related software and visualisation tools are available in the open-source Icy program.

Keywords : inverse problems, biophysics, imaging, mechanobiology, cytoplasm, adjoint method, variational data assimilation, optical flow, fluid dynamics, continuum mechanics, uncertainty